



UNIVERSITAT DE  
BARCELONA

## Time Dependent Processes in Magnetic Systems

Oscar Iglesias



Aquesta tesi doctoral està subjecta a la llicència **Reconeixement- NoComercial – SenseObraDerivada 3.0. Espanya de Creative Commons.**

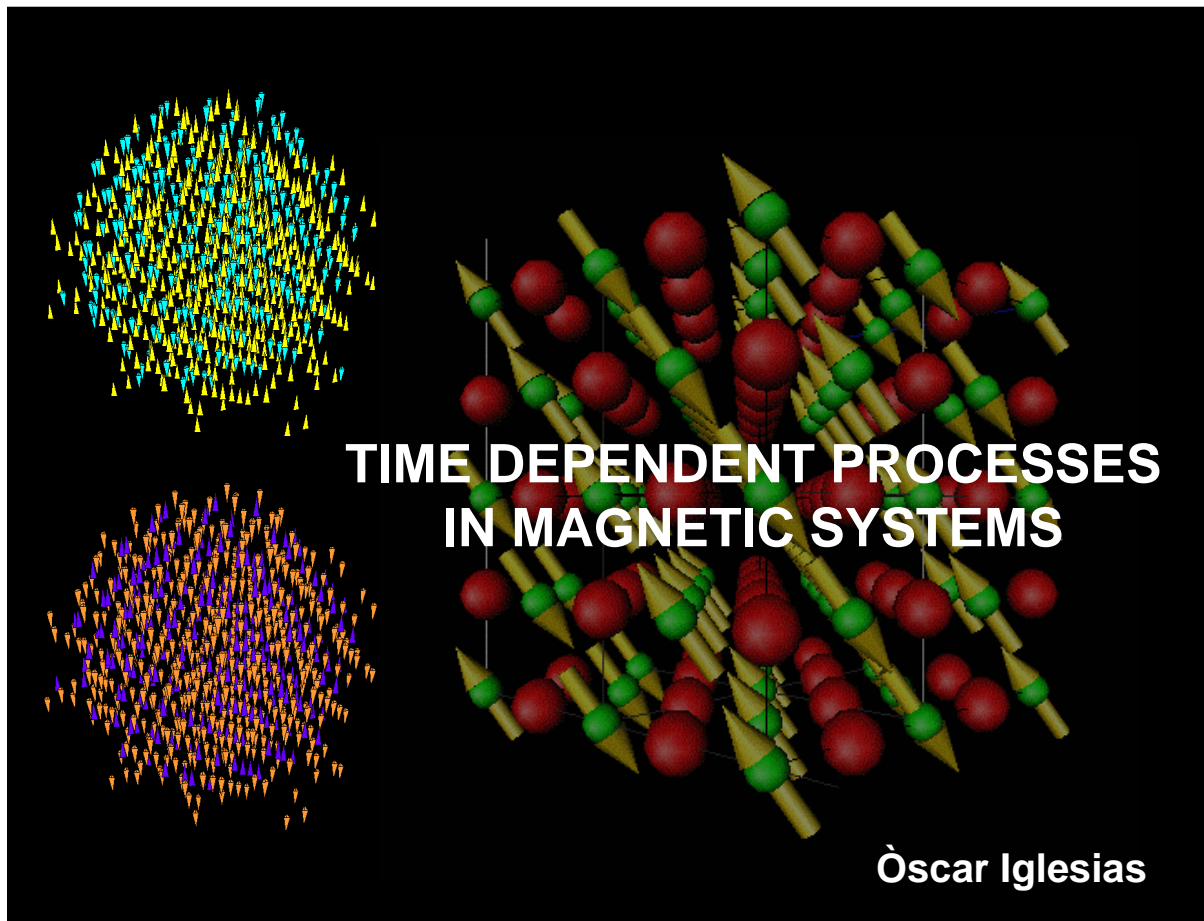
Esta tesis doctoral está sujeta a la licencia **Reconocimiento - NoComercial – SinObraDerivada 3.0. España de Creative Commons.**

This doctoral thesis is licensed under the **Creative Commons Attribution-NonCommercial-NoDerivs 3.0. Spain License.**



UNIVERSITAT DE BARCELONA

Doctoral Thesis



Barcelona, April 2002

**UNIVERSITAT DE BARCELONA**  
**DEPARTAMENT D'ESTRUCTURA I CONSTITUENTS DE LA MATÈRIA**

*Programa de Doctorat Estructura i Constituents de la Matèria (1991-1993)*

**TIME DEPENDENT PROCESSES IN  
MAGNETIC SYSTEMS**

**Memòria presentada per Òscar Iglesias**  
**per optar al grau de doctor en Ciències Físiques.**

**Barcelona, Abril de 2002**

Director de la Tesi:

Tutor de la Tesi:

Amílcar Labarta  
Departament de Física Fonamental

Francesc Salvat  
Departament d'Estructura i Constituents de la  
Matèria

---

*Per l'Alaia i l'Anna,  
els dos peixets que m'han dut a bon port.  
Elles són l'amor de la meva ciència.*

*- No puede estar claro, si lo estuviera sería falso,  
sería científicamente verdadero, quizá, pero falso  
como absoluto. La claridad es una exigencia intelectual y nada más.  
Ojalá pudiéramos saber claro, entender claro al margen de  
la ciencia y de la razón. [. . .]. Probablemente la única  
áncora de salvación sea la ciencia, [. . .].  
Pero además hay que vivir.*

JULIO CORTÁZAR  
*Rayuela, Cap. 28*

*Desde que me he convertido en un esforzado de la pluma, el placer de  
la lectura ha terminado para mí. Lo que hago tiene como fin el estado  
de ánimo de esa mujer en la tumbona enmarcada por las lentes de mi  
catalejo, y es un estado de ánimo que me está vedado...*

ÍTALO CALVINO  
*Si una noche de invierno un viajero...*

*Ponte en marcha sólo.  
Todos los demás solitarios irán a tu lado  
aunque no los veas.*

MIGUEL DE UNAMUNO





# Contents

<b>1</b>	<b>INTRODUCTION</b>	<b>1</b>
1.1	Energy terms in magnetic systems . . . . .	2
1.1.1	Exchange interaction . . . . .	2
1.1.2	Anisotropy energy . . . . .	3
1.1.3	Dipolar interactions . . . . .	5
1.1.4	Magnetostatic energy . . . . .	7
<b>I</b>	<b>SMALL PARTICLE SYSTEMS. THERMAL RELAXATION</b>	<b>13</b>
<b>IA.</b>	<b>Single particle Properties</b>	<b>15</b>
<b>2</b>	<b>EQUILIBRIUM PROPERTIES</b>	<b>17</b>
2.1	Model and parameters . . . . .	18
2.2	Properties of the energy function . . . . .	19
2.3	Energy barriers . . . . .	23
2.4	Low field approximation . . . . .	24
2.5	Effective energy barrier distribution . . . . .	25
2.6	Magnetization curves . . . . .	27
2.6.1	Aligned particles . . . . .	29
2.6.2	Randomly oriented particles with $f(K)$ . . . . .	31
2.7	The Two-State Approximation . . . . .	31
2.8	Conclusions and Discussion . . . . .	35
<b>3</b>	<b>SINGLE PARTICLE MODEL</b>	<b>39</b>
3.1	Introduction . . . . .	39
3.2	Model . . . . .	40
3.3	Equilibrium Properties . . . . .	43
3.3.1	Energy and specific heat . . . . .	43

3.3.2	Magnetization . . . . .	45
3.4	Hysteresis Loops . . . . .	47
3.5	Effects of disorder . . . . .	52
3.5.1	Disorder on the lattice . . . . .	52
3.5.2	Surface disorder . . . . .	53
3.6	Discussion and conclusions . . . . .	55
<b>IB.</b>	<b>Collective effects</b>	<b>62</b>
<b>4</b>	<b>RELAXATION PROCESSES IN ZERO MAGNETIC FIELD</b>	<b>63</b>
4.1	Phenomenological model of relaxation . . . . .	64
4.2	On the logarithmic approximation . . . . .	66
4.2.1	Origin of the logarithmic law . . . . .	67
4.2.2	Range of validity of the logarithmic approximation . . . . .	68
4.3	The $T \ln(t/\tau_0)$ scaling . . . . .	71
4.4	Numerical calculations . . . . .	73
4.5	Energy barrier distributions from the $T \ln(t/\tau_0)$ scaling . . . . .	75
4.6	Experimental verification of the model . . . . .	76
4.6.1	Experimental implementation of the $T \ln(t/\tau_0)$ scaling . . . . .	76
4.6.2	Experimental derivation of energy barrier distributions . . . . .	79
4.7	Magnetic viscosity: a critical review . . . . .	81
<b>5</b>	<b>RELAXATION PROCESSES IN THE PRESENCE OF A MAGNETIC FIELD</b>	<b>85</b>
5.1	Relaxation dynamics in a magnetic field . . . . .	85
5.2	Numerical calculations . . . . .	88
5.2.1	Relaxation curves: $T \ln(t/\tau_0)$ scaling and normalization factors . . . . .	88
5.2.2	Scaling of relaxation curves at different magnetic fields . . . . .	90
5.3	Normalization factors for the relaxation curves . . . . .	95
5.4	Experimental verification . . . . .	98
5.5	Magnetic viscosity and energy barrier distribution . . . . .	100
5.6	Conclusions . . . . .	102
<b>6</b>	<b>1D INTERACTING SYSTEMS</b>	<b>107</b>
6.1	Models . . . . .	108
6.2	Computational details . . . . .	110
6.2.1	Calculation of dipolar energies . . . . .	110
6.2.2	The Monte Carlo algorithm . . . . .	111
6.3	Dipolar fields in 1D . . . . .	112

6.4	Effective energy barrier distributions . . . . .	113
6.5	Relaxation curves: $T \ln(t/\tau_0)$ scaling with interactions . . . . .	114
6.5.1	Simulations of the time dependence of the magnetization . . . . .	114
6.5.2	$T \ln(t/\tau_0)$ scaling in presence of interaction. . . . .	117
6.6	Evolution of $f_{\text{eff}}(E_b)$ and of dipolar fields . . . . .	118
6.7	Effective energy barrier distributions from $T \ln(t/\tau_0)$ scaling . . . . .	120
6.8	Hysteresis Loops . . . . .	122
6.9	Conclusions . . . . .	125
<b>II THIN FILMS WITH PERPENDICULAR ANISOTROPY</b>		<b>129</b>
<b>7</b>	<b>2D INTERACTING SYSTEMS</b>	<b>131</b>
7.1	Review of previous studies . . . . .	131
7.2	Model Hamiltonian . . . . .	133
7.3	Dipolar interactions in spin systems . . . . .	134
7.3.1	Dipolar interaction matrices . . . . .	135
7.4	Computational details . . . . .	135
7.4.1	Boundary conditions . . . . .	137
7.4.2	Symmetries of the dipolar matrices . . . . .	138
7.5	Simulation procedure . . . . .	139
7.5.1	Simulated annealing . . . . .	139
7.5.2	Calculation of dipolar fields . . . . .	140
7.6	Ground state properties . . . . .	141
7.6.1	Phase diagram . . . . .	141
7.6.2	Configurations . . . . .	145
7.6.3	Order parameters . . . . .	148
7.7	Magnetic history dependence . . . . .	149
7.7.1	Relaxation after perpendicular saturation . . . . .	150
7.7.2	Demagnetizing field cycling . . . . .	153
7.8	Conclusions . . . . .	153
<b>III QUANTUM RELAXATION IN MAGNETIC SYSTEMS</b>		<b>161</b>
<b>8</b>	<b>QUANTUM RELAXATION EFFECTS</b>	<b>163</b>
8.1	Macroscopic Quantum Phenomena (MQP) . . . . .	165
8.2	Tunneling rates in the semiclassical approximation at $T=0$ . . . . .	167
8.2.1	Calculation of decay rates (MQT) . . . . .	168

8.2.2	Calculation of ground state splitting (MQC) . . . . .	170
8.3	MQT of the Magnetization . . . . .	172
8.3.1	MQT in single domain particles . . . . .	173
8.4	MQT of Domain Walls . . . . .	173
8.4.1	The Model and the action . . . . .	173
8.4.2	Connection to micromagnetic theory . . . . .	177
8.4.3	The Pinning Potential . . . . .	180
8.4.4	The WKB Exponent . . . . .	181
8.4.5	The crossover temperature . . . . .	184
8.4.6	The Pre-Exponential Factor . . . . .	185
8.5	Quantum nucleation of nonuniform magnetic structures . . . . .	187
8.5.1	Effective action and Sine- Gordon models . . . . .	187
8.6	The role of dissipation . . . . .	189
8.6.1	Conduction electrons . . . . .	189
8.6.2	Magnons . . . . .	189
8.6.3	Phonons . . . . .	191
8.6.4	Photons . . . . .	192
8.6.5	Dissipation in terms of mobility . . . . .	192
8.7	Dicussion and Experimental evidences of MQT and MQC of Domain Walls . . . . .	192
<b>9</b>	<b>CONCLUSIONS</b>	<b>205</b>
<b>IV</b>	<b>APPENDIX: MONTE CARLO METHOD</b>	<b>207</b>
<b>10</b>	<b>MONTE CARLO METHOD FOR CONTINUOUS SPIN SYSTEMS</b>	<b>209</b>
10.1	Finding the ground states of a spin system: Simulated annealing . . . . .	209
10.1.1	Adaptive method for the cone of trial angles . . . . .	210
10.2	Simulation of dynamics: relaxation . . . . .	211
10.2.1	Election of trial jumps . . . . .	211
10.2.2	Variation of the relaxation rates with $\alpha$ and $T$ . . . . .	211
10.2.3	Low temperature dynamics: Non-Arrhenius behaviour . . . . .	214
<b>11</b>	<b>LIST OF PUBLICATIONS</b>	<b>219</b>
<b>12</b>	<b>RESUM EN CATALÀ</b>	<b>221</b>
12.1	Presentació . . . . .	222
12.2	Models d'una única partícula . . . . .	222
12.2.1	Propietats d'equilibri . . . . .	223

---

12.2.2 Model d'una partícula . . . . .	226
12.3 Efectes col·lectius . . . . .	231
12.3.1 Processos de relaxació en absència de camp magnètic . . . . .	231
12.3.2 Processos de relaxació en presència de camp . . . . .	235
12.3.3 Sistemes interactuants en 1D . . . . .	239
12.4 Capes primes amb anisotropia perpendicular . . . . .	241
12.5 Relaxació quàntica . . . . .	247
12.6 Conclusions . . . . .	250



# CHAPTER 1

## INTRODUCTION

*I'm locked up, I'm in something, it's not I.*

SAMUEL BECKETT  
*The Unnameable*

Magnetism of magnetic materials is a quantum effect originating at an atomic level. However, a treatment based on atomic physics is too far from the final objective of this work, which is the description of magnetization processes on the macroscopic scale. Therefore, the magnetic systems of interest will be described in this work as classical continuous media with properties varying continuously in space and time and described by differential equations governing the static and dynamic behaviour. This approach is at the essence of what is called Micromagnetics and will be the point of view adopted here when no interactions between the spins are present. In this case, numerical, if not analytical, solutions can be found by direct solution of the micromagnetic equations. When interactions are present, any attempt to find numerical or analytical solutions for a system of macroscopic size must start from a continuous media approximation and computer simulations must be employed when treating problems from a microscopic level. It is for this reason that the methods employed throughout this work cover from theoretical models and numerical solutions to phenomenological models and computer simulations with even the sporadic inclusion of experimental results.

From a microscopic point of view, hysteresis and time dependent properties are related to the properties of the free energy of the system. Due to the complexity of interactions among constituents contributing to the energy and the presence of structural disorder and distributed properties, the free energy of magnetic systems acquires a complicated multivalley structure with many local minima in which the system can be trapped. This microscopic metastability, together with thermal fluctuations, is the origin of the time dependence of macroscopic magnetic properties. The way by which a system attain its true equilibrium state depends, in general, on the initial state it has been prepared and on the magnetic history it has been submitted to. These are the conditions that will determine the path through the multivalley landscape for the system to reach its final equilibrium state. Therefore, we will be dealing with nonequilibrium thermodynamics and we will be mainly interested here in the description of the laws by which magnetic systems approach equilibrium states.

The work that will be presented is organized as follows: after this introductory chapter (Chapter 1), the rest of the presentation has been divided in three parts. In the first part (Part I), we will present results concerning the thermal relaxation of small particle systems. For this purpose, we will start presenting models concerning a single particle (Part IA). In particular, in Chapter 2, we discuss general equilibrium properties of magnetic particles, and in Chapter 3 we introduce a model for a particle with the internal structure of



maghemite which will be the basis for a study of the magnetic properties by means of Monte carlo simulations. Next, we will continue with the study of collective effects on the thermal relaxation of ensembles of particles (Part IB). In Chapter 4, we describe a phenomenological model for relaxation processes in the absence of magnetic field in terms of what will be called  $T \ln(t/\tau_0)$  scaling. This model will be extended to relaxation processes in the presence of a magnetic field in Chapter 5. In Chapter 6, we consider systems of interacting particles, in particular, we show what are the effects of dipolar interactions on the thermal relaxation of a one dimensional chain of spins, using for these purpose Monte carlo techniques.

The second part (Part II) is devoted to the study of the a model of a thin film with perpendicular anisotropy. Thus, in Chapter 7, the results of Monte Carlo simulations of the ground state properties and the influence of the magnetic history on thin films will be discussed.

The last part (Part III) is dedicated to the study of the influence of quantum phenomena to the time dependence of the magnetization of magnetic systems. In this way, in Chapter 8, we present a theory of the macroscopic quantum tunneling effects on magnetic systems. In particular, the results of calculations of quantum relaxation rates for domain walls based on instanton calculus will be presented. Finally, we close with an appendix dedicated to some details of the Monte Carlo method used throughout this work (Chapter 9) and a presentation of conclusions.

## 1.1 Energy terms in magnetic systems

Different kinds of interactions contribute to the total energy of magnetic systems. In this section the main relevant kinds are described.

### 1.1.1 Exchange interaction

The exchange interaction has its origin on the overlap of the quantum mechanical wave functions of electrons of atoms located at different lattice sites. It is a direct consequence of the exclusion principle and can be phenomenologically described by the Heisenberg exchange Hamiltonian

$$\mathcal{H}_{ex} = \sum_{i \neq j} J_{ij} \mathbf{S}_i \cdot \mathbf{S}_j \quad (1.1)$$

where  $J_{ij}$  is the exchange constant that is related to the overlap integral and has dimensions of energy per unit volume. It can be negative or positive depending on the ferro- or antiferromagnetic character of the magnetic material. Depending on the crystalline structure in which the spins are arranged, and the number of magnetic atoms per unit cell, the value of  $J_{ij}$  may depend on the particular pair of spins considered, so  $J$  may not be a characteristic constant of the material.

Due to the short range of the exchange interaction, the sum in (1.1) is usually restricted to nearest neighbours of a given spins, so that we will write the exchange energy term as

$$\mathcal{H}_{ex} = -J \sum_{n,n} \mathbf{S}_i \cdot \mathbf{S}_j . \quad (1.2)$$

Although the spin appears explicitly in this expression, it is worth remembering that, at an atomic scale, the exchange interaction is concerned only with the spatial part of the electronic wave-function, and that

$\mathbf{S}$  was introduced in the Heisenberg Hamiltonian in a purely phenomenological way. However, for the systems at interest,  $\mathbf{S}$  will represent in the following the direction of the magnetic moment  $\mu$  of a magnetic atom, an object that, for most of the studied phenomena, will be taken as a classical quantity in the sense that the quantization of the degrees of freedom of this high spin are irrelevant.

The Heisenberg Hamiltonian is isotropic with respect to the orientation of the spins. It does not mark any privileged direction in space while we know that magnetic materials orient their magnetic moments in certain preferred spatial directions depending on the microscopic ordering of their atoms or molecules even if no external magnetic field is applied. To account for this fact, it is necessary to introduce a new term in the energy.

### 1.1.2 Anisotropy energy

Anisotropy reflects the existence of privileged spatial directions that magnetization prefers to point along. It is an experimental evidence that in a real material not all orientations of  $\mathbf{M}$  are equally probable. There are different sources of anisotropy, but their contribution to the energy can always be written in similar functional dependence on  $\mathbf{M}$ . This energy is usually (but not always) small compared with exchange energy, this means that the magnitude of  $\mathbf{M}$  is mainly determined by the exchange energy and the interaction with a magnetic field but its direction is determined mainly by the anisotropy.

In bulk materials, magnetocrystalline and magnetostatic anisotropy are the most relevant ones, while in systems with reduced dimensions, the contribution of surface anisotropy must also be taken into account.

#### Magnetocrystalline anisotropy

This kind of anisotropy has its origin in the crystal field created by the atoms or ions on every site of the crystal and it is mainly due to the spin-orbit coupling. Due to this coupling, the electronic orbitals are in some way "tied" to the electronic spin, tending to follow the spin when the magnetization changes. (For a more detailed discussion see Bertotti [1]). As the orbital moment of electrons is inevitably related to the crystallographic structure, the magnetocrystalline anisotropy reflects the symmetry properties of the crystal lattice. The characteristic symmetry elements, like symmetry planes or symmetry axes, determine the directions along which the crystal field points and along which magnetic moments are aligned.

At difference with the exchange energy, the anisotropy energy of a magnetic system can be expressed as a sum of single-site energies of every spin of the lattice. Although, in principle, it would be possible to derive an expression for the energy from *ab initio* calculations, one usually writes a phenomenological expressions by searching a linear combination of all possible products of the spin components compatible with the symmetry group of the crystal. Among all these combinations, only those containing even powers of the spin components are taken into account since changing the sign of any of the spin components should give the same energy for the system.

Thus, for the simplest case of hexagonal crystals, there is only one symmetry axis usually taken as the  $z$  direction, so that the energy can be written as an expansion containing powers of  $\mathbf{m} = \mathbf{M}/M$ , a unit vector pointing in the direction of the magnetic moment

$$E_{anis} = -Km_z^2 + K_2m_z^4 + \dots \quad (1.3)$$

The coefficients  $K$ ,  $K_2$  are called anisotropy constants. They have units of energy per unit volume and depend on temperature. Usually,  $K_2$  is much smaller than  $K$  and is omitted in the calculations.

For cubic crystals, for which there are three privileged axis, the corresponding expression starts with fourth order terms

$$E_{anis} = -K_1(m_x^2 m_y^2 + m_x^2 m_z^2 + m_y^2 m_z^2) + K_2(m_x^2 m_y^2 m_z^2) + \dots \quad (1.4)$$

### Surface anisotropy

Other sources of anisotropy arise because of the finite size of the samples, the application of external strains and magnetostatic interactions.

The surface anisotropy arises because of the reduced symmetry at the surface of a sample. Spins at the surface have a reduced number of neighbours as compared to those in the bulk and, therefore, the exchange interaction is reduced for them. From a phenomenological point of view, we know that independently of its microscopic derivation, this energy term must favour the alignment of the spins either parallel or perpendicularly to the sample surface, as is the case in thin films. Therefore any theory should lead to first order to a term of the form

$$E_{surf} = \frac{1}{K_s} \int dS (\mathbf{m} \cdot \mathbf{n})^2. \quad (1.5)$$

The value of  $K_s$  in the case of small particle systems can be indirectly evaluated from measurements of the hysteresis loops and, in most samples, values ranging from  $1 - 5 \times 10^4$  erg/cm<sup>2</sup> are found in the literature.

There has been recently a renewed interest in the consideration of the contribution of this term to explain certain anomalous magnetic properties of fine particles systems [2, 3, 4, 5, 6] and on the role of surface spins on the spin-glass like behaviour observed in experiments that measure the relaxation of the magnetization in this systems resulting in a controversy that does not seem completely solved.

### Strain anisotropy

There are two mechanisms that may induce strain anisotropy, both related to the magnetoelastic coupling that arises as a consequence of the interplay between lattice distortions and the relative position of the magnetic ions. On the one hand, there is the phenomenon of magnetostriction: magnetic systems are deformed when they are magnetized thus changing the crystallographic structure and anisotropy directions. On the other hand, the application of an external stresses to the system favours the orientation of its magnetization along certain directions.

From the theory of elasticity we know that the elastic energy of the system is essentially quadratic in the components of the deformation tensor. For small deformations, this tensor is related to the stress tensor and thus, for small deformations, proportional to the magnetization of the material. So, we can conclude that the functional dependence of the magnetoelastic energy on  $\mathbf{m}$  will be again of the same form as crystalline anisotropy. In other words, it results in an increase or decrease of the effective anisotropy constants of the material  $K_i$ .

### Shape or configurational anisotropy

Shape anisotropy has its origin in the magnetostatic energy, which for a ferromagnetic body of volume  $V$  can be written as

$$E_{magn} = -\frac{1}{2} \int_V dV \mathbf{M} \cdot \mathbf{H}, \quad (1.6)$$

where  $\mathbf{M}$  is the magnetization of the body. The magnetic field  $\mathbf{H}$  has to be calculated with the help of Maxwell's equations

$$\begin{aligned} \vec{\nabla} \times \mathbf{H} &= 0 \\ \vec{\nabla} \cdot \mathbf{H} &= -4\pi\mu_0 \vec{\nabla} \cdot \mathbf{M}. \end{aligned} \quad (1.7)$$

The first one indicates that  $\mathbf{H}$  can be derived from a magnetic potential  $\Phi$ , for which the following equations hold

$$\begin{aligned} \mathbf{H} &= -\vec{\nabla}\Phi \\ \nabla^2\phi &= -\vec{\nabla} \cdot \mathbf{M} \end{aligned} \quad (1.8)$$

together with boundary conditions at the surface of the body that can be expressed as

$$\Phi_{in} = \Phi_{out} \quad , \quad \frac{\partial}{\partial n}(\Phi_{in} - \Phi_{out}) = \mathbf{M} \cdot \mathbf{n}. \quad (1.9)$$

Here  $\mathbf{n}$  is a unit vector normal to the surface of the body.

For uniformly magnetized bodies of ellipsoidal shape the magnetic field  $\mathbf{H}$  is proportional to  $\mathbf{M}$  and, therefore, the magnetostatic energy is quadratic in the magnetic field components

$$E_{magn} = -\frac{VM_s^2}{2} \mathbf{m} \hat{D} \mathbf{m} \quad (1.10)$$

exactly in the same functional form as the anisotropy energy. The quantity  $\hat{D}$  is known as demagnetizing tensor, its components being known as demagnetizing factors. For spheroidal bodies,  $\hat{D}$  is diagonal with only two different components along ( $D_{\parallel}$ ) and perpendicular ( $D_{\perp}$ ) to the symmetry axis, so that the magnetostatic energy can be rewritten as

$$E_{magn} = -(K_m)m_z^2 + \text{const} \quad (1.11)$$

with  $K_m = \frac{VM_s^2}{2}(D_{\perp} - D_{\parallel})$  playing the role of an effective uniaxial anisotropy constant.

Therefore, the external shape of magnetized bodies favours the orientation of the magnetic moments along the most elongated direction of the body.

### 1.1.3 Dipolar interactions

A magnetic dipole is an idealized concept: the mathematical limit of an infinitesimal current distribution that allows to describe the magnetic properties of macroscopic bodies in terms of a collection of magnetic dipoles interacting one with each other through the magnetic field they create. In order to better understand the concepts of magnetic moment and magnetic dipole, let us start by the calculation of the magnetic field

created by a current distribution  $\mathbf{j}(\mathbf{r})$  confined to some region of space  $\Omega$  at large distances from this region. From Maxwell's equations, we know that the magnetic vector potential created by the current is

$$\mathbf{A} = \frac{\mu_0}{4\pi} \int_{\Omega} d^3r' \frac{\mathbf{j}(\mathbf{r}')}{|\mathbf{r} - \mathbf{r}'|}. \quad (1.12)$$

Expanding the term  $1/|\mathbf{r} - \mathbf{r}'|$  as  $1/r + \mathbf{r} \cdot \mathbf{r}'/r^3 + \dots$  and inserting it into (1.12) the integral of the first term vanishes and that of the second one can be written as

$$\mathbf{A} = \frac{\mu_0}{4\pi} \frac{\mathbf{m} \times \mathbf{r}}{r^3} + \dots \quad (1.13)$$

where the magnetic moment  $\mathbf{m}$  of the current distribution has been defined as

$$\mathbf{m} = \int_{\Omega} d^3r' \frac{\mathbf{r}' \times \mathbf{j}(\mathbf{r}')}{2}. \quad (1.14)$$

Now, for most of the cases of interest, elementary currents are usually carried by the orbital and spin angular momentum of the electrons in atoms, and it makes sense to introduce the idealized concept of elementary magnetic moment, also called magnetic dipole, as a point-like source of strength  $\mathbf{m}$ , generating a vector potential giving exactly by Eq.(1.13). It is in this sense that a magnetic dipole can be thought as a pair of magnetic poles of strength  $m$  placed at an infinitesimal distance  $d \rightarrow 0$  apart, such that the product  $md$  is constant in this limit. Moreover, from quantum mechanics we know that the magnitude of this moment is  $g\mu_B S$ , with  $g$  the Landé factor and  $\mu_B = e\hbar/2m_e c$  the Bohr's magneton. From this equation the magnetic field generated by the dipole can be derived by taking the curl ( $\mathbf{B} = \nabla \times \mathbf{A}$ ) with the result

$$\mathbf{B}_{\text{dip}} = \frac{\mathbf{m}}{r^3} - \frac{3(\mathbf{m} \cdot \mathbf{r})\mathbf{r}}{r^5}, \quad (1.15)$$

that will be usually used expressed in terms of the  $\mathbf{H}$  field as

$$\mathbf{H}_{\text{dip}} = -\frac{\mathbf{m}}{r^3} + \frac{3(\mathbf{m} \cdot \mathbf{r})\mathbf{r}}{r^5}. \quad (1.16)$$

This is what it is called dipolar field.

A plot of the lines of dipolar field  $\mathbf{H}_{\text{dip}}$  is drawn in Fig. 1.1. We see that the dipolar field created by a dipole is of opposite direction to its moment at points perpendicular to it  $\mathbf{H}_{\parallel}^{\text{dip}} = -\mathbf{m}/r^3$  and its stronger and points in the same direction that  $\mathbf{m}$  at points placed along the line of  $\mathbf{m}$   $\mathbf{H}_{\perp}^{\text{dip}} = 2\mathbf{m}/r^3$ .

The energy of a dipole  $\mathbf{m}$  placed in a magnetic field  $\mathbf{H}_{\text{dip}}$  is  $-\mathbf{m} \cdot \mathbf{H}_{\text{dip}}$ . Therefore, the energy of a system of  $N$  dipoles may be obtained by adding the energy that each dipole has due to the interaction with the dipolar fields created by the rest of dipoles

$$E_{\text{dip}} = \sum_{i \neq j}^N \left\{ \frac{\mathbf{m}_i \cdot \mathbf{m}_j}{r^3} - \frac{3(\mathbf{m}_i \cdot \mathbf{r}_j)(\mathbf{r}_i \cdot \mathbf{m}_j)}{r^5} \right\}. \quad (1.17)$$

From this expression a first comment is obvious: in contrast to exchange interactions, dipolar interactions are long-ranged because they decrease with the distance as  $1/r^3$ . The strength of the dipolar energy is essentially given by the parameter  $g = \mu^2/a^3$ , where  $\mu$  is the atomic magnetic moment and  $a$  is the linear size of the lattice where the magnetic moments are placed. In most of the magnetic systems, typical values for  $E_{\text{dip}}$ , in temperature units, lie in the range of 1-10 K, which is two or three orders of magnitude smaller

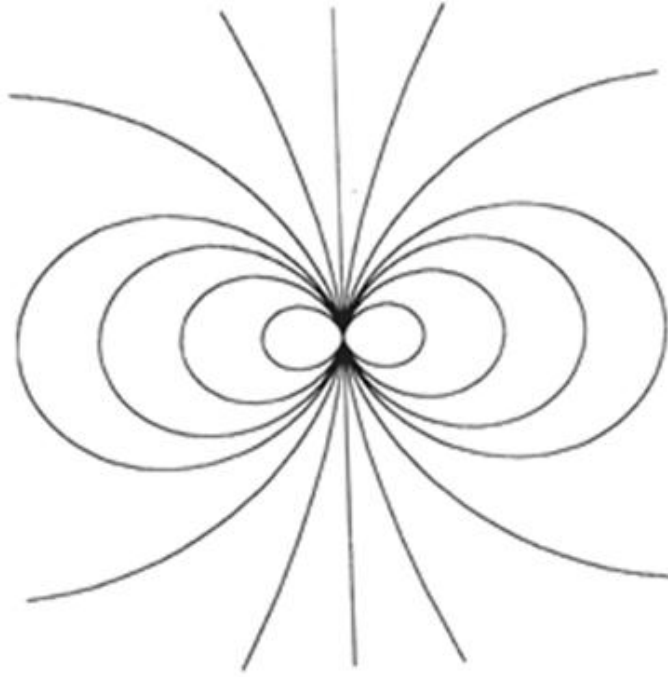


Figure 1.1: Lines of dipolar magnetic field  $\mathbf{H}$  created by a dipolar moment  $\mathbf{m}$ .

than the other energies involved. However, this does not mean that the dipolar or magnetostatic interactions can be neglected or plays no role on the magnetic properties of materials. The total dipolar energy of a system, being long-ranged, is proportional to its volume and therefore, can be much larger than the total exchange energy that it is rather small, because its range is not more than some unit cells [7]. We can say that exchange controls the details of the microscopic magnetic structure, while the magnetostatic energy is responsible for the magnetization distribution over the whole system.

In the expression of the dipolar interaction there are two terms. The first part  $\sim \mathbf{m}_i \cdot \mathbf{m}_j$  is rotationally invariant, and represents a long-range antiferromagnetic coupling. The second term is anisotropic and couples the spin space to real space inducing an easy-plane anisotropy. In 2D systems, like thin films, in-plane magnetized configurations are always favoured by the dipolar interaction with respect to perpendicular collinear states, because for the first ones the first term vanishes and the second reduces to an anisotropic expression  $E_{\text{dip}} \sim -K_{\text{dip}} \sin^2 \theta$  for a collinear configuration forming an angle  $\theta$  with the  $z$  axis. In general, the dipolar interaction favours parallel alignment of dipoles placed in the direction of  $\mathbf{m}$  and antiparallel alignment of dipoles placed at directions perpendicular to  $\mathbf{m}$  (see Fig. 1.2).

#### 1.1.4 Magnetostatic energy

Here, we want to clarify the connection between the microscopic origin of dipolar interactions given in the last subsection and the expression for the magnetostatic energy of magnetized body as given by the well-known formula [7]

$$E_{\text{magn}} = -\frac{1}{2} \int dV \mathbf{M} \cdot \mathbf{H}. \quad (1.18)$$

This energy is the energy that a material with magnetization  $\mathbf{M}$  has because of the influence of its own field and it is termed magnetostatic energy. It accounts for the interaction of each dipole in the material with the

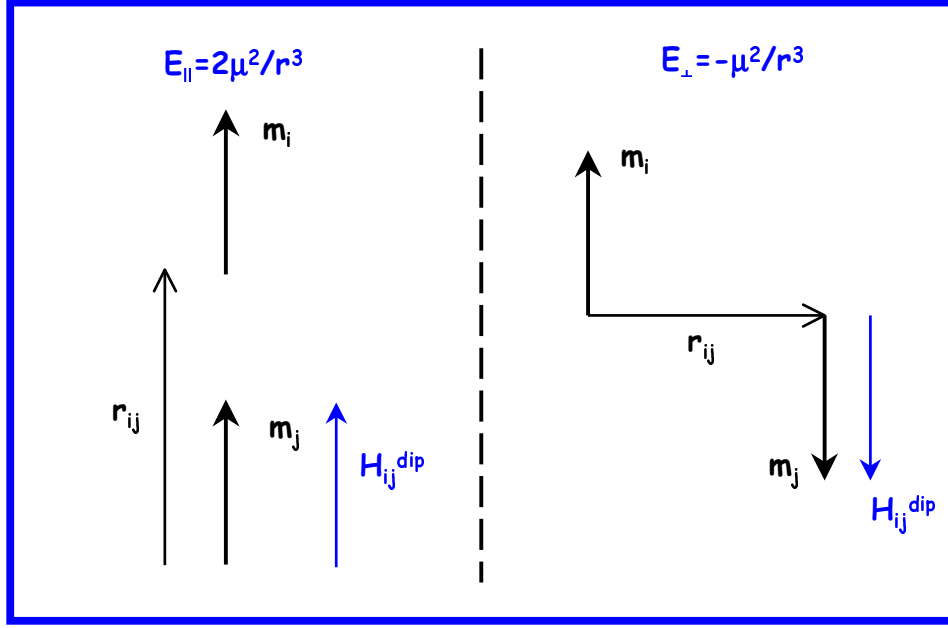


Figure 1.2: Magnetic moment configurations favoured by the dipolar interaction and associated energies.

field  $\mathbf{H}$  created by the other dipoles. The factor  $1/2$  appears to avoid double counting of the interactions. Let us consider the local magnetic field  $\mathbf{H}_{\text{loc}}$  acting on a lattice site occupied by an atom with magnetic moment  $\mathbf{m}$ . This field does not coincide with the macroscopic field due to the magnetization  $\mathbf{M}$ . In order to see this, let us consider a magnetic moment placed at any site inside a lattice and let us consider also a small sphere (Lorentz cavity) centered at the site of the considered moment and containing some of the surrounding dipoles. Then the local field can be thought as the sum of two contributions: the demagnetizing field due to the macroscopic magnetization created by the dipoles out from the cavity ( $\mathbf{H}_1$ ), and the sum of the dipolar fields created by the moments inside the cavity ( $\mathbf{H}_2$ ).

The first contribution is the demagnetizing field of the whole system taken as a continuum, that for a uniformly magnetized system is  $-4\pi D\mathbf{M}$  ( $D$  is the demagnetizing factor of the system), minus the field due to magnetic charges on the surface of the sphere, which is called Lorentz field and can be easily calculated [8, 7, 9] as  $\mathbf{H}_{\text{Lor}} = 4\pi\mathbf{M}/3$ , the demagnetizing field of a homogeneously magnetized sphere.

Assuming that the dipolar moments are aligned along the  $z$  direction and ordered in a cubic lattice, the second contribution is given by the sum

$$\mathbf{H}_2 = m \sum_i \left( -\frac{1}{r_i^3} + \frac{3z_i^2}{r_i^5} \right) = m \sum_i \frac{-r_i^2 + 3z_i^2}{r_i^5}, \quad (1.19)$$

and since by the symmetry of the cubic lattice all spatial directions are equivalent, we have

$$\sum_i \frac{x_i^2}{r_i^5} = \sum_i \frac{y_i^2}{r_i^5} = \sum_i \frac{z_i^2}{r_i^5} = \frac{1}{3} \sum_i \frac{1}{r_i^3}, \quad (1.20)$$

and therefore  $\mathbf{H}_2 = 0$ . For a non-cubic lattice this sum is not zero but,  $\mathbf{M}$  being constant inside the sphere,  $\mathbf{H}_2$  will be a lineal function of  $\mathbf{M}$  and therefore can be expressed as  $\mathbf{H}_2 = \hat{\Lambda}\mathbf{M}$ , with  $\hat{\Lambda}$  a tensor that depends

on the crystalline symmetry. Then, this field is of the form of an anisotropy field and its contribution to the total energy of the system can be included in the anisotropy energy, as was already explained in the previous section.

Hence, summarizing, the local field acting on a dipole is the sum of the demagnetizing field that depends on the external shape of the material, the Lorentz field mentioned above and an anisotropy field depending on the geometry of the lattice

$$\mathbf{H}_{loc} = \mathbf{H}_{demagn} + \frac{4\pi}{3}\mathbf{M} + \hat{\Lambda}\mathbf{M} . \quad (1.21)$$

In order to calculate the demagnetizing energy of a system of dipoles,  $E_{demagn} = -1/2 \sum \mathbf{m}_i \cdot \mathbf{H}_i$ , we can now change the sum to an integral over the volume of the sample substituting  $\mathbf{H}_i$  by the local field (1.21) to obtain

$$E_{magn} = -\frac{1}{2} \int dV \mathbf{M} \cdot \mathbf{H} - \frac{2\pi}{3} \int dV \mathbf{M} \cdot \mathbf{M} - \frac{1}{2} \int dV \mathbf{M} \hat{\Lambda} \mathbf{M} . \quad (1.22)$$

The second term is constant for a uniformly magnetized system and can be absorbed into the zero of energies and as already mentioned, the last one has the same formal form than an anisotropy energy and by an appropriate redefinition of the anisotropy constants may be included in the anisotropy energy.





## Bibliography

- [1] G. Bertotti, *Hysteresis in Magnetism* (Academic Press, London, 1998).
- [2] R. H. Kodama, A. E. Berkowitz, E. J. McNiff, and S. Foner, *Phys. Rev. Lett.* **77**, 394 (1996).
- [3] R. H. Kodama, S. A. Makhlof, and A. E. Berkowitz, *Phys. Rev. Lett.* **79**, 1393 (1997).
- [4] R. H. Kodama and A. E. Berkowitz, *Phys. Rev. B* **59**, 6321 (1999).
- [5] R. H. Kodama, A. E. Berkowitz, E. J. McNiff, and S. Foner, *J. Appl. Phys.* **81**, 5552 (1997).
- [6] R. H. Kodama, *J. Magn. Magn. Mater.* **200**, 359 (1999).
- [7] A. Aharoni, *Introduction to the Theory of Ferromagnetism* (Oxford University Press, New York, 1996).
- [8] A. H. Morrish, *The Physical Principles of Magnetism* (Wiley and Sons, New York, 1965).
- [9] C. Kittel, *Introduction to Solid State Physics* (Wiley and Sons, New York, 1993).



**Part I**

**SMALL PARTICLE SYSTEMS.  
THERMAL RELAXATION**



## IA. Single particle properties

*We must simplify things as much as possible, but not more.*

A. EINSTEIN

In this part, we will concentrate on the magnetic properties of a single ferromagnetic particle, that is to say, we will study a magnetic nanoparticle without taking into account its interaction with the rest of the particles. Two levels of description will be proposed: In Chapter 2 we will treat the particle as a macrospin, forgetting about the internal distribution its constituent of the magnetization. This will allow us to understand the equilibrium properties of ensembles of non-interacting single domain particles. b) In a second step, in Chapter 3, we will consider the detailed internal distribution of magnetic moments in the particle, taking into account the crystallographic structure and the interactions among the spins.



## CHAPTER 2

### EQUILIBRIUM PROPERTIES

The sizes of magnetic particles used in modern magnetic recording technologies have decreased already to the nanometric range. For most of the magnetic materials, this is below the critical size for the single-domain state. This critical size is essentially determined by two characteristic lengths: 1) the domain wall width  $\delta_{DW} \sim \sqrt{J/K}$ , and 2) the exchange length  $\lambda_{Exch} \sim \sqrt{J/M_s}$ . The first one, indicates that strong anisotropy widens the domain wall width, thus favouring a single-domain state, while the second measures the competition between exchange (short-ranged) and magnetostatic (long-ranged) energies and gives a characteristic length for uniform rotation processes.

Let us illustrate this for a spherical particle, the critical radius can be easily computed by equating the domain wall energy to the magnetostatic energy of a single domain [1, 2] with the result

$$r_c \approx 9 \frac{\sqrt{JK}}{\mu_0 M_s^2}. \quad (2.1)$$

For iron, this gives  $r_c = 3$  nm, which, in fact, is smaller than the domain wall width because we have not taken into account the cost in exchange energy to form such a domain wall (a valid approximation for strong anisotropy). For moderate anisotropy the domain wall width increases and its contribution to the exchange energy has to be taken into account, thus increasing the critical radius (up to  $r_c = 25$  nm for the case of iron [3]).

However, even if particles are single domain, the magnetization processes can proceed via different reversal modes depending on the magnitude and direction of the magnetic field and the specific shape and geometric parameters of the particle. Among the most important non-uniform reversal modes in ellipsoidal particles there are curling, buckling and fanning [1, 2, 4]. However, the uniform reversal mode, in which magnetization reversal proceeds by coherent rotation of their magnetic moments in unison, is the dominant mode for sizes  $r_c < \lambda_{Exch}$  [5], that is to say, for particles with high aspect ratio and high crystalline anisotropy [6]. Thus, usually, magnetization processes in ensembles of ferromagnetic particles can be studied by viewing each particle as a single magnetic moment that rotates in space under the torque of the external field.

In this chapter, we will study the equilibrium magnetic properties of systems of single domain particles that can be simply modeled by a single magnetic moment. We will start by giving a brief review of the properties of the energy function of one particle after which we will calculate the corresponding energy barriers. Then, we will consider how the magnetic field modifies these energy barriers. By introducing the concept of effective energy barrier distribution we will study the influence of the magnetic field on the energy barriers of particle systems with distributed properties (distribution of easy-axes and anisotropy constants). Finally, we will compute the equilibrium magnetization curves, taking into account the magnetocrystalline



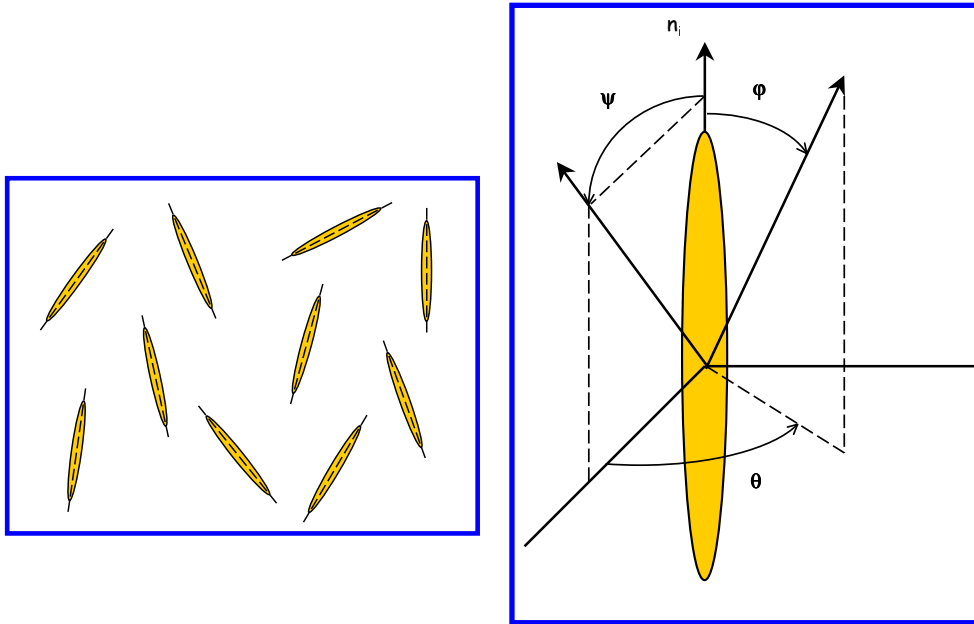


Figure 2.1: Schematic representation of the quantities involved in the definition of the system. The easy-axis of the particles  $\mathbf{n}$  are in the  $x$ - $z$  plane forming an angle  $\psi$  with the magnetic field  $\mathbf{H}$ , which points along the  $z$  axis.  $\theta$  and  $\varphi$  are the spherical angles of the magnetization vector  $\mathbf{M}$ .

anisotropy energy of the particles, often disregarded in calculations and which, in real materials, is high to avoid the loss of information by thermal demagnetization not considered. Moreover, as it will be useful for the study of the magnetic relaxation at low temperatures, treated later on in Chapter 5, we will introduce the so-called Two-State Approximation (TSA) for the calculation of equilibrium quantities.

## 2.1 Model and parameters

We will begin with a system without interactions among the constituents. It consists of an ensemble of single-domain ferromagnetic particles each characterized by its volume  $V$  and by the orientation of its magnetization vector  $\mathbf{M}$ , or the equivalent unit vector  $\mathbf{m} = \mathbf{M}/M_0$ , since the particles have no domain,  $\mathbf{m}$  is always saturated in a certain direction. The particles exhibit anisotropy, either due to magnetocrystalline or to shape effects. For simplicity, we will assume the simple case of uniaxial anisotropy which is suitable for ellipsoidal particles with a symmetry axis. In order to account for the spread of particle volumes in real samples, we will allow the particles anisotropy constants,  $K$ , to be distributed according to a normalized distribution function  $f(K)$ . Note that a distribution of  $K$ 's is equivalent to a distribution of particle volumes because, in general, the anisotropy energy is proportional to  $V$ . When necessary, we will also take into account the random orientation of the easy-axis with respect to the direction of the magnetic field. According to the well-known Stoner-Wohlfarth model [7], we will assume that the static and dynamic properties of the system can be accounted by the uniform rotation of  $\mathbf{M}$  over the energy barriers induced by the anisotropy.

## 2.2 Properties of the energy function

The behaviour of a particle as described above is governed by the competition of two energy terms: the uniaxial anisotropy energy and the energy of interaction with the external field  $\mathbf{H}$ , the total energy can be written as

$$E = -K(\mathbf{m} \cdot \mathbf{n})^2 - \mathbf{M} \cdot \mathbf{H} , \quad (2.2)$$

where  $\mathbf{n}$  is a unitary vector pointing in the direction of the easy-axis. This formula is more conveniently expressed in terms of angular coordinates of Fig. 2.1. In the frame of reference of the particle, in which  $\mathbf{n}$  points along the z axis, and with the magnetic field in the x-z plane forming an angle  $\psi$  with respect to the z axis, it reads

$$\begin{aligned} \bar{E} &= E/KV = -\cos^2 \theta - 2h_{\perp} \sin \theta - 2h_{\parallel} \cos \theta \\ &= -\cos^2 \theta - 2h(\cos \theta \cos \psi + \sin \theta \sin \psi \cos \varphi) . \end{aligned} \quad (2.3)$$

The angles  $\theta$  and  $\varphi$  are defined in Fig. 2.1.  $h_{\parallel} = h \sin \psi$  and  $h_{\perp} = h \cos \psi$  are the parallel and perpendicular field to the easy-axis components.

Only when  $\mathbf{M}$  lies in the plane formed by  $\mathbf{H}$  and  $\mathbf{n}$  [two dimensional (2D) model,  $\varphi = 0$ ], the energy maxima and minima can be calculated analytically, and then the above expressions reduce to

$$\bar{E}(\theta, \psi) = E/KV = -\cos^2 \theta - 2h \cos(\theta - \psi) \quad (2.4)$$

In both expressions we have used dimensionless energy normalized to the maximum anisotropy energy of the particle,  $KV$  and we have also defined a dimensionless *reduced field*  $h = H/H_c$ , in terms of what is called the *critical field*  $H_c(0) = 2K/M_0$ . Several typical cases are plotted in Fig. 2.2.

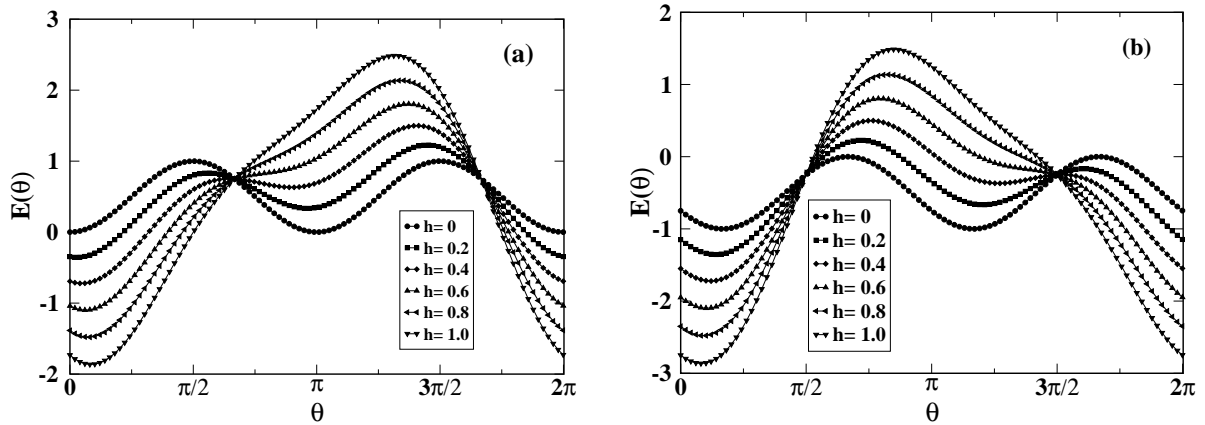


Figure 2.2: Plots of the energy  $\bar{E}(\theta, \psi)$  as given by Eq. (2.4) as a function of  $\theta$  for several angles (a)  $\psi = 30^\circ$ , (b)  $\psi = 120^\circ$  and different values of the magnetic field  $h$  as indicated in the figures.

Minima of the energy determine the equilibrium properties of the particle as they correspond to stable magnetization directions. Let us now consider how the extrema of  $\bar{E}(\theta, \psi)$ , taken as a function of  $\theta$ , depend on the field  $h$  and the particle orientation  $\psi$ . The minima of the energy must satisfy the two simultaneous conditions

$$\frac{\partial E(\theta, \psi)}{\partial \theta} = 0 , \quad \frac{\partial^2 E(\theta, \psi)}{\partial^2 \theta} > 0 . \quad (2.5)$$

Differentiating Eq. (2.3) we obtain

$$\sin(2\theta) + 2h \sin(\theta - \psi) = 0 \quad (2.6)$$

with the condition

$$2 \cos(2\theta) + h \cos(\theta - \psi) > 0. \quad (2.7)$$

There are two cases for which this equation can be solved. The first corresponds to oriented particles ( $\psi = 0$ ), for which the solutions are  $\sin \theta = 0$ ,  $\cos \theta = -h$ . The first one correspond to energy minima located at  $\theta_{min}^{1,2} = 0, \pi$  and the second, to energy maxima located at  $\theta_{max}^1 = \arccos(h)$ ,  $\theta_{max}^2 = \pi - \theta_{max}^1$  for  $|h| < 1$ . The second solvable case corresponds to particles oriented perpendicularly to  $\mathbf{h}$  ( $\psi = \pi/2$ ). In this case, Eq. (2.6) has solutions  $\cos \theta = 0$ ,  $\sin \theta = h$ , the minima are at  $\theta_{min}^1 = \arcsin(h)$  and  $\theta_{min}^2 = \pi - \theta_{min}^1$  and the maxima are at  $\theta_{max}^1 = 0$ ,  $\theta_{max}^2 = \pi$ .

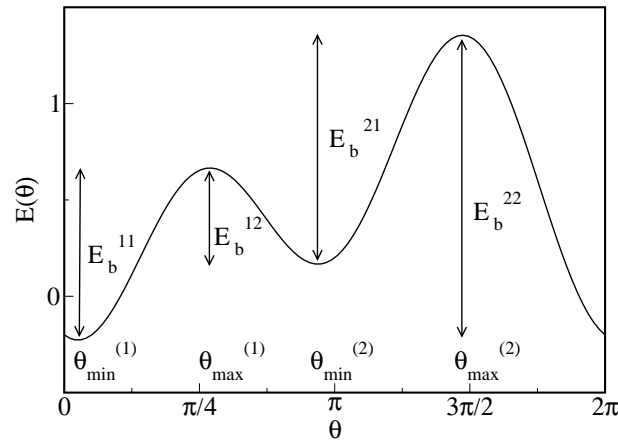


Figure 2.3: Energy function  $E(\theta, \psi)$  as a function of the angle between the magnetization vector  $\mathbf{m}$  and the magnetic field  $\mathbf{h}$ , for  $\mathbf{m}$  in the plane of the easy-axis  $\varphi = 0$ , as given by Eq. (2.3). The plot is for a particle whose easy-axis  $\mathbf{n}$  forms an angle  $\psi = 30^\circ$  with  $\mathbf{h}$ , and  $H = 0.3$ . We have used the following notation to designate the extrema of the energy:  $\theta_{min}^1$  and  $\theta_{max}^1$  refer to the extrema closer to the field direction while  $\theta_{min}^2$  and  $\theta_{max}^2$  refer to those further from the direction of the field. The four possible energy barriers between them are  $E_b^{ij} \equiv E(\theta_{max}^i) - E(\theta_{min}^j)$ .

For particles oriented at an angle  $\psi$  there is no analytical solution to (2.6). In Fig. 2.4 we show the solutions obtained by solving Eqs. (2.6) and (2.7) with a numerical minimization algorithm, as a function of the particle orientation  $\psi$  and for different values of  $h$ . Here minima and maxima have been labeled according to the following notation:  $\theta_{min}^1$  and  $\theta_{max}^1$  refer to the extrema closer to the field direction while  $\theta_{min}^2$  and  $\theta_{max}^2$  refer to those further from the direction of the field. The four possible energy barriers between them are  $E_b^{ij} \equiv E(\theta_{max}^i) - E(\theta_{min}^j)$  as graphically displayed in Fig. 2.3.

As we see in Fig. 2.4, for  $H \leq 0.5$ , the minima and maxima are always comprised in a well defined range of  $\theta$ :  $-\pi/4 < \theta_{min}^1 < \pi/4$ ,  $3\pi/4 < \theta_{min}^2 < 5\pi/4$ ,  $\pi/4 < \theta_{max}^1 < 3\pi/4$ ,  $5\pi/4 < \theta_{max}^2 < 7\pi/4$ . This will facilitate the calculations of relaxation curves presented in the following chapters.

It is clear that for a given  $\psi$ , the number of minima of the energy will depend on the value of  $h$ . For small  $h$  the two minima allowed by the anisotropy energy still exist. The one closer to the field direction is stable, while the other is a metastable state that disappears when the field reaches a critical value  $h_c(\psi)$ , above which the Zeeman energy dominates the anisotropy energy.

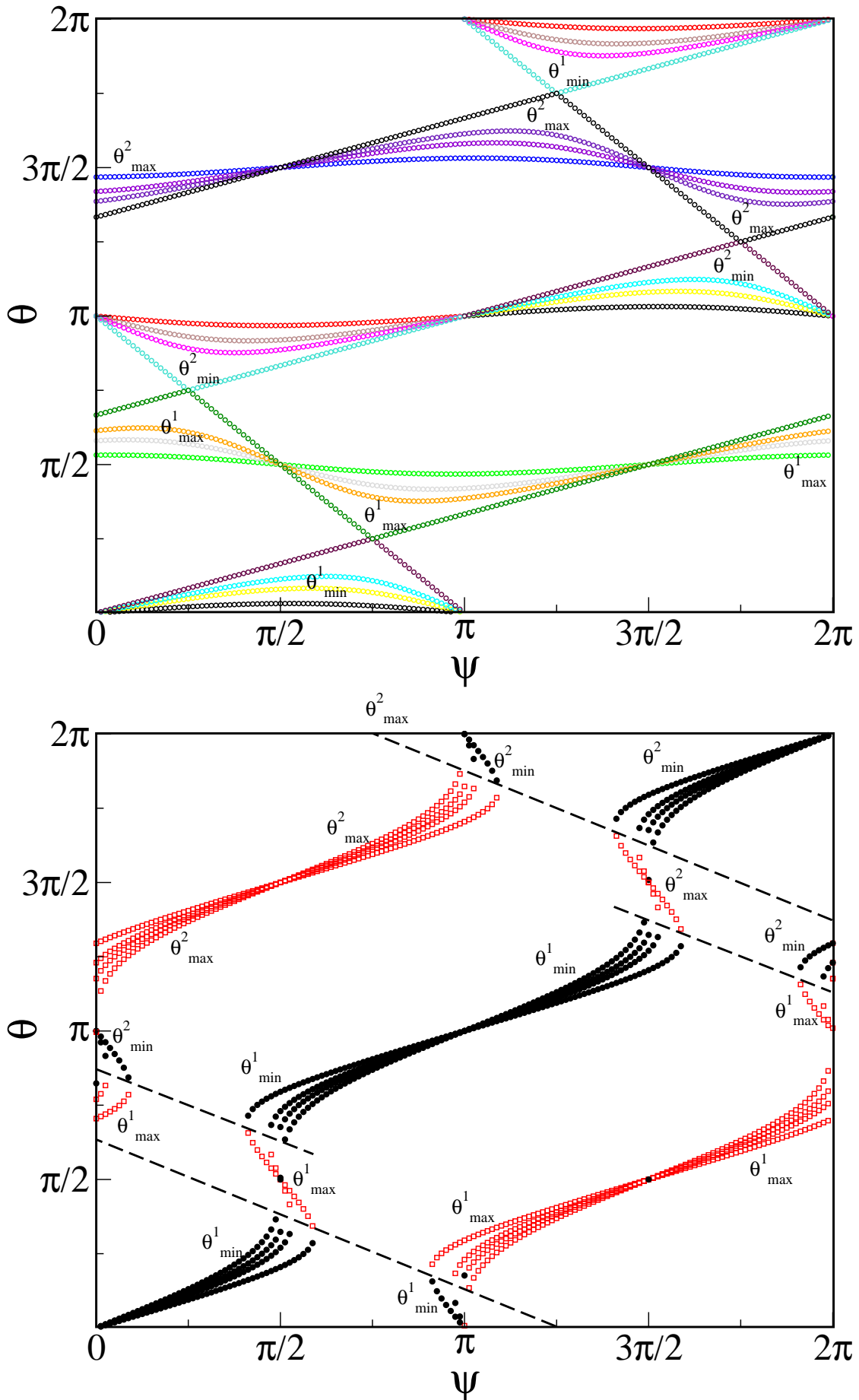


Figure 2.4: Extrema of the energy (2.4) as a function of the orientation of the particle for different values of the magnetic field: left panel  $H = 0.2, 0.5, 0.7, 1.0$ ; right panel  $H = 1.2, 1.5, 1.7, 2.0$ . The lowest (higher) curve at  $\psi \approx 0$  for  $\theta_{\min}^{(2)}, \theta_{\max}^{(2)}$ , corresponds to the lowest field value.

The value of this critical field can be found by equating the right hand side of Eq. (2.7) to zero, giving

$$\sin(2\theta) + 2h_c \sin(\theta - \psi) = 0, \quad \cos(2\theta) + h_c \cos(\theta - \psi) = 0. \quad (2.8)$$

From these two expressions  $\theta$  can be eliminated to obtain the critical field as function of the orientation of the particle as

$$h_c(\psi) = (\sin^{2/3} \psi + \cos^{2/3} \psi)^{-3/2}. \quad (2.9)$$

As can be seen in Fig. 2.5, for an applied magnetic field  $h_{app} < 0.5$ , all particles have two energy minima independently of their orientation (see also the left panel in Fig. 2.4. When  $h$  exceeds the minimum critical field value of 0.5, barriers start to be destroyed for particles having orientations close to  $\psi = \pi/4$ . Particles with  $h_c(\psi) > h_{app}$  have two energy minima while those with  $h_c(\psi) < h_{app}$  have only one energy minimum, the one closer to the direction of the field (see the right panel in Fig. 2.4. Finally, when  $h_{app} > 1$ , this is, for fields higher than the anisotropy field, there are no energy barriers for any orientation, there is only one energy minimum.

This means that, for a given  $h$ , particles with orientations  $\psi < \psi_c$  have two minima. This critical angle can be found from Eq. (2.9). Setting  $h_c$  equal to  $h$  and solving for  $\psi$ , we have

$$\sin^2(2\psi_c) = \frac{4(1 - h^2)^3}{27h^4}. \quad (2.10)$$

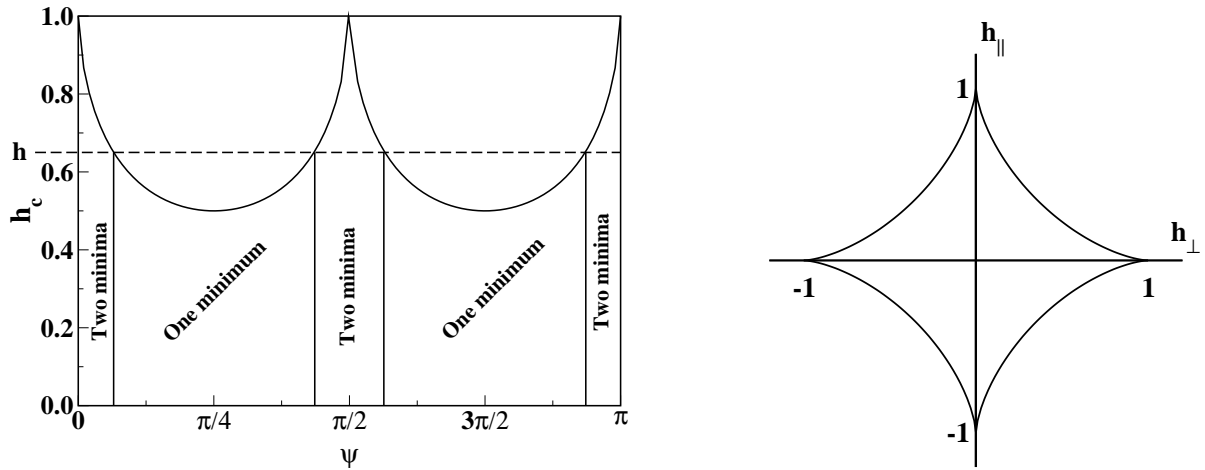


Figure 2.5: Left panel: Critical field as a function of the angle between the easy-axis and the field,  $\psi$ . Right panel: Astroid curve in the plane defined by the components of the magnetic field  $h_{\perp}$ ,  $h_{\parallel}$ .

Another way to understand this is from the point of view of the astroid curve introduced by Slonczewski [8, 9, 10, 11] to explain hysteresis. If from Eq. (2.4) we calculate  $\partial \bar{E} / \partial \theta = 0$  and  $\partial^2 \bar{E} / \partial^2 \theta = 0$ , one arrives at the parametric representation

$$h_{\perp} = \sin^3 \theta, \quad h_{\parallel} = -\cos^3 \theta, \quad (2.11)$$

that eliminating  $\theta$  becomes

$$h_{\perp}^{2/3} + h_{\parallel}^{2/3} = 1. \quad (2.12)$$

When this curve is represented in the  $h_{\perp}$ ,  $h_{\parallel}$  plane it has the shape of the astroid represented in Fig. 2.5. For field orientations inside the astroid curve the energy has two energy minima while for field orientations out from it only one.

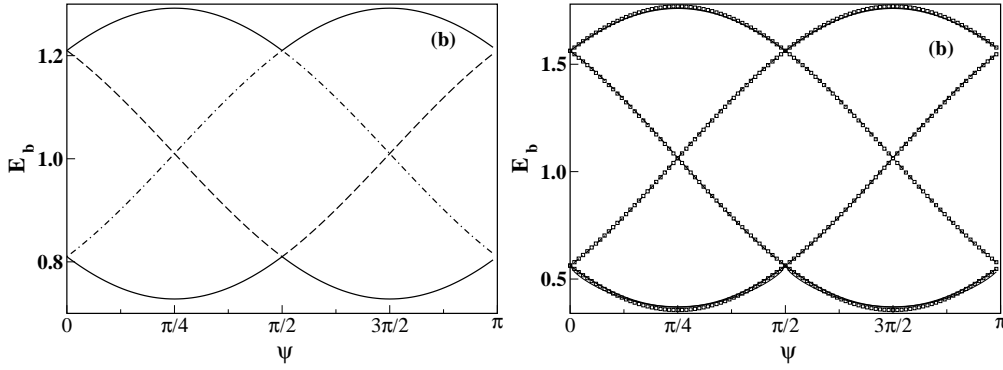


Figure 2.6: Energy barriers between the extrema of Fig. (2.4) as a function of the orientation of the particle  $\psi$  and for two values of  $h$  (a)  $h = 0.1$ ; (b)  $h = 0.25$ . Continuous lines stand for  $E_b^{11}$ ; dot-dashed for  $E_b^{12}$ ; long dashed for  $E_b^{21}$ ; dotted-dashed for  $E_b^{22}$ .

## 2.3 Energy barriers

The energy barriers of the system are essentially provided by the anisotropy term, and in the absence of a field are simply given by  $E_b^0 = KV$ , independently of the orientation of the particle and, therefore, they are proportional to the volume of the particle. The application of a magnetic field breaks the degeneracy, inducing a bias between the energy minima and creating a metastable state corresponding to the minima oriented further from the direction of the field. Consequently, energy barriers are now modified to  $E_b(h) = KVf(h)$ .

The function  $f(h)$  can only be calculated analytically for oriented particles ( $\psi = 0$ ). In this case the values of the energy at the minima and maxima are

$$\begin{aligned} \bar{E}_{min}^1 &= -2h & \bar{E}_{min}^2 &= +2h \\ \bar{E}_{max}^1 &= 1 + h^2 & \bar{E}_{max}^2 &= 1 - h^2, \end{aligned} \quad (2.13)$$

so that there are only two different energy barriers given by

$$\bar{E}_b^{11}(h, \psi = 0) = (1 + h)^2, \quad \bar{E}_b^{22}(h, \psi = 0) = (1 - h)^2. \quad (2.14)$$

For a general orientation  $\psi$ , the energy barriers have to be found numerically. The results of numerical calculations of the dependence of  $E_b^{ij}$  on  $\psi$  based on Eq. 2.6 are shown in Fig. 2.6 for two values of  $h < 1$ . None of the  $E_b$  are a monotonous function of  $\psi$  and presents a maximum at  $\psi = \pi/4$  and then decreases with increasing  $\psi$  as the easy-axis gets closer to the field direction, being minimum at  $\psi = 3\pi/4$ . The minimum and maximum energy barriers are for particles aligned at  $\psi = 45^\circ, 135^\circ$ , while those at  $\psi = 0, \pi/2$  have only two different energy barriers with the same value.

It is also interesting to calculate the dependence of  $E_b^{ij}$  on  $h$  for a given orientation. As is shown in Fig. 2.7 the curves have a similar dependence on  $h$  independently of the orientation. The higher barriers  $E_b^{22}, E_b^{21}$  for rotation out of the field direction increase monotonously with  $h$  while the smallest barriers  $E_b^{11}, E_b^{12}$  decrease until the critical field  $h_c(\psi)$  is reached and then become zero.

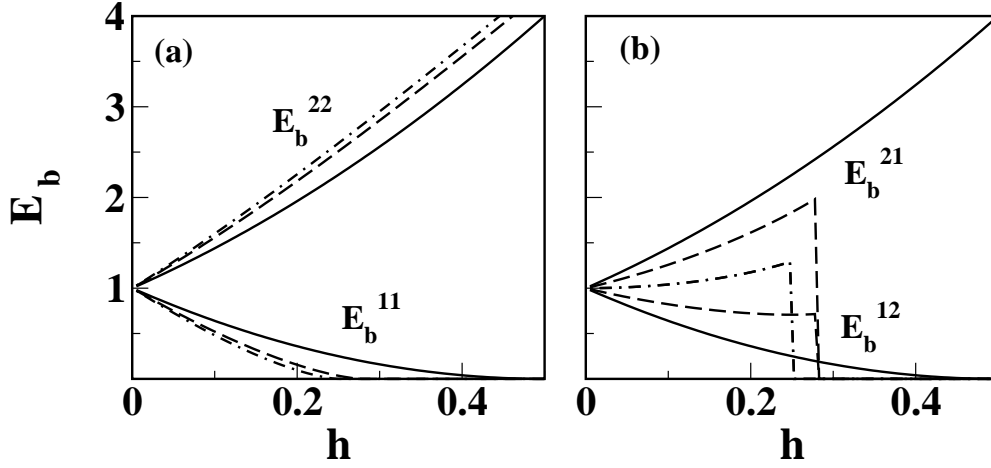


Figure 2.7: Energy barriers as a function of  $h$  for different values of the particle orientation: continuous line,  $\psi = 0$ ; dashed line,  $\psi = \pi/8$ ; dot-dashed,  $\psi = \pi/4$ .

## 2.4 Low field approximation

For low fields,  $h \ll 1$ , it is possible to find approximate analytical expressions for the extrema of the energy function as well as for the energy barriers which will be useful when we study the equilibrium magnetization in subsequent sections.

For this purpose, we start by expanding Eq. (2.6) around the zero field solutions (i.e.,  $\theta_{\min}^{1,2} = 0, \pi$ ,  $\theta_{\max}^{1,2} = \pi/2, 3\pi/2$ ) up to first order in  $h$ , the following expression can be obtained

$$\begin{aligned}
 \theta_{\min}^1 &= h \sin \psi \\
 \theta_{\min}^2 &= \pi - h \sin \psi \\
 \theta_{\max}^1 &= \frac{\pi}{2} + h \cos \psi \\
 \theta_{\max}^2 &= \frac{3\pi}{2} - h \cos \psi .
 \end{aligned} \tag{2.15}$$

When substituting in Eq. (2.4), these expressions give the following approximations for the energies of the extrema of the energy function  $\bar{E}$

$$\begin{aligned}
 \bar{E}_{\min}^1 &\simeq -1 - 2h \cos \psi - h^2 \sin^2 \psi \\
 \bar{E}_{\min}^2 &\simeq -1 + 2h \cos \psi - h^2 \sin^2 \psi \\
 \bar{E}_{\max}^1 &\simeq -2h \sin \psi + h^2 \cos^2 \psi \\
 \bar{E}_{\max}^2 &\simeq 2h \sin \psi + 2h^2 \cos^2 \psi ,
 \end{aligned} \tag{2.16}$$

from which we find the following formulae for the energy barriers

$$\begin{aligned}
 \bar{E}_b^{11} &\simeq 1 - 2h(\sin \psi - \cos \psi) - h^2 \\
 \bar{E}_b^{12} &\simeq 1 + 2h(\sin \psi + \cos \psi) - h^2 \\
 \bar{E}_b^{21} &\simeq 1 - 2h(\sin \psi + \cos \psi) + h^2 \\
 \bar{E}_b^{22} &\simeq 1 + 2h(\sin \psi - \cos \psi) + h^2 .
 \end{aligned} \tag{2.17}$$

These approximations are plotted in symbols in Fig. 2.8, the agreement with the exact expressions is very good even for  $h$  as high as 0.25. Pfeiffer [12] has also given an empirical approximate expression for the energy barriers which works surprisingly well for all the fields

$$\bar{E}_b^{11} = [1 - h/h_c(\psi)]^{0.86+1.14h_c(\psi)}. \quad (2.18)$$

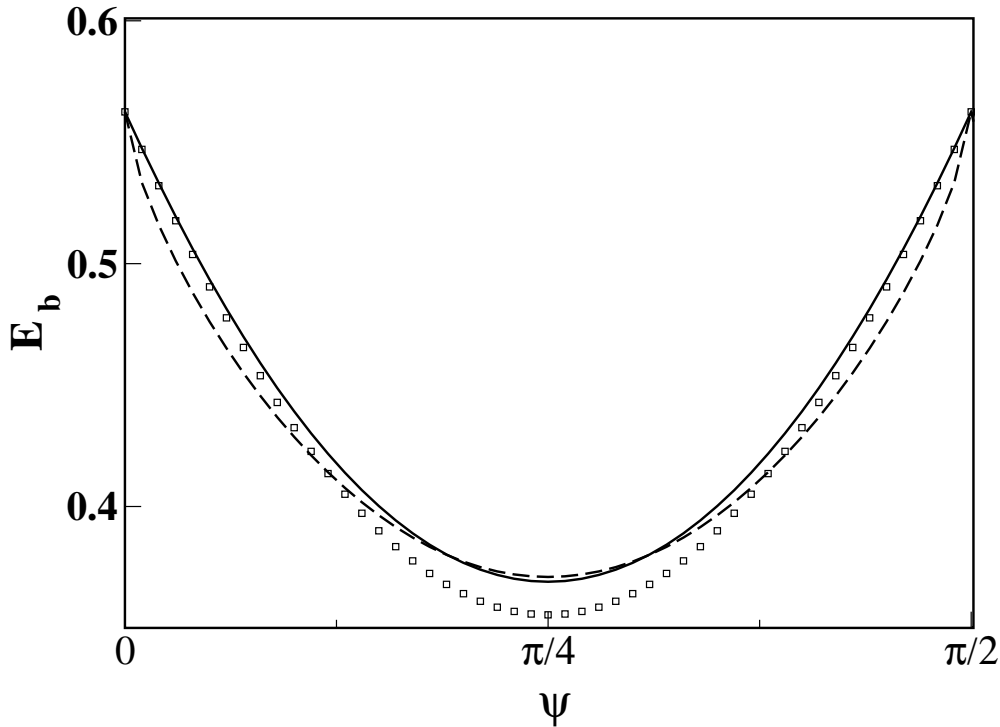


Figure 2.8: Different approximations to the variation of the energy barrier  $E_b^{11}$  with particle orientation  $\psi$  for  $h = 0.25$ . Symbols: low field approximation of Eq. (2.17). Dashed line: Pfeiffer's approximation, Eq. (2.18). Continuous line: exact result.

## 2.5 Effective energy barrier distribution

Up to now, we have presented the main properties of a single mono-domain particle. In particular, we have studied the influence of particle orientation and the magnetic field on the energy barriers and metastable states, which are the essential quantities in order to understand the equilibrium properties of the magnetization. In what follows, we will consider an ensemble of particles with distributed orientations and/or distributed anisotropies. Now, the properties of the ensemble will be described in a statistical fashion with the help of distribution functions that collect the energy barriers of all the single particles of the ensemble.

As it has been shown in Sec. 2.3, the magnetic field modifies the energy barriers of a particle system depending on the particle orientation and anisotropy value. If  $E_b^0$  is the energy barrier in zero field,  $h$  will modify it by a multiplicative factor in form

$$E_b = E_b^0 g(h, \psi). \quad (2.19)$$



This change depends on the orientation of the particle as shown in Fig. 2.6. Consequently, in an ensemble of particles, the distribution of energy barriers in absence of a field,  $f(E_b^0)$  (which has in fact the same functional dependence than distribution of anisotropy constants  $f(K)$ ), will be changed accordingly to

$$f_{\text{eff}}(h, E_b, \psi) = f(E_b^0) \left( \frac{\partial E_b^0(E_b)}{\partial E_b} \right) = f(E_b^0)/g(h, \psi), \quad (2.20)$$

which we will call effective energy barrier distribution.

In order to understand the qualitative change of  $f_{\text{eff}}$  with  $h$ , let us first consider its effect on an ensemble of particles with random orientations and anisotropy constant  $K_0 = 1$ . In this case,  $f_{\text{eff}}(E_b)$  becomes

$$f_{\text{eff}}(h, E_b, \psi) = \int_0^{\pi/2} d\psi f(E_b^0)/g(h, \psi). \quad (2.21)$$

We have calculated this quantity by making energy barriers histograms for a collection of 40 000 particles. The results for different values of  $h$  are presented in Fig. 2.9. Since, in this case, the maximum and minimum barriers present in the ensemble correspond to particles oriented at  $\pi/4, 3\pi/4$  (see Fig. 2.6),  $f_{\text{eff}}(E)$  is peaked at this two values and has a shallow minimum at  $E_b^{12}(\pi/4)$ . An increasing  $h$ , increases the separation between peaks and shifts the minimum towards higher energies,  $E_b(\psi)$ . The global effect is, thus, a widening of  $f_{\text{eff}}(E_b)$ .

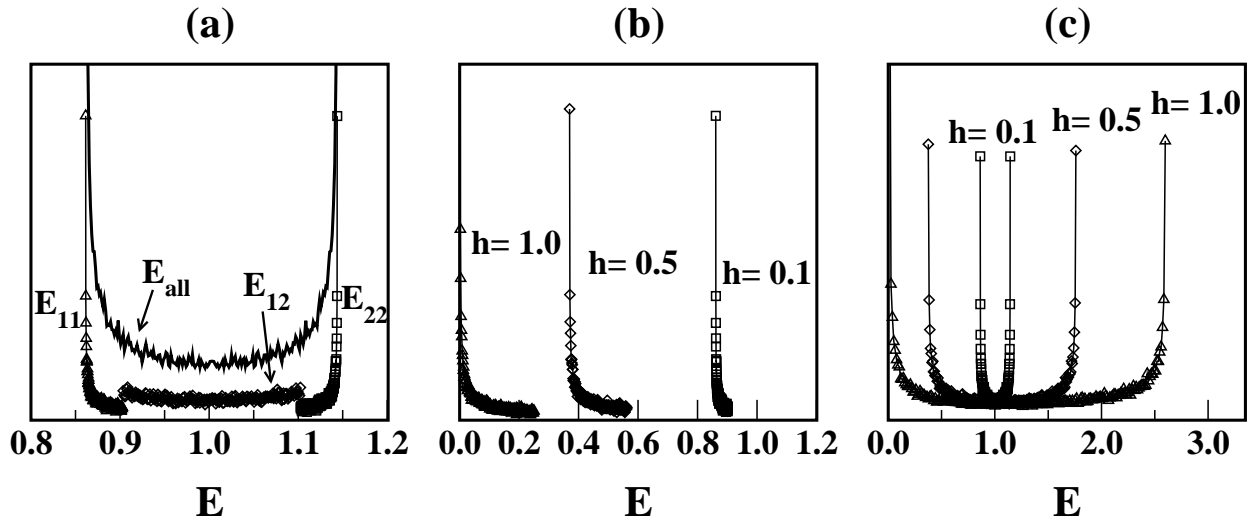


Figure 2.9: Effective energy barrier distributions for particles with anisotropy constant  $K = 1$  and random orientations for different values of  $h$ . (a) Contributions of the different  $E_b^{ij}$  to the total energy barrier distribution for  $h = 0.1$ . (b) Effective distributions of  $E_b^{11}$  barriers. (c) Effective distribution of all the energy barriers.

Next, we have numerically calculated  $f_{\text{eff}}(E_b)$  from Eq. (2.20) for a system of oriented particles with logarithmic-normal distribution of anisotropies

$$f(K) = \frac{1}{\sqrt{2\pi}K\sigma} e^{-\ln^2(K/K_0)/2\sigma^2}, \quad (2.22)$$

for different widths  $\sigma$  and  $K_0 = 1$ , and several values of  $h$ . The results are given in Fig. 2.10. In all the cases, we observe the progressive splitting of the original distribution  $f(E_b^0)$  in two subdistributions

of high and low barriers as  $h$  increases from zero. The field tends to make deeper one of the minima, therefore increasing the two energy barriers for rotation of  $\mathbf{M}$  out of the field direction while the other two are reduced. In this way, the global effect of  $h$  is a splitting of  $f(E_b)$  towards lower and higher values of  $E_b$ .

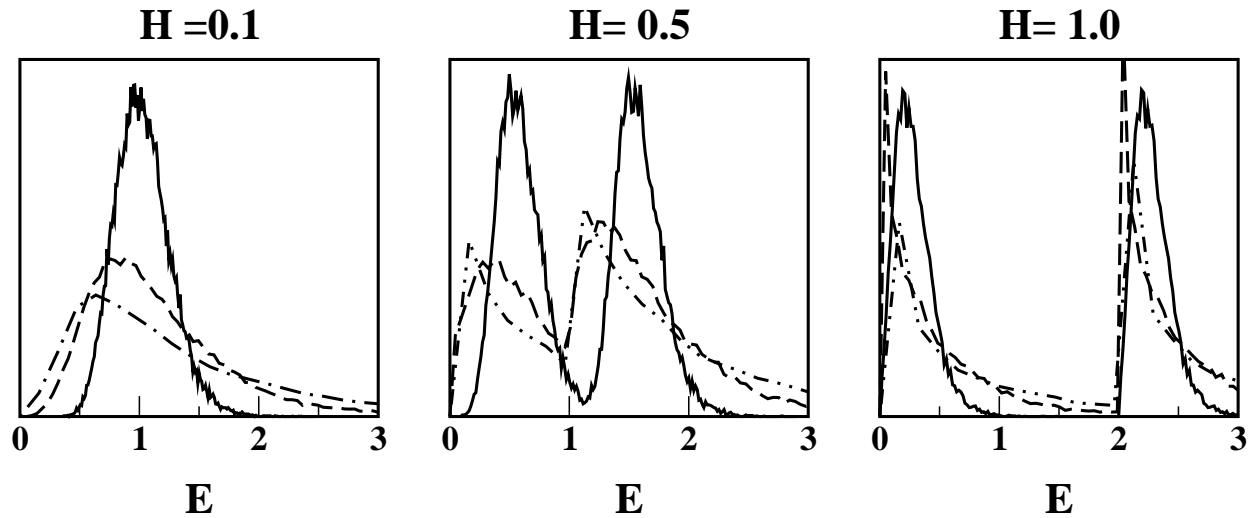


Figure 2.10: Effective energy barrier distributions for aligned particles with distribution of anisotropy constants of Eq.(2.22) with  $K_0 = 1$ ,  $\sigma = 0.2$  (continuous lines), 0.5 (dashed lines), 0.8 (dot-dashed lines) for different values of  $h$ .

As  $h$  attains the critical value  $h_c$  for the particles with smaller  $K$ , a peak of zero or almost zero energy barriers starts to appear (see for example the curves for  $h = 0.5, 1.0$  in the case  $\sigma = 0.5$ ); while most of the non-zero barriers are distributed according to a distribution identical to  $f(E_b^0)$ , but centered at higher energies. The higher the width of the distribution  $\sigma$ , the higher the  $h$  at which the lowest energy barriers start to be destroyed by the field.

Finally, the combined effect of random orientations and  $f(K)$  has been considered. The results are shown in Fig. 2.11, where we can see that the features of the preceding case are still observed. Now, at high  $h$ , the distributions are smeared out by the disorder, and the minima becomes less pronounced due to the spread in particle orientations.

In Chapter 5 we will discuss how these results can be used to understand the time dependence of magnetization in relaxation experiments.

## 2.6 Magnetization curves

Perhaps, the most important equilibrium property of an ensemble of magnetic particles is the macroscopic magnetization. The magnetization law, i. e. the acquisition of magnetization by a progressively increasing magnetic field of an initially demagnetized sample at a fixed temperature  $T$ , is a characteristic of a material and indicates the microscopic mechanisms by which a material gets magnetized. The calculation for a single classical magnetic moment was given long ago in terms of the famous Langevin function for paramagnets, which only takes into account the interaction of the magnetic moment with the magnetic field. However, in small particle systems, the distribution of particle volumes (and the corresponding effect on the individual magnetic moments), the easy-axes distribution and the spread in anisotropy constants, will cause

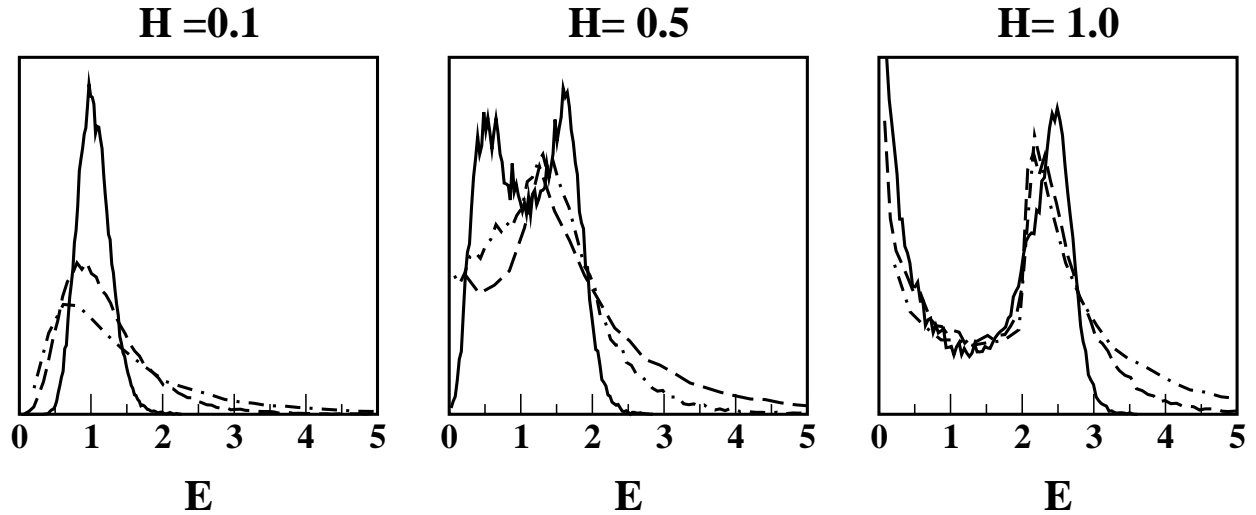


Figure 2.11: Effective energy barrier distributions for particles with random orientations and the distribution of anisotropy constants of Eq.(2.22) with  $K_0 = 1$ , and widths  $\sigma = 0.2$  (continuous lines),  $0.5$  (dashed lines),  $0.8$  (dot-dashed lines), for different values of  $h$ .

the magnetization law to deviate from the ideal situation posed by Langevin. In this section, we will study how these properties, more specifically, the disorder and the anisotropy, modify the magnetization curves.

The calculation of the equilibrium magnetization at non-zero  $T$  and finite  $K$  proceeds along the standard techniques of statistical mechanics. For particles oriented at an angle  $\psi$ ,  $m(H, T)$  is simply given by the average of the projection of the magnetic moment of the particles onto the field direction over all their possible orientations  $\theta$ . In our model, this is [13, 14]

$$m(\alpha, \xi, \psi) = \frac{1}{\mathcal{Z}} \int_{\Omega} d\Omega \cos \theta e^{-U(\theta, \varphi, \psi)}, \quad (2.23)$$

where  $\Omega$  is the solid angle and  $\mathcal{Z}$  is the partition function of the system defined as

$$\mathcal{Z}(H, T, \psi) = \int_0^{\pi} d\Omega e^{-U(\theta, \varphi, \psi)}. \quad (2.24)$$

Here, the energy  $U(\theta, \psi)$  appearing in the Boltzmann probability, has to be calculated from Eq. (2.3), then

$$U(\theta, \varphi, \psi) = -\alpha \sin^2 \theta + \xi(\cos \theta \cos \psi + \sin \theta \sin \psi \cos \varphi), \quad (2.25)$$

where the two dimensionless parameters

$$\alpha \equiv \frac{\mu KV}{k_B T} \quad \xi \equiv \frac{\mu HV}{k_B T}, \quad (2.26)$$

have been introduced.

For bulk ferromagnetic systems, it is usual to disregard the anisotropy energy contribution and, thus, use the Langevin function

$$m(H, T) = \mathcal{L}(\xi) = \coth(\xi) - 1/\xi \quad (2.27)$$

to model the field and temperature dependencies of the equilibrium magnetization. However, in real small particle systems, the anisotropy energy, mainly of shape and magnetocrystalline origin, can be comparable

Element	K(erg/cm <sup>3</sup> )	M <sub>0</sub> (emu/cm <sup>3</sup> )	H (Oe)	r=100 Å		r= 50Å	
				T=10 K	T=300 K	T=10 K	T=300 K
Fe (fcc)	4.81 × 10 <sup>5</sup>	1714	10	α = 1460 ξ = 52	α = 42 ξ = 1.7	α = 182 ξ = 6.5	α = 6 ξ = 0.21
			1000	α = 1460 ξ = 5200	α = 42 ξ = 173	α = 182 ξ = 650	α = 6 ξ = 21.6
Co (hcp)	4.12 × 10 <sup>6</sup>	1422	10	α = 1250 ξ = 43	α = 416 ξ = 1.43	α = 1552 ξ = 5.35	α = 52 ξ = 0.18
			1000	α = 1250 ξ = 4310	α = 416 ξ = 143	α = 1552 ξ = 539	α = 52 ξ = 18

Table 2.1: Values of physical parameters for two ferromagnetic elements and typical energy scales for a spherical particle of radius 100 Å (volume,  $V = 4.18 \times 10^{-24} \text{ m}^3$ ) 50 Å (volume,  $V = 5.2 \times 10^{-25} \text{ m}^3$ ), under different applied fields and temperatures.

to the Zeeman energy induced by the magnetic field. To illustrate this point, we have calculated in Table 2.6 typical values of  $\alpha$  and  $\xi$  for spherical Co particles of radius 50 and 100 Å. For a wide range of  $T$ , the values of  $\alpha$  are in both cases larger than  $\xi$  for moderate magnetic fields. Therefore, it is necessary to modify the Langevin law in order to include the first term in Eq.(2.3).

### 2.6.1 Aligned particles

The calculation can be performed analytically only for the case of oriented particles ( $\psi = 0$ ) and proceeds along the standard techniques of statistical mechanics [15]. Starting from Eq. (2.23), with  $\psi = 0$ , and after a change of variables to  $x = \cos \theta$ , we immediately obtain

$$m_{or} = I / (e^{-\alpha} \mathcal{J}), \quad (2.28)$$

where the following integrals have to be evaluated

$$\begin{aligned} \mathcal{J} &\equiv \int_{-1}^{+1} dx e^{\alpha x^2 + \xi x} \\ I &\equiv e^{-\alpha} \int_{-1}^{+1} dx x e^{\alpha x^2 + \xi x}. \end{aligned} \quad (2.29)$$

The second integral can be rewritten in terms of the first integrating by parts

$$I = \frac{1}{\alpha} \sinh \xi e^{\alpha} - \frac{\xi}{2\alpha} e^{\alpha} \mathcal{J}, \quad (2.30)$$

so that the magnetization law becomes

$$m_{or} = \frac{\sinh \xi e^{\alpha}}{\alpha \mathcal{J}} - \frac{\xi}{2\alpha}. \quad (2.31)$$

Finally,  $\mathcal{J}$  can be evaluated in terms of the error function as

$$\mathcal{J} = \frac{1}{\sqrt{\alpha}} [e^{\alpha+\xi} E(z_+) - e^{\alpha-\xi} E(z_-)], \quad (2.32)$$

and the final result for  $m_{or}$  is

$$m_{or}(\alpha, \xi) = \frac{\sinh(\xi)}{\sqrt{\alpha}[e^{\xi}E(z_+) - e^{-\xi}E(z_-)]} - \frac{\xi}{2\alpha}. \quad (2.33)$$

where  $z_{\pm} = \sqrt{\alpha}(1 \pm \frac{\xi}{2\alpha})$  and  $E(z)$  is the Dawson's integral [15]. In Fig.2.12 the result is compared to the usual Langevin law for different values of the anisotropy energy  $\alpha$ . We observe that, at low temperatures, and even for small values of  $\alpha \sim 0.5$  and  $\xi$  there is a significant departure from the Langevin law that becomes smaller as the field increases. With increasing  $\alpha$ , the particles are easier to magnetize, because the magnetization equilibrium direction approach to the easy-axis. In the  $\alpha = \infty$  limit, the curves tend to the Ising limit,  $m_{\text{Ising}} = \tanh(\xi)$ .

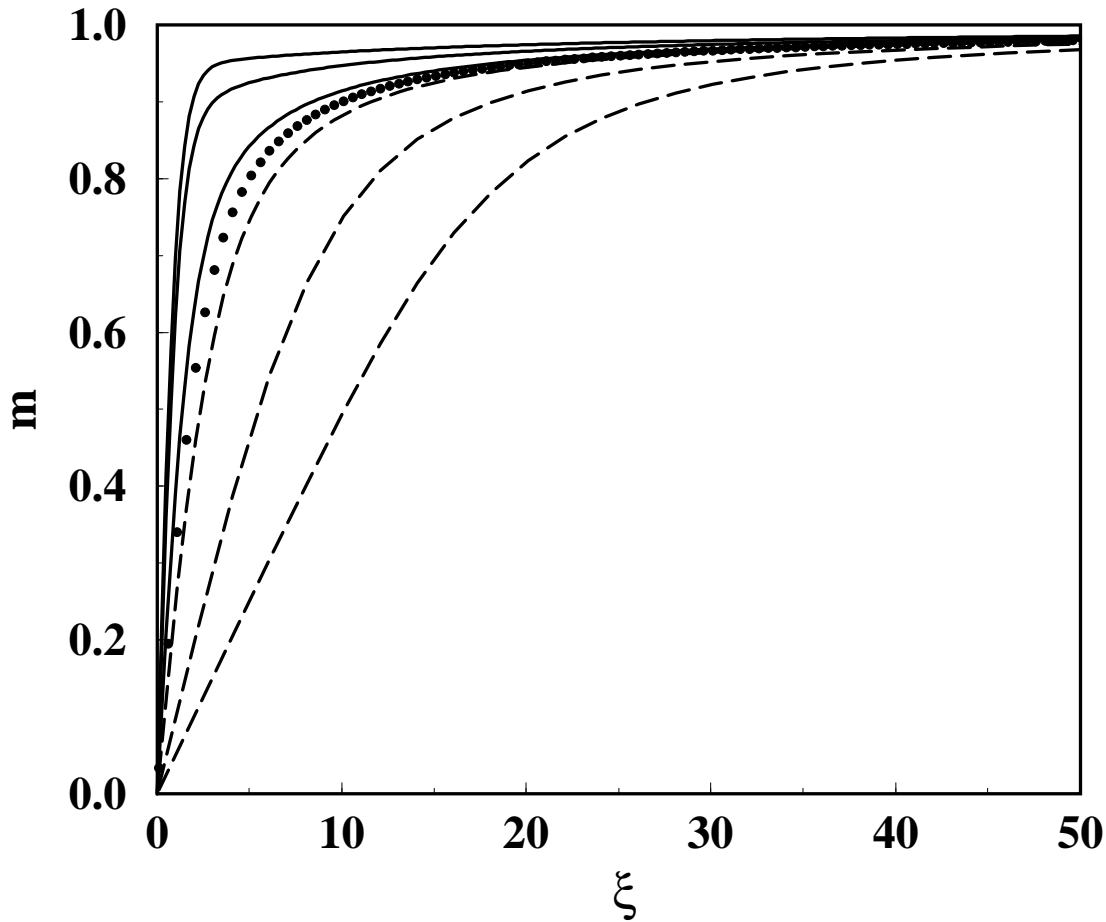


Figure 2.12: Magnetization curves for a 3D system, as a function of the dimensionless Zeeman energy  $\xi = \mu HV/k_B T$ . Continuous lines are for a particle aligned in the direction of  $\mathbf{h}$  ( $\psi = 0$ ) and anisotropy energies  $\alpha = 1, 5, 10$  from the lowermost curve, they have been evaluated from the exact expression Eq. (2.33). Dashed lines are for a system of randomly oriented particles and anisotropy energies  $\alpha = 1, 5, 10$  starting from the uppermost curve, they are the result of the numerical evaluation of Eq. (2.34). The Langevin law ( $\alpha = 0$ ) is shown in symbols for comparison.

### 2.6.2 Randomly oriented particles with $f(K)$

In systems with distributed properties, random distribution of easy-axis and distribution of anisotropy constants, the magnetization laws have to be found by numerical integration of the corresponding equations. Now the magnetization (2.23) has to be averaged with the corresponding texture function that accounts for the distribution of particle orientations ( $\sin \theta$  for random orientations) and weighted with the anisotropy distribution  $f(K)$

$$m(\alpha, \xi) = \frac{1}{Z} \int_0^\infty dK f(K) \int_{-1}^{+1} d(\cos \psi) m(\alpha, \xi, \psi). \quad (2.34)$$

The effect of the random orientation of the particles on the magnetization law (see dashed lines in Fig. 2.12) is opposite to that of the aligned case. Now, the consideration of finite  $K$  results in a decrease of the magnetization due to the misalignment of the particles with respect to the field direction. The inclusion of an anisotropy distribution  $f(K)$  does not change appreciably the previous results for  $K_0 = 1$ , since the main contribution to  $m(\alpha, \xi)$  still comes from particles with  $K = 1$  for such a logarithmic-normal distribution.

## 2.7 The Two-State Approximation

At  $T$  such that the thermal energy  $k_B T$  is smaller than the relevant energy barriers of the system, typically of the order of the anisotropy energy  $KV$  ( $\alpha \gg 1$ ), the main contribution to thermodynamic averages comes from states around the energy minima, since thermally activated jumps out of the stable directions of the magnetization have extremely low probability to succeed. This can be more clearly understood by looking at the shape of the equilibrium probability distribution given by the Boltzmann distribution  $g(\theta, \phi)$ . This quantity which gives the probability density to find the particle magnetization pointing at an angle  $\theta$ . For an aligned particle ( $\psi = 0$ ), it can be written as

$$g(\theta) = \frac{1}{Z} \sin \theta e^{-U(\theta)}. \quad (2.35)$$

This function has maximum near the energy minima, the equilibrium states of the system.

In Fig. 2.13, we can see that, at low temperatures ( $\alpha \ll 1$ ),  $g(\theta)$  is almost zero except for the two narrow peaks around the energy minima at 0 and  $\pi$ . This is so because, in this regime, the energy barriers are large and cannot be surmounted by thermal fluctuations. Consequently, one can truncate the continuum of possible states for  $\theta$  to the two states given by the stable equilibrium magnetization directions. This is what we will refer to as Two State Approximation (TSA) and will be used in calculations of the magnetization curves in the next subsection and Monte Carlo simulations in Chapter 5. Moreover, in the same figure, we can clearly see the combined effect of applying a magnetic field and the temperature. On one hand,  $H$  increases the probability around the field direction, and on the other the temperature widens the probability distribution.

Therefore, as it will be useful for the numerical calculations of the relaxation curves in Chapter 5, we will consider the so-called *Two-State Approximation* (TSA). [16, 17] In this approximation, the continuum of states corresponding to all the possible orientations of  $\mathbf{m}$  is truncated to the two local energy minima states. This will allow us to replace the integrations over magnetization directions by sums over the two energy minima. If the particle has only one minimum, the two states considered in the calculation will be the minimum and the maximum of the energy function. Therefore, for a particle with  $\varphi = 0$  (2D model)

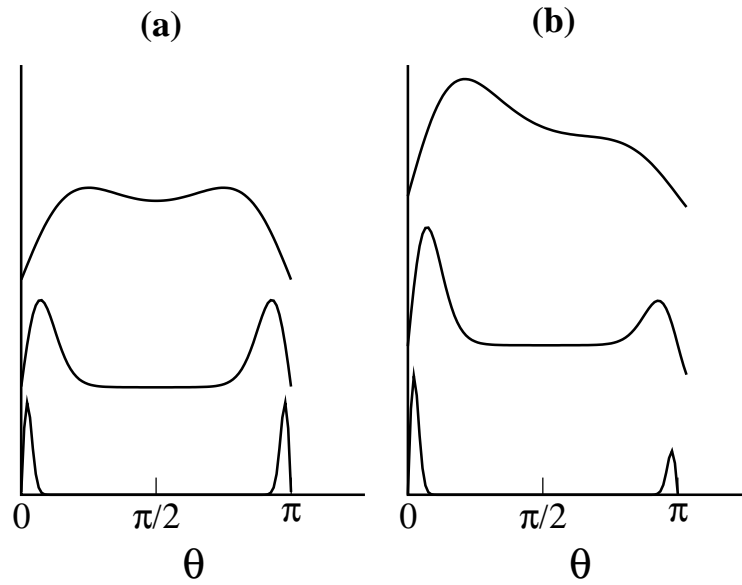


Figure 2.13: Boltzmann distributions  $g(\theta)$  (defined in Eq. 2.35) for the magnetization orientation  $\theta$  at three different values of the anisotropy energy  $\alpha = 1, 10, 100$  from top to bottom, (a) without magnetic field  $\xi = 0$  and (b) for a magnetic field energy  $\xi = 0.5$ .

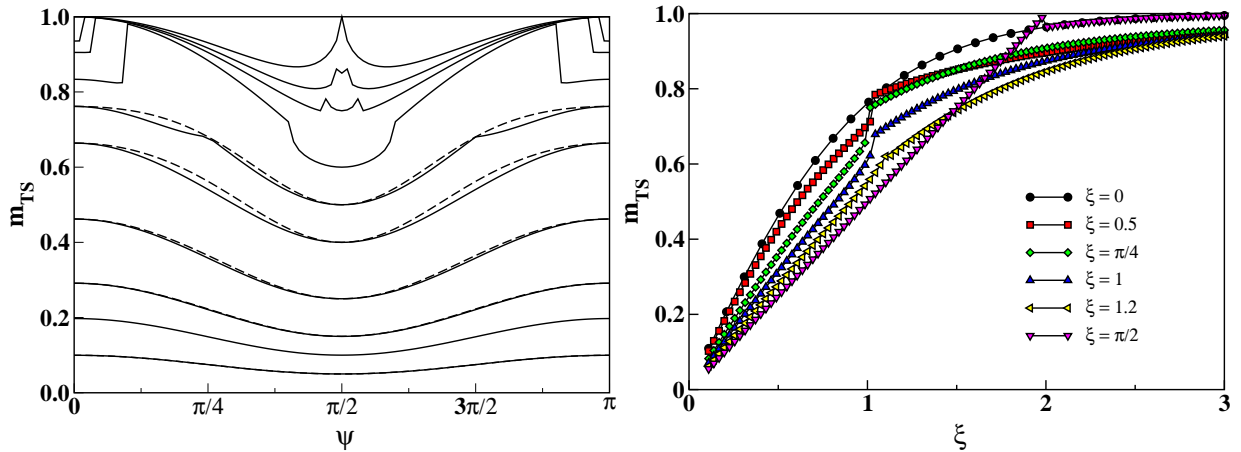


Figure 2.14: Left panel: Magnetization of a particle in the TSA as a function of the orientation of the particle easy-axis,  $\psi$ , and different values of the magnetic field  $\xi = 0.1, 0.2, 0.3, 0.5, 1.0, 1.2, 1.5, 1.7, 2.0$ , starting from the lowermost continuous curve, as calculated from Eq. (2.36). The dashed lines correspond to the low  $h$  approximation of Eq. (2.38). Right panel: Magnetization of a particle in the TSA as a function of the reduced field  $\xi$  for different orientations of the easy-axis  $\psi$ .  $\psi = 0, 0.5, \pi/4, 1.0, 1.2, \pi/2$ , starting from the uppermost curve.

oriented at an angle  $\psi = 0$  the magnetization [Eq. (2.23)] becomes

$$\bar{m}_{TS}(K, \psi) = \frac{1}{Z} \sum_{i=1,2} \cos[\theta_{\min}^i(\psi)] e^{-E_{\min}^i(K, \psi)\beta}, \quad (2.36)$$

where  $\beta = 1/k_B T$ .

As in the continuum case, for  $\psi \neq 0$ , this calculation can only be performed numerically although in the small field limit it is easy to derive an analytical expression. For this purpose we simply use the expressions for the energy minima obtained in Sec. (2.4) to approximate the projections of the magnetization into the field direction by

$$\begin{aligned} \cos(\theta_{\min}^1) &\simeq \cos \psi + h \sin^2 \psi \\ \cos(\theta_{\min}^2) &\simeq -\cos \psi + h \sin^2 \psi, \end{aligned} \quad (2.37)$$

after substituting into Eq. (2.36) and keeping only leading order terms in  $h$  we obtain

$$\bar{m}_{TS}(K, \psi) \simeq \cos \psi \tanh(\xi \cos \psi) + h \sin^2 \psi \quad (2.38)$$

which reduces to  $m(K, 0) = \tanh(\xi)$  when  $\psi = 0$ .

The variation of the magnetization as a function of the orientation of the particle is shown in Fig. 2.14 (left panel) for several values of  $h$ , together with the above approximation. First, let us notice that, for reduced field energies that correspond to  $H \leq 1$  (the minimum critical field), the magnetization increases as particle orientation changes from transverse towards the field direction. However, as  $H$  is increased from 1, particles with critical fields less than the applied field (first the ones oriented around  $\psi = \pi/4, 3\pi/4$ ) become magnetized into the the direction of the only energy minimum, which is closer to the field direction and, consequently, their magnetization increases. This results in the abrupt jumps of the upper curves. The low field approximation, represented by the dashed lines in the same figure (invisible for the lowermost curves), is in very good agreement with the exact results even for fields up to the minimum critical one, so it can be faithfully used in analytic calculations.

For a system of randomly oriented particles and with a distribution of anisotropy constants  $f(K)$  Eq. 2.36 has to be integrated over orientations and weighted with  $f(K)$ . Therefore, the approximation to Eq. (2.23) becomes in the TSA

$$m_{TS}(H, T) = \int_0^\infty dK \int_0^\pi d\psi f(K) \bar{m}_{TS}(K, \psi), \quad (2.39)$$

Eq. (2.39) has been numerically evaluated for a system of randomly oriented particles and several values of  $K_0$  and the results are displayed in Fig. 2.15. For the smallest  $K_0$  values, the curves present a small jump at a certain value of  $\xi$ . This may seem unphysical but, in fact, this jump appears at an  $h$  equal to the critical field for the disappearance of one of the energy minima. In fact, when averaging over a distribution of anisotropies  $f(K)$  with  $K_0 = 1$  and  $\sigma = 0.5$ , this jump disappears.

As expected, the TSA curves coincide with the results obtained from the exact expression Eq. (2.36) for high enough  $K_0$  (compare the  $K_0 = 10$  case with the dashed-dotted line in Fig. 2.15). On the other hand, at low enough  $K_0$ , the TSA reproduces the exact result for aligned particles, for which the magnetization curve reduces to  $m_{TS} = \tanh(\xi)$ , since the magnetization does not depend on  $\alpha$  in this case (compare the continuous line with the case  $K_0 = 0.5$ ) [18].



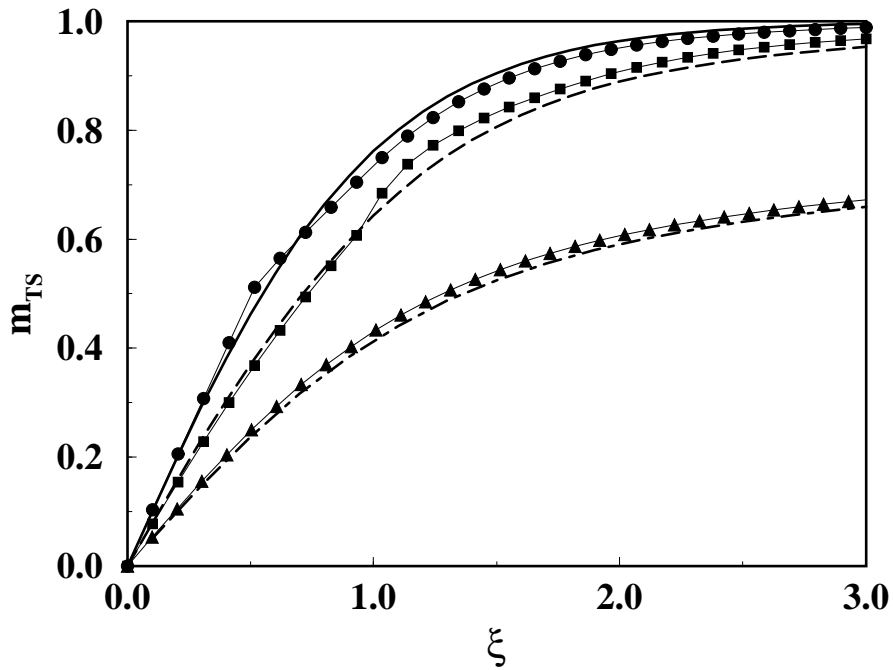


Figure 2.15: Magnetization curves as a function of the dimensionless Zeeman energy  $\xi = \mu HV/k_B T$  in the TSA. Symbols stand for randomly oriented particles with  $K_0 = 0.5, 1.0, 10.0$  (from the uppermost curve). The case  $K_0 = 10$  is compared to the exact result given by Eq. (2.23) in 2D (dash-dotted line). The case  $K_0 = 1$  is compared with a system of randomly oriented particles with  $f(K)$ ,  $K_0 = 1$  and  $\sigma = 0.5$  (long-dashed line). The result for aligned particles is displayed as a continuous line, for which  $m_{TS} = \tanh(\xi)$  ( $m_{TS}$  is independent of  $\sigma$  in this case).

## 2.8 Conclusions and Discussion

In this chapter, we have presented the bases of the model for the description of an individual magnetic monodomain particle, studying the properties of its magnetic free energy in terms of the energy barriers and using the concept of effective energy barrier distributions. They give information on how the external parameters like the magnetic field modify the energy landscape traced out by the magnetic anisotropy and the distribution of the intrinsic properties of the particle such as the volume and easy-axis direction. In particular, we have seen that the magnetic field narrows the effective energy barrier distributions and shift them towards lower value of the energy. This behaviour has been observed experimentally through indirect measurements by several authors. Peleg et al. [19] deduced the distribution of blocking temperatures  $f(T_B)$  from measurements of the field-cooled (FC) and reversed field-cooled (RFC) magnetization at different  $H$  on granular AuCo films. It can be easily seen that  $f(T_B)$  is proportional to the temperature derivative of the difference  $M_{FC} - M_{RFC}$ . In this way, the authors observed distributions with peaks that shifted towards lower  $T$  with increasing  $H$ , and a monotonic narrowing of the peaks with  $H$ . The peak shift  $T_B(H)$  did not agree with simple laws expected for aligned particles with no volume distribution. Since  $T_B$  is proportional to the anisotropy energy barrier, their observations are in accordance with our result for the  $f_{\text{eff}}(E)$ .

This general analysis has been subsequently used to compute the magnetization curves of ensembles of particles taking into account the anisotropy energy, the random orientation of the easy-axes and the distribution of volumes or anisotropies  $f(K)$ . The calculations have shown that, when anisotropy is taken into account, clear departures from the Langevin law are observed. On one hand, when the particles are aligned, the magnetization increases for all fields when the anisotropy is taken into account. On the other hand, when the easy-axes of the particles are random distributed, the effect is the opposite. These effects has been observed in small particle systems of different composition. They can be evidenced by a failure to adjust the magnetization curves by a distribution of Langevin laws or by a lack of superposition of the magnetization curves measured at different  $T$  when using the  $H/T$  superparamagnetic scaling variable. For example, early experiments by Williams et al. [20] observed departures from Langevin behaviour in ferrofluids below the freezing temperature and the results were qualitatively compared to theoretical expressions given in [14]. Hanson et al. [21] found similar results for the low  $T$  ( $T < 50$  K) on FeC amorphous particles, even for fields of 1.2 T. Among the recent experiments, let us mention the works by Mamiya and Nakatani [22], where departures from Langevin behaviour are observed already at  $T = 100$  K in FeN fine particles; experiments by Jamet et al. [23] on highly anisotropic Co nanoparticles on A Nb matrix and by Luis et al. [24] on similar particles in an alumina matrix.



## Bibliography

- [1] R. C. O'Handley, *Modern Magnetic Materials: Principles and Applications* (Wiley and Sons, New York, 2000).
- [2] A. Aharoni, *Introduction to the Theory of Ferromagnetism* (Oxford University Press, New York, 1996).
- [3] A. Aharoni, *J. Magn. Magn. Mater.* **306**, 1 (2001).
- [4] E. H. Frei, S. Shtrikman, and D. Treves, *Phys. Rev.* **106**, 446 (1949).
- [5] W. Wernsdorfer, *Adv. Chem. Phys.* **118**, 99 (2000).
- [6] H. J. Richter, *IEEE Trans. Magn.* **29**, 2185 (1993).
- [7] E. C. Stoner and E. P. Wohlfarth, *Philos. Trans. R. Soc. London A* **240**, 599 (1948), reprinted in *IEEE Trans. Magn.* **27**, 3475 (1991).
- [8] J. C. Slonczewski, research memorandum RM 003.111.224, IBM Research Center Poughkeepsie (unpublished).
- [9] A. Thiaville, *J. Magn. Magn. Mater.* **182**, 5 (1998).
- [10] A. Thiaville, *Phys. Rev. B* **61**, 12221 (2000).
- [11] G. Bertotti, *Hysteresis in Magnetism* (Academic Press, London, 1998).
- [12] H. Pfeiffer, *Phys. Stat. Sol. A* **118**, 295 (1990).
- [13] P. J. Clegg and L. Bessais, *J. Magn. Magn. Mater.* **203**, 265 (1999).
- [14] R. W. Chantrell, N. Y. Ayoub, and J. Popplewell, *J. Magn. Magn. Mater.* **53**, 199 (1985).
- [15] F. G. West, *J. Appl. Phys.* **32**, 249S (1961).
- [16] H. Pfeiffer, *Phys. Stat. Sol. A* **120**, 233 (1990).
- [17] H. Pfeiffer, *Phys. Stat. Sol. A* **122**, 377 (1990).
- [18] J. L. García-Palacios, *Adv. Chem. Phys.* **112**, 1 (2000).
- [19] N. Peleg, S. Shtrikman, and G. Gorodetsky, *J. Magn. Magn. Mater.* **191**, 349 (1997).
- [20] H. D. Williams, K. O'Grady, M. E. Hilo, and R. W. Chantrell, *J. Magn. Magn. Mater.* **122**, 129 (1993).
- [21] M. Hanson, C. Johansson, and S. M. rup, *J. Phys.: Condens. Matter* **5**, 725 (1993).

- [22] H. Mamiya and I. Nakatani, *IEEE Trans. Magn.* **34**, 1126 (1998).
- [23] M. Jamet, V. Depuis, P. Mélion, G. Guiraud, A. Pérez, W. Wernsdorfer, A. Traverse, and B. Baguenard, *Phys. Rev. B* **62**, 493 (2000).
- [24] F. Luis, J. M. Torres, L. M. García, J. Bartolome, J. Stankiewicz, F. Petroff, F. Fettar, J. Maurice, and A. Vaurés, *Phys. Rev. B* **65**, 094409 (2002).

## CHAPTER 3

### SINGLE PARTICLE MODEL

#### 3.1 Introduction

The magnetic properties of fine particles are strongly influenced by finite-size and surface effects, their relevance increasing as the particle size decreases. Finite-size effects are due to the nanometric size of the particles, while surface effects are related to the symmetry breaking of the crystal structure at the boundary of each particle. These effects are manifested in nanometric particles through a wide variety of anomalous magnetic properties with respect to those of bulk materials. The magnetic characterization of these systems has put forward the controversial issue of distinguishing between the contributions coming from finite-size and surface effects to their peculiar magnetic properties. For instance, alternately explanations to the reduction of the saturation magnetization  $M_s$  - a common experimental observation in fine particle systems - has been given in the past. Early models postulated the existence of a so-called dead magnetic layer induced by the demagnetization of the surface spins, which causes a reduction in  $M_s$  because of its paramagnetic response. In more recent works devoted to the study of different ferrimagnetic oxides -  $\gamma$ - $\text{Fe}_2\text{O}_3$ ,  $\text{NiFe}_2\text{O}_4$ ,  $\text{CoFe}_2\text{O}_4$ ,  $\text{CuFe}_2\text{O}_4$ , in the form of nanometric particles [1, 2, 3, 4, 5] - a random spin canting at the surface, caused by competing antiferromagnetic (AF) interactions, was observed by Mössbauer spectroscopy [2], polarized [4] and inelastic [6] neutron scattering, and ferromagnetic (FM) resonance [7]. The origin of this non-collinear arrangement of the spins was discussed by several authors supporting the surface [2, 8, 9, 10] or the finite-size explanations [11, 12, 13, 14, 15], but up to the moment no clear conclusions have been established.

All these ferrimagnetic fine particles share a singular phenomenology at low temperatures. Among the static properties, experiments have shown that the hysteresis loops display high closure fields and do not saturate [14, 16, 17] even at fields of the order of 50 T, which indicates that the anisotropy fields cannot be the only responsible mechanism for the magnetization reversal. Low magnetization as compared to bulk, shifted loops after field cooling and irreversibilities between the field cooling and zero field cooling processes even at high fields are also observed [5, 16, 17]. Moreover, the existence of aging phenomena [18, 19] in the time-dependence of the magnetization, indicates that there must be some kind of freezing leading to a complex hierarchy of energy levels. Whether these phenomena can be ascribed to intrinsic properties of the particle itself (spin-glass state of the surface which creates an exchange field on the core of the particle [14, 17]), or they are due to a collective behaviour induced by interparticle interactions [20, 21, 22], has been the object of controversy [23].

Up to the moment there has been no model giving a clear-cut explanation of all the above mentioned phenomenology, but some works addressing part of the issues have been published in recent years. The first atomic-scale model of the magnetic behaviour of individual ferrimagnetic nanoparticles is due to Kodama

and Berkowitz [24]. The authors presented results of calculations of a micromagnetic model of maghemite particles which were based on an energy minimization procedure instead of the Monte Carlo (MC) method. They used Heisenberg spins with enhanced anisotropy at the surface with respect to the core and included vacancies and broken bonds at the surface, arguing that these are indeed necessary to obtain hysteresis loops with enhanced coercivity and high-field irreversibility. Later, Kachkachi et al. [25, 26, 27] performed MC simulations of a maghemite particle described by a Heisenberg model, including exchange and dipolar interactions, using surface exchange and anisotropy constants different to those of the bulk. Their study was mainly focused on the thermal variation of the surface (for them consisting of a shell of constant thickness) and core magnetization, concluding that surface anisotropy is responsible for the non-saturation of the magnetization at low temperatures. No attention was paid, however, to the magnetic properties under a magnetic field.

Other computer simulations studying finite-size and surface effects on ferro- and antiferromagnetic cubic lattices have also been published. Trohidou et al. [28, 29] performed MC simulations of AF small spherical clusters. By using an Ising model on a cubic lattice [28], they computed the thermal and magnetic field dependencies of the magnetization and structure factor, concluding that the particle behaved as a hollow magnetic shell. By means of a Heisenberg model [29] with enhanced surface anisotropy, they studied the influence of different kinds of surface anisotropy on the magnetization reversal mechanisms and on the temperature dependence of the switching field. Dimitrov and Wysin [30, 31] studied the hysteresis phenomena of very small spherical and cubic FM fcc clusters of Heisenberg spins by solving the Landau-Lifshitz equations. They observed an increase of the coercivity with decreasing cluster size and steps in the loops due to the reversal of surface spins at different fields. However they did not consider the finite temperature effects.

In order to contribute to elucidate the above mentioned experimental controversies and to further develop the previously published numerical simulations, we present the results of a MC simulation of a single spherical particle which aim at clarifying what is the specific role of the finite size and surface on the magnetic properties of the particle, disregarding the interparticle interactions effects. In particular, we will study the magnetic properties under a magnetic field and at finite temperature, thus extending other simulation works. In choosing the model, we have tried to capture the main features of real particles with the minimum ingredients allowing to interpret the results without any other blurring effects.

The rest of the chapter is organized as follows. In Sec. 3.2 we present the model of a maghemite particle upon which the MC simulations are based. In Sec. 3.3, the study of the basic equilibrium magnitudes - energy, specific heat, and magnetization - in absence of magnetic field is presented, comparing results for different particle sizes with those for periodic boundaries. Sec. 3.4 is devoted to the study of magnetization processes under the presence of a magnetic field. The thermal dependence of hysteresis loops and coercive field are computed, and a detailed analysis of these quantities in terms of the surface and core contributions is performed. The effects of the introduction of different kinds of disorder on the magnetic properties are presented in Sec. 3.5, where we study both the deviation from ideal stoichiometry by random removal of magnetic ions on the whole particle, as well as the introduction of vacancies only at the surface of the particle. In Sec. 3.6, we end up with a discussion of the obtained results and a presentation of the conclusions.

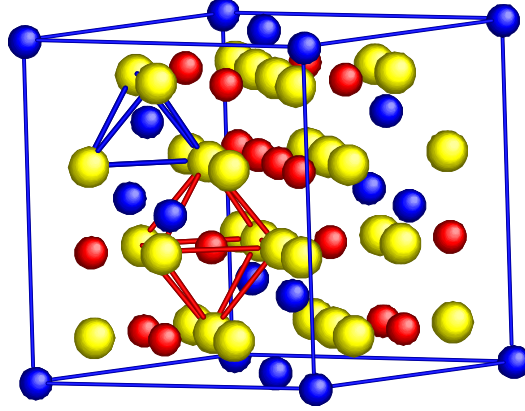


Figure 3.1: Unit cell of maghemite. The magnetic  $\text{Fe}^{3+}$  ions occupying the two sublattices, in different coordination with the  $\text{O}^{2-}$  ions (white colour), are coloured in black (T sublattice, tetrahedral coordination) and in grey (O sublattice, octahedral coordination).

## 3.2 Model

$\gamma\text{-Fe}_2\text{O}_3$ , maghemite, is one of the most commonly studied nanoparticle compounds [24] presenting the above mentioned phenomenology. Maghemite is a ferrimagnetic spinel in which the magnetic  $\text{Fe}^{3+}$  ions with spin  $S = 5/2$  are disposed in two sublattices with different coordination with the  $\text{O}^{2-}$  ions. Each unit cell (see Fig. 3.1) has 8 tetrahedral (T), 16 octahedral (O) sites, and one sixth of the O sites has randomly distributed vacancies to achieve neutrality charge. The T sublattice has larger coordination than O, thus, while the spins in the T sublattice have  $N_{TT} = 4$  nearest neighbours in T and  $N_{TO} = 12$  in O, the spins in the O sublattice have  $N_{OO} = 6$  nearest neighbours in O and  $N_{OT} = 6$  in T. In our model, the  $\text{Fe}^{3+}$  magnetic ions are represented by Ising spins  $S_i^\alpha$  distributed in two sublattices  $\alpha = \text{T, O}$  of linear size  $N$  unit cells, thus the total number of spin sites is  $(24N^3)$ . The choice of Ising spins allows to reproduce a case with strong uniaxial anisotropy, while keeping computational efforts within reasonable limits. In spite of the fact that this choice could be a crude approximation for moderate anisotropy, which is not the case of maghemite, this will not affect the conclusions of our study, since our main goal is to clarify the effect of the intrinsic magnetic frustration of the maghemite lattice at the surface of the particle. With this aim, we have taken into account the real lattice structure and interactions in the most realistic way. In particular, the possible existence of a spin-glass state at the surface of the particle should be better checked with Ising spins than with a model with continuous spins, since in the former frustration effects are enhanced [32]. Moreover, the Heisenberg version of the particle without disorder does not show irreversibility in the hysteresis loops, whereas the Ising version does [24, 33, 34], being easier to observe independently the effects of disorder and finite size in the last case.

The spins interact via antiferromagnetic (AF) exchange interactions with the nearest neighbours on both sublattices and with an external magnetic field  $H$ , the corresponding Hamiltonian of the model being

$$\mathcal{H}/k_B = - \sum_{\alpha, \beta = \text{T, O}} \sum_{i=1}^{N_\alpha} \sum_{n=1}^{N_{\alpha\beta}} J_{\alpha\beta} S_i^\alpha S_{i+n}^\beta - h \sum_{\alpha = \text{T, O}} \sum_{i=1}^{N_\alpha} S_i^\alpha. \quad (3.1)$$



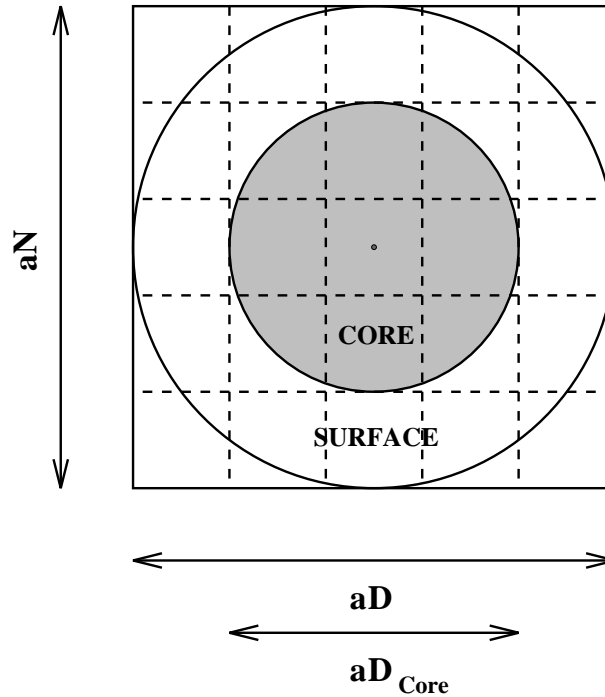


Figure 3.2: Schematic drawing of the spherical particles simulated in this study, showing the basic geometric parameters. The unit cells are indicated by the dashed grid, being the cell parameter  $a$ , and  $N$  the number of unit cells along each axis.

where we have defined the field in temperature units as

$$h = \frac{\mu H}{k_B}, \quad (3.2)$$

being  $S$  and  $\mu$  the spin value and magnetic moment of the  $\text{Fe}^{3+}$  ion, respectively. Hereafter,  $S_i = \pm 1$  and the maghemite values of the nearest neighbour exchange constants will be considered [24, 25]:  $J_{TT} = -21$  K,  $J_{OO} = -8.6$  K,  $J_{TO} = -28.1$  K. Since the intersublattice interactions are stronger than those inside each sublattice, at low temperatures, there must be bulk ferrimagnetic order with spins in each sublattice ferromagnetically aligned and antiparallel intrasublattice alignment. To simulate the bulk behaviour, we have used periodic boundary (PB) conditions for a system of large enough size as to minimize finite-size effects (for systems of linear size  $N > 8$  these effects are already negligible). When studying finite-size effects, we have considered a spherically shaped particle with  $D$  unit cells in diameter and free boundaries (FB). In the latter case, two different regions are distinguished in the particle: the surface formed by the outermost unit cells and an internal core of diameter  $D_{Core}$  unit cells (see Fig. 3.2). The quantities measured after each MC step are the energy, specific heat, susceptibility and different magnetizations: sublattice magnetizations ( $M_O, M_T$ ), surface and core magnetization ( $M_{Surf}, M_{Core}$ ), and total magnetization ( $M_{Total}$ ). Each of them have been normalized to the respective number of spins so that they can range from 1 to -1. In particular,  $M_{Total}$  is 1 for ferromagnetic order, 0 for a disordered system and 1/3 for ferrimagnetic order of the O and T sublattices.

The size of the studied particles ranges from  $D = 3$  to 10 corresponding to real particle diameters from 25 to 83 Å (see Table 3.2). In this table, we have also included the number of surface and core spins  $N_{Surf}, N_{Core}$ , together with the normalized magnetization values of a ferrimagnetic configuration  $M_{Unc}$ . Note that due to the finite size of the particles, the ratio of T and O spins produces  $M_{Unc}$  values that, in

general, do not coincide exactly with the 1/3 value for perfect ferrimagnetic order in an infinite lattice. In order to make the measured magnetizations for different diameters comparable, we have normalized them to the corresponding  $M_{Unc}$  values given in Table 3.2.

D	$D_{Real}$ (Å)	$N_{Surf}$	$N_{Core}$	$M_{Unc}^{Surf}$	$M_{Unc}^{Core}$	$M_{Unc}$
3	25	330 (95%)	17	0.285	0.412	0.291
4	33	724 (87%)	111	0.337	0.369	0.341
5	41	1246 (78%)	347	0.355	0.291	0.341
6	50	1860 (69%)	841	0.350	0.332	0.344
8	66	3748 (58%)	2731	0.345	0.330	0.338
10	83	6485 (48%)	12617	0.329	0.337	0.333

Table 3.1: Characteristic parameters of some of the spherical particles simulated: particle diameter  $D$  in units of the lattice constant  $a$ , diameter of the corresponding real  $D_{Real}$ , number of total spins  $N_{Total}$ , number of spins at the surface and in the core  $N_{Surf}$ ,  $N_{Core}$ , and magnetization of the noncompensated spins  $M_{Unc} = (N_O - N_T)/N_{Total}$ . The data are for particles with no vacancies in the O sublattice.

### 3.3 Equilibrium Properties

#### 3.3.1 Energy and specific heat

We start by studying the effect of free boundary conditions and finite-size effects on the equilibrium properties in zero magnetic field. The simulations have been performed using the standard Metropolis algorithm. Starting from a high enough temperature ( $T = 200$  K) and an initially disordered state with spins randomly oriented, the system was cooled down at a constant temperature step  $\delta T = -2$  K and, after discarding the first 1000 MC steps in order to allow the system to thermalize, the thermal averages of the thermodynamic quantities were computed at each temperature during a number of MC steps ranging from 10000 to 50000 depending on the system size. The starting configuration at each new temperature was the one obtained at the end of the averaging process at the previous temperature. Systems with periodic and free boundary conditions with spherical shape have been considered with sizes ranging from 3 to 14. In Fig. 3.3, we compare the thermal dependence of the energy for spherical particles of different diameters  $D$  with the corresponding results for a system of size  $N = 14$  and PB (lowermost curve, left triangles). A second order transition from paramagnetic to ferrimagnetic order signaled by a sharp peak at  $T_c(D)$  in the specific heat (see the Inset in Fig. 3.3) is clearly observed. Finite size effects on both the energy and the specific heat are very important even for  $D$ 's as large as 14 in the FB case, while for PB conditions they are negligible already for  $N = 8$ . The energy difference between the disordered and ferrimagnetic phases as well as the critical temperature  $T_c(D)$  increases as  $D$  is increased. This last quantity is strongly size dependent and approaches the infinite size limit ( $T_c(\infty) = 126 \pm 1$  K as evaluated for the  $N = 14$  system with PB conditions) as  $D$  increases (see Fig. 3.4, in which the variation of the peak in the specific heat with  $1/D$  has been plotted).  $T_c(D)$  can be fitted to the scaling law

$$\frac{T_c(\infty) - T_c(D)}{T_c(\infty)} = \left(\frac{D}{D_0}\right)^{-1/\nu} \quad (3.3)$$

as predicted by finite-size scaling theory [35, 36] with  $D_0 = 1.86 \pm 0.03$  a microscopic length scale (in this case, it is roughly twice the cell parameter), and a critical exponent  $\nu = 0.49 \pm 0.03$ , which seems to indicate a mean field behaviour [37]. This result can be ascribed to the high coordination of the O and

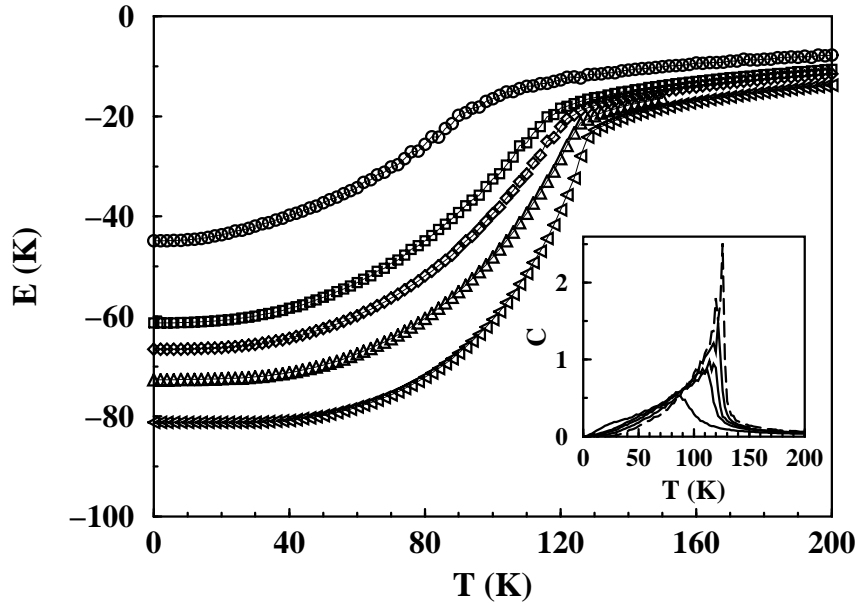


Figure 3.3: Thermal dependence of the energy for different diameters  $D = 3, 6, 8, 14$  (from the uppermost curve) and periodic boundary conditions  $N = 14$  (lowermost curve). Inset: Thermal dependence of the specific heat for the same cases (the periodic boundary case is drawn with a dashed line).

$T$  sublattices. The fitted curve is drawn in Fig. 3.4 where deviations from scaling are appreciable for the smallest diameters for which corrections to the finite-size scaling of Eq. 3.3 may be important [35].

### 3.3.2 Magnetization

To study the effects of a free surface and of finite size on the magnetization of the particles, we compare in Fig. 3.5 the results for four particle diameters ( $D = 3, 4, 6, 8$ , open circles) with that corresponding to a  $N = 14$  system with PB (representing the behaviour of the bulk). In this figure, we have distinguished the surface (dashed lines) and core (dot-dashed lines) contributions to the total magnetization (symbols). The results have been recorded during the same cooling procedure used to obtain the energy. The main feature observed is the reduction of the total magnetization  $M_{Total}$  with respect to the PB case (continuous line) due to the lower coordination of the spins at the surface, which hinders ferrimagnetic order at finite temperatures. Fig. 3.5 clearly shows the roles played by the surface and the core in establishing the magnetic order. On one hand, independently of the particle size, the core (dot-dashed lines) tends to a perfect ferrimagnetic order at low  $T$  (marked by  $M = 1/3$ ), progressively departing from the bulk behaviour as  $T$  approaches  $T_c$ , this finite-size effect being more important as the particle size decreases. However, the surface magnetization does not attain perfect ferrimagnetic order at  $T = 0$  even for  $D = 8$  due to the reduced coordination of the spins. For this reason, a rapid thermal demagnetization is observed which significantly departs  $M_{Surf}$  from the bulk behaviour.

It is worthwhile to note that for all the diameters studied there is a temperature range in which this demagnetization process is linear, this range being wider as the particle size decreases. In this linear regime, the particle demagnetization becomes dominated by the surface effects, being the core and surface behaviours strongly correlated. Linear demagnetization is indicative of the effective 3D-2D dimensional re-

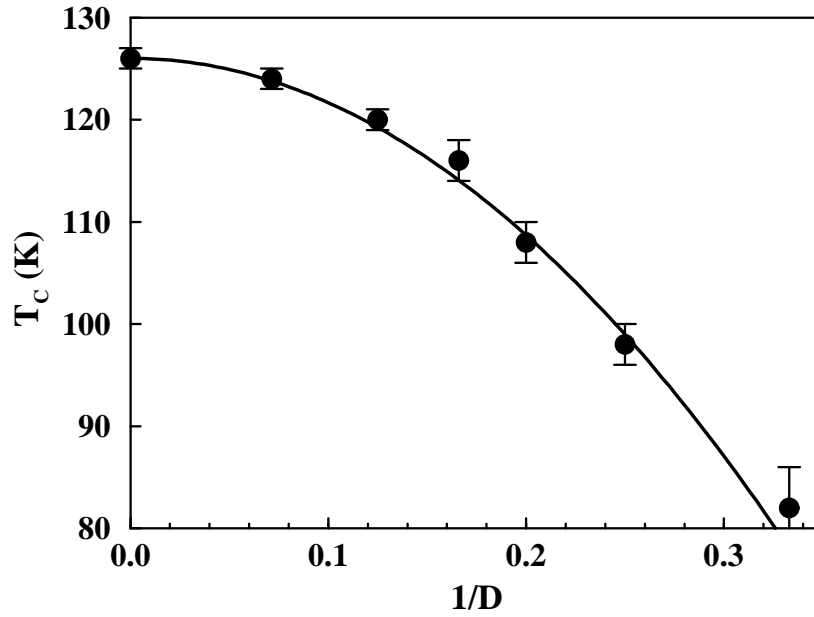


Figure 3.4: Particle size dependence of the transition temperature  $T_c$  from paramagnetic to ferrimagnetic phases for spherical particles with FB. The displayed values have been obtained from the maximum in the specific heat. The continuous line is a fit to Eq. 3.

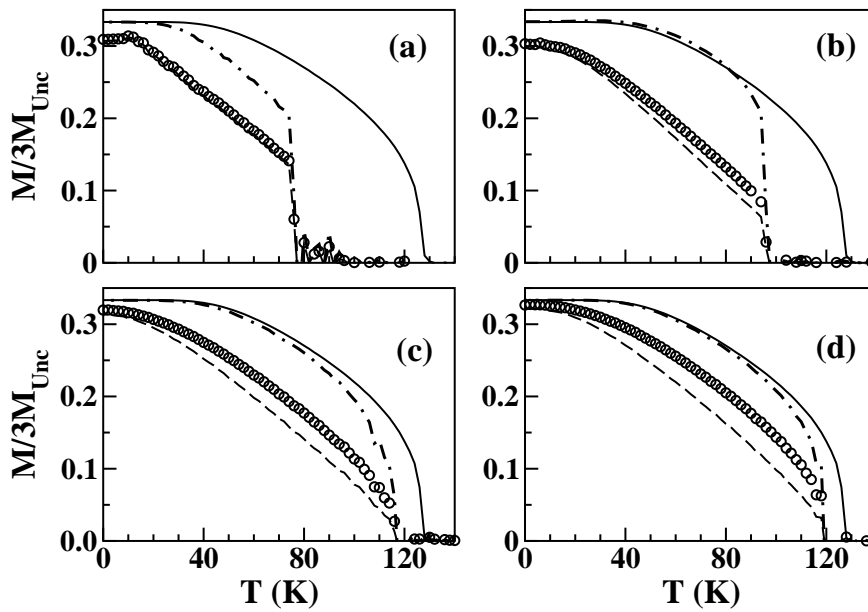


Figure 3.5: Thermal dependence of the magnetization  $M$  obtained by progressive cooling from high  $T$  at a constant rate,  $\delta T = -2$  K, and starting from a random configuration of spins. The results for four particle diameters are shown:  $D = 3$  (a),  $D = 4$  (b),  $D = 6$  (c), and  $D = 8$  (d). The contributions of the surface (dashed line) and core spins (dot-dashed line) have been distinguished from the total magnetization (circles). The results for PB conditions, in a system of linear size  $N = 14$ , have also been included for comparison (continuous line).

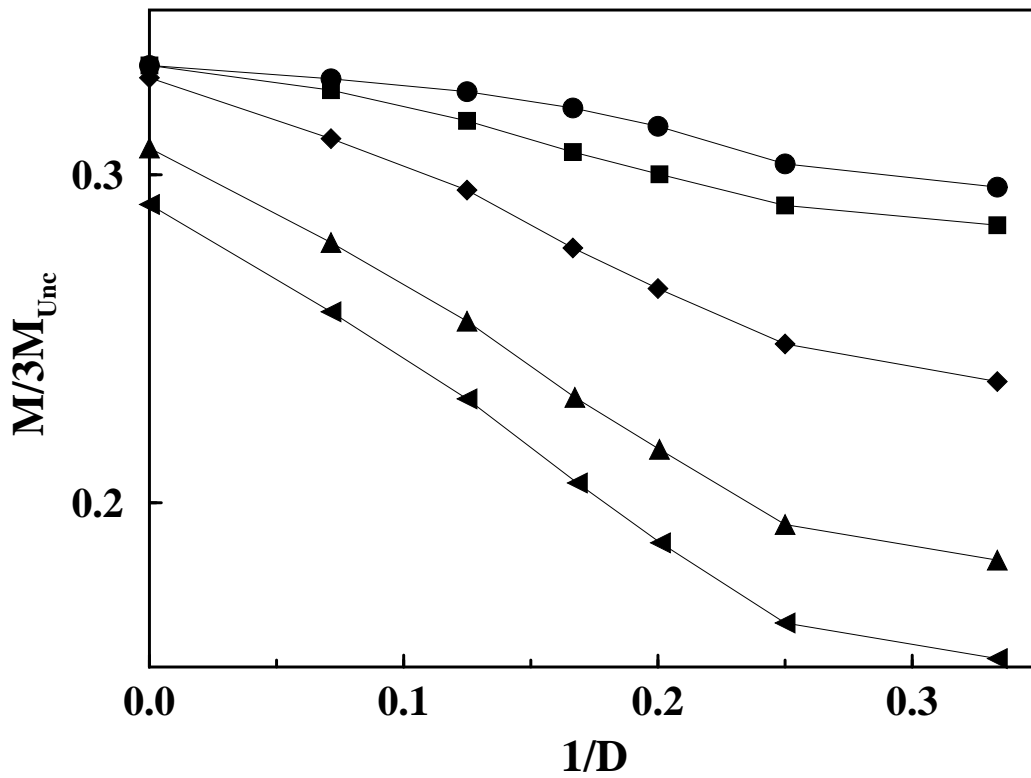


Figure 3.6: Size dependence of the magnetization of a spherical particle at different temperatures  $T = 0, 20, 40, 60, 70$  K (from upper to lowermost curves).

duction of the surface shell and has previously been observed in thin film systems [38, 39, 40, 41] and in simulations of rough FM surfaces [42].  $M_{Total}$  is always strongly dominated by the surface contribution, progressively tending to the bulk behaviour as the particle size is increased.

In Fig. 3.6 we show the size dependence of the  $M_{Total}$  at different temperatures. All the curves follow a quasi-linear behaviour with  $1/D$  except for very small particle sizes ( $D = 3$ ). This is consistent with the existence of a surface layer of constant thickness  $\Delta r$  independently of  $D$  and with reduced magnetization with respect to the core. With these assumptions, the size dependence of  $M$  can be expressed as

$$M(D) = M_{Core} - \Delta M \frac{\Delta r S}{V} = M_{Core} - \Delta M \frac{6\Delta r}{D}, \quad (3.4)$$

where  $S$  and  $V$  are the surface and volume of the particle, and  $\Delta M = M_{Core} - M_{Surface}$ .

### 3.4 Hysteresis Loops

In Fig. 3.7, we show the hysteresis loops of particles with diameters  $D = 3, 6$  for different temperatures. The loops have been computed by starting from a demagnetized state at  $h = 0$  and increasing the magnetic field in constant steps,  $\delta h = 1$  K, during which the magnetization was averaged over  $\approx 3000$  MC steps after thermalization. The results shown have been averaged for several independent runs starting with different random seeds. First of all, let us note that the saturation field and the high field susceptibility increase

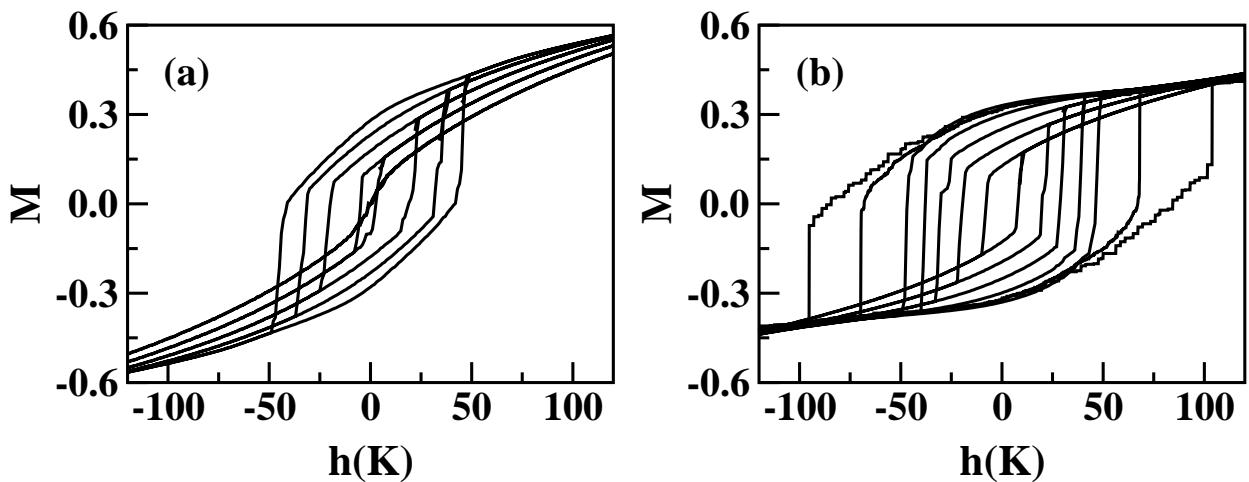


Figure 3.7: Temperature dependence of the hysteresis loops for particles of diameter  $D = 3$  (a),  $D = 6$  (b). The temperatures starting from the outermost loop are  $T = 0, 5, 20, 40, 60, 80, 100$  K, except for case  $D = 3$  in which  $T = 0, 5$  K curves are omitted for clarity.

as the particle size is reduced, since this quantities are mainly associated to the progressive alignment of the surface spins towards the field direction. Thus, the loops of the smallest particles resemble those found in ferrimagnetic nanoparticles [3, 14, 24] and other bulk systems with disorder [32, 43], increasing their squaredness (associated to the reversal of  $M$  as a whole) with the size. In fact, by plotting separately the contributions of the core and the surface to the total magnetization (see Fig. 3.9, dashed lines), we see that the loop of the core is almost perfectly squared independently of temperature and particle size, indicating a reversal of its magnetization with a well-defined ferrimagnetic moment. Instead, the loop of the surface reveals a progressive reversal of  $M$ , which is a typical feature associated to disordered or frustrated systems

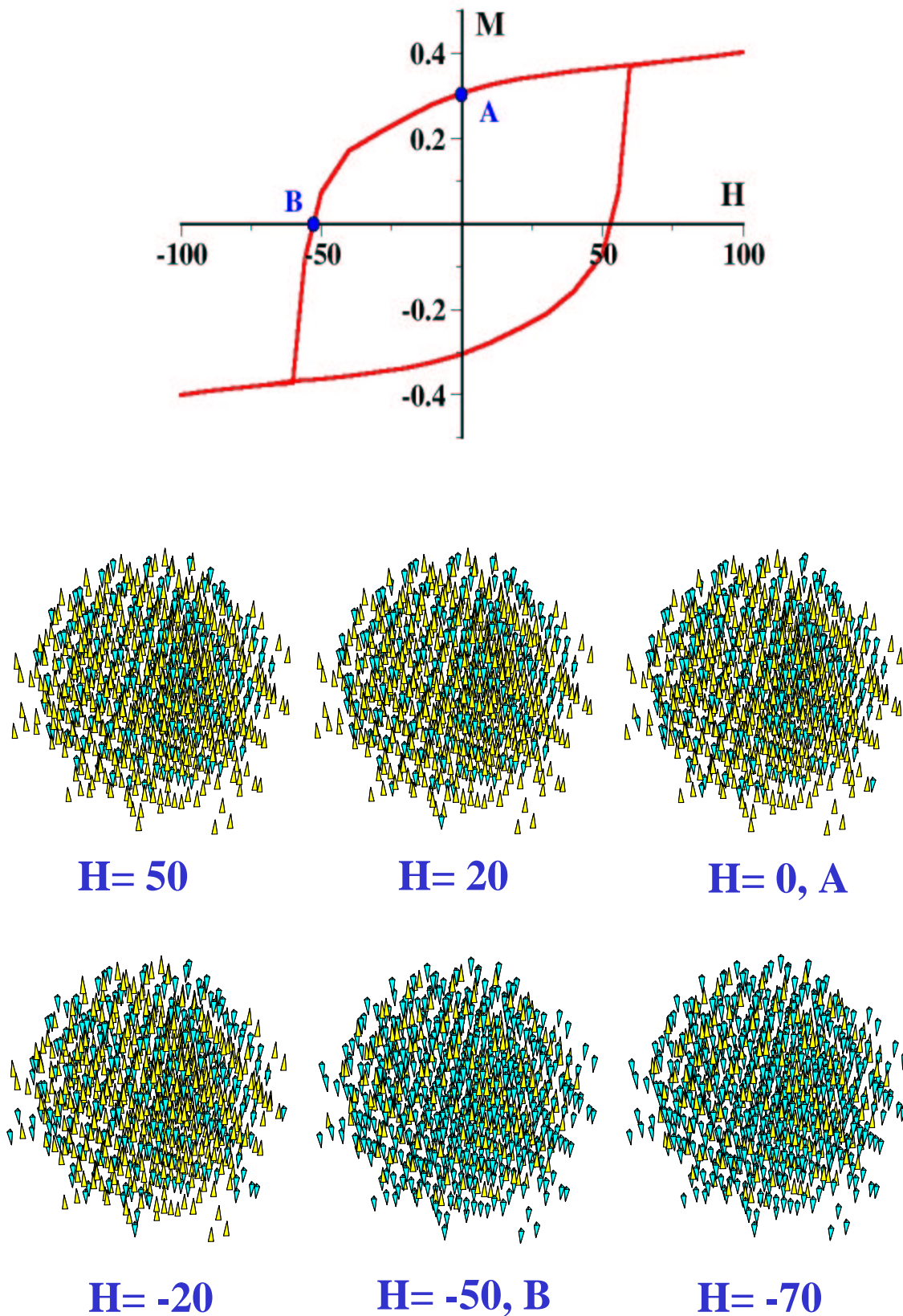


Figure 3.8: Spin configurations of a particle of diameter  $D = 4$  at different points of the hysteresis loop for  $T = 20$ . Configuration A corresponds to the remanent magnetization whereas B corresponds to zero magnetization state. Up and down spins are distinguished by yellow and blue colours respectively.

[32, 43]. Nonetheless, for a wide range of temperatures and particle sizes, it is the reversal of the surface spins which triggers the reversal of the core. This is indicated by the fact that the coercive field of the core is slightly higher but very similar to the one of the surface.

Since for all the studied particle sizes the  $h_c(T)$  curves show a complex behaviour mainly related to the frustration of the antiferromagnetic intra and intersublattice exchange interactions, we start by studying the case of a ferromagnet with no frustration. In Fig. 3.10a, the  $h_c(T)$  dependence for a system with  $N = 8$  and with the same lattice structure as maghemite but equal FM interactions  $J_{\alpha\beta} = J$  and PB conditions is shown. The  $h_c(T)$  dependence is now a monotonously decreasing curve with no inflection point, which at high enough temperatures ( $T/J \gtrsim 1$ ) can be fitted to a power law of the kind

$$h_c(T) = h_c(0)[1 - (T/T_c)^{1/\alpha}], \quad (3.5)$$

with  $\alpha = 2.26 \pm 0.03$ ; close but different to what would be obtained by a model of uniform reversal such as Stoner-Wohlfarth [44] ( $\alpha = 2$ ). Even in this simple case, for which  $M$  reverses as a whole, the thermal variation of  $h_c(T)$  cannot be only ascribed to the thermal activation of a constant magnetization vector over an energy barrier landscape, since actually  $M$  is of course temperature dependent. Therefore, the reversal mechanism cannot be inferred from the  $\alpha$  value obtained from a fit to Eq. 3.5 in any range of temperatures for which  $M$  significantly varies with  $T$ .

The thermal dependence of  $h_c$  for the maghemite particles with AF interactions is shown in Fig. 3.10b. Both for the PB and spherical cases, the  $h_c(T)$  curves are qualitatively different from the FM case: they have opposite curvature and two regimes of thermal variation.

Let us start by analyzing the PB case. At high  $T$  ( $T \gtrsim 20$  K),  $h_c(T)$  can be fitted to the power law of Eq. 3.5 with  $\alpha = 0.94 \pm 0.02$ ,  $h_c(0) = 134 \pm 2$  K. Values of  $\alpha$  close to 1 have been deduced in the past for some models of domain wall motion [45, 46]. At low  $T$ , a different regime is entered but tending to the same  $h_c(0) = 134.2$  K. This change in behaviour is associated to the wandering of the system through metastable states with  $M_{Total} \simeq 0$ , which are induced by the frustration among AF interactions. Consequently, when lowering  $T$ , the hysteresis loops become step-like around  $h_c$  as shown in Fig. 3.11 (similar features are observed in related studies [30, 31, 47]). The jumps at  $T = 0$  are located at  $h = 117, 134.2, 151.4$  K, the values at which the magnetic field energy is enough to invert one O spin having 0, 1, 2 O nearest neighbours inverted, respectively [47]. While the O sublattice reverses progressively, the T sublattice, instead, reverses as a whole after the reversal of O, at  $h = 151.4$  K. When  $T$  is increased from 0, the steps are rounded by the progressive population of states with greater degree of configurational disorder and less metastability, finally giving rise to the suppression of the steps for  $T$  around 12 K, when  $h_c \lesssim 117$  K and the high  $T$  regime of  $h_c(T)$  is entered.

The general  $h_c(T)$  behaviour for spherical particles with FB strongly depends on the particle size. For  $D = 3, 6$  and  $T \gtrsim 20$  K, the  $h_c$  decay is similar to that for PB, but, at any given  $T$ , being smaller than for PB and as the size of the particle is decreased. At these temperatures,  $h_c(T)$  is dominated by the surface, which nucleates the reversal of the magnetization, as indicated by the proximity between the surface and core  $h_c$  (see Fig. 3.9). However, when lowering  $T$  below 20 K,  $M_{Surf}$  and  $M_{Core}$  tend to be equal, the surface becomes less efficient as nucleation center for spin reversal, and  $h_c$  becomes dominated by the core ( $h_c^{Surf} < h_c^{Core}$  for any particle size, see Fig. 3.9). This is the cause of the rapid increase of  $h_c$  towards the PB values for the  $D = 6$  curve (see Fig. 3.10b). For  $D = 3$ , instead,  $h_c$  saturates when lowering  $T$  due to the smaller ratio of core to surface spins, which actually hinders the prevalence of the core.

Finally, it is worth noticing that, independently of the size of the particles with FB, the  $h_c$  values are always smaller than that for PB, since the existence of spins with less coordination at the surface favours the



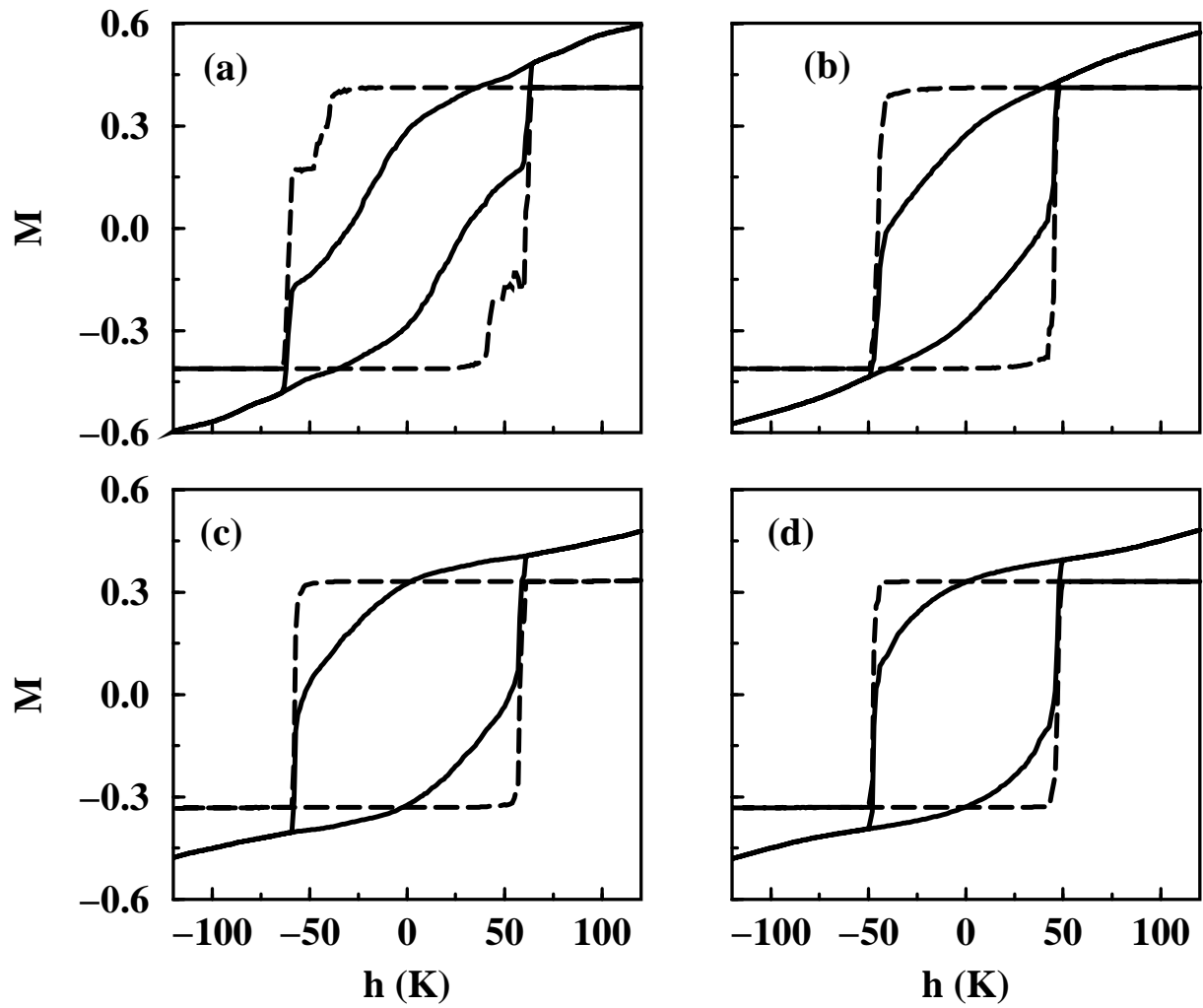


Figure 3.9: Surface (continuous line) and core (dashed line) contributions to the hysteresis loops for particles of diameters  $D = 3$ ,  $T = 10$  K (a);  $D = 3$ ,  $T = 20$  K (b);  $D = 6$ ,  $T = 10$  K (c);  $D = 6$ ,  $T = 20$  K (d).

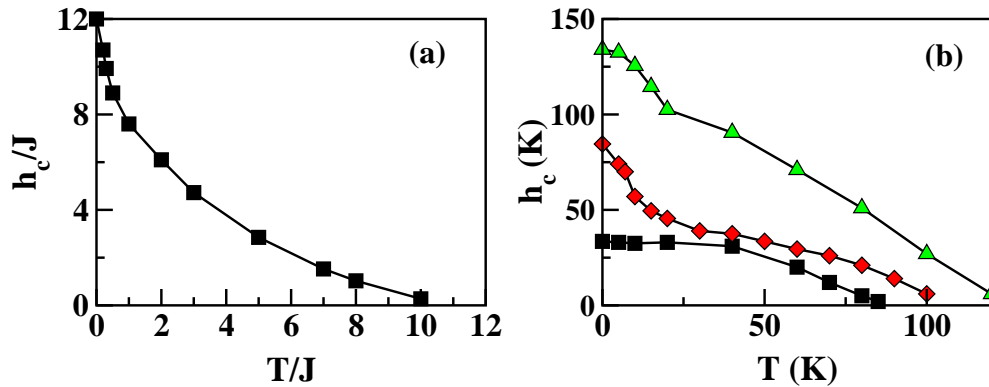


Figure 3.10: (a) Temperature dependence of the coercive field  $h_c$  for a system with the same structure as maghemite but ferromagnetic interactions ( $J_{\alpha\beta} = J$ ) and PB conditions and  $N = 8$ ; (b) Temperature dependence of the coercive field  $h_c$  for the real AF values of the exchange constants for maghemite for the case of FB spherical particles of diameters  $D = 3$  (circles),  $D = 6$  (squares), and for a system of linear size  $N = 8$  with PB conditions (diamonds).

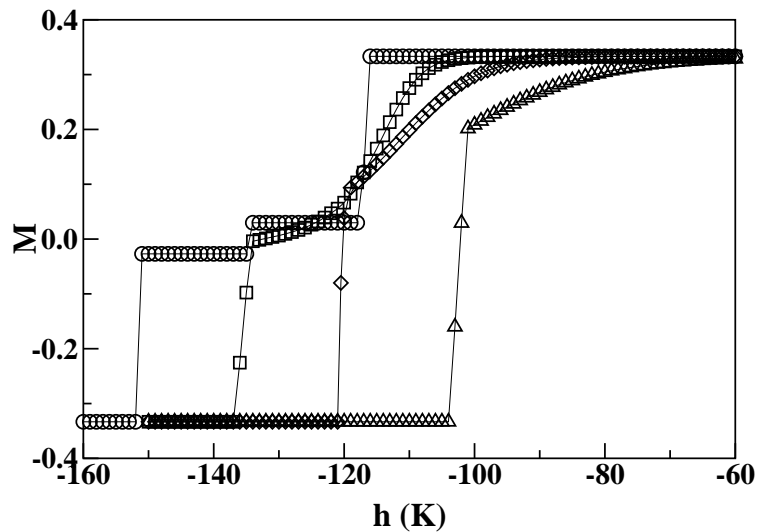


Figure 3.11: Detail of low temperature hysteresis loops for PB conditions around the coercive field  $h_c$ . The corresponding temperatures are  $T = 0$  (circles), 5 K (squares), 10 K (diamonds), 20 K (triangles).

formation of reversed nuclei of spins acting as a seed for the reversal process, which is not the case of PB, where all equivalent spins have the same coordination. Therefore, the  $h_c$  values for PB are only recovered at low  $T$  in the limit of large particle size, at difference with other extensive magnitudes such as the energy or the magnetization, for which we have checked that finite-size scaling is accomplished.

### 3.5 Effects of disorder

In real particles, disorder and imperfections are present departing the system from perfect stoichiometry and distort the position of the atoms on the lattice, being their effect more important at the surface [15]. There are several ways to implement this disorder on the model. The simplest way to simulate the deviation of the O and T sublattice atoms from ideal stoichiometry is by random removal of magnetic ions on the O/T sublattices.

#### 3.5.1 Disorder on the lattice

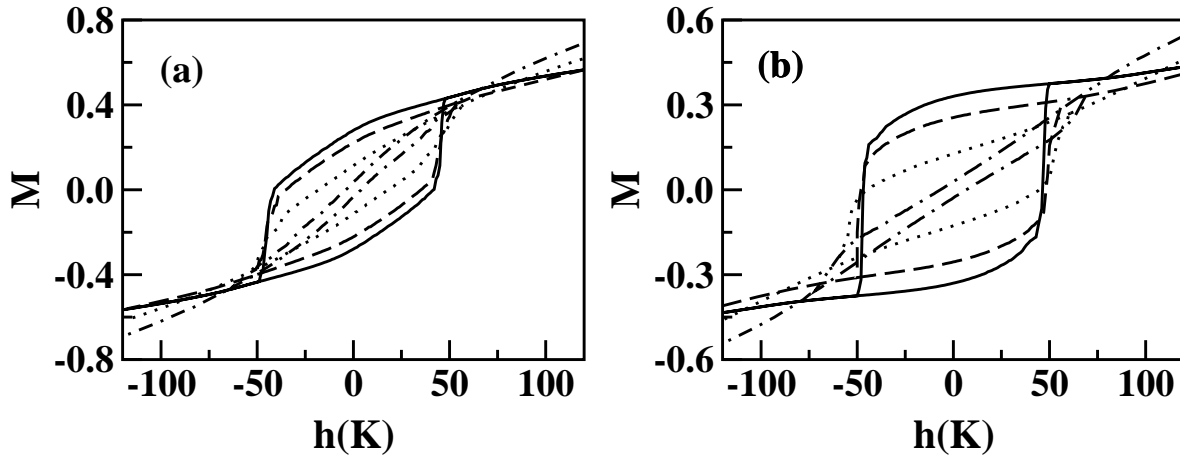


Figure 3.12: Hysteresis loops for systems with vacancy concentrations  $\rho_v = 0.0, 0.166, 0.4, 0.6$  (from outer to innermost) on the O sublattice at  $T = 20$  K. Particle diameters  $D = 3$  (a), and  $D = 6$  (b). Results have been averaged over 10 disorder realizations.

Up to the moment, the existence of vacancies in the O sublattice in real maghemite structure has not been considered. It is important to note that, in this system, intra and intersublattice magnetic interactions are antiferromagnetic. Consequently, inclusion of vacancies in one of the sublattices may destabilize the FM parallel alignment of the other one, resulting in a system with a great degree of magnetic disorder. In particular, this effect will be much stronger when vacancies are introduced in the O sublattice, since  $N_{OT}$  is greater than  $N_{TO}$ . To show the effect of these kind of disorder, we have simulated the hysteresis loops for different vacancy concentrations  $\rho_v$  on the O sublattice at two cooling fields  $h_{FC} = 20, 100$  K. As can be seen in Fig. 3.12, the introduction of a low concentration of vacancies ( $\rho_v = 1/6$  as in the real material) results in a reduction of the magnetization and increases the high field susceptibility without any substantial change in the general shape of the loops. However, if  $\rho_v$  is increased beyond the actual value, the loops progressively closes, losing squaredness and progressively resembling those for a disordered [32, 43] system, with high values of the high field susceptibilities and much lower coercivity.

### 3.5.2 Surface disorder

In what follows, we will study the effects of the disorder at the surface of the particle, considering a  $\rho_v = 1/6$  vacancy density on the O sublattice. Since the surface of the particles is not an ideal sphere, the outermost unit cells may have an increased number of vacancies on both sublattices with respect to those present in the core. Reduced coordination at the surface may also change the number of links between the surface atoms. We will denote by  $\rho_{sv}$  the concentration of surface vacancies in the outermost primitive cells.

#### Field Coolings

The magnetic ordering of the system can be characterized by studying the behaviour of the equilibrium magnetization in a magnetic field. These curves have been obtained by the same cooling procedure used in the magnetization simulations at zero field with  $\delta T = -2$  K in presence of different cooling fields  $h_{FC}$ . Several such curves are shown in Figs. 3.13, 3.14, in which the surface (continuous lines) and the core (dashed lines) contributions to the total magnetization (open symbols) have been distinguished. Let us first analyze the case with no surface disorder ( $\rho_{sv} = 0$ ). The curves at different cooling fields do not collapse to the perfect ferrimagnetic order value at low  $T$  (i.e.  $M_{Total} = 1/4$  for  $\rho_{sv}=1/6$ ), reaching higher values of the magnetization the higher  $h_{FC}$ , being this effect greater as the particle size is reduced (compare Fig. 3.13a and Fig. 3.14a). This is in contrast with the results for PB (not shown), for which the system reaches perfect ferrimagnetic order at low  $T$ , even at fields higher than 100 K, evidencing that the main effect of the surface is the breaking of ferrimagnetic correlations within the particle. As a consequence, at a given temperature, the FM order induced by a magnetic field increases when decreasing  $D$ .

By separately analyzing in detail the behaviour of the surface and core contributions to the total magnetization, deeper understanding of finite-size effects can be gained. As in the case of  $h = 0$ , the total magnetization for small particles is completely dominated by the surface contribution (continuous lines in Fig. 3.13, 3.14) and this is the reason why the ferrimagnetic order is less perfect at these small sizes and the magnetic field can easily magnetize the system. However, the behaviour of the core of the smallest particles is still very similar to that of the case with PB, although its contribution to  $M_{Total}$  is very small. At low fields, the surface is always in a more disordered state than the core: its magnetization lies below  $M_{Total}$  at temperatures for which the thermal energy dominates the Zeeman energy of the field (see the continuous lines in Fig. 3.13a, 3.14a). In this regime, the total magnetization closely follows that of the surface (see the curves in Figs. 3.13a and 3.14a for  $h_{FC} = 20$  K) for the two simulated sizes. In contrast, a high field is able to magnetize the surface easier than the core due to the fact that the broken links at the surface worsen the ferrimagnetic order, while the core spins align towards the field direction in a more coherent way. Only for the biggest particles the surface contribution departs from the  $M_{Total}$  indicating the increasing contribution of the core (see the curves in Figs. 3.13a and 3.14a for  $h_{FC} = 20$  K). Note also, that in this high  $h_{FC}$  regime, a maximum appears which is due to the competition between the FM alignment induced by the field and the spontaneous ferrimagnetic order (as the temperature is reduced the strength of the field is not enough as to reverse the spins into the field direction).

The introduction of vacancies does not change the low field behaviour of the total magnetization, which is still dominated by the surface both for  $D = 3, 6$ , although the smallest particles are easily magnetized by the field. However, at high fields,  $M_{Total}$  is lower than  $M_{Surf}$ , the surface progressively decouples from  $M_{total}$  with the introduction of vacancies in the surface, being this effect more remarkable for the biggest particle. With respect to the core, at difference with the non disordered case ( $\rho_v = \rho_{sv} = 0$ ), the low temperature plateau of  $M_{Core}$  tends to a higher value than that for perfect ferrimagnetic order, since the main

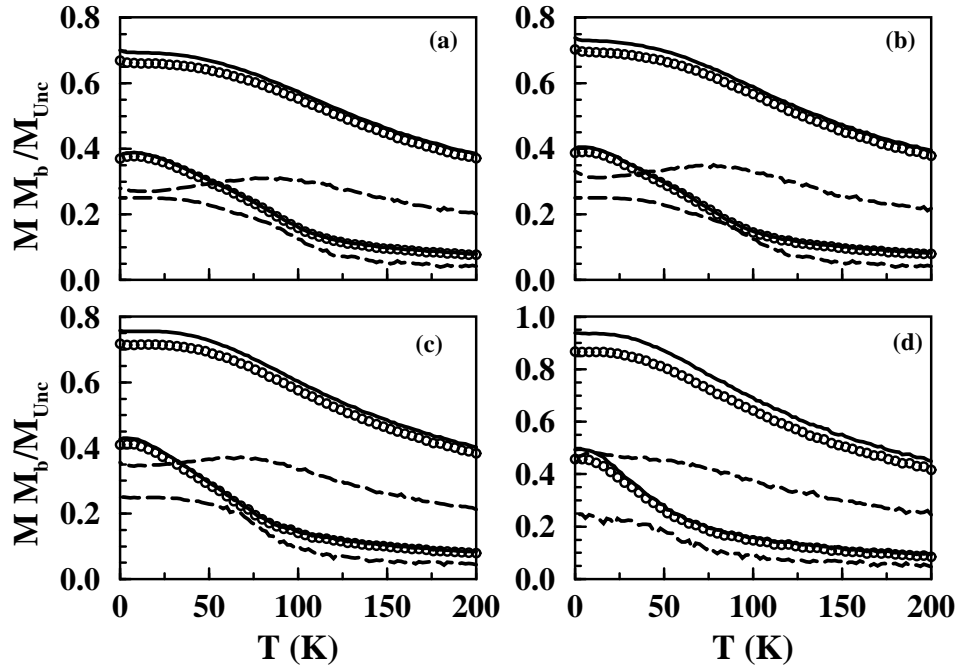


Figure 3.13: Thermal dependence of  $M$  after cooling under a magnetic field for a spherical particle with  $D = 3$ , with vacancy densities on the surface of the O and T sublattices  $\rho_{sv} = 0$  (a), 0.1 (b), 0.2 (c), 0.5 (d), and  $\rho_v = 0.166$  on the O sublattice. The results for two cooling fields  $h_{FC} = 20, 100$  K (lower and upper curves respectively in each panel) are shown. The contributions of the surface (thick lines) and the core (dashed lines) to the total magnetization (circles) have been plotted separately. The magnetization has been normalized to  $M_b$ , the magnetization of a perfect ferrimagnetic configuration for a system of infinite size.

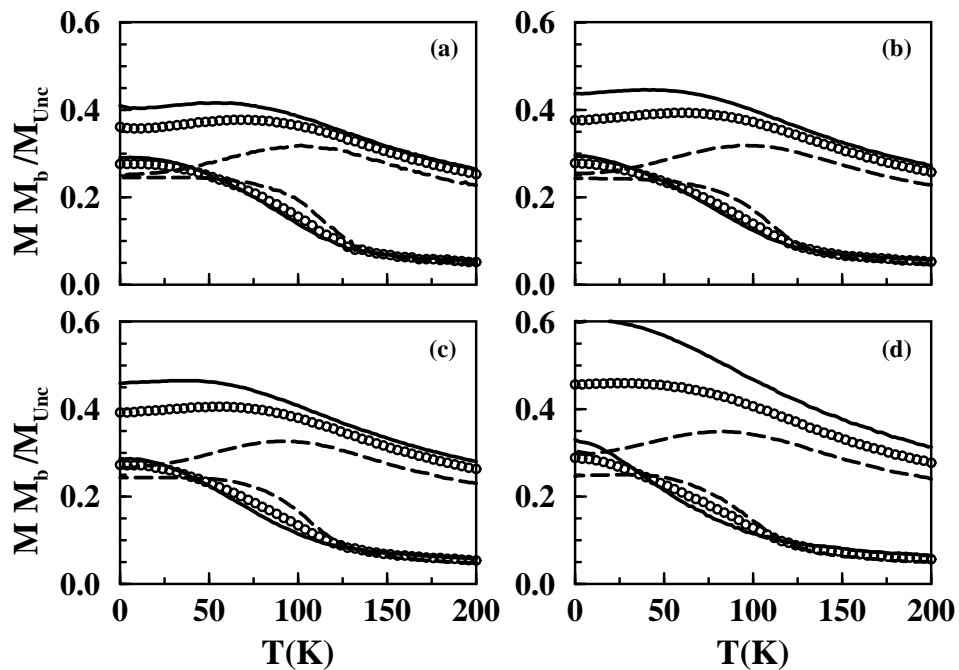


Figure 3.14: Same as Fig. 3.13 but for a spherical particle of diameter  $D = 6$ .

effect of the disorder is to break ferrimagnetic correlations in the core; increasing the ferromagnetic order induced by the field. This is reflected in a progressive departure of the high and low field  $M_{Core}$  curves with increasing disorder (see the dashed lines in the sequence b-d of Figs. 3.13, 3.14). The maximum appearing at high  $h_{FC}$  is only slightly affected by disorder, shifting to lower temperatures and eventually disappearing for  $D = 3$  and  $\rho_{sv} = 0.5$ .

### Hysteresis loops

Hysteresis loops with surface disorder are given in Fig. 3.15 for two particle diameters. The introduction of surface vacancies facilitates the magnetization reversal by progressive rotation, producing a rounding of the hysteresis loops when approaching  $h_c$ , in the same way that occurs when particle size is reduced. The same fact explains the increase of the high field susceptibility, since the vacancies act as nucleation centers of FM domains at the surface, which, from there on, extend the FM correlations to the inner shells of spins. Moreover, a considerable decrease of  $h_c$  is observed. All these facts yield to a progressive elongation of the loops, giving loop shapes resembling those of disordered systems [32, 43]. Fig. 3.16, where the surface and core contributions are shown separately, clearly evidences that the increase of FM correlations at the surface, facilitated by the vacancies, induce FM order in the core. That is to say,  $M_{Core}$  follows the evolution of  $M_{Surf}$  at moderate fields above  $h_c$ , in contrast with the case with no surface vacancies (see Fig. 3.9) where the core keeps the ferrimagnetic order for the same field range.

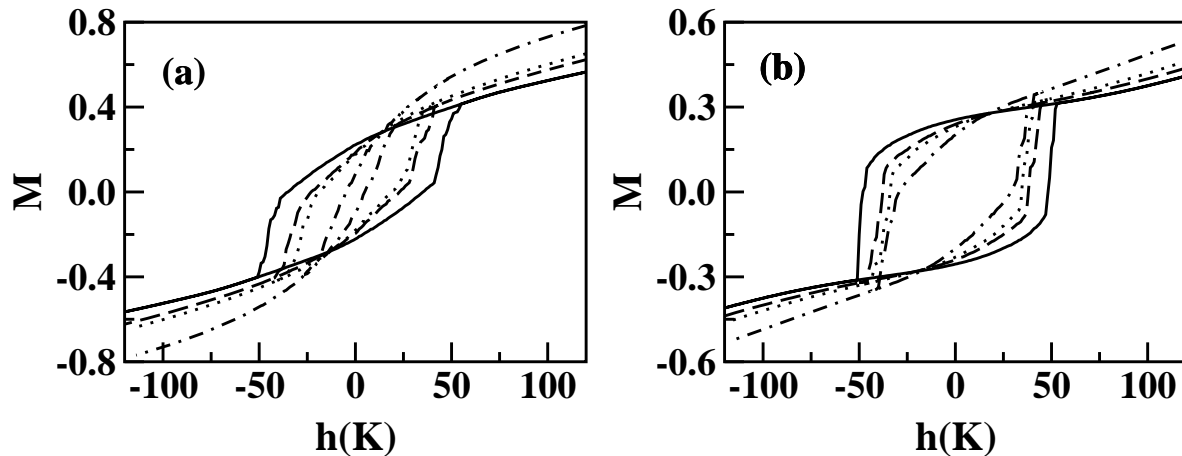


Figure 3.15: Hysteresis loops for systems with vacancy densities on the surface of the O and T sublattices  $\rho_{sv} = 0, 0.1, 0.2, 0.5$ , vacancy density  $\rho_{sv} = 0.1666$  on the O sublattice, and  $T = 20$  K. Particle diameters  $D = 3$  (a),  $D = 6$  (b). Results have been averaged over 10 disorder realizations.

## 3.6 Discussion and conclusions

We have presented a simple model of a maghemite nanoparticle with the minimal ingredients necessary to faithfully reproduce the magnetic structure of the real material. The model has proven successful in reproducing several key features present in ferrimagnetic nanoparticle systems: (1) the reduction of  $T_c$ , spontaneous magnetization  $M_{Total}$ , and coercive field  $h_c$ , for small sizes, as  $D$  decreases; (2) the increase,

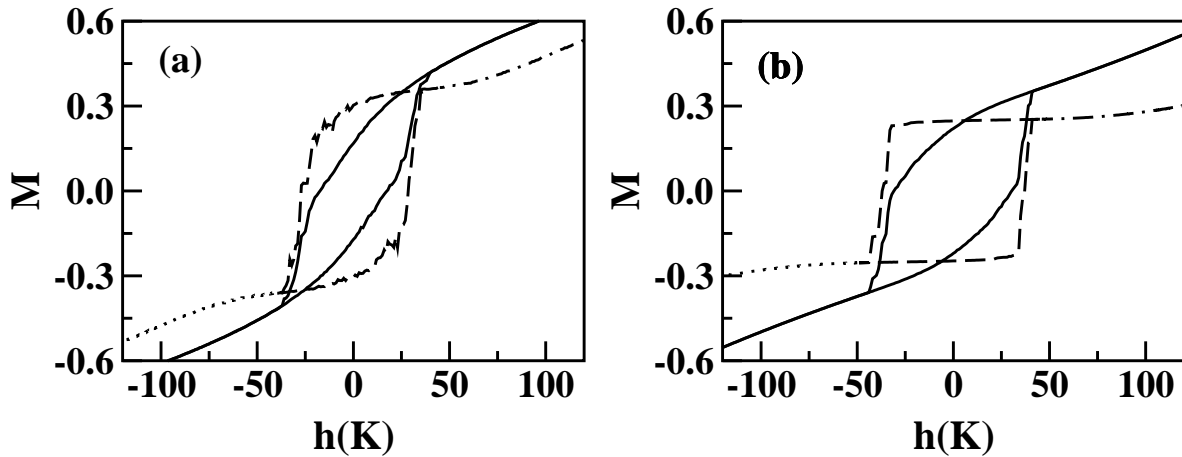


Figure 3.16: Core (dashed lines) and Surface (solid lines) contributions for the case  $\rho_{sv} = 0.2$  of Fig. 13.

with the reduction of the particle size and with the increase of surface disorder, of the differential susceptibility and the elongation of the hysteresis loops in resemblance with those of frustrated systems; and (3) the existence of a surface layer with higher magnetic disorder than the core. Let us further comment these points in deeper detail.

First of all, we find that  $T_c(D)$  follows conventional finite-size scaling, discarding any important surface effect on this quantity. The results are consistent with spin-wave calculations [48] and old MC simulations [49]. Similar finite-size effects have been found in fine particles [50] of  $\text{MnFe}_2\text{O}_4$ , but with a surprising increase of  $T_c(D)$  as  $D$  decreases. However, the spontaneous magnetization  $M_{Total}$ , at any temperature, follows a quasi-linear behaviour with  $1/D$ , see Fig. 3.6, indicating that the reduction of  $M_{Total}$  is simply proportional to the ratio of surface to core spins, so it is mainly a surface effect. Similar experimental behaviour has been found in  $\gamma\text{-Fe}_2\text{O}_3$  [51] and the above mentioned system [50].

The  $h_c(T)$  thermal decay for the spherical particles is in qualitative agreement with the experimental results for maghemite particles of sizes 9-10 nm shown in Fig. 4 of Ref. [17], taking into account that in real samples there are additional contributions coming from the blocking process associated to the particle size distribution ( $h_c$  drops to zero above the blocking temperature). In both cases, the curvature of the  $h_c(T)$  curve is similar, suggesting a progressive reversal of the magnetization, a point that is also confirmed by the shape of the hysteresis loops around  $h_c$ . However, our model for spherical particles gives reduced coercivities with respect to the bulk (represented by the PB case). A fact that is in contrast with the enhancement observed experimentally [14, 17, 20], and indicating that finite-size effect cannot cause it. Increased anisotropy at the surface may be the responsible for it. In any case, the model qualitatively reproduces the  $h_c$  reduction with  $D$  for small sizes [see Fig. 1 in Ref. [14]], which may be indeed a finite-size effect.

The  $M(T)$  and  $M(h)$  dependencies obtained in our simulation lead to the conclusion that, in spherical particles, there is a surface layer with much higher degree of magnetic disorder than the core, which is the Ising version of the random canting of surface spins occurring in several fine particle with spinel structure [1, 2, 3, 4, 5]. As opposite with the suggestion given by some authors [14, 17] that below a certain freezing temperature the surface layer enters a spin-glass-like state, our model does not give any indication of this phenomenology at any of the studied sizes and temperatures. Furthermore, the surface layer, by partially breaking the ferrimagnetic correlations, diminishes the zero-field  $M_{Total}$  but, at the same time, enhances  $M_{Total}$  at moderate fields. Although the surface is easily thermally demagnetized and easily magnetized by the field than the core, it does not behave as a dead layer, since, at any  $T$ , it is magnetically coupled to the

core. All these facts put forward that the surface has higher magnetic response than the core, excluding a spin-glass freezing. Moreover, we do not observe irreversibilities between field and zero-field cooled magnetization curves, which is a key signature that in the scope of our model, neither finite-size or surface effects, nor the inclusion of surface vacancies are enough to account for the postulated spin-glass-like state.

Finally, let us mention that our model does not reproduce the experimentally observed shift of the hysteresis loops under field cooling adduced as a prove of the existence of the spin-glass-like state at the surface [14, 24, 17]. Only when  $h_{FC}$  smaller than irreversibility fields  $h_{irr}$  are used in the numerical experiment, hysteresis loops that are apparently shifted are obtained, which in fact are minor loops. In any case, the absence of this phenomenology is in agreement with the non-observation of a spin-glass-like state at the surface, indicating that other *ad hoc* ingredients must be included in the model. For instance, enhanced surface anisotropy or exchange constants at the surface different than at the bulk, as is the case in exchange coupled multilayers [52, 53]. Further work is needed to elucidate the possible influence of these new ingredients and of interparticle interactions.





## Bibliography

- [1] J. M. D. Coey, Phys. Rev. Lett. **27**, 1140 (1971).
- [2] A. H. Morrish and K. Haneda, J. Appl. Phys. **52**, 2496 (1981).
- [3] R. H. Kodama, A. E. Berkowitz, E. J. McNiff, and S. Foner, Phys. Rev. Lett. **77**, 394 (1996).
- [4] D. Lin, A. C. Nunes, C. F. Majkrzak, and A. E. Berkowitz, J. Magn. Magn. Mater. **145**, 343 (1995).
- [5] J. Z. Jiang, G. F. Goya, and H. R. Rechenberg, J. Phys.: Condens. Matter **11**, 4063 (1999).
- [6] F. Gazeau, E. Dubois, M. Hennion, R. Perzynski, and Y. L. Raikher, J. Magn. Magn. Mater. **40**, 575 (1997).
- [7] F. Gazeau, J. C. Bacri, F. Gendron, R. Perzynski, Y. L. Raikher, V. I. Stepanov, and E. Dubois, J. Magn. Magn. Mater. **186**, 175 (1998).
- [8] A. Ochi, K. Watanabe, M. Kiyama, T. Shinjo, Y. Bando, and T. Takada, J. Phys. Soc. Jpn. **50**, 2777 (1981).
- [9] T. Okada, H. Sekizawa, F. Ambe, and T. Yamada, J. Magn. Magn. Mater. **31-34**, 105 (1983).
- [10] K. Haneda and A. H. Morrish, J. Appl. Phys. **63**, 4258 (1988).
- [11] Q. A. Pankhurst and R. J. Pollard, Phys. Rev. Lett. **67**, 248 (1991).
- [12] F. T. Parker, M. W. Foster, D. T. Margulies, and A. E. Berkowitz, Phys. Rev. B **47**, 7885 (1993).
- [13] S. Linderoth, P. V. Hendriksen, F. Bødker, S. Wells, K. Davis, S. W. Charles, and S. Mörup, J. Appl. Phys. **75**, 6583 (1994).
- [14] R. H. Kodama, S. A. Makhlof, and A. E. Berkowitz, Phys. Rev. Lett. **79**, 1393 (1997).
- [15] M. P. Morales, C. J. Serna, F. Bødker, and S. Mörup, J. Phys.: Condens. Matter **9**, 5461 (1997).
- [16] M. García del Muro, X. Batlle, and A. Labarta, Phys. Rev. B **59**, 13584 (1999).
- [17] B. Martínez, X. Obradors, L. Balcells, A. Rouanet, and C. Monty, Phys. Rev. Lett. **80**, 181 (1998).
- [18] T. Jonsson, J. Mattson, C. Djurberg, P. Nordblad, and P. Svedlindh, Phys. Rev. Lett. **75**, 4138 (1995).
- [19] T. Jonsson, P. Nordblad, and P. Svedlindh, Phys. Rev. B **57**, 497 (1998).
- [20] X. Batlle, M. García del Muro, and A. Labarta, Phys. Rev. B **55**, 6440 (1997).

- 
- [21] J. Dormann, R. Cherkaoui, L. Spinu, M. Nogués, F. Lucari, F. D’Orazio, D. Fiorani, A. García, E. Tronc, and J. Jolivet, *J. Magn. Magn. Mater.* **187**, L139 (1998).
- [22] S. Mørup and E. Tronc, *Phys. Rev. Lett.* **72**, 3278 (1994).
- [23] P. Jonsson and P. Nordblad, *Phys. Rev. B* **62**, 1466 (2000).
- [24] R. H. Kodama and A. E. Berkowitz, *Phys. Rev. B* **59**, 6321 (1999).
- [25] H. Kachkachi, A. Ezzir, M. Nogués, and E. Tronc, *Eur. Phys. J. B* **14**, 681 (2000).
- [26] H. Kachkachi, M. Nogués, and E. Tronc, *J. Magn. Magn. Mater.* **221**, 158 (2000).
- [27] H. Kachkachi and D. Garanin, *Physica A* **300**, (487) (2001).
- [28] K. N. Trohidou and J. A. Blackman, *Phys. Rev. B* **41**, 9345 (1990).
- [29] X. Zianni and K. N. Trohidou, *J. Appl. Phys.* **85**, 1050 (1999).
- [30] D. A. Dimitrov and G. M. Wysin, *Phys. Rev. B* **50**, 3077 (1994).
- [31] D. A. Dimitrov and G. M. Wysin, *Phys. Rev. B* **51**, 11947 (1995).
- [32] K. Binder and A. P. Young, *Rev. Mod. Phys.* **58**, 801 (1986).
- [33] C. M. Soukoulis, K. Levin, and G. S. Grest, *Phys. Rev. Lett.* **48**, 1756 (1982).
- [34] C. M. Soukoulis, G. S. Grest, and K. Levin, *Phys. Rev. Lett.* **50**, 80 (1983).
- [35] D. P. Landau, *Phys. Rev. B* **14**, 255 (1976).
- [36] M. N. Barber, in *Phase Transitions and Critical Phenomena*, edited by C. Domb and J. L. Lebowitz (Academic Press, New York, 1983), Vol. 8, p. 145.
- [37] H. E. Stanley, *Introduction to Phase Transitions and Critical Phenomena* (Oxford University Press, New York, 1987).
- [38] B. Martínez and R. E. Camley, *J. Phys.: Condens. Matter* **4**, 5001 (1992).
- [39] G. Xiao and C. L. Chien, *J. Appl. Phys.* **61**, 4313 (1987).
- [40] A. Corciovei, *Phys. Rev.* **61**, 4313 (1963).
- [41] J.-H. Park, E. Vescovo, H.-J. Kim, C. Kwon, R. Ramesh, and T. Venkatesan, *Phys. Rev. Lett.* **81**, 1953 (1998).
- [42] D. Zhao, F. Liu, D. L. Huber, and M. G. Lagall, *Phys. Rev. B* **62**, 11316 (2000).
- [43] H. Maletta, in *Excitations in Disordered Solids*, edited by M. Thorpe (Plenum, New York, 1981).
- [44] E. C. Stoner and E. P. Wohlfarth, *Philos. Trans. R. Soc. London A* **240**, 599 (1948), reprinted in *IEEE Trans. Magn.* **27**, 3475 (1991).
- [45] P. Gaunt, *J. Appl. Phys.* **59**, 4129 (1986).
- [46] P. Gaunt, *Philos. Mag. B* **48**, 261 (1983).

- 
- [47] E. Viitala, J. Merikowski, M. Manninen, and J. Timonen, *Phys. Rev. B* **55**, 11541 (1997).
- [48] P. V. Hendriksen, S. Linderorth, and P. A. L. rd, *Phys. Rev. B* **48**, 7259 (1993).
- [49] K. Binder, H. Rauch, and V. Wildpaner, *J. Phys. Chem. Sol.* **31**, 391 (1970).
- [50] Z. X. Tang, C. M. Sorensen, K. J. Klabunde, and G. C. Hadjipanayis, *Phys. Rev. Lett.* **67**, 3602 (199).
- [51] D. H. Han, J. P. Wang, and H. L. Luo, *J. Magn. Magn. Mater.* **136**, 176 (1994).
- [52] P. Milténi, M. Gierlings, J. Keller, B. Beschoten, G. Guntherodt, U. Nowak, and K. D. Usadel, *Phys. Rev. Lett.* **84**, 4224 (2000).
- [53] R. L. Stamps, *J. Phys. D: Appl. Phys.* **33**, R247 (2000).

## IB. Collective effects

*Hay una cosa que se llama tiempo, Rocamadour,  
es como un bicho que anda y anda.  
No te puedo explicar porque eres tan chico,  
pero quiero decir que Horacio llegará en seguida.*

JULIO CORTÁZAR  
*Rayuela, Cap. 32*

In this part, we will study the time dependence of the magnetic properties of ensembles of small particles. In a first stage, the interparticle interactions will not be taken into account. The only collective properties considered will be the distribution of physical parameters concerning the magnetic properties of the system. Among them, the most important are the distribution of volumes, anisotropy constants and easy-axes directions. Accordingly, in Chapter 4, we will establish a phenomenological model of relaxation for non-interacting particle systems when no external magnetic field is applied. As an extension of it, in Chapter 5, the effects of a magnetic field on the magnetic relaxation will be incorporated, extending the results of the preceding chapter.

In a second step, long-range dipolar interactions among the particles will be taken into account in addition to the aforementioned properties. Thus, in Chapter 6, we will consider the influence of the dipolar interactions on the magnetic properties through the effective energy barrier distribution concept already introduced in Chapter 2. Moreover, magnetic relaxation in the presence of interaction will be studied through Monte Carlo simulations.

## CHAPTER 4

### RELAXATION PROCESSES IN ZERO MAGNETIC FIELD

As already mentioned in the introductory chapter, the loss of magnetization with time is a well-known phenomena that became relevant to technology, due to the progressive reduction in the dimensions of the constituents of the materials used for technological applications that has been taken place during the second half of this century.

As particle sizes are decreased, the superparamagnetic limit is approached. Therefore, the energy barrier separating the two energy degenerate magnetic orientations becomes small enough to be overcome by thermal fluctuations, leading to spontaneous switching of the magnetization. Since this phenomenon leads to the degradation of the recorded information, the challenge for magnetic recording engineering has been to maintain the energy barrier of individual particles high while keeping the materials magnetically soft enough to enable recording. Hence, in order to improve the quality of the materials needed for high recording densities, it is essential to understand the physics of nanometric particle ensembles near the superparamagnetic limit.

Why the magnetization of a material changes with time and how this phenomena can be modeled are the questions that we address in this section. The first attempts towards an understanding of relaxation phenomena were performed by Street and Wooley in the late 40's [1]. The motivation here was the observation that experimental relaxation curves were always approximated by straight lines when plotting the time axis on a logarithmic scale although even to the naked eye they had a remarkable curvature. As it will be explained later, the logarithmic decay should only be valid for a system with a flat energy barrier distribution, which is of course not the case of real samples. We aimed at finding a way to avoid any aprioristic assumption about the energy barrier distribution of the system. The idea was to find a phenomenological way to deal with the complex phenomenon of relaxation which did not evolve starting from a microscopic hamiltonian to derive a relaxation law.

The underlying hypothesis is that the magnetic system can be described in terms of a distribution of energy barriers, which accounts for the different interactions among the constituents. This distribution may change with time because of the dynamic character of the interactions, but this does not mean that these energy barrier fluctuations will be necessarily reflected on the time dependence of macroscopic quantities. At the end, one can always analyze the dynamics of the system as being produced by an effective distribution of energy barriers that correspond to the barriers jumped by the system in the experimental time window in its path through energy barriers landscape towards thermal equilibrium, so that even if the distribution of energy barriers is changing with time, there will always be an effective distribution independent of time that characterizes the dynamics.

## 4.1 Phenomenological model of relaxation

Let us consider a general magnetic system, not necessarily a system of small particles. We will only assume that, whatever is the underlying microscopic model used to describe it, it can be thought in terms of effective energy barriers that separate the metastable states of the appropriate degree of freedom of the constituents. Therefore, we will be thinking now of a magnetic system as a collection of energy barriers  $E$  that can be characterized by a certain distribution function  $f(E)$  which contains the specific composition of the system. We are interested in the time dependence of the order parameter  $m(t)$ , which we will call magnetization thinking in applications to small particle systems. Particular examples are:

- Single-domain particles and granular materials, systems in which the energy barriers due to the anisotropy are, in principle, proportional to the volume of the particle or grain. In this case  $f(E)$  reflects the scattering of particle volumes or anisotropy constants. It should be noted that using a distribution of energies or of relaxation times is better and more general than using a distribution of volumes or particle sizes since in this way no assumption about the relation between these parameters has to be made. So in principle the same treatment would be valid for multidomain particles. In this case, the degree of freedom relevant for the relaxation is the total magnetization of the particle, which we consider as that of a giant spin, and the barriers separate different magnetization directions.
- Continuous magnetic systems, like thin films or metallic alloys, where the magnetization changes are due to the motion of domain walls. As stated before this is not a problem since we only take into account the energy barriers separating stable states for the domain wall coordinate.
- Superconducting systems in which the barriers responsible for the relaxation are associated to the individual or collective pinning of vortices by impurities, defects or twin boundaries. The inhomogeneities of these defects give also rise to a distribution of pinning potentials represented by  $f(E)$ . The degree of freedom is in this case the magnetization of the vortices.

Let us think for the moment that there is no external perturbation on the system (no magnetic field) and that only thermal fluctuations can drive the system to thermal equilibrium. Then the relaxation law of the system is given by

$$m(t) = \int_0^{\infty} dE f(E) e^{-t/\tau(E)}. \quad (4.1)$$

The exponential factor is the classical Boltzmann probability for a particle to change its equilibrium magnetization value, and  $\tau(E)$  is the relaxation time used in Néel's theory [2], given by:

$$\tau(E) = \tau_0 e^{E/k_B T}, \quad (4.2)$$

where  $1/\tau_0$  is an attempt frequency of the order  $10^8 - 10^{12} \text{ s}^{-1}$ ,  $k_B$  the Boltzmann constant and  $T$  the temperature.

We can also express the relaxation law (4.1) in terms of a distribution of relaxation times  $P(\tau)$  as

$$m(t) = k_B T \int_0^{\infty} d\tau \frac{1}{\tau} f(T \ln(\tau/\tau_0)) e^{-t/\tau} = \int_{\tau_0}^{\infty} d\tau e^{-t/\tau} P(\tau), \quad (4.3)$$

where  $P(\tau)$  is related to the energy barrier distribution through

$$P(\tau) = \frac{k_B T}{\tau} f(T \ln(\tau/\tau_0)). \quad (4.4)$$

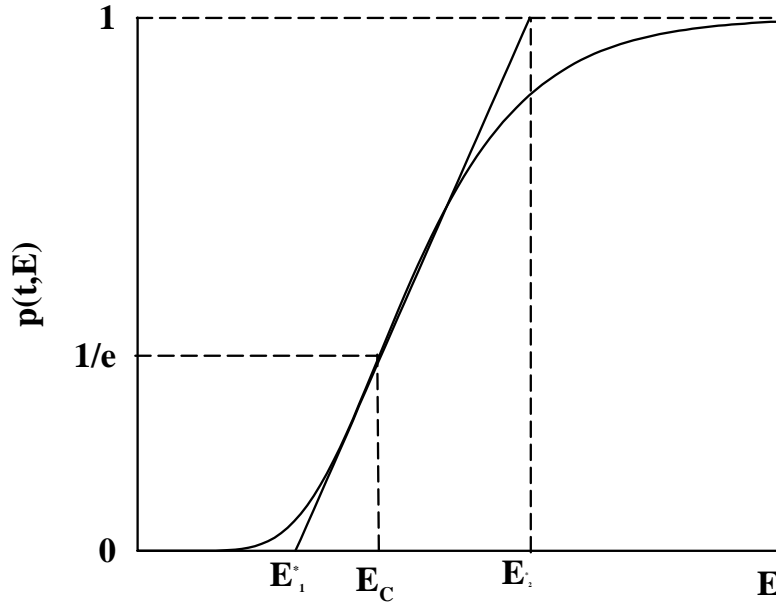


Figure 4.1: Function  $p(t, E)$  defined in Eq. (4.7) as a function of the energy barrier  $E$ . The straight solid line corresponds to the approximation 4.10. We have taken  $\tau_0 = 1$ ,  $k_B = 1$ , and  $T = 1$ .

Yet another alternative expression can be obtained by using as a variable the relaxation frequency defined by  $\nu(E) = 1/\tau(E) = \nu_0 e^{-E/T}$ . Changing variables in (4.1) we arrive at

$$m(t) = k_B T \int_0^{\nu_0} d\nu \frac{1}{\nu} f(T \ln(\nu_0/\nu)) e^{-\nu t} = \int_0^{\nu_0} d\nu e^{-\nu t} Q(\nu), \quad (4.5)$$

where now the distribution of frequencies  $Q(\nu)$  is

$$Q(\nu) = \frac{k_B T}{\nu} f(T \ln(\nu_0/\nu)). \quad (4.6)$$

Let us introduce the function  $p(t, E)$  defined by

$$p(t, E) = e^{-(t/\tau_0) \exp(-E/k_B T)} \quad (4.7)$$

and let us analyze in detail its behaviour as a function of  $t$  and  $E$ . As can be seen in Fig. 4.1, for a given time  $t$ ,  $p(t, E)$  varies abruptly from 0 to 1 as the energy barrier  $E$  increases, this is why the usual simplification [1] consists on approximating  $p(t, E)$  by a step function whose discontinuity  $E_c(t)$  moves to higher values of  $E$  as time elapses. As a consequence, the integral is "cutoff" at the lower limit by the value of  $E_c(t)$ , which is the only time dependent parameter, and the expression (4.7) is approximated by

$$m(t) \simeq \int_{E_c(t)}^{\infty} dE f(E). \quad (4.8)$$

$E_c(t)$  corresponds to the energy barrier value for which the function  $p(t, E)$  has the inflection point and is given by

$$E_c = k_B T \ln(t/\tau_0). \quad (4.9)$$



From Eq. (4.9) we conclude that the remanent magnetization  $M(t)$  obtained after integration over the energy barriers  $E$  is a function of the parameter  $E_c(t) = k_B T \ln(t/\tau_0)$ . The existence of this scaling variable implies that measuring the magnetization as a function of the temperature at a given time is equivalent to measure the magnetization as a function of the  $\ln(t)$  at a fixed temperature. This time-temperature correspondence is characteristic of activated processes governed by the Arrhenius law.

The approximation of  $p(t, E)$  by a step function cutting off the integral in (4.8) can be improved by taking into account the essential temperature and time dependence of  $m(t)$ . It is clear from (4.1) that the interval of energies for which  $p(t, E)$  differs significantly from 0 and 1, for a given value of the time, will depend on the temperature. To have an idea of the influence of this region on  $M(t)$  let us approximate  $p(t, E)$  by (see Fig.4.1)

$$p(t, E) \simeq \begin{cases} 0, & E \leq E_1^* \\ r(E), & E_1^* \leq E \leq E_2^* \\ 1, & E \geq E_2^*, \end{cases} \quad (4.10)$$

where we have approximated  $p(E)$  by a straight line passing by the inflection point of this function, which is placed at an energy  $E_c$ , with  $p(E_c) = 1/e$ , a constant independent of time, and with slope equal to the derivative of  $p(E)$  at the inflection point. This straight line has the following equation:

$$r(E) = \frac{1}{e} \left[ \frac{E}{k_B T} + \left[ 1 - \ln\left(\frac{t}{\tau_0}\right) \right] \right], \quad (4.11)$$

and  $E_1^* = k_B T \left[ \ln\left(\frac{t}{\tau_0}\right) - 1 \right]$ ,  $E_2^* = E_1^* + k_B T e$ . Only for  $T = 0$  does Eq. (4.11) reduce to the cut-off approximation. Then, we can characterize  $p(t, E)$  by its width,  $\lambda = E_2^* - E_1^* = k_B T e$ , which is time independent. Thus, as time elapses,  $p(t, E)$  moves to higher values of the energy without changing its shape.

By expanding (4.1) about  $E = E_c(t)$  (which is equivalent to consider  $t = \tau$ ) we obtain the similar expression

$$p(t, \tau) \simeq \frac{1}{e} \left( 1 + \left( \frac{E - E_c}{T} \right) - \frac{1}{3!} \left( \frac{E - E_c}{T} \right)^3 + \dots \right). \quad (4.12)$$

Now substituting into (4.1) we arrive at

$$m(t) \simeq \int_{E_1^*}^{E_2^*} dE f(E) r(t, E) + \int_{E_2^*}^{\infty} dE f(E), \quad (4.13)$$

which is an improved approximation to the relaxation law (4.1) with respect to the critical volume approximation (4.8), that takes into account the temperature dependence.

## 4.2 On the logarithmic approximation

By looking at the literature, it might be surprising the fact that many experimental relaxation data fit a logarithmic time dependence of the type

$$M(t) = M_0 - S \ln(t/\tau_0) \quad (4.14)$$

with  $S$  a constant parameter for a given temperature.  $S$  is known as magnetic viscosity and it is defined as the logarithmic time derivative of the relaxation law:

$$S(t) = -\frac{\partial M(t)}{\partial \ln(t)}. \quad (4.15)$$

It is in general a temperature and time dependent quantity that depends also on the particular choice of energy distribution  $f(E)$ .

One may wonder if the ubiquitous presence of this law in nature is the reflection of any underlying characteristic physical property common to all of them, or it is merely an spurious coincidence that has its origin on mathematics. We will see in the following that both answers to the question are partially correct.

The first objection that one can aduce to the use of logarithmic laws is that the logarithmic function is singular both at the origin and at infinity and thus it is invalid to describe the short and long time dependence of any physical phenomena. Nevertheless, experimentalists insist in using the logarithmic function to describe relaxation phenomena in the whole time range of the experiment, even when departures of the experimental data from this law are evident to the naked eye. The use of a certain mathematical function when describing a relaxation law phenomenologically should not preclude any specific choice for the distribution function  $f(E)$  in (4.1), on the contrary the aim of the experiment should be to show that the main characteristics of the system (*i.e.*  $f(E)$ ) can be inferred from the experimental observation of  $m(t)$ . Therefore, one should have first a theoretical justification for the use of logarithmic decay and, second, demonstrate that the physical system under consideration fulfills these assumptions.

### 4.2.1 Origin of the logarithmic law

Let us start by establishing the first point. We have already seen in the preceding section that ,because of the exponential dependence of relaxation time in the Arrhenius law, the dependence between energy and time is always logarithmic and given by the scaling variable  $E_c(t)$ .

Following the original derivation of (4.14) by Street and Wooley [1] we start by considering the rate of variation of the magnetization with time

$$\frac{dm}{dt} = -\int_0^\infty dE f(E) \frac{e^{-t/\tau(E)}}{\tau(E)} \quad (4.16)$$

and assuming a uniform distribution of barriers  $f(E) = E_0$  ( $0 < E < \infty$ ), then  $f(E)$  can be factored out of the integral leading to

$$\frac{dm}{dt} = -E_0 \int_0^\infty dE \frac{e^{-t/\tau(E)}}{\tau(E)}. \quad (4.17)$$

Changing variables to  $\nu = 1/\tau(E)$  we finally obtain

$$\frac{dm}{dt} = E_0 T \int_0^{1/\tau_0} d\nu e^{-\nu t} = \frac{E_0 T}{t} (1 - e^{-t/\tau_0}). \quad (4.18)$$

Now we see that, at long times ( $t \gg \tau_0$ ), the relaxation becomes logarithmic

$$m(t) \simeq 1 - E_0 T \ln(t/\tau_0) \quad (4.19)$$

and at short times ( $t \ll \tau_0$ ) it is linear in  $t$ . Therefore, we can conclude that the logarithmic law is valid only for systems with constant and infinitely wide energy distributions. Of course, this kind of distribution is not

physically acceptable and one should consider instead a "flat hat" distribution, of finite width  $\sigma$ , constant between some range of energies  $E_1, E_2$  and zero elsewhere, like the one in Fig.4.2.1. In this case,

$$\begin{aligned} \frac{\partial m}{\partial t} &= \frac{1}{\sigma} \int_{E_1}^{E_2} dE \frac{e^{-t/\tau}}{\tau} = -\frac{T}{\sigma} \int_{\nu_1}^{\nu_2} d\nu e^{-t\nu} \\ &= \frac{T}{\sigma t} e^{-t/\tau_2} (1 - e^{-t(1/\tau_1 - 1/\tau_2)}), \end{aligned} \quad (4.20)$$

which also leads to logarithmic behaviour when  $\tau_2 \gg \tau_1$  and long enough times, that is to say, in the limit of a very broad distribution.

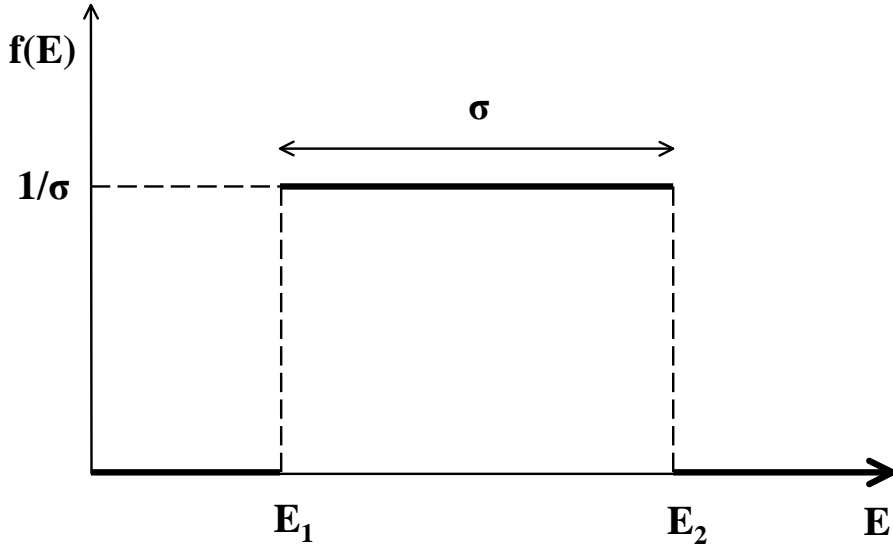


Figure 4.2: Flat hat energy uniform distribution of energies of finite width  $\sigma$ .

#### 4.2.2 Range of validity of the logarithmic approximation

Up to now we have answered only one part of the question, we have seen that logarithmic decay is justified only for very broad constant distributions and that it is due to the natural correspondence between time and energy given by the Arrhenius law. But we positively know that, in real systems, the distribution of energy barriers is far from being flat and, nevertheless, the time dependence of the magnetization is well described by a logarithmic law in a certain range of times and temperatures, why is this so?.

To give an answer to this question let us start first from the phenomenological model presented in the previous section. Let us consider the time derivative of Eq. (4.13)

$$\begin{aligned} S(t) = \frac{\partial M(t)}{\partial(\ln(t))} &\simeq \int_{E_1^*(t,E)}^{E_2^*(t,E)} dE f(E) \frac{\partial r(t, E)}{\partial(\ln(t))} - f(E_2^*) \frac{\partial E_2^*}{\partial(\ln(t))} \\ &\quad + r(E_2^*) f(E_2^*) \frac{\partial E_2^*}{\partial(\ln(t))} - r(E_1^*) f(E_1^*) \frac{\partial E_1^*}{\partial(\ln(t))} \end{aligned} \quad (4.21)$$

which can be reduced to:

$$S(t) \simeq -\frac{1}{e} \int_{E_1^*(t,E)}^{E_2^*(t,E)} dE f(E). \quad (4.22)$$

In the critical volume approximation [1, 3], where the function  $p(t, E)$  is approximated by a step function centered at the activation energy  $E_c(t) = k_B T \ln(t/\tau_0)$ , the equivalent to this expression is

$$S(t) = -k_B T f(E_c(t)). \quad (4.23)$$

Obviously Eq. (4.22) reduces to Eq. (4.23) if the width,  $\lambda$ , of the function  $p(t, E)$  is small enough to consider the distribution function as a constant, approximately equal to  $f(E_c)$ , in this interval.

For a better understanding of the limits of validity of the logarithmic approximation, let us consider first the case of a flat-hat distribution. From Eq. (4.22), we see that we will have logarithmic decay (constant viscosity) as long as  $E_1^*(t) > E_1$  and  $E_2^*(t) < E_2$ . If this is the case, the magnetic viscosity is time independent, it increases with the temperature and it is inversely proportional to the width of the distribution  $\sigma$  as

$$S(t) \simeq -\frac{1}{e} \lambda = -\frac{T}{\sigma}. \quad (4.24)$$

Then we see that, at least for a uniform distribution of energy barriers, the range of validity of the logarithmic decay of the magnetization, at a fixed temperature, is given by the instants of time at which  $p(t, E)$  crosses the beginning  $E_1$  and end  $E_2$  of the distribution function of energies.

Let us look more carefully at the behaviour of the function  $p(t, E)$  as a function of time within the scope of our phenomenological theory. At every instant of time  $t$ , the center of  $p(t, E)$  is at  $E_c(t) = k_B T \ln(t/\tau_0)$ , and this means that it will arrive at the beginning of the distribution  $E_1$  at an instant of time:

$$\ln\left(\frac{t_1}{\tau_0}\right) = \frac{E_1}{k_B T} \quad (4.25)$$

and to the end,  $E_2$ , at a time

$$\ln\left(\frac{t_2}{\tau_0}\right) = \frac{E_2}{k_B T}. \quad (4.26)$$

Since we have approximated  $p(E)$  by a straight line in the range  $[E_1^*, E_2^*]$  (see Sec. 4.1), we can estimate the widths  $\lambda_1 = E_c - E_1^*$  and  $\lambda_2 = E_2^* - E_c$  of  $p(t, E)$  to be:

$$\lambda_1 = k_B T; \quad \lambda_2 = k_B T(e - 1). \quad (4.27)$$

The logarithmic law will be valid only when the whole  $p(t, E)$  curve is inside the region  $[E_1, E_2]$  (see Fig. 4.3), *i.e.*, in the range of times:

$$\frac{E_1 + \lambda_1}{k_B T} < \ln\left(\frac{t}{\tau_0}\right) < \frac{E_2 - \lambda_2}{k_B T}. \quad (4.28)$$

If the width of the energy distribution,  $\sigma$ , is much larger than that of  $p(t, E)$ ,  $\lambda$ , at a given temperature, the logarithmic approximation is valid in a wide range of times. In the opposite case, when  $\lambda \ll \sigma$ , the range of validity can be very small (the logarithmic approximation could be no longer valid), not only because  $p(t, E)$  does never really lie completely inside the peak of the distribution, but also because the approximation of  $p(E)$  by a straight line is poor. It is worth noting at this point that, even in the case of the uniform energy-barrier distribution, which is the most favorable candidate for a logarithmic law, the validity of the logarithmic approximation depends crucially on the temperature of the system, and not only on the width or the shape of the distribution.

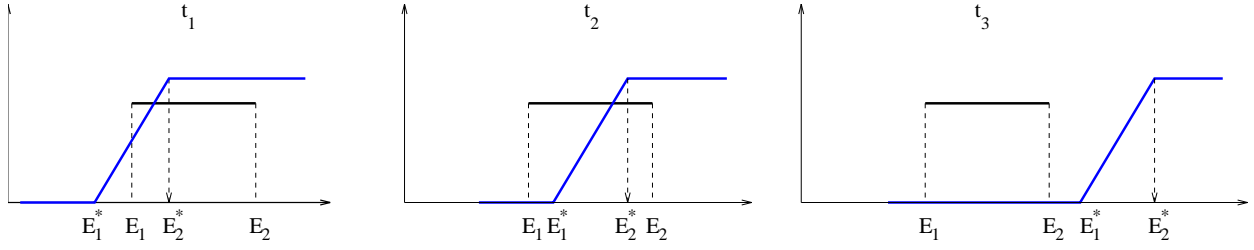


Figure 4.3: Evolution in time of the function  $p(t, E)$  for the flat-hat distribution of energies. The images corresponds to three different times increasing from left to right. The logarithmic law is valid in this example only at the intermediate time  $t_2$  when the function  $p(t, E)$  lies completely within the range of energies over which the distribution spans.

For the case of a general distribution of energy barriers, like a logarithmic-linear or similar distributions found in real systems, the logarithmic approximation is, strictly speaking, nowhere valid, and it is possible to choose other laws for  $M(t)$  (like potential or stretched exponential laws common in the literature, or even a single exponential [4]) that fit experimental data with equal or similar success compared to the logarithmic law, which assumes a uniform distribution of energies. The only region for which a logarithmic law is a reasonable approximation is the range of times corresponding to energy barriers near the maximum of the distribution function, as long as it can be considered uniform around this value. So, we can estimate the range of times for which logarithmic approximation will be approximately accomplished simply substituting  $E_1$  and  $E_2$  in Eq. (4.28) by the position of the inflection points of the energy barrier distribution. For instance, in the case of a normal distribution, these positions are  $E_0 - \sigma$  and  $E_0 + \sigma$ , where  $\sigma$  is the standard deviation of the distribution and  $E_0$  is the position of the maximum. If a logarithmic-linear distribution is assumed, the inflection points are located at

$$E_1; E_2 = E_0 \exp \left[ -1.5\sigma^2 \pm \sqrt{0.25\sigma^4 + \sigma^2} \right], \quad (4.29)$$

where  $\sigma$  is the dimensionless width of the logarithmic-normal distribution.

This last point, as well as our original question, can be better understood by deriving an exact expression for the relaxation rate  $S(t)$  obtained by expanding  $f(E)$  about  $E = E_c$  [5, 6]. Starting from Eq. (4.5) for the relaxation law, the viscosity can be expressed in terms of the inverse of the relaxation time,  $\nu$ , as

$$S(t) = tk_B T \int_0^\infty dE f(E) \nu e^{-\nu t}. \quad (4.30)$$

Here the function  $G(t) = \nu e^{-\nu t}$  under the integral has a maximum at  $t\nu_{max} = 1$  corresponding to an energy barrier  $\bar{E} = E(\nu_{max}) = T \ln(\nu_0 t)$ , so it is possible to expand the distribution function  $f(E)$  around this value as

$$f(E) = f(\bar{E}) + \sum_{n=1}^{\infty} \frac{f^{(n)}(\bar{E})}{n!} (E - \bar{E})^n. \quad (4.31)$$

When substituting this inside the integral 4.30 we get

$$S(t) = tk_B T \left\{ f(\bar{E}) \int_0^\infty dE \nu e^{-\nu t} + \sum_{n=1}^{\infty} \frac{f^{(n)}(\bar{E})}{n!} \int_0^\infty dE (E - \bar{E})^n \nu e^{-\nu t} \right\}$$

$$= tk_B T \left\{ \frac{f(\bar{E})}{t} + \sum_{n=1}^{\infty} \frac{f^{(n)}(\bar{E})}{n!} I_n(t) \right\}, \quad (4.32)$$

where

$$I_n(t) = \int_0^{\infty} dE (E - \bar{E})^n v e^{-vt}. \quad (4.33)$$

This integral can be evaluated to give

$$I_n(t) = (-1)^n \frac{T^{n+1}}{t} A_n \quad \text{with} \quad A_n = \int_0^{\infty} dx (\ln x)^n e^{-x}, \quad (4.34)$$

so, finally,  $S(t)$  can be reexpressed as

$$S(t) = k_B T \left[ f(\bar{E}) + \sum_{n=1}^{\infty} \frac{f^{(n)}(\bar{E})}{n!} (-T)^n A_n \right] \quad (4.35)$$

From this expression, we clearly observe that the critical volume approximation is nothing but the first term in an expansion of the kind

$$S(t) = k_B T f(\bar{E}) (1 + S^{(1)} + S^{(2)} + \dots), \quad (4.36)$$

of which the higher order terms are of order  $S^{(n)} \sim T^n \frac{f^{(n)}(\bar{E})}{f(\bar{E})}$ .

Now we can understand when this higher order corrections can be dropped. For typical distributions  $\frac{f^{(n)}(\bar{E})}{f(\bar{E})} \sim \frac{1}{\sigma^n}$ , with  $\sigma$  the characteristic width of the distribution. So that, from this point of view, the logarithmic law is valid at low  $T$  and for wide distributions.

### 4.3 The $T \ln(t/\tau_0)$ scaling

Experiments on magnetic relaxation are limited to a range of at most four decades in time, but during this range of times the magnetization of most physical systems only varies in a small percentage of the initial value, so that the range of energy barriers explored during the experiment is limited to a small fraction of the real distribution  $f(E)$ . This is so because of the spread of the physical properties of the systems and the exponential variation of the relaxation times with the energy. So, it would be interesting to find a method to extend the experimental relaxation curves to much longer times without having to perform impossibly long measurements. This is what the phenomenological  $T \ln(t/\tau_0)$  scaling pretends.

The method relies on the fact that under certain conditions there is a natural scaling variable in the relaxation law that relates temporal to temperature scales, thus making possible to deduce relaxation curves at long times and a given temperature from the knowledge of the short time relaxations at different higher temperatures. The idea resembles that found in earlier works by Préjean et al. in the context of relaxation in spin glasses at the beginning of the 80's [7].

In order to illustrate its origin, let us start from a real experimental example. Let us consider a set of relaxation curves measured at different temperatures as the ones displayed in Fig. 4.4a. At a first glance, they all seem to follow a logarithmic law. One is even tempted to make linear fits which probably would be accurate enough, and that is what is usually done in the literature [8]. But let us take a closer inspection to every particular curve. In Figs. 4.4b we have selected a low, intermediate and high temperature curves and plotted them separately. It can be clearly seen that only at intermediate temperatures the curves are straight

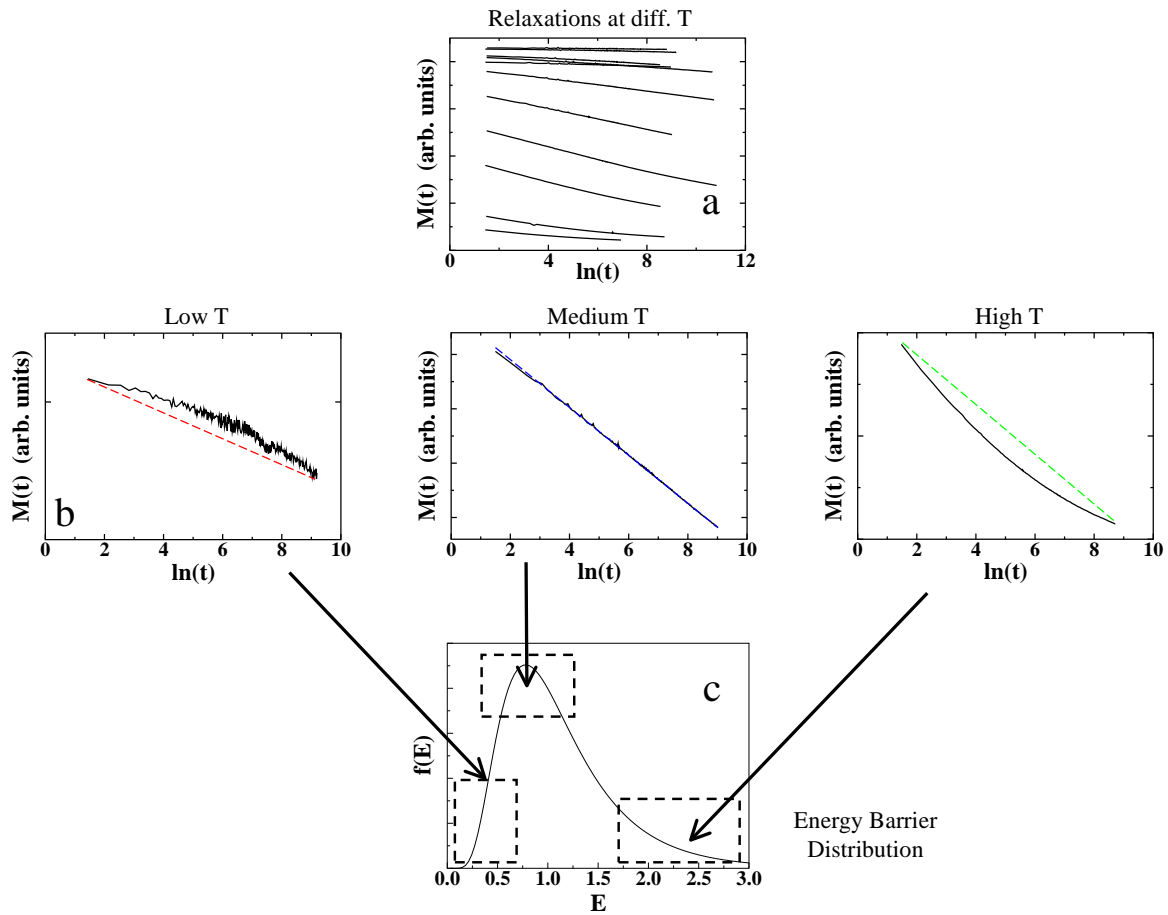


Figure 4.4: Illustration of the origin of the  $T \ln(t/\tau_0)$  scaling for relaxation curves at different  $T$ . (a) Relaxations curves at different  $T$  (the lowest  $T$  is for the uppermost curve) in logarithmic time scale as measured in an experiment. (b) Details of a low, medium and high  $T$  curves. The dashed lines correspond to logarithmic time dependence, departure from this law are clearly seen at low and high  $T$ . (c) Diagram showing the fraction of energy barriers that contribute to the above relaxation curves.

lines corresponding to a logarithmic law, but that, at high and low  $T$ , they are curved downward and upward respectively, showing a clear deviation from a logarithmic law.

In order to understand this change of curvatures, let us notice that during the time of the experiment only a small fraction of all the energy barriers of the system are sampled. Moreover, this fraction is not the same at different temperatures. The typical energy barriers explored during the measuring time of the experiment,  $t_m$ , are of the order of  $E_m = T \ln(t_m/\tau_0)$ , proportional to the temperature, so that relaxation curves at different temperatures are not directly comparable because they collect results from different portions of the energy barrier distribution of the system. As Fig. 4.4c illustrates, the low temperature curve samples the low energy part of the energy barrier distribution  $f(E)$ , at intermediate temperatures the mean energy barriers are explored, and at high temperatures the high energy part of  $f(E)$  is sampled. Moreover, this explains why only relaxations at intermediate temperatures are logarithmic, since, in this range, the fraction of barriers explored are near the maximum of the distribution where  $f(E)$  is almost flat. The curvature of the relaxation curves is, therefore, directly related to the curvature of the energy distribution. This clearly indicates that, even though all the measurements have been performed during the same time window, the energy barriers responsible for the relaxation are not the same at every temperature.

It could seem that this observation rules out any attempt to characterize magnetic systems through their relaxation curves because of the impossibility to explore all the energy barrier landscape during a reasonable time scale (to cover a range of energies involved in a typical particle system with a spread of 5 nm in diameter one would need to measure the relaxation over  $10^{10}$  s) but in fact this is not the case. From Fig. 4.4a, we may already notice that if the lowest temperature relaxation could be continued to longer times it would eventually coincide with the data recorded at an intermediate temperature at shorter times. In other words, relaxation curves at different temperatures superimpose one into another after appropriate shifts in the horizontal axis.

This intuitive observation is, in fact, supported by the phenomenological model of relaxation described in the preceding section. According to Eq. 4.8, the relaxation law  $M(t)$  must be a function of the cutoff variable  $E_c = T \ln(t/\tau_0)$ , implying that the relaxation law observed at a time scale  $t_1$  at a certain high temperature  $T_1$  corresponds to a relaxation law at a lowest temperature  $T_0$  at much longer time scales  $t_0 = t_1 e^{(T_1 - T_0)}$ . Thus, even though relaxation experiments lasting more than four decades in time are impossible in practice, by relating relatively short relaxation curves at different temperatures by means of  $T \ln(t/\tau_0)$  scaling it is possible to extend relaxation data to times as long as it is needed.

## 4.4 Numerical calculations

In order to verify all these assumptions, we have calculated the decay of the magnetization for a small-particle system with a logarithmic-linear distribution of energy barriers (which is a more realistic distribution than the normal one) by numerical integration of expression 4.1. With the aim to obtain more general results, we will define reduced variables as follows: a dimensionless magnitude  $T_0$  as  $T_0 = E_0/k_B$ , where  $E_0$  is the energy corresponding to the peak of the distribution, the reduced temperature of the system as  $T/T_0$ , and the reduced time as  $t/\tau_0$ . The results of these calculations for three values of the  $\sigma$  parameter of the logarithmic-linear distribution, and reduced temperatures ranging from 0.001 to 0.5, are shown in Fig. 4.3. The inserts of these figures show the dependence of the magnetization for a constant value of the scaling variable  $E_c$  as a function of the reduced temperature. Clearly the scaling is valid in the range of temperatures for which a constant behavior of the magnetization is observed in the inserts of Fig. 4.3. From these figures the obvious fact can be verified that the range of validity of the scaling increases as the



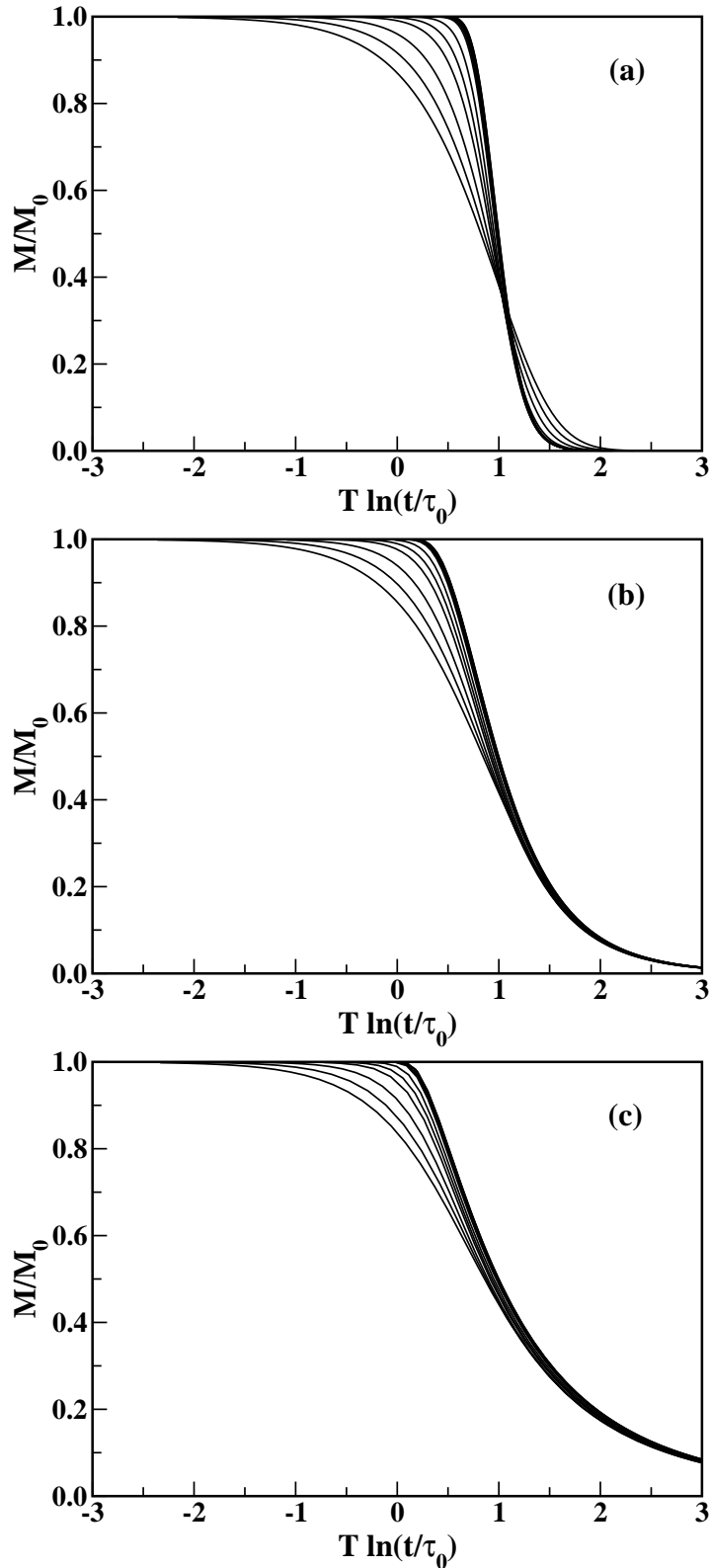


Figure 4.5: (a) The scaling plot of the calculated data by numerical integration of Eq. (4.1) with a logarithmic-normal distribution of energy barriers of dimensionless width,  $\sigma=0.2$ . The reduced temperatures,  $T/T_0$ , corresponding to each curve are as follows: 0.001, 0.005, 0.01, 0.02, 0.04, 0.1, 0.2, 0.3, 0.4 and 0.5. The lowest reduced temperature corresponds to the highest curve. In the inset, the reduced magnetization as a function of the reduced temperature for constant value of the scaling variable  $E_c$  is shown. Each curve corresponds to a different value of  $E_c$ , indicated to the right of each curve. The log scale of the  $T/T_0$  axis has been chosen for better observation of the behavior at temperatures below the blocking temperature. (b) Same as (a) but for  $\sigma=0.5$ . (c) Same as (a) but for  $\sigma=0.8$ .

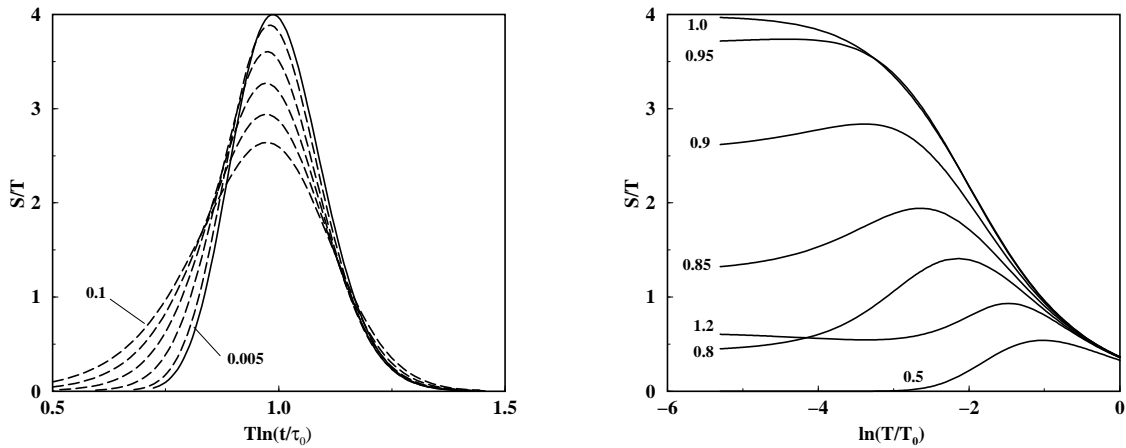


Figure 4.6: (a) The magnetic viscosity of the calculated data by numerical integration of the logarithmic time derivative of Eq. 4.1 with a logarithmic-linear distribution of energy barriers of dimensionless width,  $\sigma = 0.1$ , plotted in a continuous line. The reduced temperatures corresponding to each curve are as follows: 0.005, 0.02, 0.04, 0.06, 0.08, 0.1. The lowest reduced temperature corresponds to the highest curve at the maximum. (b) The magnetic viscosity as a function of the reduced temperature for a constant value of the scaling variable  $E_c$  as calculated in (a). Every curve corresponds to a different value of  $E_c$ , indicated at the left of each curve. The log scale of the x axis has been chosen for better observation of the behaviour at temperatures below the blocking temperature.

width of the distribution increases. It is important to note that in these figures curves corresponding to temperatures much above the mean blocking temperature, which in reduced units is approximately 0.04, have been included and that at temperatures below or around the mean blocking temperature scaling is almost fulfilled in the whole range of the scaling variable  $T/T_0 \ln(t/\tau_0)$  for the three widths of the studied energy distributions.

## 4.5 Energy barrier distributions from the $T \ln(t/\tau_0)$ scaling

In Section 4.2.2 we saw that the magnetic viscosity may be written as an expansion of the form

$$S(t) = k_B T f(E_C) \left[ 1 + S^{(1)} + S^{(2)} + \dots \right] \quad (4.37)$$

where  $S^{(n)}$  is proportional to  $(k_B T/\sigma)^n$ ,  $\sigma$  being the characteristic width of the energy barrier distribution. Therefore, at temperatures low enough so that the width  $\lambda$  of the  $p(t, E)$  function is small compared to the width of the energy distribution, the corrections introduced by the  $S^{(n)}$  terms can be neglected and the magnetic viscosity becomes directly proportional to the distribution of energy barriers.

In the scope of this model we have performed calculations of the magnetization decay by numerical integration of the logarithmic time derivative of Eq. 4.1, using a logarithmic-linear distribution for  $f(E)$  [4] with dimensionless width,  $\sigma$ , and centered at the reduced value of energy  $E_0 = 1$ . Using reduced time and temperature variables as before. The results are shown in Fig. 4.6 and 4.7, where  $S(t)/T$  is represented as a function of the activation energy  $T \ln(t/\tau_0)$  for different values of the reduced temperatures and  $\sigma = 0.1$  and 0.5 respectively, together with the  $f(E)$  distribution used in the calculations.

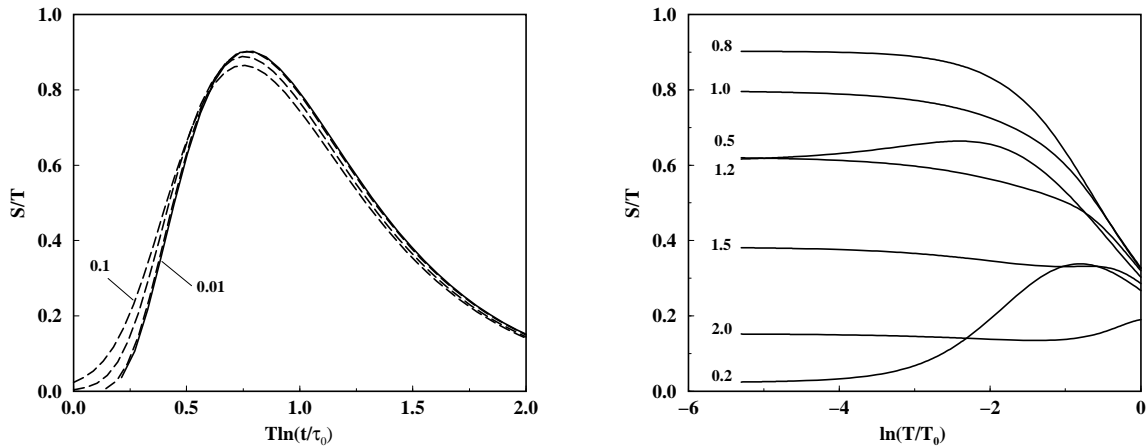


Figure 4.7: (a) Same as Fig. 2 but for  $\sigma = 0.5$ . The reduced temperatures corresponding to each curve are: 0.01, 0.02, 0.06, 0.1. (b) Same as Fig. 4.6a but for  $\sigma = 0.5$ .

In the case of a narrow distribution ( $\sigma=0.1$ ), good agreement between the calculated distribution and  $f(E)$  is achieved at reduced temperatures of less than or about 0.01 (which corresponds approximately to 0.25 times the reduced blocking temperature for an observational time window of about 100 s which in reduced units is  $T_B = T_0/\ln(t/\tau_0)=0.04$ ). While for a broad distribution ( $\sigma=0.5$ ) the agreement is already achieved at higher temperatures (about 0.05), as expected from the argument given above.

In order to show the approach of  $S[T \ln(t/\tau_0)]$  to the actual distribution of energy barriers  $f(E)$  as the temperature is decreased, we have also calculated numerically the thermal dependence of  $S$  at different values of the scaling variable  $E_C$ . The results are shown in Fig. 4.6b and 4.7b. From them it can be clearly seen that at least for temperatures lower than the reduced blocking temperature ( $\ln T_B=-3.2$ ) all the curves tend to the constant value  $f[T \ln(t/\tau_0)]$ , thus confirming the validity of our hypothesis. Only in the low energy region there is an appreciable departure of  $S(T)$  from  $f(E)$ . As  $E_C$  approaches the high energy region the agreement is much better because the exact dependence of  $M(t)$  is less influenced by the particular form of  $f(E)$ . As  $\sigma$  is increased the approach of  $S(T)$  to  $f(E)$  is obtained at higher temperatures.

## 4.6 Experimental verification of the model

### 4.6.1 Experimental implementation of the $T \ln(t/\tau_0)$ scaling

In order to verify the validity of the  $T \ln(t/\tau_0)$  scaling law in real small particles systems, the magnetic relaxation data obtained for different samples were analyzed within the scope of the scaling hypothesis. The first sample is a ferrofluid of  $\text{Fe}_3\text{O}_4$  small particles dispersed in a hydrocarbon oil [9]. The average particle diameter ranges from 50 to 60 Å. Although the degree of dilution is not large enough to completely remove the interaction among particles, it was estimated to be very small [10]. The second sample consists on FeC small particles in stable dilution with a hydrocarbon oil that freezes at 19° C [11]. The average diameter of these particles was measured to be 36 Å [12]. The procedure to measure the relaxation of the magnetization was the same for samples 1 and 2. It consists on cooling down the sample from a temperature above the blocking temperature, down to the measurement temperature, that is always lower

than the blocking temperature, under an applied field of 10 Oe. Once the temperature is stabilized, the field was switched off and magnetization data versus time were recorded. The superconducting quantum interference device magnetometer used for this purpose was a commercial one with a modified procedure of measurement which is described in Ref.[13].

According to the scaling hypothesis discussed in Sec. 4.3, for each sample, all the different curves corresponding to different temperatures, would have to scale onto one single master curve when plotted as a function of the scaling variable  $T \ln(t/\tau_0)$ . In order to verify the validity of this model, we try to scale the relaxation data of the referred samples. The procedure used for this purpose consists on plotting the relaxation curves in a  $M$  vs  $\ln(t)$  plot and trying to connect each of them continuously with the adjoining curves corresponding to the nearest measured temperatures. To do that, we shifted the experimental curves in the  $T \ln(t)$  axis by an amount equal to  $T \ln(\tau_0)$ , where  $\tau_0$  is a characteristic time which governs the relaxation processes on an atomic scale. For each sample  $\tau_0$  is the same for all of the measured temperatures and it was chosen to be the best in bringing all the curves into one. These values are given in Table 4.1. The values obtained for sample 2 lie in the range of expected values in small-particle systems [14, 15]. However, the value of  $\tau_0$  for sample 1 is somewhat larger than the expected one. This fact may be related to the lower degree of dilution of sample 1 with respect to sample 2, which increases the strength of the dipolar interactions among particles. In any case, it is not clear how these interactions would affect the atomic scale constant  $\tau_0$  and how the relaxation law would be modified.

Due to the inaccuracy in the determination of the initial value of the magnetization (for each temperature, the value of  $M$  at  $t = 0$ ), it was also necessary to normalize the experimental data dividing them by an arbitrary reference magnetization value,  $M_0$ .

In Figs. 4.8 the results of this scaling for the two samples are shown. One of the most interesting aspects of these results is that, in fact, measuring the relaxation at a given temperature is completely equivalent to measure it at a different temperature but shifting the observation time window according to the law  $T \ln(t/\tau_0)$ . In this sense, the method enables us to obtain the relaxation curve at a certain temperature, in a time range that is not experimentally accessible, by simply dividing the  $T \ln(t/\tau_0)$  axis by this temperature. For instance, in the case of sample 2, we can obtain the relaxation curve at the lowest measured temperature of 1.8 K at times as large as  $10^{119}$  s, which is obviously an experimentally inaccessible time. For sample 1, where the highest temperature that we have measured was 37 K, we are observing the relaxation curve corresponding to 2 K at times as large as  $10^{173}$  s.

One way to test the validity of these scaling plots consists in trying to reproduce the experimental curves shown in Figs. 4.8, by using a reasonable model for the magnetic relaxation of these systems. As was done in Sec. 4.1, we can assume that the evolution towards equilibrium of a system consisting of an assembly of randomly oriented particles is governed by the Arrhenius law with a given distribution of energy barriers. The particular mathematical form of this distribution is not very important as far as it agrees with some reasonable conditions, and usually a logarithmic-linear distribution is assumed. Consequently, we have fitted the experimental master curves of Figs. 4.8 to the theoretical one calculated from Eq. 4.1 at an intermediate temperature and using a log-normal distribution of energy barriers. The free parameters for the fitting were  $\sigma$  and  $T_0$  as defined in Sec. 4.4, and the obtained values are summarized in Table I, while solid lines in Figs. 4.8 represent the corresponding theoretical curves. In all the cases, reasonably good agreement is achieved and the only significant departures between theoretical and experimental data are observed for small values of the scaling variable which for a given temperature corresponds to short times. In our case, this small discrepancy could indicate that the logarithmic-linear distribution is not very realistic for the lowest energy barriers (which are overcome at shortest times) and underestimates their contribution to the total relaxation process of the system. Recently, some authors [16, 17, 18, 19] have also suggested that

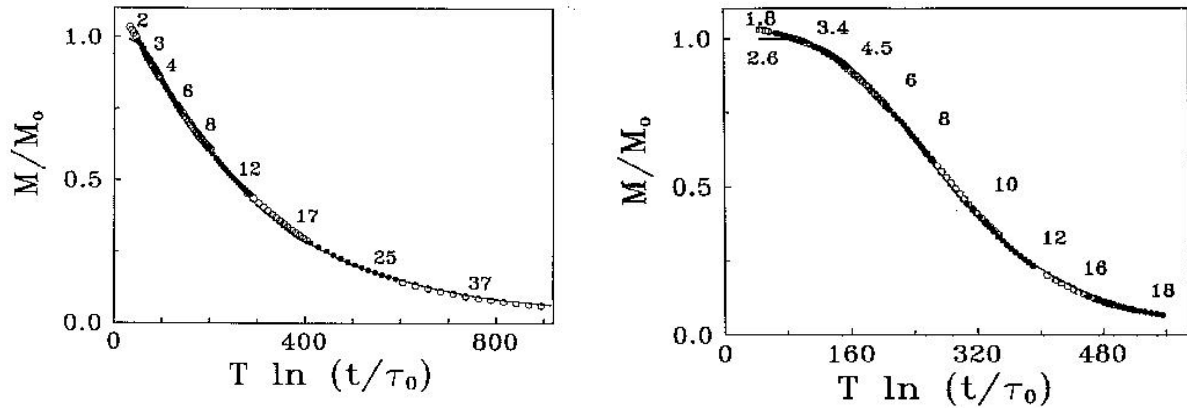


Figure 4.8: Master curves obtained by  $T \ln(t/\tau_0)$  scaling of the relaxation curves for a ferrofluid composed of  $\text{Fe}_3\text{O}_4$  small particles (Sample 1, left panel) and a sample of FeC particles (Sample 2, right panel) are shown. The figures show the reduced magnetization as a function of the scaling variable. Open and full circles correspond alternatively to adjoining temperatures, that are indicated above the corresponding interval. The solid line is the theoretical curve calculated by using Eq. (4.1) and the values of the fitting parameters indicated in Table 4.1.

Sample	$\tau_0(\text{s})$	$\sigma$	$T_0(\text{K})$
1	$(4.7 \pm 5) \times 10^{-7}$	$0.85 \pm 0.05$	$245 \pm 50$
2	$(3.5 \pm 5) \times 10^{-11}$	$0.44 \pm 0.05$	$287 \pm 50$

Table 4.1: Values of the parameters obtained by fitting the experimental scaled curves to Eq. (4.1) with a logarithmic-linear distribution of energy barriers.

below a certain crossover temperature, non-thermal processes (quantum tunneling) dominate the evolution of the magnetization towards equilibrium in zero-dimensional systems with high or moderate degree of anisotropy as is the case of the small-particle systems studied in this paper. The main effect of this quantum contribution is to increase the rate of variation of the magnetization below the crossover temperature, with respect to the thermal value. This fact could explain the small discrepancies observed for small values of the scaling variable, taking into account that this interval of the master curve corresponds to the relaxation curves measured at the lowest temperatures.

Samples 1 and 2 were measured in the same way, with no applied field while recording the data, so that what one is measuring is the decay of the magnetization after field cooling the sample and removing the field. So in these two cases the existence of a distribution of energy barriers is only due to the distribution of particle sizes, which usually can be well approximated by a logarithmic-normal distribution. As a consequence, the fitting values for the parameter  $\sigma$  can be compared with those obtained by other more direct granularimetric methods. For instance, in the case of sample 2,  $\sigma$  was also determined to be  $0.45 \pm 0.03$  from the distribution of blocking temperatures,[12] which is in very good agreement with that deduced by the scaling procedure. From the values of the anisotropy constant and the mean size of the particles, reported in Ref. ([12]), one can evaluate the value of the parameter  $T_0$  for the FeC particles to be  $320 \pm 70$  K, which also compares well with the corresponding value reported in Table 4.1.

### 4.6.2 Experimental derivation of energy barrier distributions

According to expression 4.36, the viscosity is a function of the scaling variable  $T \ln(t/\tau_0)$  and is proportional to  $T$ , so if we plot  $S/T$  as a function of  $T \ln(t/\tau_0)$  at low enough temperatures, the resulting curve will be the energy distribution function of the sample. As has already been mentioned, it is not possible to obtain an experimental relaxation curve covering enough time decades to map the whole energy barrier distribution at any temperature. However, the master curve can be used to obtain the relaxation curve at the lowest measured temperature extrapolated to experimentally inaccessible times. We have obtained  $S$  for the two samples by making the numerical derivative of the respective master curves (see Fig. 4.10). The results are shown in Fig. 4.9. In Fig. 4.9 we also show the derivative of the thermoremanence relative to the saturation magnetization versus the temperature ( $dM_r/dT$ ) [12] which is known to be proportional to the distribution function of blocking temperatures [20] and consequently to the distribution function of energy barriers. The results obtained by the two methods are in very good agreement.

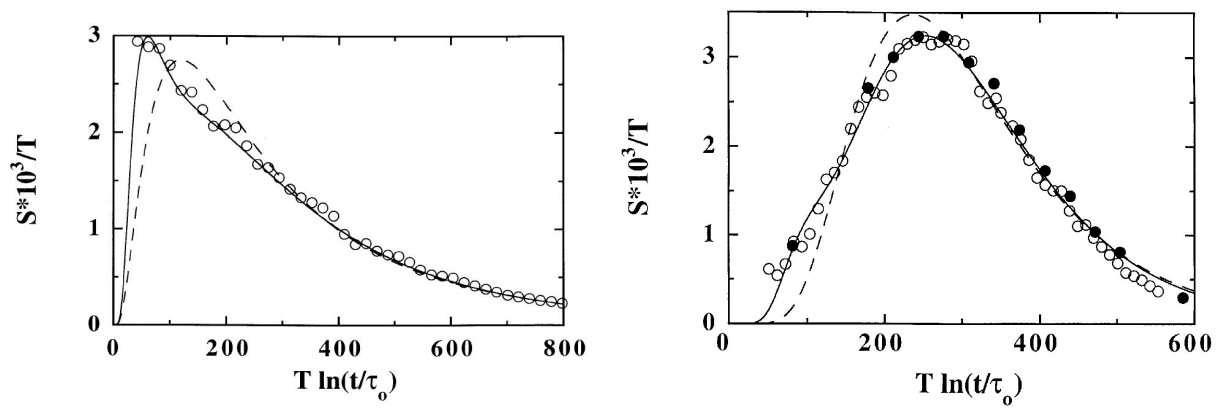


Figure 4.9: Left panel: Numerical derivative of the master curve with respect to the scaling variable for sample I (open circles) and the energy distribution functions as obtained by fitting the master relaxation curve to expression (4.1) assuming a single logarithmic-normal distribution (dashed curve) and two logarithmic-normal distributions 4.38 with parameters given in Table 4.2. Right panel: Same as left panel, but for sample 2. The differential of the thermoremanence relative to the saturation magnetization versus the temperature is also shown in full circles for comparison.

One way to check the self consistency of the method is to compare  $f(E)$  as obtained from the viscosity with the one obtained by fitting the master relaxation curve to Eq. 4.1 assuming only a logarithmic-linear distribution of energy barriers. The corresponding values of  $\sigma$  and  $T_0$  for one logarithmic-linear are shown in the Table 4.1. The resulting distribution function is shown in Fig. 4.10 in dashed lines. One can see that there is a very significant discrepancy between the experimental points and the fitted logarithmic-linear distribution, especially in the low energy barrier region. In fact, this discrepancy is also reflected in Fig. 4.10, where we plot the experimental master curves for the magnetization together with the theoretical curve obtained from 4.1. At low temperatures (or short times) the experimental points lie above the theoretical curve for both cases (see insets in Fig. 4.10), indicating that the measured magnetization decays faster than the predicted by the model. A similar low temperature behaviour has been also observed in a sample consisting of an assembly of nanocrystalline Co-Ti doped barium ferrite [21].

There are several possibilities to account for this discrepancy which will be discussed in more detail later. However, we will first focus on the most evident: the existence of a larger amount of low energy barri-

ers than the considered by assuming a log-normal distribution (or other bell-shaped distribution functions).

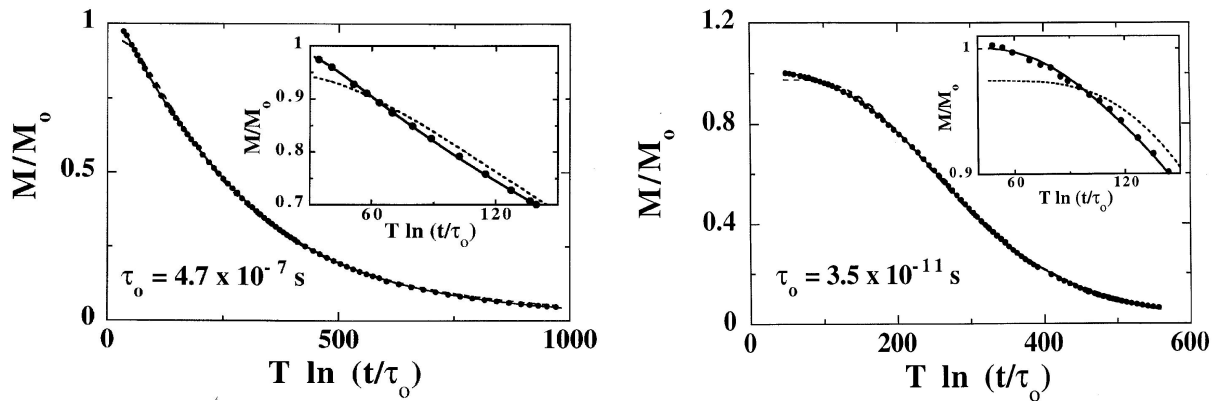


Figure 4.10: (a) Master curve for relaxation data recorded from 2 to 39 K for sample 1. Dashed and solid lines correspond to the fits with one and two logarithmic-normal distributions respectively. The inset details the low values region of the scaling variable. (b) Same as in (a), for sample II and temperatures ranging from 1.8 to 18 K.

This assumption would imply a faster relaxation rate at low values of the activation energy as these are the first to be overcome. This possibility is clearly suggested by the shape of  $S[T \ln(t/\tau_0)]$ , which always lies at higher values than the logarithmic-linear distribution used to fit  $M[T \ln(t/\tau_0)]$  (see Fig. 4.9). One way to incorporate this fact into our model is to fit the experimental master curves to Eq. 4.1 taking the distribution function to be the sum of two logarithmic-linear distributions:

$$f(E) = \frac{w}{\sqrt{2\pi E\sigma_1}} e^{-\frac{1}{2\sigma_1^2} \ln^2(\frac{E}{k_B T_{01}})} + \frac{(1-w)}{\sqrt{2\pi E\sigma_2}} e^{-\frac{1}{2\sigma_2^2} \ln^2(\frac{E}{k_B T_{02}})} \quad (4.38)$$

where the free parameters for the fitting were  $\sigma_1$ ,  $\sigma_2$ ,  $T_{01}$ ,  $T_{02}$  and the weighting factor  $w$ , which is included to account for the relative contribution of the lowest energy barriers. The results of the fitting are shown in the Fig. 4.10 for the master curves of sample I and II respectively, together with the fit with only one logarithmic-linear and the fitted values of the parameters are given in the Table I where the values obtained by using only one logarithmic-linear distribution,  $T_0$  and  $\sigma$  have also been included. As one can see, the values of  $T_{01}$  and  $\sigma_1$  corresponding to the logarithmic-linear centered at higher energy barriers are only slightly changed with respect to  $T_0$  and  $\sigma$ , and the relative contribution of the second logarithmic-linear is small (about 10 and 20 %) and it is centered at lower energy values.

The obtained distribution functions are plotted in Fig. 4.9 together with  $S(t)$  to show that the election of Eq. 4.38 as  $f(E)$  is not an arbitrary choice. Now, the experimental points for the viscosity follow perfectly the shape of the distribution used to fit the master curve, thus demonstrating the existence of low energy barriers and that they are observable in the time dependent behaviour of the magnetization. It is important to note that, probably, the distribution given by Eq. 4.38 does not represent the exact mathematical law of the actual distribution. In fact, Eq. 4.38 is only a way to model the experimental distribution using the most relevant terms of a complete set of realistic bell-shaped functions.

One could think of another possible explanation which would be the observation of non-thermal acti-

Sample	$\sigma$	$T_0(\text{K})$	$\sigma_1$	$\sigma_2$	$T_{01}(\text{K})$	$T_{02}(\text{K})$	$w$
1	0.85	245	0.73	0.57	301	70	0.79
2	0.44	287	0.40	0.38	303	123	0.89

Table 4.2: Values of the parameters obtained by fitting the experimental scaled curves to Eq. 4.1 with a logarithmic-linear distribution of energy barriers and with the distribution of Eq. 4.38. The error in the determination of the dimensionless parameters  $\sigma$  is about 0.05 and the error in the parameters  $T_0$  is about 50 K in all the cases.

vated processes: quantum tunnelling of the magnetization. But if this was the case the  $T \ln(t/\tau_0)$  scaling would not be accomplished because one would fail to connect continuously the relaxation curves below a certain temperature. Then, at low temperatures, the master curve would break into different segments because one would be multiplying by a factor  $T$  the corresponding relaxation curves and in fact they would be temperature independent. As a consequence, the scaling approach provides a very powerful method to prove the existence of quantum tunnelling effects as the results of E. Vincent [22, 23], Arnaudus [24], Tejada [] and other authors support also.

## 4.7 Magnetic viscosity: a critical review

On the other hand, the usual methods used to observe macroscopic quantum tunnelling effects in different magnetic systems [18, 17, 25] and superconductors [26, 27, 28] by studying the thermal dependence of the rate of decay of the magnetization (viscosity) have some drawbacks and can lead to misinterpretations. In this experiments constancy of  $S$  below the so called crossover temperature is ascribed to quantum tunnelling dominated processes. We would like to point out that the non-thermal dependence of  $S$  can also arise in the context of purely thermally activated models in several cases: in systems for which there is a relevant contribution from the low energy barriers distribution centered at values comparable to  $k_B T_{\min}$ , where  $T_{\min}$  is the minimum measured temperature, (as it is the case of sample I) if the magnetization decay is analyzed according to the logarithmic approximation, one would observe no variation of  $S$  below a certain temperature within the experimental resolution (as is the case for example of sample I, see Fig. 4.10). On the other hand, the specific form of  $S(T)$  depends crucially on the specific dependence of  $f(E)$  on the energy as has been pointed out by other authors [29]. In particular, an inverse dependence on  $E$  ( $f(E) \sim 1/E$ ) gives a constant viscosity at low temperatures. Other dependencies can even give a nonmonotonous behaviour of  $S(T)$  with an eventual increase at low  $T$  [30].

Finally, we would like to emphasize the usefulness of the scaling method to analyze different properties from magnetic relaxation. With this method it is possible to obtain the relaxation curve corresponding to the lowest measured temperature extended to completely experimentally inaccessible range of times and, therefore, to compare it with those obtained from theoretical predictions. At the same time, it is also possible to obtain the energy distribution function by simply performing the time logarithmic derivative of the scaling curve, while other commonly used methods require experimental measurements which are more difficult to obtain (magnetic saturation and remanence) or are based on different aprioristic assumptions about the distribution function, the time dependence of the relaxation or the field dependence of the energy barriers. Moreover, the scaling method can be extended to more general situations, for example the case for which there is an applied magnetic field or for a system for which a distribution of anisotropy fields must be considered [30].





## Bibliography

- [1] R. Street and J. C. Wooley, Phys. Soc. A **62**, 562 (1949).
- [2] L. Néel, C. R. Acad. Sci. Paris **228**, 664 (1949).
- [3] K. O'Grady, R. W. Chantrell, J. Popplewell, and S. W. Charles, IEEE Trans. Magn. **17**, 2943 (1981).
- [4] A. Aharoni, *Introduction to the Theory of Ferromagnetism* (Oxford University Press, New York, 1996).
- [5] D. V. Berkov, J. Magn. Magn. Mater. **111**, 327 (1992).
- [6] D. V. Berkov, J. Magn. Magn. Mater. **117**, 431 (1992).
- [7] J. J. Préjean and J. Souletie, J. Physique (France) **41**, 1335 (1980).
- [8] R. Sappey, E. Vincent, M. Ocio, and J. Hammann, J. Magn. Magn. Mater. **221**, 87 (1998).
- [9] S. W. Charles and R. E. Rosensweig, J. Magn. Magn. Mater. **39**, 190 (1983).
- [10] W. Luo, S. R. Nagel, T. F. Rosenbaum, and R. E. Rosensweig, Phys. Rev. Lett. **67**, 2721 (1991).
- [11] J. van Wontherghem, S. Mørup, S. W. Charles, and J. Villadsen, Phys. Rev. Lett. **55**, 410 (1985).
- [12] S. Linderoth, L. Balcells, A. Labarta, J. Tejada, P. V. Hendriksen, and S. A. Sethi, J. Magn. Magn. Mater. **124**, 269 (1993).
- [13] A. Labarta, R. Rodríguez, L. Balcells, J. Tejada, X. Obradors, and F. J. Berry, Phys. Rev. B **44**, 691 (1991).
- [14] W. F. Brown, Jr., Phys. Rev. **130**, 1677 (1963).
- [15] L. Bessais, L. Ben Jaffen, and J. L. Dormann, Phys. Rev. B **45**, 7805 (1992).
- [16] M. Uehara and B. Barbara, J. Phys. (Paris) **47**, 235 (1986).
- [17] X. X. Zhang, L. Balcells, J. M. Ruiz, O. Iglesias, J. Tejada, and B. Barbara, Phys. Lett. A **163**, 130 (1992).
- [18] L. Balcells, X. X. Zhang, F. Badia, J. M. Ruiz, C. Ferrate, and J. Tejada, J. Magn. Magn. Mater. **109**, L159 (1992).
- [19] E. M. Chudnovsky and L. Gunther, Phys. Rev. Lett. **60**, 661 (1988).
- [20] R. W. Chantrell, M. El-Hilo, and K. O'Grady, IEEE Trans. Magn. **27**, 3570 (19).

- 
- [21] X. Batlle, M. García del Muro, A. Labarta, B. Martínez, and P. Gørnert, *J. Magn. Magn. Mater.* **140-144**, 473 (1995).
- [22] E. Vincent, J. Hammann, P. Prené, and E. Tronc, *J. Phys. I France* **4**, 273 (1994).
- [23] R. Sappey, E. Vincent, N. Hadacek, F. Chaput, J. P. Boilot, and D. Zins, *Phys. Rev. B* **56**, 14551 (1997).
- [24] J. I. Arnaudas, A. del Moral, C. de la Fuente, M. Ciria, and P. A. J. de Groot, *Phys. Rev. B* **50**, 547 (1994).
- [25] J. I. Arnaudas, A. del Moral, C. de la Fuente, and P. A. J. de Groot, *Phys. Rev. B* **47**, 11924 (1993).
- [26] L. Fruchter, A. P. Malozemoff, I. A. Campbell, J. Sánchez, M. Konczykowski, R. Griesser, and F. Holtzberg, *Phys. Rev. B* **43**, 8709 (1991).
- [27] A. C. Mota, G. Juni, P. Visani, A. Pollini, T. Teruzzi, K. Aupke, and B. Hilti, *Physica C* **185-189**, 343 (1991).
- [28] R. Griessen, J. G. Lensink, and H. G. Schnack, *Physica C* **185-189**, 337 (1991).
- [29] B. Barbara, C. Paulsen, L. C. Sampaio, M. Uehara, F. Fruchard, J. L. Tholence, A. Marchand, J. Tejada, and S. Linderorth, in *Proceedings of the International Workshop on Studies of Magnetic Properties of fine Particles*, edited by J. L. Dormann and D. Fiorani (North Holland, Amsterdam, 1992), Vol. 301, p. 235.
- [30] B. Barbara, L. C. Sampaio, A. Marchand, O. Kubo, and H. Takeuchi, *J. Magn. Magn. Mater.* **136**, 183 (1994).

## CHAPTER 5

### RELAXATION PROCESSES IN THE PRESENCE OF A MAGNETIC FIELD

*No pienses, mira.*  
LUDWIG WITTGENSTEIN

The application of a magnetic field defines a preferential direction for the magnetization moment and breaks the energy degeneracy among equivalent equilibrium states induced by anisotropy. In this case, relaxation rates become field dependent and the calculation of relaxation curves cannot be cast into the simplified situation presented in the previous chapter. An equation equivalent to (4.1) has to be rederived from more basic principles, since the relaxation rate  $\tau$  entering that law depends now on the particle orientation and on the magnetic field value. In this chapter, we will extend the phenomenological approach of the previous chapter to relaxation in the presence of a magnetic field, showing how  $T \ln(t/\tau_0)$  of relaxation curves can be performed and finding a new scaling variable for curves measured at a given  $T$  and different fields.

In what follows, we want to account for the experimental studies on the relaxation of small-particle systems, which essentially measure the acquisition of magnetization of an initially demagnetized sample under the application of a magnetic field [1, 2, 3, 4, 5]. In this kind of experiments, the field modifies the energy barriers of the system that are responsible for the time variation of the magnetization, as well as the final state of equilibrium towards which the system relaxes. The fact that usually the magnetic properties of the particles (anisotropy constants, easy-axis directions and volumes) are not uniform in real samples, adds some difficulties to this analysis because the effect of the magnetic field depends on them in a complicated fashion.

#### 5.1 Relaxation dynamics in a magnetic field

The time dependence of the magnetization of single-domain ferromagnetic particles was first correctly addressed in a seminal paper by Néel [6], in which he estimated the time  $\tau$  required for  $\mathbf{M}$  to surmount the anisotropy energy barrier by thermal fluctuations in terms of what is called now diffusional relaxation time. Later Brown, [7] derived the Fokker-Planck (FP) equation for the probability density of orientations of  $\mathbf{M}$  which is the starting point for a calculation of the relaxation rate. This equation was solved by the same author in the limiting cases of high ( $\alpha \gg 1$ ) and low energy barrier ( $\alpha, \xi \ll 1$ ), showing that the time dependence of the magnetization is dominated by a single exponential with relaxation rate given by the lowest eigenvalue of the FP equation. In the intermediate region ( $\alpha, \xi \sim 1$ ), no general solution

can be found analytically and the relaxation is given by a sum of exponentials and the relevant parameter describing the relaxation is now the integral relaxation time [8, 9, 10, 11]. Trying to obtain an expression for  $M(t)$  from a FP equation for a system of particles with distributed properties in terms of microscopic parameters would be a formidable (and possibly unattainable) task, which, in any case, is out of the scope of this work. Therefore, we will simplify things by making some reasonable assumptions and approximations whose validity will be proved consistently.

In the FP equation the orientations of  $\mathbf{M}$  span a continuum of values but in practice calculations show that in the limits relevant to real experimental systems  $\mathbf{M}$  spends most of the time in orientations near to the local minima of the energy so that it is possible to treat the FP equation in the discrete orientation approximation and it can be transformed to a master rate equation [12, 13, 14] that can be solved following the methods of transition state theory [15, 16, 17].

Within this context, we will assume that the rotation of the magnetization due to thermal fluctuations can be modeled by a markovian stochastic process. Its dynamics can then be described by a master equation for  $P_i$ , the probability to find the magnetization vector of the particle at time  $t$  in the equilibrium state  $i$ . Furthermore, we will assume that we are in the regime where the TSA (introduced in Chapter 2 for the study of the equilibrium magnetization) is valid and, consequently, only transitions between the two equilibrium directions of the magnetization given by the minima of the energy (2.3) will be considered.

Moreover, in models considering continuous variables for the numerical evaluation of relaxation dynamics [18, 19, 20], the elementary time step depends on  $T$  and  $H$ , giving rise to relaxation curves which are not directly comparable. In a recent work, Novak and Chantrell [21] have faced the problem of the quantification of the time step used in Monte Carlo simulation, giving a method to quantify the time step in real units. As an alternative, we propose a simple dynamical model that avoids this problem since, in the TSA, it can be solved analytically in terms of intrinsic parameters. Taking into account that the transitions

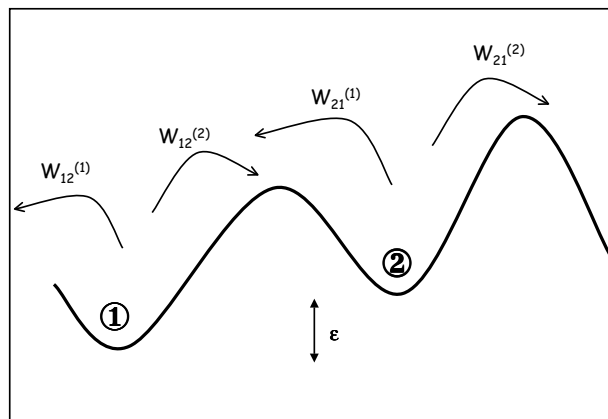


Figure 5.1: Transition rates in the definition of the master equation Eq. (5.1)

between the two minima can take place either by jumping over the barrier placed to the right or to the left of the initial state with equal probability, the master equation governing the time dependence of the magnetization of one particle can be written as [22]

$$\frac{dP_i}{dt} = \sum_{k=1,2} \sum_{j \neq i} \{w_{ji}^{(k)} P_j - w_{ij}^{(k)} P_i\}, \quad (5.1)$$

where  $w_{ij}^{(k)}$  designates the transition rate for a jump from the state  $i$  to the state  $j$  separated by the maximum

$k$  (see Fig. 2.3 and 5.1). The transition rates can be freely assigned as long as to fulfill the detailed balance condition [22]. It is a common choice to consider the Boltzmann probability with the energy difference between the two minima in the exponent. This choice, in spite of giving the correct thermodynamic averages in a Monte Carlo simulation, may not be appropriate to describe the dynamics of the system, since the energy barriers between the minima are not taken into account.

For this reason, in the exponential of the Boltzmann probability, we have considered the energy difference between the initial minimum  $i$  and the maximum  $k$  that separates it from the final state  $j$

$$w_{ij}^{(k)} = \frac{1}{\tau_{ij}^{(k)}} = \frac{1}{\tau_0} e^{-E_b^{ki}\beta}, \quad (5.2)$$

where  $\tau_0^{-1}$  is the attempt frequency.

It is a trivial matter to prove that the following detailed balance equation holds

$$\frac{w_{21}^T}{w_{12}^T} = \frac{w_{21}^{(1)} + w_{21}^{(2)}}{w_{12}^{(1)} + w_{12}^{(2)}} = e^{-\beta\varepsilon}, \quad (5.3)$$

guaranteeing that thermal equilibrium is reached in the long time limit [22].  $\varepsilon = E_{\min}^1 - E_{\min}^2$  is a measure of the asymmetry of the energy function as depicted in Fig. 5.1.

Taking into account the normalization condition  $P_1 + P_2 = 1$ , one can easily solve Eq. (5.1) for  $P_1$ :

$$\begin{aligned} P_1(t) &= \frac{w_{21}^T}{W} - \frac{w_{12}^T}{W} e^{-tW} \\ P_2(t) &= 1 - P_1(t), \end{aligned} \quad (5.4)$$

where  $W = w_{12}^T + w_{21}^T$ . After substituting  $w_{ij}$  this becomes

$$\begin{aligned} P_1 &= \frac{1 - e^{\beta\varepsilon} e^{-t/\tau}}{1 + e^{\beta\varepsilon}} \\ P_2 &= \frac{e^{\beta\varepsilon}(1 + e^{-t/\tau})}{1 + e^{\beta\varepsilon}}. \end{aligned} \quad (5.5)$$

where  $\tau$  is the characteristic relaxation time of the system that takes into account all possible channels of jump

$$\begin{aligned} \tau^{-1} \equiv W &= \sum_{k,i \neq j} \frac{1}{\tau_{ij}^k} \\ &= \tau_0^{-1} \left( e^{-\beta E_b^{22}} + e^{-\beta E_b^{12}} \right) \left( e^{1+e^{\beta\varepsilon}} \right). \end{aligned} \quad (5.6)$$

The time-dependence of the system is thus characterized by an exponential function with a single relaxation time  $\tau$  that takes into account all possible probability fluxes

$$\begin{aligned} \tau^{-1} \equiv W &= \sum_{k,i \neq j} \frac{1}{\tau_{ij}^k} \\ &= \tau_0^{-1} \left( e^{-\beta E_b^{22}} + e^{-\beta E_b^{12}} \right) \left( 1 + e^{\beta\varepsilon} \right). \end{aligned} \quad (5.7)$$

As we see,  $\tau$  is dominated by the lowest energy barrier  $E_b^{22}$ , but with non-negligible pre-factors that take into account the possibility of recrossing from the equilibrium to the metastable state and the two different

possibilities of jumping. Notice that this two prefactors are often neglected in theoretical studies of the dependence of the blocking temperature with the field [23] and Monte Carlo simulations [19, 24]. This is due to the fact that, usually, the possibility of jumping between minima by any of the two channels is not considered. However, at small non-zero fields ( $\varepsilon \gtrsim 0$ ), and for particles oriented at  $\psi \neq 0$ , they can be equally relevant. This expression reduces to the usual one

$$\tau^{-1} = \tau_0^{-1} e^{-\beta E_b^{22}} \quad (5.8)$$

when the energy function is symmetric ( $\varepsilon = 0$ ) and there is only one energy barrier, except for a factor 4 that can be absorbed in the definition of the prefactor  $\tau_0$ .

The time dependence of the magnetization of the particle is then finally given by:

$$\begin{aligned} m(t; K, \psi) &= \cos[\theta_{\min}^1(\psi)]P_1(t) + \cos[\theta_{\min}^2(\psi)]P_2(t) \\ &= \bar{m}_{TS}(K, \psi) + [m_0 - \bar{m}_{TS}(K, \psi)]e^{-t/\tau(K, \psi)}. \end{aligned} \quad (5.9)$$

In this equation,  $\bar{m}_{TS}(K, \psi)$  is the equilibrium magnetization in the TSA [Eq. (2.36)], that has already been calculated in subsection 2.7, and  $m_0$  is the initial magnetization. If we have an ensemble of randomly oriented particles and a distribution of anisotropy constants  $f(K)$ , then the relaxation law of the magnetization is given by

$$m(t) = \int_0^\infty dK f(K) \int_0^\pi d\psi m(t; K, \psi). \quad (5.10)$$

This will be the starting point for all the subsequent numerical calculations of the relaxation curves and magnetic viscosity.

## 5.2 Numerical calculations

### 5.2.1 Relaxation curves: $T \ln(t/\tau_0)$ scaling and normalization factors

In this section, we present the results of numerical calculations of the magnetization decay based on Eq. (5.10) for a system of particles with logarithmic-linear distribution of anisotropy constants and random orientation of the easy-axis. For the sake of simplicity we have assumed zero initial magnetization  $m_0 = 0$ , so particles have initially their magnetic moments at random and evolve towards the equilibrium state  $m_{eq}$ . In the following, we will use dimensionless reduced variables for temperature and time defined as:  $T/T_0$  and  $t/\tau_0$  with  $T_0 = E_0/k_B$  where  $E_0$  is the value of the energy at which  $f(K)$  is centered.

We have assumed that the magnetic moment of each particle is independent of the volume although in fact it can be proportional to it but this effect can be easily accounted by our model by simply changing  $f(K)$  by  $Kf(K)$  in all the expressions. For the case of a logarithmic-linear distribution this change does not qualitatively change the shape of the distribution.

Other works [25, 26, 27] consider also a distribution of anisotropy fields  $H_c$  due to the spread of coercive fields in some real samples but they study only relaxation on zero applied field. Here we have preferred to distribute  $K$  and the easy-axes directions, which has a similar effect, in order to separate as much as possible the effects of an applied magnetic field from other effects that may lead to non-conclusive interpretation of the results.

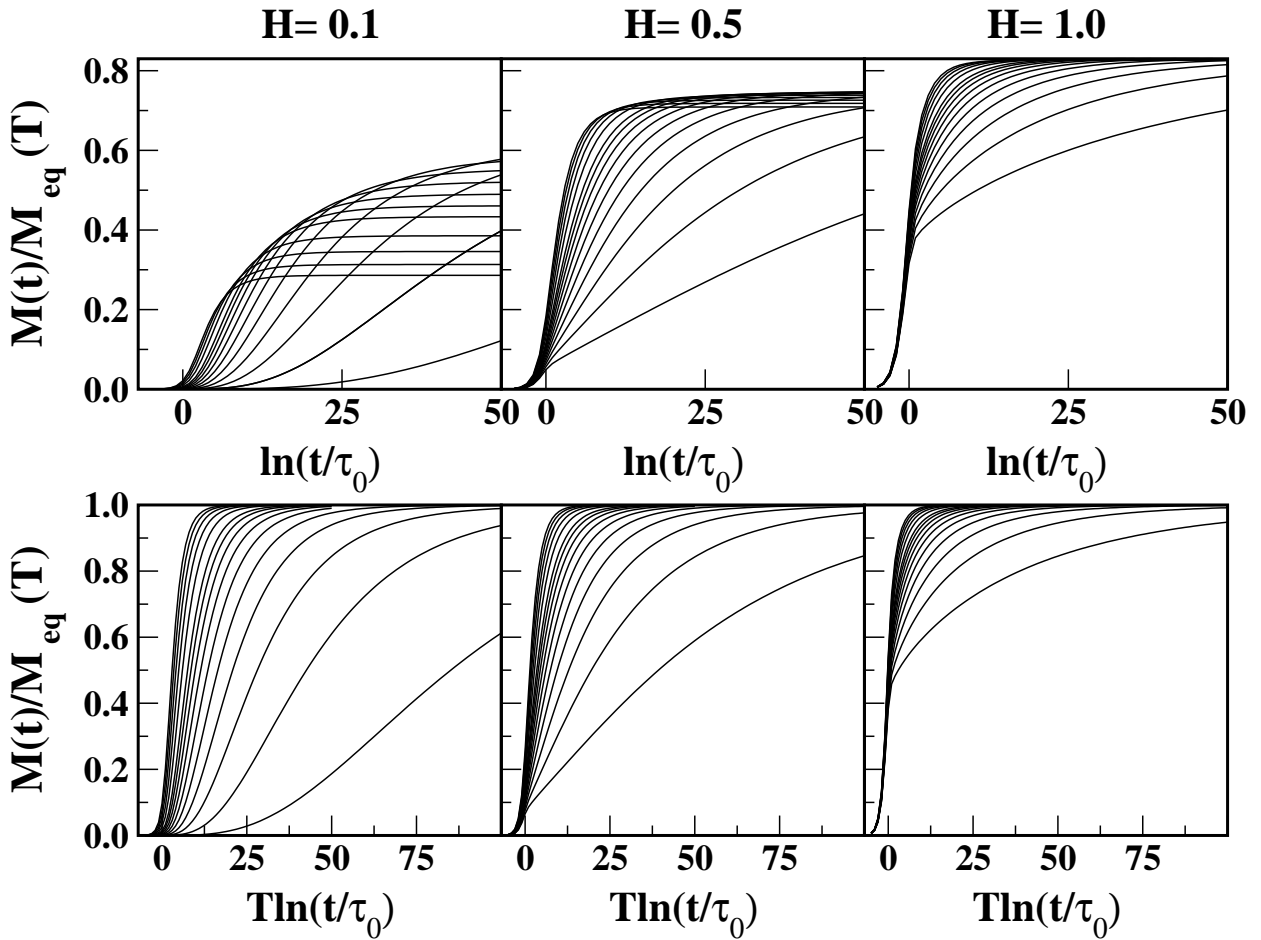


Figure 5.2: Relaxation curves for an ensemble of particles with randomly oriented anisotropy axes and a logarithmic-normal distribution of anisotropies  $f(K)$  of width  $\sigma = 0.5$  and  $K_0 = 1$  calculated by numerical integration of Eq. (5.10). The initial magnetization has been set to  $M_0 = 0$ . Reduced temperatures  $T/T_0$ , starting from the lowermost curve, range from 0.01 to 0.1 with 0.01 increments, and from 0.1 to 0.2 with 0.02 increments. The applied fields are  $H = 0.1, 0.5, 1.0$  as indicated. The upper panels show the original relaxation curves in logarithmic scale. In the lower panels, the same curves have been normalized to the equilibrium magnetization  $m_{TS}(T)$  given by Eq. (2.39).



In Fig. 5.2, we show the results of the numerical calculations for a system with  $\sigma = 0.5$  for three different fields  $H = 0.1, 0.5, 1.0$  and temperatures ranging from 0.02 to 0.2. In the upper panels, we present the original relaxations, while in the lower ones, the same curves have been normalized to the equilibrium magnetization given by Eq. 2.39. As it is clearly seen from comparison of the upper and lower rows of figures, normalization is essential in order to compare relaxations at different temperatures, especially at low fields where the temperature dependence of the equilibrium magnetization is more pronounced.

Our next goal is to show that, in the spirit of the previous chapter [28], in spite of the presence of an applied magnetic field, it is still possible to scale the relaxation curves at different temperatures so that they superimpose when plotted as a function of the  $T \ln(t/\tau_0)$  variable. For this purpose, in Fig. 5.3 we show the relaxation curves of Fig. 5.2 as a function of the scaling variable  $T \ln(t/\tau_0)$ . According to Eq. (4.28) [28], in absence of a magnetic field, scaling should be valid up to temperatures such that  $Te$  is of the order of  $\sigma$ . Instead, we observe in Fig. 5.3 that the higher the field the higher the temperature until which the scaling

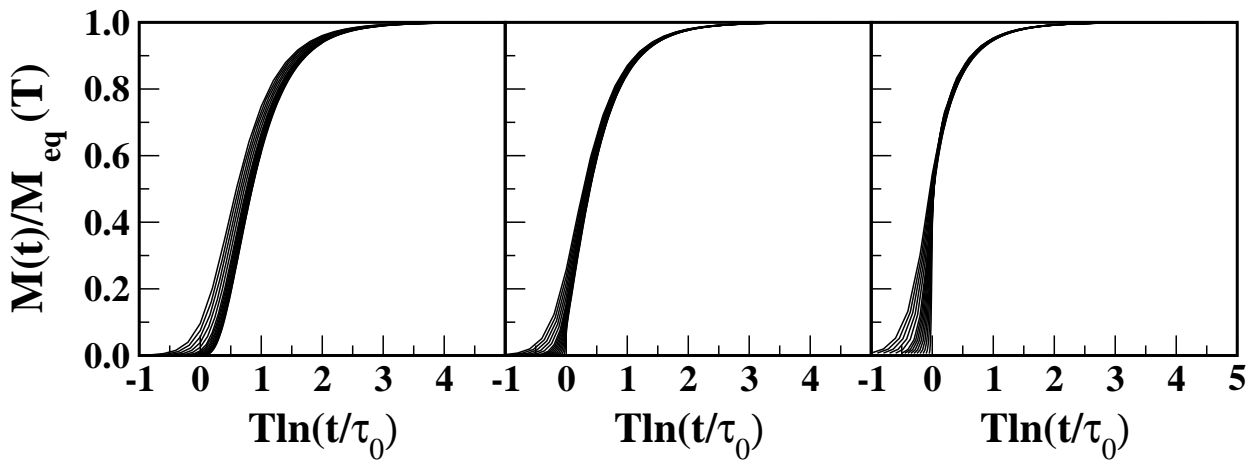


Figure 5.3: Master relaxation curves obtained from the normalized relaxation curves of the lower panels of Fig. 5.2 by the multiplicative scaling factor  $T$ . The corresponding magnetic fields are  $H = 0.1, H = 0.5, H = 1.0$  from left to right.

law is valid. This observation holds independently of the value of  $\sigma$ , indicating that it is a consequence of the application of a magnetic field.

This can be understood with the help of the effective energy barrier distribution introduced in Sec. 2.5. As it was shown in Fig. 2.11,  $h$  widens  $f_{\text{eff}}(E)$  and shifts the lowest energy barriers towards the origin, giving rise to a subdistribution of almost zero energy barriers that narrows with  $h$ , and, consequently, the requirements for  $T \ln(t/\tau_0)$  scaling are worse fulfilled at small  $T \ln(t/\tau_0)$  values. On the contrary, as we will show in the next subsection,  $h$  broadens the high energy tail of energy barriers that contribute to the relaxation,  $f(E_b^{22})$ , improving the scaling requirements at large  $T \ln(t/\tau_0)$  values.

### 5.2.2 Scaling of relaxation curves at different magnetic fields

Another interesting point is the possibility of finding an appropriate scaling variable to scale relaxation curves at different fields for a given  $T$ , in a way similar to the case of a fixed field and different temperatures, in which  $T \ln(t/\tau_0)$  is the appropriate scaling variable. In a first attempt, we will study the effect of  $h$  on a system with random anisotropy axes and the same  $K = 1$ .

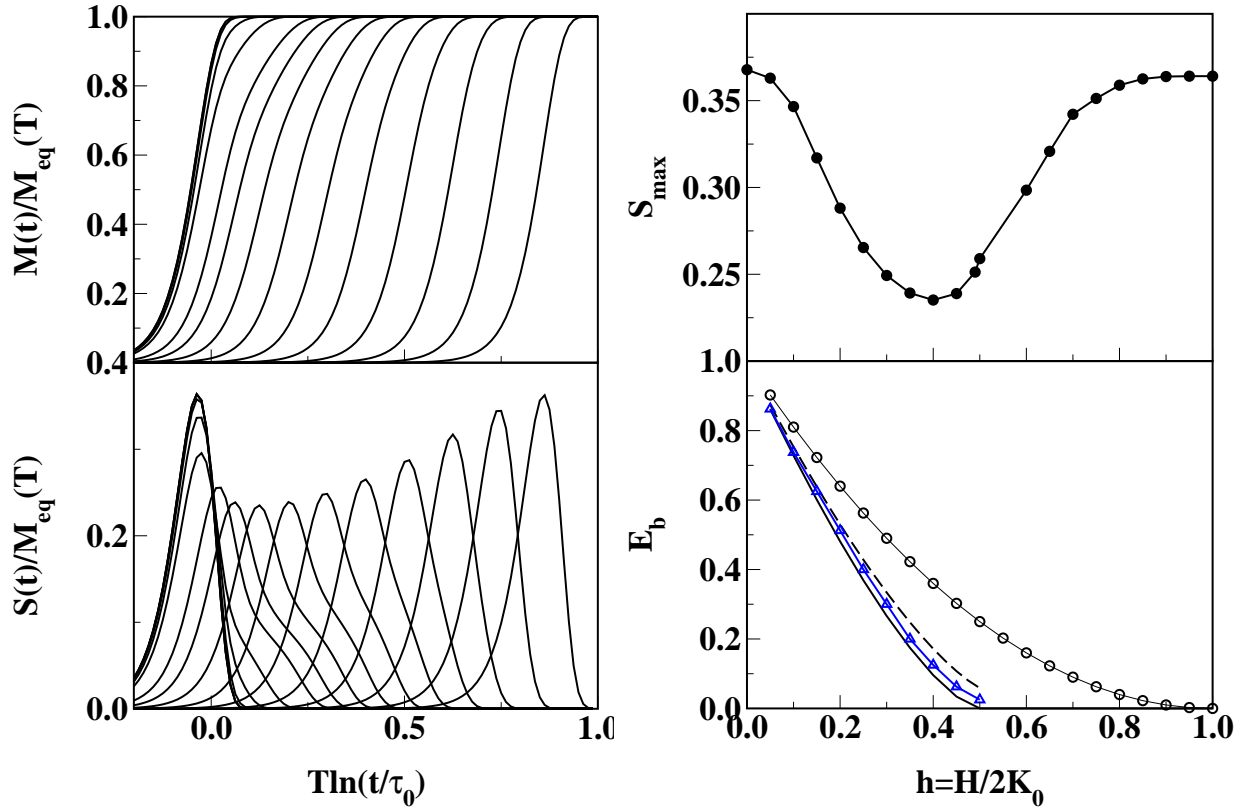


Figure 5.4: Left panels: (a) Low temperature ( $T = 0.05$ ) relaxation curves for a system of randomly oriented particles with the same anisotropy constant  $K_0 = 1$ . The curves have been normalized to the equilibrium magnetization  $M_{eq}(T)$  and correspond to magnetic fields  $H = 0.1, 0.2, \dots, 1.0, 1.2, 1.4, 1.6, 1.8, 2.0$  increasing from right to left. (b) Viscosity curves corresponding to the relaxations given above calculated by performing the time derivative. Right panels: (a) Field dependence of the time corresponding to the maximum relaxation rate,  $T \ln(t_{max}/\tau_0)$ , as derived from the viscosity curves of panel (b) (triangles). The field dependence of the mean lowest energy barrier  $E_{av}^{(2,2)}$  (continuous line), lowest energy barrier for particles oriented at  $\psi = 45^\circ$ ,  $E^{(2,2)}(\pi/4)$  (dashed line) and  $\psi = 0$  (circles),  $E^{(2,2)}(0^0)$  are also shown for comparison. (b) Field dependence of the maximum relaxation rate  $S_{max}$ .

### Randomly oriented particles with $K = 1$

We have calculated the relaxation curves for this system at  $T = 0.05$  and several values of the field. The obtained curves have been normalized to the equilibrium magnetization as given by Eq. (2.39).

The effect of  $h$  on  $M(t)$  is better understood in terms of the logarithmic time derivative of  $M(t)$

$$S(t) = \frac{dM}{d(\ln(t))} = - \int_0^\pi d\psi \left(\frac{t}{\tau}\right) e^{-\frac{t}{\tau}}, \quad (5.11)$$

which is the so-called magnetic viscosity  $S(t)$ . As can be clearly seen from Fig. 5.4b, the viscosity curves at different  $h$  cannot be scaled neither by shifting them in the horizontal axis, nor by multiplicative factors, since the high and low field curves have different shapes. As soon as the field starts to destroy some of the energy barriers ( $h \geq 0.5$ ), the qualitative form of the relaxation changes. This fact hinders, in principle, finding a field dependent scaling variable, valid in all the range of fields, in systems of non-aligned particles. Nevertheless, even though viscosity curves are qualitatively different at different fields, all of them present a well-defined maximum corresponding to the inflection point of the relaxation curves. This maximum appears at a time  $t_{max}$  and it is associated to a certain energy barrier of the system  $E_{max} = T \ln(t_{max}/\tau_0)$  that decreases with increasing magnetic fields for a given temperature. This barrier is approximately equal to the averaged lowest energy barrier of the particles ( $E^{22}$  in the notation of Sec. 2.2) and this value is nearer from the lowest possible barrier (corresponding to particles oriented at  $\psi = 45^\circ$ ) than from the barrier of a particle aligned with the field.

In Fig. 5.4d, we have plotted the field dependence of all this quantities, together with the position of the maximum of the viscosity in energy units  $E_{max}$ , and in Fig. 5.4e the value of the corresponding viscosity  $S_{max}$ . The reduction of  $t_{max}$  with  $h$  can be understood in terms of the progressive reduction of the energy barriers by  $h$ . At  $h = 0$ , the barriers are independent of the orientation of the particle and equal to 1 so that the maximum is placed at  $E_{max} = 1$  and  $S_{max} = 1/e$  according to (5.11)

For  $h \geq 0.5$  (the critical field for particles oriented at  $\psi = 45^\circ$ ), the lowest energy barriers start to be destroyed by  $h$  and consequently the relaxation rates peak at  $E_{max} = 0$  with an increasing  $S_{max}$  value that increases as more particles loose their barriers. For  $h \geq 1$  all barriers have been destroyed and relaxations become field independent, with  $E_{max} = 0$  and  $S_{max} = 1/e$ . For fields up to  $h = 0.5$ , the variation of  $E_{max}$  and  $S_{max}$  with  $h$  can be used to scale the magnetic relaxation curves at constant  $T$  and different  $h$ . Therefore, although in this case the inflection points of the relaxation curves could be brought together by shifting them in the  $T \ln(t/\tau_0)$  axis in accordance with the variation of  $E_{av}^{22}$ , the full scaling cannot be accomplished because of the complicated variation of  $S_{max}$  (see Fig. 5.4c).

### Random oriented particles with $f(K)$

In spite of the lack of scaling of the preceding case, in what follows, we will demonstrate that the inclusion of a distribution of  $K$ , always present in experimental systems, allows to scale the relaxation curves for a wide range of  $h$ .

Let us consider a logarithmic-linear distribution of anisotropy constants of width  $\sigma$ , Eq. (2.22). Low temperatures relaxation rates corresponding to  $\sigma = 0.2, 0.5$  are presented in Fig. 5.6. In this case, the qualitative shape of the viscosity curves is not distorted by  $h$ . It simply shifts the position of the maxima towards lower values of  $T \ln(t/\tau_0)$  and narrows the width of the peaks, being these effects similar for both studied  $\sigma$ .

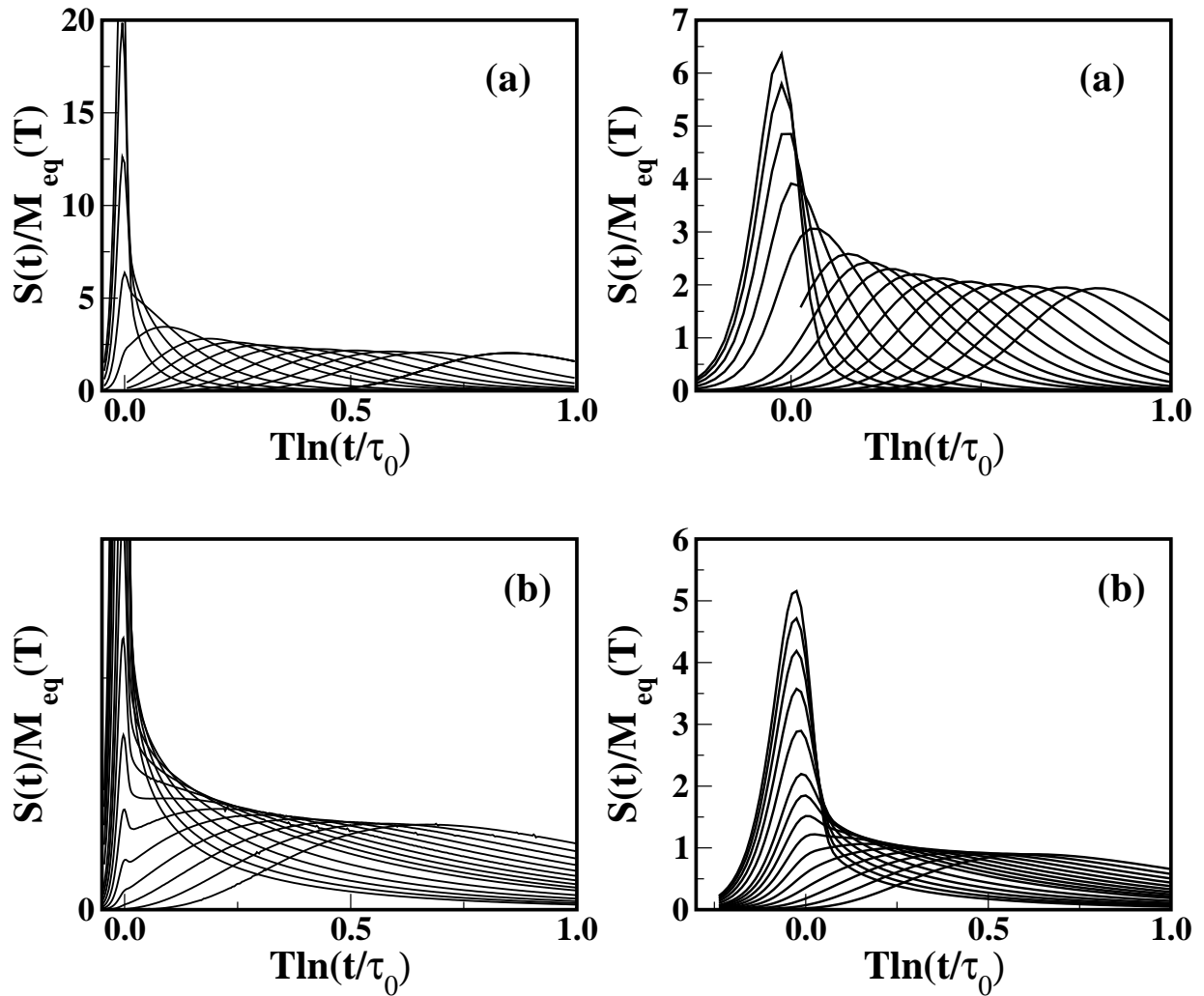


Figure 5.5: Low temperature (left panels:  $T = 0.01$ , right panels:  $T = 0.05$ ) viscosity curves for a system of aligned particles and logarithmic-normal distribution of anisotropies with (a)  $\sigma = 0.2$  and (b)  $\sigma = 0.5$ . The curves have been normalized to the equilibrium magnetization and correspond to magnetic fields  $H = 0.1$  to 1.0 in 0.1 steps and  $H = 1.2$  to 2.0 in 0.2 steps starting from the right.

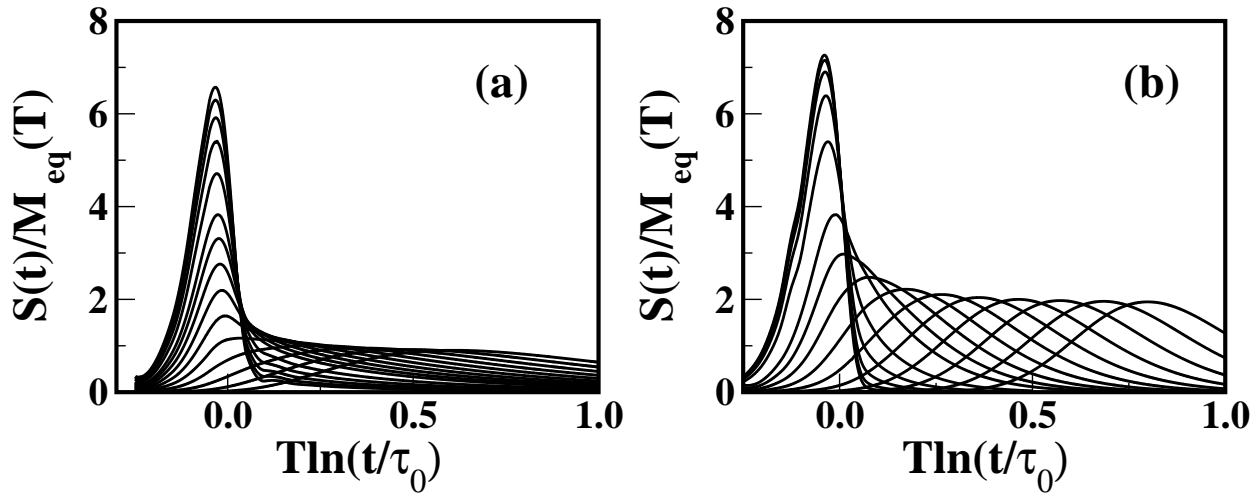


Figure 5.6: Low temperature  $T = 0.05$  viscosity curves for a system of randomly oriented particles and logarithmic-normal distribution of anisotropies with (a)  $\sigma = 0.2$  and (b)  $\sigma = 0.5$ . The curves have been normalized to the equilibrium magnetization and correspond to magnetic fields  $H = 0.1$  to  $1.0$  in  $0.1$  steps and  $H = 1.2$  to  $2.0$  in  $0.2$  steps starting from the right.

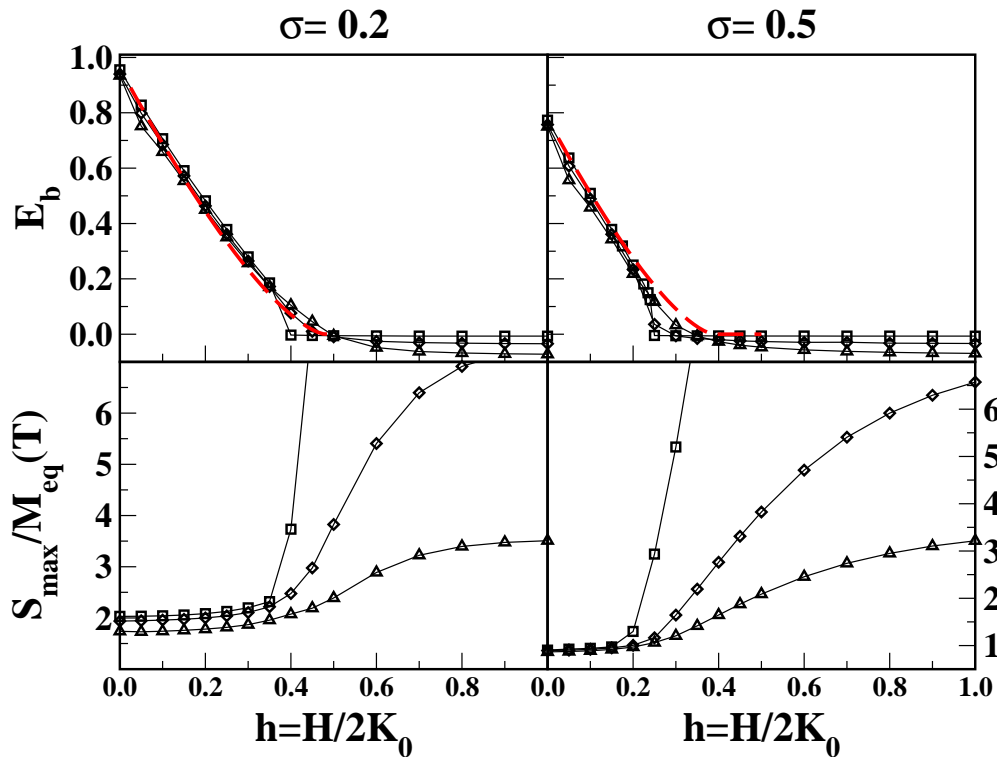


Figure 5.7: Upper panels: Field dependence of the energy corresponding to the maximum relaxation rate,  $T \ln(t_{max}/\tau_0)$ , as derived from the viscosity curves in Fig. 5.6 for temperatures  $T = 0.01$  (circles),  $0.05$  (squares),  $0.1$  (diamonds). The dashed lines indicate the field dependence of the lowest energy barriers for particles oriented at  $\psi = \pi/4$  and  $K = K_{max}$ . Lower panels: Field dependence of the maximum relaxation rate  $S_{max}$  for the same curves and temperatures. Left column is for  $\sigma = 0.2$  and the right one for  $\sigma = 0.5$ .

As in the preceding case,  $E_{\max}$  goes to zero when  $h$  starts to destroy the lowest energy barriers. The difference is now that, due to the spread of the anisotropy constants, lower fields  $h_0$  are needed to start extinguishing the lowest energy barriers (see Fig. 5.7), being this reduction greater, the greater  $\sigma$  is, since the most probable anisotropy constant [ $K_{\max}=K_0 \exp(-\sigma^2/2)$ ] becomes smaller and, consequently,  $E_{\max}$  drops to zero at smaller  $h_0$ . This field corresponds to the one for which  $f_{\text{eff}}(E_b^{22})$  starts to develop a peak corresponding to zero energy barriers. As in the preceding case, we have also tried to identify the variation of  $E_{\max}$  with the microscopic energy barriers of the system. As can be clearly seen in the dashed lines of the upper panels of Fig. 5.7, the  $h$  dependence of  $E_{\max}$  follows that of the lowest energy barriers for particles oriented at  $\psi = \pi/4$  and with  $K = K_{\max}$ .

By looking in detail the  $T = 0.01$  relaxation curves (left panels in Fig. 5.7), we have observed that two relaxation regimes can be distinguished. One presents a broad peak in  $S$  at relatively high energies (long times) with a maximum at an  $E_{\max}$  which varies as the lowest energy barrier at  $\psi = \pi/4$ , this is clearly visible at the lowest  $h$  values even for the  $T = 0.05$  case of Fig. 5.6. The other regime presents a peak around  $E = 0$  that starts to develop as soon as  $h$  breaks the lowest energy barriers. What happens is that the first peak shifts towards lower energies with  $h$ , at the same time that the relative contribution of the second peak increases, the global effect being that, at a certain  $h$ , the contribution of the first peak has been swallowed by the second because at high  $h$  and low  $T$ , relaxation is driven by almost zero energy barriers.

To clarify this point, we show in Fig. 5.8  $S(t)/T$  for three different temperatures and magnetic fields  $H = 0.1, 0.5, 1.0$  for a narrow ( $\sigma = 0.2$ , upper panels) and a wide ( $\sigma = 0.5$ , lower panels) distribution. The effective distribution of lowest energy barriers  $f_{\text{eff}}(E^{22})$ , already calculated in Fig. 2.11, is also plotted as a continuous line. We observe that for a narrow distribution, at low enough  $T$ ,  $S(t)/T$  coincides with  $f_{\text{eff}}(E^{22})$  independently of  $h$ , demonstrating that only the lowest energy barriers of the system contribute to the relaxation. Finally, let us also notice that, at difference with the preceding case,  $S_{\max}$  becomes almost constant below  $h_0$  (lower panels in Fig. 5.8) and low enough  $T$ , so that now the relaxation curves at different  $h$  and fixed  $T$  may be brought to a single curve by shifting them along the  $T \ln(t/\tau_0)$  axis in accordance to the  $E_{\max}$  variation. The resulting curves are displayed in Fig. 5.9 for  $\sigma = 0.2, 0.5$ . They are the equivalent of the master curves of Fig. 5.3 for a fixed  $h$  and different  $T$ . Now the appropriate scaling variable is

$$E_{\text{sca}} = T \ln[t/t_{\max}(h)] , \quad (5.12)$$

which generalizes the scaling at fixed  $T$ . This new scaling is valid for fields lower than  $h_0$ , the field at which the lowest barriers start to be destroyed and above which the relaxation becomes dominated by almost zero energy barriers. Thus, as already discussed in the previous paragraphs, the wider  $\sigma$ , the smaller the  $h$  range for the validity of field scaling.

### 5.3 Normalization factors for the relaxation curves

In this section, we will study how the theoretical program previously outlined can be implemented to analyze real relaxation data.

In the study of time dependent processes in small particles systems two kind of experiments (which will be called type A and B) can be distinguished according to what is the final equilibrium state of the system. In Type A experiments the system evolves towards a demagnetized state in zero applied field after a previous cooling in the presence of a field  $H$  (FC process) and the variation of the thermoremanent magnetization (TRM) is measured. If  $t$  is the time elapsed after the field was reduced to zero then, in the

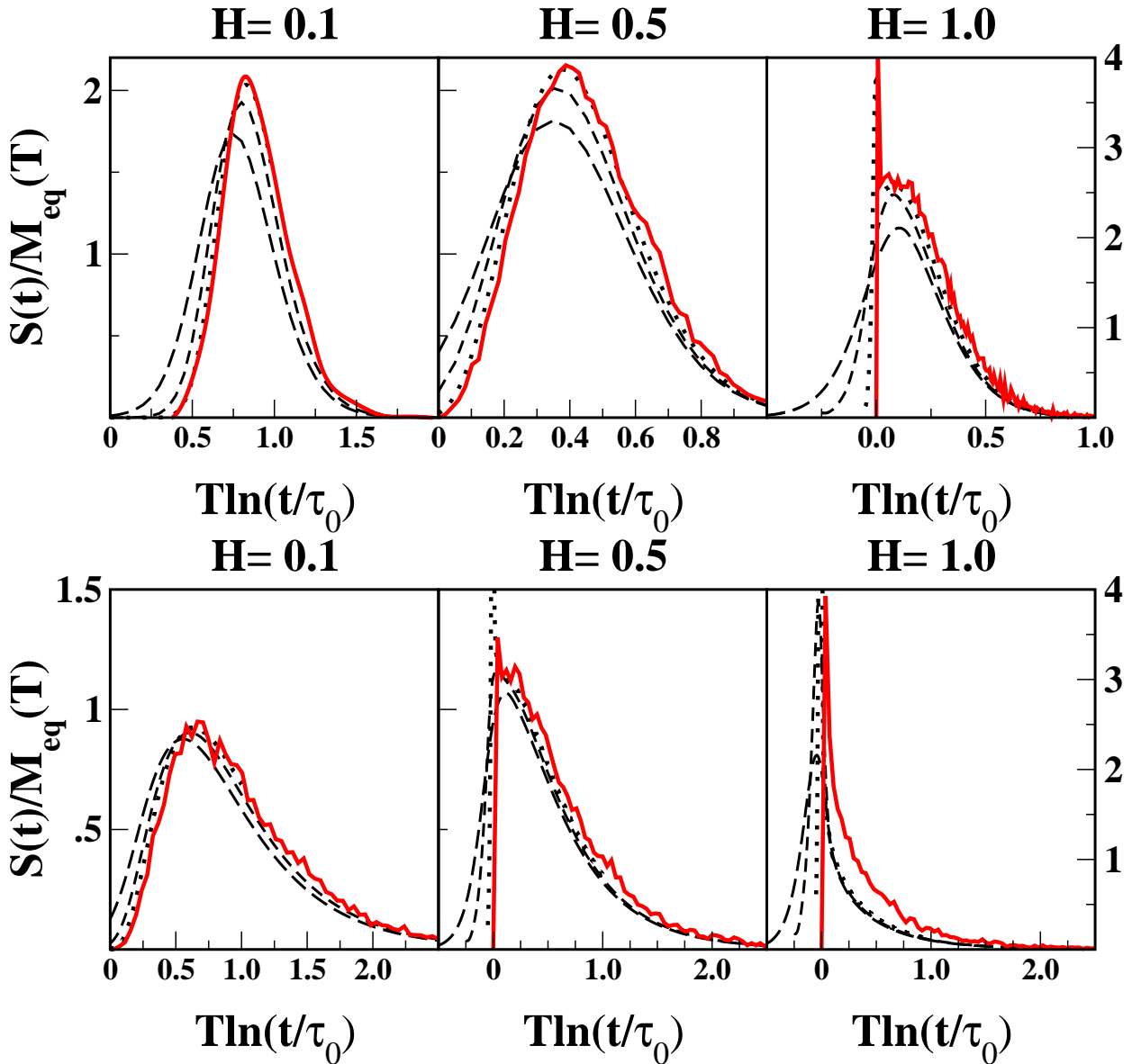


Figure 5.8: Relaxation rates as a function of the scaling variable  $T \ln(t/\tau_0)$  for different temperatures [ $T = 0.01$  (dotted line),  $0.05$  (dashed line),  $0.1$  (long-dashed line)],  $\sigma = 0.2$  (upper panels),  $\sigma = 0.5$  (lower panels) and three magnetic fields (a)  $H = 0.1$ , (b)  $H = 0.5$ , and (c)  $H = 0.8$ . The curves tend to the effective distribution of lower energy barriers  $f_{eff}(E^{22})$ , shown as a continuous line, as  $T$  decreases.

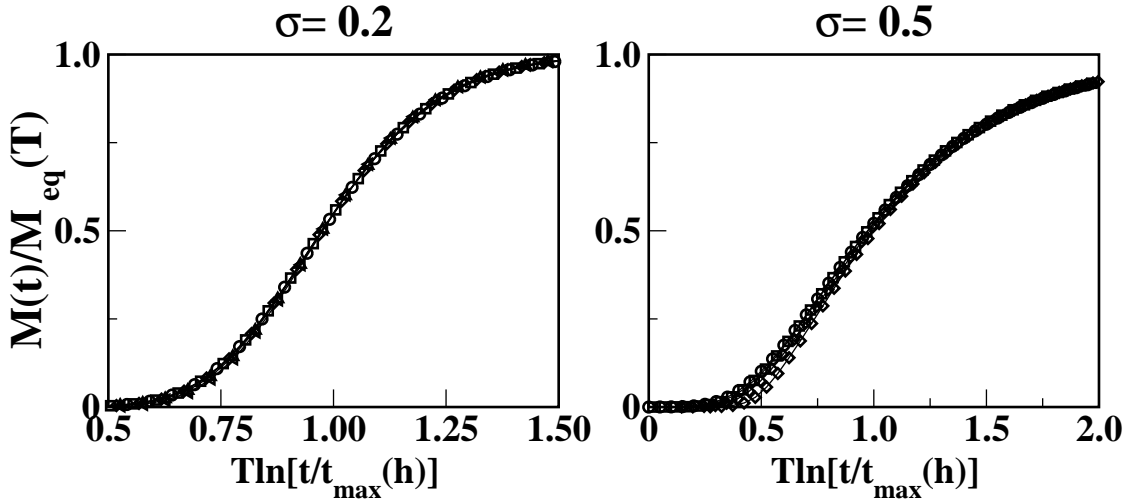


Figure 5.9: Normalized relaxation curves as a function of the scaling variable  $T \ln[(t/t_{max}(h))]$  for  $T = 0.05$ , obtained from Fig. 5.3 by shifting the curves in the horizontal axis with the position of the maximum relaxation rate (upper panels in Fig. 5.7). Left:  $\sigma = 0.2$  and  $H = 0.1, 0.2, 0.3, 0.4, 0.5$ ; Right:  $\sigma = 0.5$  and  $H = 0.1, 0.2, 0.3, 0.4$  (starting from the uppermost curve)

critical volume approximation [29]:

$$\begin{aligned}
 M_{TRM}(T, H, t) &= \int_{E_c(T,t)}^{\infty} dE M_{FC}(E) f(E) \\
 &\simeq M_{FC}(T, H) \int_{E_c(T,t)}^{\infty} dE f(E).
 \end{aligned} \tag{5.13}$$

where  $E_c$  is the critical energy barrier  $E_c(T, t) = T \ln(t/\tau_0)$  which indicates the onset of superparamagnetic (SP) behaviour.

In Type B experiments a zero-field cooled (ZFC) sample increases its magnetization in a magnetic field  $H$  and the variation of the isothermal remanent magnetization (IRM) is measured. In the critical volume approximation the time dependence of the magnetization is given in this case by [29]:

$$\begin{aligned}
 M_{IRM}(T, H, t) &= \int_0^{E_c(T,t,H)} dE M_{eq}(E) f(E) \\
 &\simeq M_{eq}(T, H) \int_0^{E_c(T,t,H)} dE f(E).
 \end{aligned} \tag{5.14}$$

In order to compare relaxation curves measured at different temperatures it is necessary to remove the thermal dependence of the initial and final states of the magnetization. It is clear from Eq. 5.13 and 5.14 that, due to the fact that in both expressions the integrals are bounded between 0 and 1, this can be simply achieved by dividing magnetization data by a normalization factor which in Type A experiments is  $M_{FC}(T, H)$  and in Type B is  $M_{eq}(T, H)$ .

In Type A experiments, the normalization factor,  $M_{FC}(T)$ , in (5.13) comes from the contribution of the blocked particles to the initial magnetization or, in other words, from the irreversible component of the FC magnetization at the temperature  $T$ . In many small particle systems at low  $T$  this quantity can be considered



as a constant in the range of temperatures usually studied [30]. In fact, when one represents the relaxation data as a function of the scaling variable  $T \ln(t/\tau_0)$  all the curves recorded at different temperature usually superimpose onto a unique master curve without any normalization factor [28].

In contrast, in Type B experiments the magnetic field is not zero and SP particles have a temperature dependent contribution to the magnetization while blocked particles are randomly oriented giving no net contribution to the magnetization in the field direction.

Now the reversible component of the ZFC magnetization gives the main contribution to the normalization factor,  $M_{eq}(T)$ . In many cases, at low fields,  $M_{eq}(T)$  follows a Curie-Weiss law and cannot be considered as a constant. The need of this temperature dependent normalization factors is clearly manifested as a vertical shift of the curves when data are represented in a  $T \ln(t/\tau_0)$  scaling plot.

## 5.4 Experimental verification

The studied sample is a ferrofluid composed of  $\text{Fe}_3\text{O}_4$  small particles with volume packing fraction  $\epsilon = 0.01$  which was obtained from chemical deposition of  $\text{Fe}^{+2}$  and  $\text{Fe}^{+3}$  sulfides and dispersed in an hydrocarbon oil. The sample analyzed by transmission electron microscopy (TEM) was prepared by wetting a carbon film mounted on an Au grid with the ferrofluid and subsequently drying it with air.

In Fig. 5.10 an electron micrograph of the magnetic particles is shown. Taking a sampling of 200 particles and considering them spherical, the particle size distribution have been fitted to a logarithmic-normal function with  $\sigma = 0.24$  and mean particle diameter of about 4 nm (see inset of Fig. 5.10).

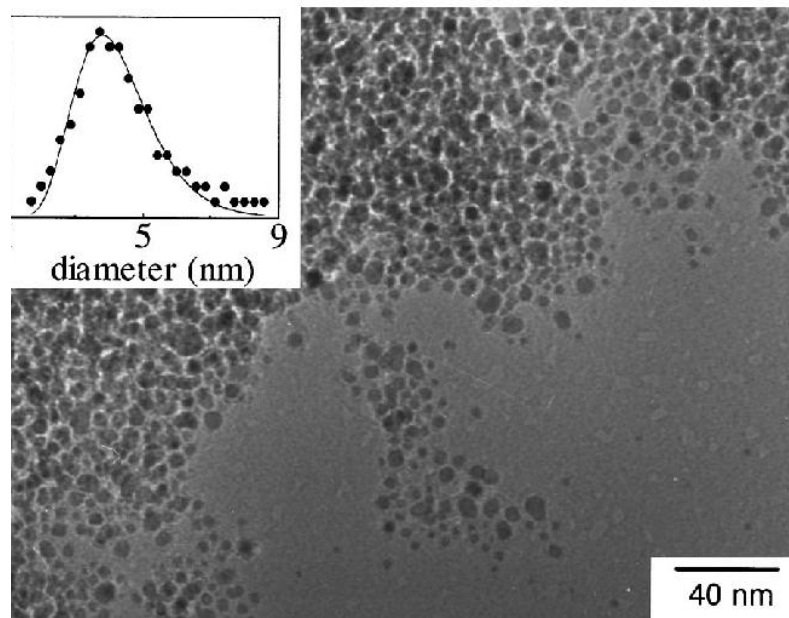


Figure 5.10: Electron micrography of the sample obtained by TEM. The inset shows the distribution of particle diameters obtained from a sampling of 200 particles. The solid line is a logarithmic-normal function with  $\sigma = 0.24$  and mean particle diameter of about 4 nm.

The magnetic relaxation curves at different temperatures were recorded with a SQUID magnetometer following the procedure described in Ref. [31]. The measurements were started 5 s after applying the field and were performed during approximately 1000 s at the lowest temperature and approximately 10000 s at the highest temperature. The relaxation curves after ZFC the system were measured in the presence of a magnetic field of 10 Oe (type B experiment) while in those measured in zero field the system was previously FC in 10 Oe (type A experiment). In the following, we will describe an experimental procedure, based on the  $T \ln(t/\tau_0)$  scaling method [28], to obtain normalization factors,  $M_{eq}(T)$ , for relaxation data recorded in the presence of a field since they cannot be directly measured due to the long-time decay of the magnetization.

First, the attempt time  $\tau_0 = 3 \times 10^{-11}$  s has been evaluated by scaling the relaxation curves in zero field after FC the system at several temperatures following the method previously described in Chapter 3.6 (see also Ref. [28]). For this purpose, we have considered that the initial magnetization  $M_{FC}(T, H)$  is constant in the temperature range of the experiment so no normalization factors are needed to scale the curves. We will assume that the field variation of  $\tau_0$  is smaller than the error in its determination at low fields, according to Brown's theory [32]. In the next step, relaxation data recorded in the presence of a field have been plotted as a function of the scaling variable using the value of  $\tau_0$  previously deduced (see Fig. 5.11).

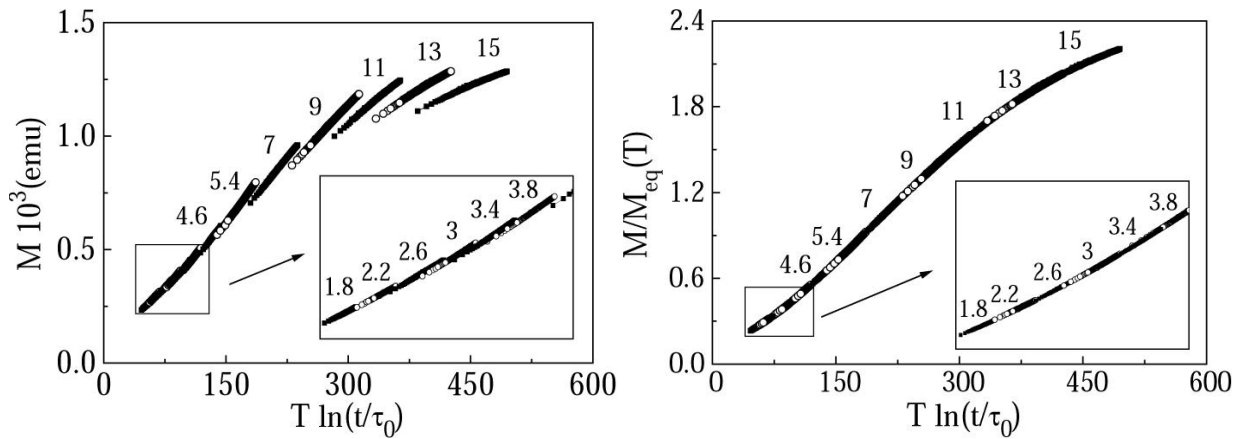


Figure 5.11: Left panel: Relaxation data recorded from 1.8 to 15 K in the presence of a magnetic field of 10 Oe after ZFC the sample as a function of the  $T \ln(t/\tau_0)$  scaling variable. Open and solid symbols correspond alternatively to the temperatures indicated. Inset: detail of the lowest temperature region. Right panel: Scaling plot for the relaxation measurements shown in the left panel Inset: detail of the lowest temperature region.

After this transformation the relaxation curves at different temperatures are separated along the vertical axis by temperature dependent shifts. Taking into account that the applied field is much lower than the anisotropy field and, therefore, the energy barriers have not been significantly affected, this lack of scaling is a clear demonstration that magnetization data must be normalized to achieve an equivalent scaling to that obtained in zero field. As has been discussed in Sec. 5.3, the normalization factors are proportional to  $M_{eq}(T, H)$ . If now we assume that  $M_{eq}(T, H)$  are given by  $M_{FC}(T, 10 \text{ Oe})$ , as suggested by some authors [33], no scaling is achieved because FC magnetization does not correspond to the true equilibrium state. Note that  $M_{eq}(T, H)$  can not be calculated without making any a priori hypothesis about the form of  $f(E)$  and the magnetic microstructure of the system.

The normalization factors can be found by referring the different curves to the lowest temperature one.

Once this process has been performed, the relaxation curves collapse onto a unique master curve that is shown in Fig. 5.11. The values of the normalization factors follow a Curie-Weiss law of the form

$$\chi \sim \frac{\bar{\mu}^2}{3k_B(T - T_0)}, \quad (5.15)$$

where  $T_0$  is due to the existence of interparticle interactions and/or the effect of  $f(E)$  [29]. In our case  $T_0 = -15 \pm 2$  K (see inset of Fig. 5.12). The extrapolation of this law superimposes with the susceptibility corresponding to the reversible (SP) region obtained from ZFC-FC measurements (see Fig. 5.12), reflecting the fact that, for long enough observation times, all the particles have become SP and demonstrating that the normalization factors are proportional to  $M_{eq}(T, H)$ .

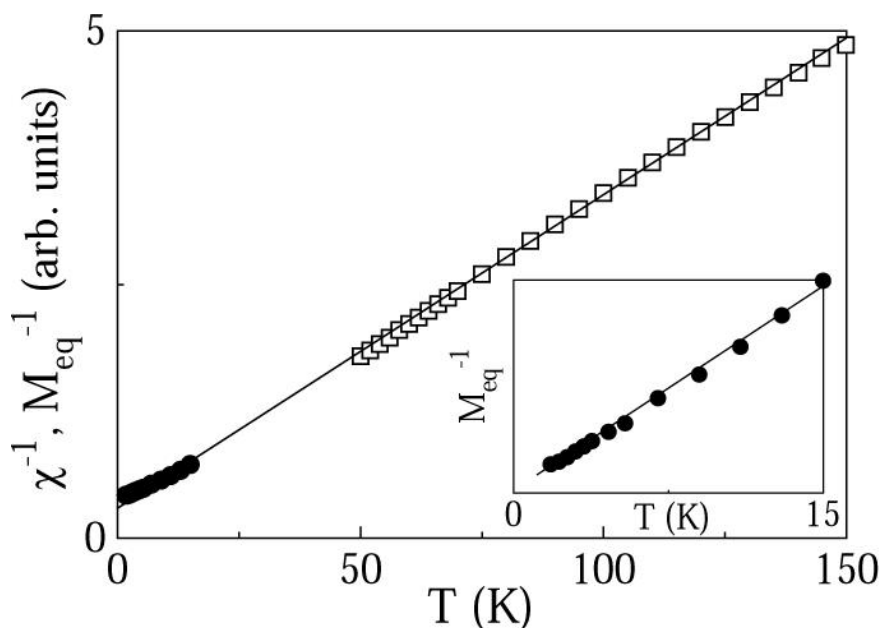


Figure 5.12: Reversible region of the reciprocal susceptibility (open squares) and thermal dependence of the inverse of the normalization factors (solid circles) necessary to join the relaxation data of Fig. 5.11 onto a unique master curve. Solid line is a linear regression of both data. Inset: inverse of the normalization factors as a function of the temperature. Normalization factors have been reduced to the same units of the susceptibility multiplying them by an arbitrary quantity.

## 5.5 Magnetic viscosity and energy barrier distribution

The classical magnetic viscosity commonly defined as  $S(t, T) = \partial M(t) / \partial(\ln t)$ , cannot be directly compared at different temperatures because: 1) usually magnetization is not normalized (initial and final states of the relaxation process change as the temperature varies) and 2) if relaxation data have been recorded in a fixed time window the energy barriers which are relaxing at different temperatures are not the same. Both problems can be circumvented by defining magnetic viscosity as  $\bar{S}(t, T) = \partial \bar{M}(t) / \partial(T \ln(t/\tau_0))$  ( $\bar{M}(t)$  is the normalized magnetization used in the scaling procedure). By performing the  $T \ln(t/\tau_0)$  derivative  $\bar{S}$  measures the relaxation rate of the magnetization due only to the energy barriers around  $T \ln(t/\tau_0)$ . On the other hand, as previously noted in Sec. 4.6.2,  $\bar{S}$  is a magnitude proportional to the energy barrier distribution and therefore it has a direct physical meaning.

These two magnitudes are simply related by

$$\bar{S} = \frac{S}{M_{FC}T} \quad (5.16)$$

in the case of type A relaxation experiments, and by

$$\bar{S} = \frac{S}{M_{eq}T} \quad (5.17)$$

for type B experiments. In the first case, and for systems with a certain degree of interaction between particles  $M_{FC}$  is usually almost temperature independent and both magnitudes differ by a  $T^{-1}$  factor. Therefore, conclusions from the thermal variation of  $S$  obtained from type A experiments must be carefully derived.

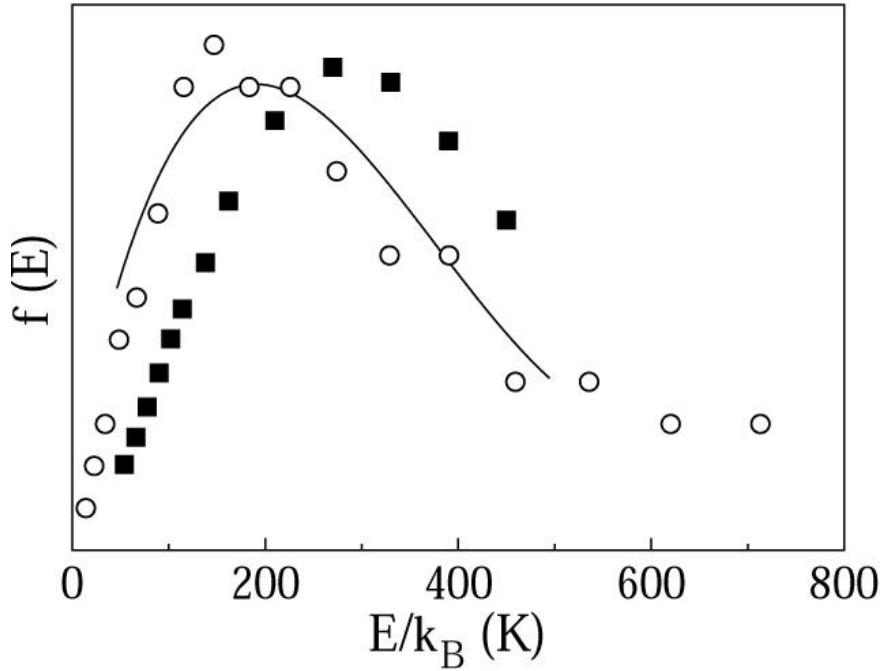


Figure 5.13: Effective distribution of energy barriers as obtained from the numerical derivative of the master relaxation curve (solid line). Magnetic viscosity  $S(T)$  as obtained from the logarithmic time derivative of the relaxation data at the temperatures indicated in Fig. 5.11 (solid squares). The energy distribution  $f(E)$  obtained from  $f(V)$  is also shown for comparison (open circles).

Note in particular that if  $S$  happens to be temperature independent in a certain range, a result which could be interpreted as a proof of the existence of quantum relaxation phenomena [34], this would be a consequence of an energy barrier distribution proportional to  $1/E$  in this range, as the  $\bar{S} \sim T^{-1}$  thermal dependence reveals. It is worth noticing that if there is not a certain degree of freezing due to magnetic interactions,  $M_{FC}$  can not be considered as a constant and its thermal variation must be corrected in  $S$ . However, in type B experiments, only if  $M_{eq}(T)$  is inversely proportional to the temperature (Curie law), as is the case for a sample with no or very small interparticle interactions and a narrow distribution of energy barriers [29], both magnitudes nearly coincide (note that this is not the case of the samples studied here) because the thermal variation of  $M_{eq}$  cancels the factor  $T$  in Eq. 5.17.

For the sample studied in this work  $\bar{S}(T \ln(t/\tau_0))$  has been obtained by performing the numerical derivative of the master curve of Fig. 5.11 and has been compared to the viscosity  $S(T)$  as obtained from the logarithmic derivative of the relaxation data at each temperature. The results are shown in Fig. 5.13 together

with the energy distribution obtained from the electron micrography by expressing the volume distribution in energy units with the help of the value of  $K$  previously derived. The coincidence between  $\bar{S}$  and  $f(E)$  shows the consistence of the normalization used in the scaling procedure for type B experiments. On the other hand, it is important to note that  $S$  does not coincide with  $\bar{S}$  because for this sample  $M_{eq}$  is not simply proportional to  $T^{-1}$ . Only the overall shape of the energy barrier distribution obtained from TEM is reproduced by  $S$ , but shifted to higher energies. Note also that the extrapolation of the quasi-linear low temperature regime of  $S$  intercepts the temperature axis at a non-zero value as has been reported in other systems [35, 36, 37]. In our case, this result is only a consequence of the lack of normalization and has no physical meaning.

## 5.6 Conclusions

We have proposed a model for the relaxation of small particle systems under a magnetic field which can be solved analytically and which allows to study the effect of the magnetic field on the energy barrier distribution. In particular, we have shown that the original  $f(E_b)$  is splitted into two subdistributions which evolve towards higher and lower energy values, respectively, as  $h$  increases. It is precisely the subdistribution of lowest energy barriers, the one that completely dominates the relaxation as it is evidenced by its coincidence with the relaxation rate at low  $T$ .

For fields smaller than the critical values for the smallest barriers, the relaxation curves at different  $h$  and fixed  $T$  can be collapsed into a single curve, in a similar way than  $T \ln(t/\tau_0)$  scaling for curves at fixed  $h$ . Whereas the latter allows to extract the barrier distribution by differentiation of the master curve [38], the shifts in the  $T \ln(t/\tau_0)$  axis necessary to produce field scaling, give the field dependence of the mean relaxing barriers, a microscopic information which cannot easily be inferred from other methods [33]. Moreover, we have stressed the importance of proper normalization whenever relaxation curves measured at different temperatures must be compared. In the case of experiments performed in zero field, care must be taken in systems for which  $M_{FC}(T)$  cannot be considered as a constant. When this is the case, non-normalization could give place to a spurious thermal dependence.

In the case of relaxation experiments performed in an applied magnetic field, there exists a certain controversy in the literature about the nature of the normalization : either no normalization factors are used at all [34, 39, 40] or the FC magnetization value, corresponding to the field at which the experiment is performed [1], is used. In systems for which the  $M_{eq}(T)$  follows a Curie law (non-interacting particles, neglectible  $T_0$ ) the first option happens to be correct by chance as can be easily seen in (5.17). In this kind of systems the second option is particularly wrong when applied to low temperature data because the FC magnetization is slightly temperature dependent while the SP magnetization, which is the true equilibrium state at long times, follows a  $T^{-1}$  behaviour. In fact, when  $T \ln(t/\tau_0)$  scaling is used to evidence quantum relaxation mechanisms through a lack of scaling of relaxation data (recorded in the presence of a field), no conclusions should be extracted without previously having tried to normalize data following the process described in Sec. 5.5. The sample studied in this Chapter is an example where a clear fail of scaling of the non-normalized data does not indicate any non-thermal process ( $\bar{S}$  agrees with the energy distribution deduced from  $f(V)$ , see Fig. 5.13). This does not mean that it is always possible to find scaling factors for data corresponding to low  $T$  if MQT occurs. If this is the case, even a multiplicative factor is not enough to superimpose relaxation curves obtained at different  $T$  ( $T$  is then an irrelevant parameter that would not have to be included in the scaling variable).

In conclusion, we have shown that the  $T \ln(t/\tau_0)$  scaling method provides a useful tool to obtain the

normalization factors and the energy barrier distribution in both kinds of experiments and even in systems that cannot be considered as an assembly of independent small particles (i.e. multilayered systems, cluster glasses, amorphous alloys, etc.) without making any assumptions about the nature of the magnetic microstructure.



## Bibliography

- [1] E. Vincent, J. Hammann, P. Prené, and E. Tronc, *J. Phys. I France* **4**, 273 (1994).
- [2] P. L. Kim, C. Lodder, and T. Popma, *J. Magn. Magn. Mater.* **193**, 249 (1999).
- [3] A. Lisfi, J. C. Lodder, P. de Haan, T. Bolhuis, and F. J. G. Roesthuis, *J. Magn. Magn. Mater.* **193**, 258 (1999).
- [4] I. D. Mayergoyz, A. Adly, C. Korman, M. Huang, and C. Krafft, *J. Appl. Phys.* **85**, 4358 (1999).
- [5] M. García del Muro, X. Batlle, and A. Labarta, *Phys. Rev. B* **59**, 13584 (1999).
- [6] L. Néel, *C. R. Acad. Sci. Paris* **228**, 664 (1949).
- [7] W. F. Brown Jr., *Magnetostatic Principles in Ferromagnetism* (North-Holland, Amsterdam, 1962).
- [8] W. T. Coffey, D. S. F. Crothers, Y. P. Kalmykov, E. Massawe, , and J. T. Waldron, *Phys. Rev. E* **49**, 1869 (1994).
- [9] J. T. Waldron, Y. P. Kalmykov, , and W. T. Coffey, *Phys. Rev. E* **49**, 3976 (1994).
- [10] D. A. Garanin, *Phys. Rev. E* **54**, 3250 (1996).
- [11] D. A. Garanin, *Phys. Rev. E* **55**, 2569 (1997).
- [12] H. Pfeiffer, *Phys. Stat. Sol. A* **118**, 295 (1990).
- [13] H. Pfeiffer, *Phys. Stat. Sol. A* **120**, 233 (1990).
- [14] H. Pfeiffer, *Phys. Stat. Sol. A* **122**, 377 (1990).
- [15] H. A. Kramers, *Physica* **7**, 284 (1940).
- [16] I. Klik and C. R. Chang, *Phys. Rev. B* **47**, 9091 (1993).
- [17] W. Luo, S. R. Nagel, T. F. Rosenbaum, and R. E. Rosensweig, *Phys. Rev. Lett.* **67**, 2721 (1991).
- [18] U. Wolff, *Phys. Rev. Lett.* **62**, 361 (1989).
- [19] A. Lyberatos, *J. Phys. D: Appl. Phys.* **33**, R117 (2000).
- [20] U. Nowak, *Ann. Rev. of Comp. Phys.* **9**, 105 (2001).
- [21] P. Milténi, M. Gierlings, J. Keller, B. Beschoten, G. Guntherodt, U. Nowak, and K. D. Usadel, *Phys. Rev. Lett.* **84**, 4224 (2000).



- 
- [22] F. Reif, *Fundamentals of Statistical and thermal dynamics* (Mc Graw Hill, New York, 1967).
- [23] J. L. Dormann, D. Fiorani, and E. Tronc, *Adv. Chem. Phys.* **98**, 283 (1997).
- [24] J. M. González, R. Ramírez, R. Smirnov-Rueda, and J. González, *Phys. Rev. B* **52**, 16034 (1996).
- [25] B. Barbara and L. Gunther, *J. Magn. Magn. Mater.* **128**, 35 (1993).
- [26] L. C. Sampaio, C. Paulsen, and B. Barbara, *J. Magn. Magn. Mater.* **140-144**, 391 (1995).
- [27] A. Marchand, L. C. Sampaio, and B. Barbara, *J. Magn. Magn. Mater.* **140-144**, 1863 (1994).
- [28] A. Labarta, O. Iglesias, L. Balcells, and F. Badia, *Phys. Rev. B* **48**, 10240 (1993).
- [29] M. El-Hilo, K. O'Grady, and R. W. Chantrell, *J. Magn. Magn. Mater.* **117**, 21 (1992).
- [30] K. O'Grady and R. W. Chantrell, in *Proceedings of the International Workshop on Studies of Magnetic Properties of fine Particles*, edited by J. L. Dormann and D. Fiorani (North Holland, Amsterdam, 1992), Vol. 301, p. 103.
- [31] S. Linderoth, L. Balcells, A. Labarta, J. Tejada, P. V. Hendriksen, and S. A. Sethi, *J. Magn. Magn. Mater.* **124**, 269 (1993).
- [32] W. F. Brown, Jr., *Phys. Rev.* **130**, 1677 (1963).
- [33] R. Sappey, E. Vincent, N. Hadacek, F. Chaput, J. P. Boilot, and D. Zins, *Phys. Rev. B* **56**, 14551 (1997).
- [34] Several Authors, in *Quantum Tunneling of the Magnetization-QTM'94*, Vol. 301 of *NATO ASI Series E*, edited by L. Gunther and B. Barbara (Kluwer Academic, Dordrecht, The Netherlands, 1995), pp. 121–136.
- [35] J. Tejada, X. X. Zhang, and C. Ferrater, *Z. Phys. B* **94**, 245 (1994).
- [36] J. Tejada, X. X. Zhang, and E. C. M. Chudnovsky, *Phys. Rev. B* **47**, 14977 (1993).
- [37] J. Tejada, X. X. Zhang, and L. Balcells, *J. Appl. Phys.* **73**, 6709 (1993).
- [38] L. Balcells, O. Iglesias, and A. Labarta, *Phys. Rev. B* **55**, 8940 (1997).
- [39] P. Perera and M. J. O'Shea, *Phys. Rev. B* **53**, 3381 (1996).
- [40] M. M. Ibrahim, S. Darwish, and M. S. Seehra, *Phys. Rev. B* **51**, 2955 (1995).

# CHAPTER 6

## 1D INTERACTING SYSTEMS

Up to now, all the systems considered consisted either of individual particles with spins interacting only via short range forces or ensembles of non-interacting particles. However, in real small particle systems, long-range forces of dipolar origin are present, and in many cases cannot be discarded. In superparamagnets (nanoscale solids or clusters), exchange or other competing interactions can be usually discarded compared to interparticle interactions so, in principle, they are good candidates for the study of dipolar interactions in pure form.

Among the wide variety of artificially prepared systems containing fine magnetic particles, some are particularly interesting for the study of the dipolar interaction in a controlled manner: **1.** First, we have granular metal solids [1, 2, 3] consisting of fine magnetic particles (Fe, Co, Ni, ...) embedded in a nonmagnetic matrix ( $\text{SiO}_2$ ,  $\text{Al}_2\text{O}_3$  ...). For insulating matrices (for which RKKY interactions are absent), the dipolar interaction between the granules dominates over superexchange mechanisms. In these materials, the interactions can be tuned because the metal volume fraction and average size of the granules can be varied in a controlled way. **2.** Frozen ferrofluids, ensembles of nanosized magnetic particles (commonly  $\text{Fe}_3\text{O}_4$ ,  $\gamma\text{-Fe}_2\text{O}_3$ , FeC, ...) dispersed in a carrier liquid, have also been extensively studied [4, 5, 6, 7, 8, 9, 10]. These are considered as experimental model random of magnet systems and in this case the strength of the interactions can be tuned easily by controlling the concentration of particles in the ferrofluid. **3.** Yet another promising kind of materials has appeared within the fast growing field of patterned media. These are regular arrays of nanoelements of different shapes stamped by nanolithographic methods which can be prepared with a high control over the size, shape and interparticle distances. Their potential use in ultra-high density magnetic storage has raised the interest in controlling the effects of interparticle interactions as they could induce demagnetization of the stored information [11, 12, 13].

While dilute systems are well understood, experimental results for dense systems are still a matter of controversy. Some of their peculiar magnetic properties have been attributed to dipolar interactions although many of the issues are still controversial. Different experimental results measuring the same physical quantities give contradictory results and theoretical explanations are many times inconclusive or unclear. In the following, we briefly outline the main subjects to be clarified:

1. It is still not clear what is the dependence of the blocking temperature and remanent magnetization with concentration,  $\varepsilon$ , in ferrofluids: while most experiments [2, 3, 4, 5, 6, 7, 8, 14] find an increase of  $T_B$  and a decrease of  $M_R$  with  $\varepsilon$ , others [9, 10] observe the contrary variation in similar systems.
2. In general, for disordered systems, the dipolar interaction diminishes the coercive field [3, 4].
3. The dependence of the effective energy barriers with concentration is unclear. While theoretical studies by the group of Dormann [2, 15] and experimental results by Luis [16] on Co clusters predict

an increase of the barrier for magnetization reversal, Mørup [9] et al. argue for a reduction of  $T_B$  with  $\varepsilon$ .

4. The complexity of dipolar interactions and the frustration provided by the randomness in particle positions and anisotropy axes directions present in highly concentrated ferrofluids seem enough ingredients to create a collective glassy dynamics in these kind of systems. Experiments probing the relaxation of the thermoremanent magnetization [17, 18, 19] have evidenced magnetic aging. Studies of the dynamic and nonlinear susceptibilities [19, 20, 21], also find evidence of a critical behaviour typical of a spin-glass-like freezing. All these studies have attributed this collective SG behaviour to dipolar interactions, although surface exchange may also be at the origin of this phenomenon. However, MC simulations of a system of interacting monodomain particles [14] show that, while the dependence of ZFC/FC curves on interaction and cooling rate are reminiscent of a spin glass transition at  $T_B$ , the relaxational behaviour is not in accordance with the picture of cooperative freezing.

It is clear that, in order to shed some light into the interpretation of these phenomena, numerical methods as Monte Carlo simulation are the only way to incorporate all the ingredients involved in the problem. Here, we will focus on the time dependent properties of these systems in terms of a simple model.

## 6.1 Models

In order to study the effect of long range interactions on the dynamics of spin systems, we will start with the simplest model capturing the essential physics of the problem. Let us consider a linear chain of  $N$  Heisenberg spins  $\mathbf{S}_i$   $i = 1, \dots, N$ , each one representing a monodomain particle with magnetic moment  $\mu_i = \mu \mathbf{S}_i$ . As indicated in Fig. 6.1, each spin has uniaxial anisotropy pointing along the direction  $\hat{\mathbf{n}}_i$ , which may be the same for all and is oriented at random, and anisotropy constants,  $K_i$ , distributed according to a distribution function  $f(K)$ . An external magnetic field  $\mathbf{H}$  may act on all the spins with the same value and pointing along the direction perpendicular to the chain. For simplicity, we will consider that particles have no internal structure, so that the only interaction taken into account will be the dipolar long-range interaction. The corresponding Hamiltonian is therefore:

$$\mathcal{H} = - \sum_{i=1}^N \{K_i (\mathbf{S}_i \cdot \hat{\mathbf{n}}_i)^2 + \mathbf{S}_i \cdot \mathbf{H}\} + g \sum_{i=1}^N \sum_{j \neq i}^N \left\{ \frac{\mathbf{S}_i \cdot \mathbf{S}_j}{r_{ij}^3} - 3 \frac{(\mathbf{S}_i \cdot \mathbf{r}_{ij})(\mathbf{S}_j \cdot \mathbf{r}_{ji})}{r_{ij}^5} \right\}, \quad (6.1)$$

where  $g = \mu^2/a^3$  characterizes the strength of the dipolar energy and  $r_{ij}$  is the distance separating spins  $i$  and  $j$ ,  $a$  is the lattice spacing, here chosen as 1.

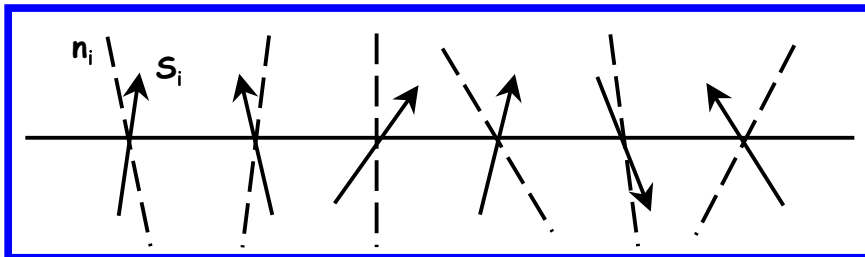


Figure 6.1: 1D chain of spins  $\mathbf{S}_i$  with random anisotropy directions  $\mathbf{n}_i$ .

We will consider systems with either uniform anisotropy  $K_i = K_0 = 1$  or with a lognormal distribution of anisotropies,  $f(K)$ , of width  $\sigma$  and centered at  $K_0 = 1$ . We will also study the effect of the random orientation of anisotropy axis  $\mathbf{n}_i$  and compare this case with the case of aligned particles. Moreover, two different spin models will be considered:

- a. **Model I** Spins in the same  $(x-z)$  plane with  $\varphi_i = 0$  characterized only by the angle  $\theta_i$  (see Fig. 6.2a).
- b. **Model II** Spins with 3 dimensional orientations characterized by the spherical angles  $\theta_i, \varphi_i$  (see Fig. 6.2b).

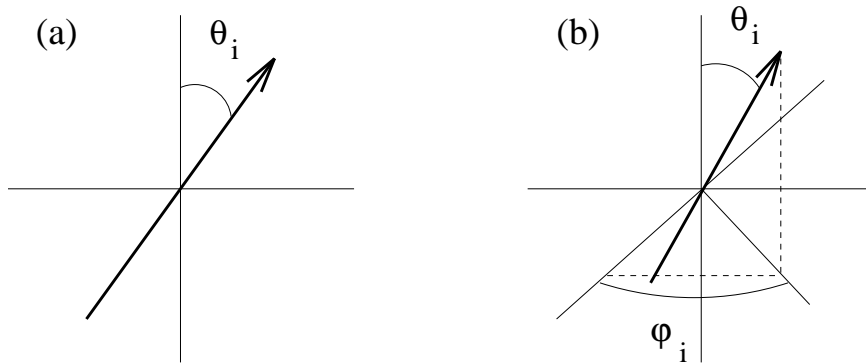


Figure 6.2: The two 1D models considered. (a) Model I: 1D chain of planar spins, (b) Model II: 1D chain of 3D spins.

Besides the dimensionality of the spin vector, the difference between the two models lies on the fact that for Model I it is possible to write down an algorithm to find the exact values of the minima of the energy function and the energy barriers, whereas for Model II this becomes extremely difficult since a new degree of freedom comes into play.

We will consider periodic boundary conditions along the chain, so that the restriction

$$\mathbf{S}_1 = \mathbf{S}_N \quad (6.2)$$

will be imposed in the simulations. In this way, we get rid of the possibility of spin reversal at the boundaries of the system because of the reduced coordination there. For this kind of boundary condition, the

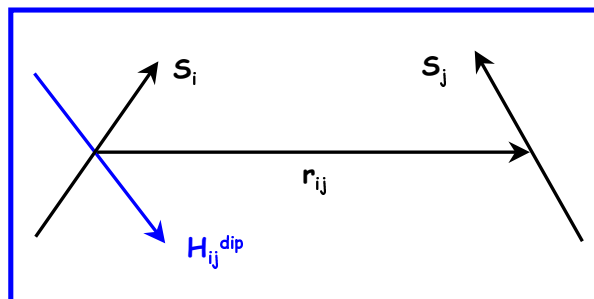


Figure 6.3: Definition of the dipolar field  $\mathbf{H}_{ij}^{dip}$  generated by the spin  $S_j$  on the spin  $S_i$ .

evaluation of dipolar fields for two or three dimensional spins would require replicating the system with several identical copies in order to minimize the rounding-off errors caused by the finite size of the system, but for our 1D model this will not be necessary.

The effect of the dipolar interaction can be more easily understood if we define the dipolar fields acting on each spin  $i$  (see Fig. 6.3)

$$\mathbf{H}_i^{dip} = - \sum_{j \neq i}^N \left\{ \frac{\mathbf{S}_j}{r_{ij}^3} - 3 \frac{(\mathbf{S}_j \cdot \mathbf{r}_{ji}) \mathbf{r}_{ij}}{r_{ij}^5} \right\} \quad (6.3)$$

and so, by rewriting the dipolar energy as

$$\mathcal{H}_{dip} = -g \sum_{i=1}^N \mathbf{S}_i \cdot \mathbf{H}_i^{dip}, \quad (6.4)$$

the total energy of the system can be expressed into the simpler form

$$\mathcal{H} = - \sum_{i=1}^N \{K_i (\mathbf{S}_i \cdot \hat{\mathbf{n}}_i)^2 - \mathbf{S}_i \cdot \mathbf{H}_i^{eff}\}. \quad (6.5)$$

Now, the system can be thought as an ensemble of non-interacting spins feeling an effective field which is the sum of an external and a locally changing dipolar field  $\mathbf{H}_i^{eff} = \mathbf{H} + \mathbf{H}_i^{dip}$ . Note now that the first term in (6.1) is a demagnetizing term since it is minimized when the spins are antiparallel, while the second one tends to align the spins parallel and along the direction of the chain. For systems of aligned Ising spins only the first term is non-zero and, consequently, the dipolar field tends to induce AF order along the direction of the chain (the ground state configuration for this case). However, for Heisenberg or planar spins, the competition between the two terms give rise to frustrating interactions, which can induce other equilibrium configuration depending on the interplay between anisotropy and dipolar energies.

## 6.2 Computational details

### 6.2.1 Calculation of dipolar energies

The long-range character of the dipolar interaction, due to the double sum over  $N$  in (6.1), makes the energy computation in the standard MC algorithm extremely costly in CPU time in comparison with the other local energy terms. So that one is almost forced to find some way to reduce the time spent in the calculation of the dipolar energy. The first thing one can think of is to cut-off the interaction range to a sufficiently large (but still small, let us say 10) number of neighbours with the hope that the contribution of the furthest spins will be negligible. But it turns out that, even in 1D, sums of the kind  $\sum_{n=1}^{\infty} 1/n^\alpha$  are very poorly convergent so that truncation may result in considerable rounding-off errors and also to the formation of artificial surface charges or magnetic poles at the truncation distance which lead to non-physical solutions.

Another strategy is to keep the exact calculation but to find an algorithm that avoids, in some way, the longest part of the calculation, i.e. the evaluation of the double sum in (6.1) at every MC trial jump. Our algorithmic implementation for the calculation of dipolar energies is based in the following considerations:

1. Let us first note that it is not necessary to recalculate the dipolar energy each time a spin flip attempt is tried during the MC procedure. By rewriting the dipolar energy as

$$\mathcal{H}^{dip} = g \sum_{i,j=1}^N S_i^\alpha W_{ij}^{\alpha\beta} S_j^\beta, \quad (6.6)$$

where  $W$  is the dipolar interaction matrix

$$W_{ij}^{\alpha\beta} = \frac{\delta_{\alpha\beta}}{r_{ij}^3} - 3 \frac{\delta_{\alpha\gamma} \delta_{\beta\eta} r_{ij}^\gamma r_{ij}^\eta}{r_{ij}^5}, \quad (6.7)$$

that represents the dipolar interaction between spins  $i$  and  $j$ . Then these quantities can be calculated before starting the MC part of the program and stored in an array for later use, as they only depend on the position of the spins along the chain and not on the particular spin value.

2. With these quantities at hand, it is more convenient to work with the dipolar fields as they are simply

$$H_{dip_i}^\alpha = \sum_{j=1}^N W_{ij}^{\alpha\beta} S_j^\beta. \quad (6.8)$$

The dipolar fields may be calculated once for the initial spin configuration before entering the MC part of the simulation and stored in an array.

3. Therefore, in the MC algorithm, the dipolar energy of a spin can be calculated simply by multiplying the stored dipolar field by the value of the spin as

$$E_{dip_i} = -\mathbf{S}_i \cdot \mathbf{H}_{dip_i}. \quad (6.9)$$

4. Finally, let us note that, only if the trial jump is accepted, the dipolar fields have to be updated by a specific subroutine as

$$\mathbf{H}_{dip_i}^{new} = \mathbf{H}_{dip_i}^{old} - W_{ij}(\mathbf{S}_j^{old} - \mathbf{S}_j^{new}) \quad (i = 1, \dots, N), \quad (6.10)$$

where  $\mathbf{S}_j$  is the spin that has been changed. This requires only  $N$  evaluations instead of the double  $N$  sum involved in the calculation of the dipolar energy. This strategy is particularly efficient at low temperatures, when the acceptance rate can be very low.

### 6.2.2 The Monte Carlo algorithm

As mentioned in the Appendix 10, in Monte Carlo simulations of continuous spins, special care has to be taken in the way the attempt jumps are done, and in the way the energy difference  $\Delta E$  appearing in the Boltzmann probability is calculated. They are mainly two choices for the dynamics of the MC procedure, independently of the way the attempt jumps are done: (a) either  $\Delta E$  is directly calculated as the energy difference between the old  $\mathbf{S}^{old}$  and the attempted  $\mathbf{S}^{new}$  values of the spin or (b)  $\Delta E$  is chosen as the energy barrier which separates  $\mathbf{S}^{old}$  and  $\mathbf{S}^{new}$  (see Fig. 6.4). Note that the second choice gives  $\Delta E$ 's that are higher than the first if there is an energy maximum separating the two states. Each of the two models previously considered are suited to probe this two different choices:

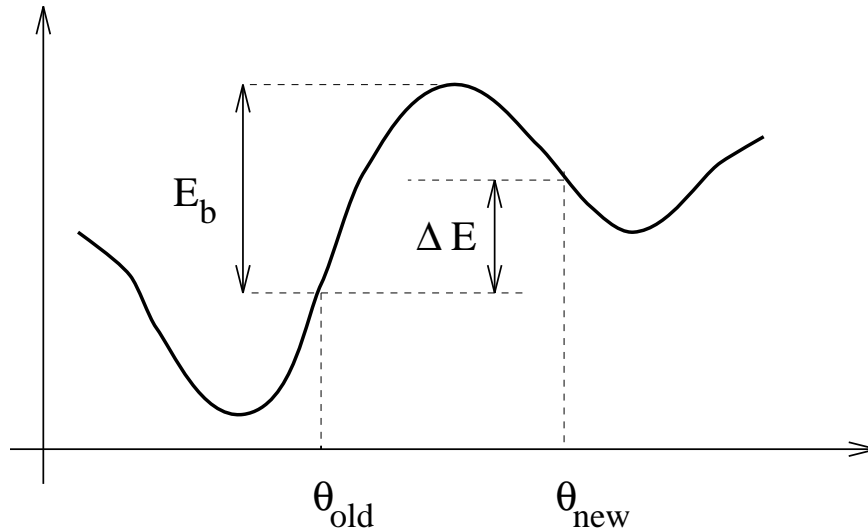


Figure 6.4: Different choices of  $\Delta E$  for the transition probability.

1. In Model I, the energy minima and the barriers separating them can be explicitly calculated, since, in this case, there is only one degree of freedom for each spin and its energy can be written as in the Stoner-Wohlfarth particle model of Section 2.1

$$E_i = -K_i \cos^2(\theta_i - \psi_i) - H_i^{eff} \cos(\theta_i^h - \theta_i), \quad (6.11)$$

with an effective field which is the sum of the external and dipolar fields. Although the energy barriers cannot be analytically calculated for all the values of  $\psi_i$  and  $\theta_i^h$ , it is not difficult to build up an algorithm that finds the minima and maxima of the energy function (6.11) and their respective energies.

Thus, we can build a MC algorithm that considers trial jumps only between orientations corresponding to energy minima randomly chosen with equal probabilities. The  $\Delta E$  in the transition probability are always equal, in this case, to one of the actual energy barriers of the system.

2. In Model II, the 3D character of the spins and the dipolar field makes it difficult to devise an efficient algorithm to find the energy minima. Then, the trial jump must be done in this case to a random orientation inside a cone of aperture  $\delta\theta$  around the current spin direction.

Of course, when the MC simulation is used to simulate the evolution in time of a system, the link between the computer artificial MC step and real time will depend on how the  $\Delta E$  is computed, but it is well-known that in either case, only in some specific situations [22, 23] this correspondence can be established.

### 6.3 Dipolar fields in 1D

- In a 1D chain of Ising spins with directions perpendicular to the line joining the spins, the ground state is AF, giving an energy  $E_{dip}^{AF} = -g/a^3$  for n.n spins. For spins pointing along the chain direction, the ground state is FM, giving now an energy  $E_{dip}^{FM} = -2g/a^3$  for n.n. spins (see Fig. 1.2).
- The local field felt by spins in a FM chain is

$$H_{dip}^{FM} = -2g \zeta(3) = -2.4041 g \quad (6.12)$$

where  $\zeta(s)$  is the Riemann's Zeta function [24]. While if the spins are AF ordered the dipolar fields are

$$H_{\text{dip}}^{AF} = \pm 2g \sum_{n=1}^{\infty} \frac{(-1)^n}{n^3} = \mp \frac{3}{2} \zeta(3) = \mp 1.80308536 g . \quad (6.13)$$

If the spins point along the chain, these values are doubled.

## 6.4 Effective energy barrier distributions

Before starting to simulate the time dependence of the magnetization, we will study first the influence of dipolar interactions on the energy function of the particles. With this purpose, in this section we will compute the distribution of energy barriers of interacting systems with distributed properties in a similar way we did when we studied in Sec. 5.2 the effect of an homogeneous external magnetic field. As in that case, we can expect that the dipolar fields acting on each particle will modify the energy barrier distribution in absence of interactions. But now, since the local dipolar fields may vary depending on the spin configuration, the effective distributions will be different from that for homogeneous magnetic field. We will concentrate on Model I, since in this case the energy barriers can be computed exactly and compared to those extracted from relaxation curves. Moreover, we will consider a system with a lognormal distribution ( $\sigma = 0.5$ ) of anisotropies  $f(K)$  (see Eq. 2.22) and random anisotropy axis.

1. Let us first consider the case of a FM chain of spins pointing along the positive y axis ( $\theta_i = 0$ ). In Fig. 6.5 (left panel), we present the calculated energy barrier distributions for several values of the dipolar interaction  $g$  and compare them with that for the non-interacting case  $g = 0$ . The distributions have been obtained from histograms for a system with 40000 particles normalized to the total area of the distribution.

In this case, the local dipolar fields on all the spins are exactly the same since periodic boundaries are assumed at the ends of the 1D chain. The dipolar field is given in this case by  $\mathbf{H}_{\text{dip } i}^{FM} = -2g\zeta(3)\hat{y}$ . So the existence of one or two energy minima and the height of the energy barriers will be ruled by the ratio of the dipolar to anisotropy energies, since the reduced field reads now

$$h_{\text{dip } i}^{FM} = \zeta(3) \frac{g}{K_i} . \quad (6.14)$$

Therefore, as we already discussed in Sec. 2.2, particles with  $h_{\text{dip } i} < h_{c_i}(\psi_i)$  have two energy minima, while the rest will have only one.

For small  $g$  ( $= 0.1$ ) there are slight changes on the  $f(E_b)$  with respect to the non-interacting case. As it was the case for an external homogeneous field, the dipolar fields shift the peak of the distribution, while its shape is undisturbed. However, when increasing  $g$ , the smallest energy barriers of particles having the smallest  $K$  start to disappear. This leads to the appearance of a peak at zero energy, an increase in the number of low energy barriers due to the reduction by the field, and to the appearance of a longer tail at high energies. As the dipolar interaction is increased further ( $g = 0.3, 0.4$ ) the original peak around  $E_b \simeq 1$  is progressively suppressed as more barriers are destroyed, and a secondary distribution peaked at high energies appears as a consequence of barriers against rotation out of the field direction.

2. The previously analyzed configuration is highly metastable even at  $T = 0$  since, in general, the spin orientations are not along the energy minima. If the system is initially prepared this way by the application of a strong external field, for example, the particles will instantaneously reorientate their magnetizations so



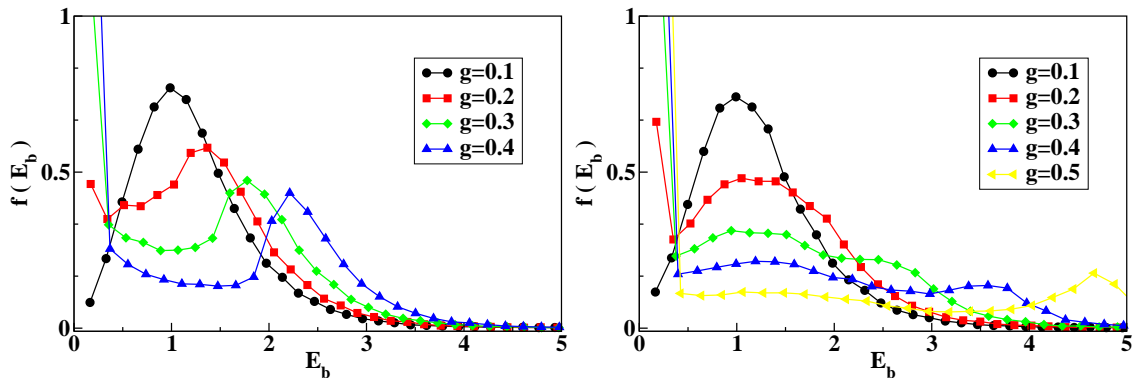


Figure 6.5: Energy barrier distributions  $f(E_b)$  for a system with lognormal distribution of anisotropy constants ( $\sigma = 0.5$ ) and random anisotropy axes directions. Left panel: spins pointing towards the y positive direction. Right panel: spin configuration achieved after equilibration at  $T = 0$  in which spins have been replaced iteratively towards the nearest energy minimum direction starting from an initial FM configuration.

that they lie along the nearest minimum. This accommodation process occurs in a time scale of the order of  $\tau_0$ , much shorter than the thermal over-barrier relaxation times  $\tau$ . Therefore, in real experiments probing magnetization at time scales of the order of  $1 - 10$  s (*i.e.* SQUID magnetometry), this will not be observed. In order to get rid of this ultra-fast relaxation during the first instants of the simulations, we submit the system to a previous equilibration process at  $T = 0$ , during which the spins are consecutively placed in the nearest energy minima. Since the dipolar field after each of this movements changes on all the spins, the energy minima positions change continuously, but, after a certain number of MCS, the total magnetization changes become negligible and the system reaches a final equilibrated state. The effective energy barrier distributions after equilibration are displayed in the right panel of Fig. 6.5. As we see, the high energy peaks observed in the FM configuration disappear almost completely after this process, indicating that they were due to the "misplacement" of the spins far from the local nearest minima.

## 6.5 Relaxation curves: $T \ln(t/\tau_0)$ scaling with interactions

Here we would like to answer the following questions: how is the relaxation rate affected by dipolar interactions between the particles?, and is the  $T \ln(t/\tau_0)$  scaling still accomplished even though the energy barrier landscape changes as time elapses in this case?. If so, then what is the meaning of the effective energy barrier distribution derived from the scaled relaxation curves?.

### 6.5.1 Simulations of the time dependence of the magnetization

Let us start with the simple case of a system with anisotropy distribution  $f(K)$  and anisotropy axes distributed at random. As already mentioned in the previous section, if the system is initially prepared with all spins aligned in the field direction, the spins relax to the nearest minimum within a time of the order  $\tau_0$  that is not usually accessible in most relaxation experiments. Therefore, the simulated relaxation will not be exactly as in typical experiments measuring the variation of the magnetization after saturation in a strong magnetic field. We will run the simulations starting from the equilibrated states achieved by the previously

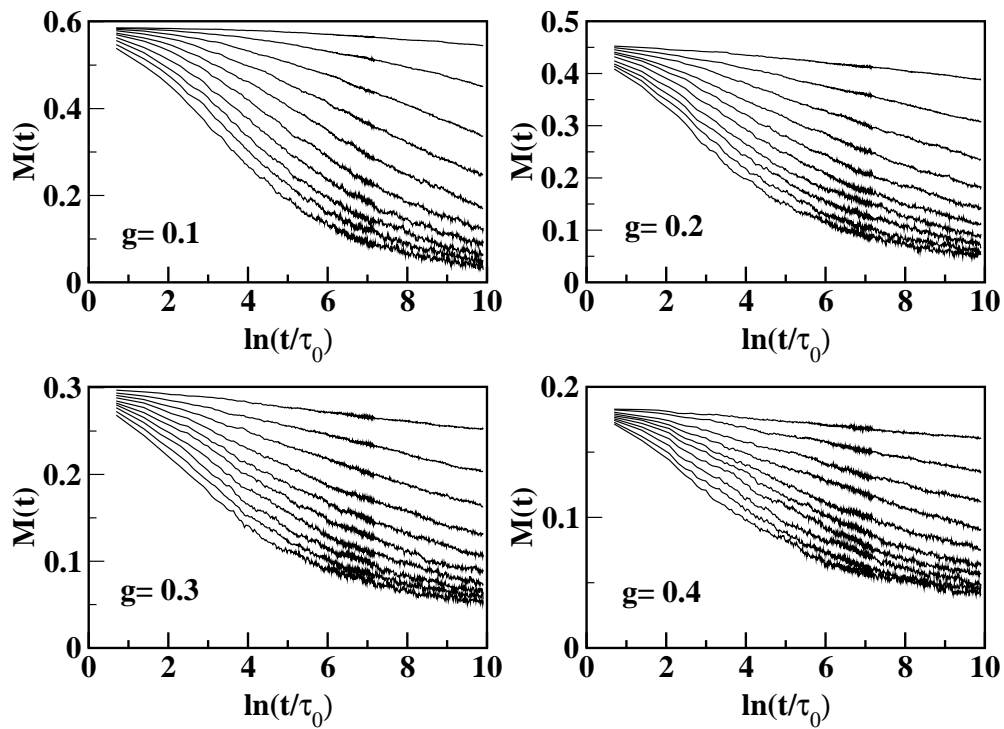


Figure 6.6: Relaxation curves for several temperatures ranging from  $T = 0.02$  (uppermost curves) to  $T = 0.2$  (lowermost curves) in 0.02 steps for a system of interacting particles with distribution of anisotropies  $f(K)$  and random orientations.  $g$  is the dipolar interaction strength. The initial state for all of them is the one achieved after the equilibration process described in the text.

described procedure. At non-zero  $T$ , thermal fluctuations will drive the system towards the equilibrium state, which for aligned particles would be AF. For a disordered system, however, the equilibrium state will have zero net magnetization. The final expected configuration will have neighbouring particles with almost parallel easy-axes in the  $y$  direction with antiparallel spins and neighbouring particles with almost parallel easy-axes in the  $x$  direction with parallel spins.

The relaxation curves at different temperatures and values of the interaction  $g$  are shown in Fig. 6.6. As in previous chapters, temperature is measured in reduced units ( $k_B T/K_0$ ), the chosen values of the interaction parameter range from the weak ( $g = 0.1$ ) to the strong ( $g = 0.5$ ) interaction regime. We observe that the stronger the interaction, the smaller the magnetization of the initial configuration due to the increasing strength of the local dipolar fields that tend to depart the equilibrium directions from the direction of the anisotropy axis. Thus, we point out that, if one is to compare relaxation curves for different  $g$  at the same  $T$ , they have to be properly normalized by the corresponding  $m(0)$  value. As it is evidenced by the logarithmic time scale used in the figure, the relaxation is slowed down by the intrinsic frustration of the interaction and the randomness of the particle orientations.

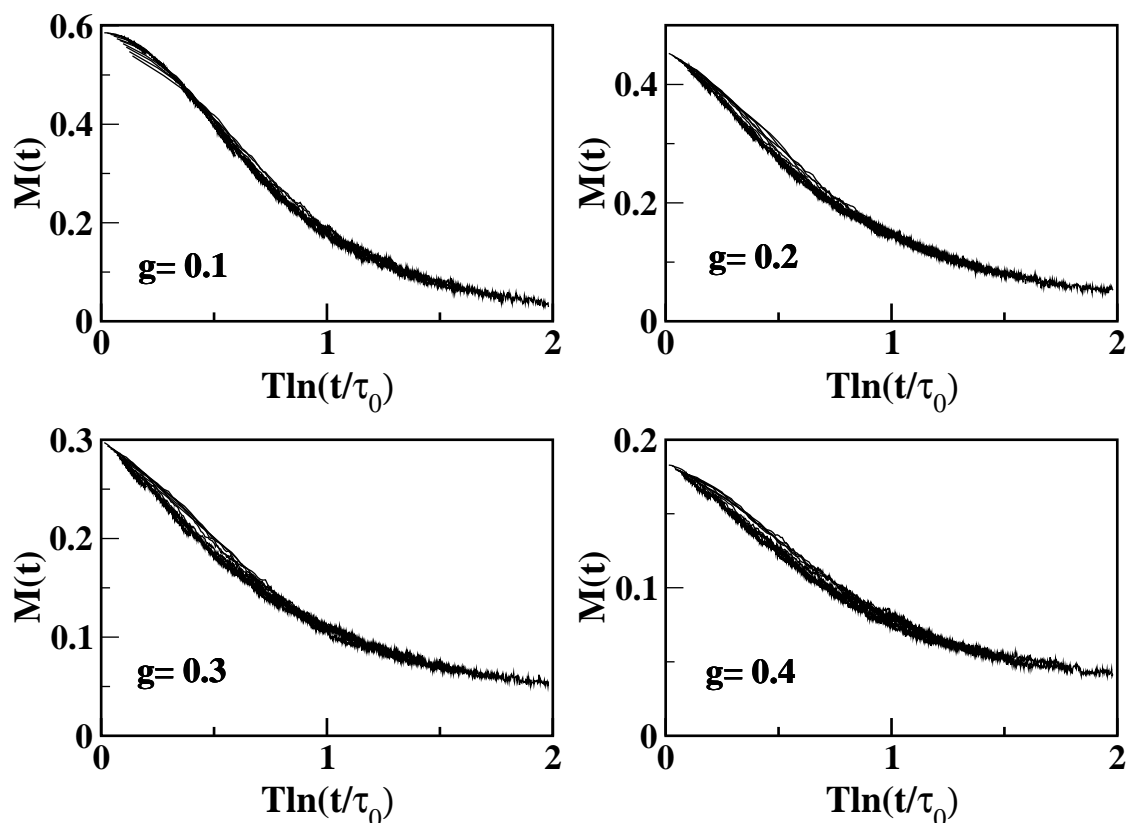


Figure 6.7: Master relaxation curves corresponding to the relaxations shown in Fig. 6.6 obtained by multiplicative scaling factor  $T$ .

More remarkable is the fact that the magnetization decay is faster the stronger the interaction is, which agrees well with the experimental results of Refs. [9, 25, 26] and also with other simulation works that model dipolar interactions by a mean-field [27, 28, 29, 30]. However, at difference with these works, the quasi-logarithmic relaxation regime is only found in our simulations in the strong interaction regime, for short times, and within a narrow time window that depends on  $T$ . This can be understood because of the

short duration of the relaxations in other works compared to ours, which were extended up to 10000 MCS, thus confirming the limitation of the logarithmic approximation to narrow time windows.

### 6.5.2 $T \ln(t/\tau_0)$ scaling in presence of interaction.

Following the ideas exposed in Chapters 3.6 and 5, we will try to analyze the relaxation curves at different temperatures according to the phenomenological approach of  $T \ln(t/\tau_0)$  scaling. The underlying hypothesis of the method was that the dynamics of the system can be described in terms of thermal activation of the Arrhenius type over the effective local energy barriers induced by the interaction. Although one could think that this assumption is only valid in non-interacting particle systems, we would like to stress that the  $T \ln(t/\tau_0)$  scaling approach was first successfully introduced in studies of spin-glasses [31, 32, 33]. Although it is true that the dipolar interaction, being long ranged, changes the energy barrier landscape in a dynamic way during the relaxation, this does not imply that the low  $T$  relaxations will not scale. In fact, if this scaling is accomplished, it will give us information of the energy barriers that are effectively probed during the relaxation process, even if they keep on changing during the process.

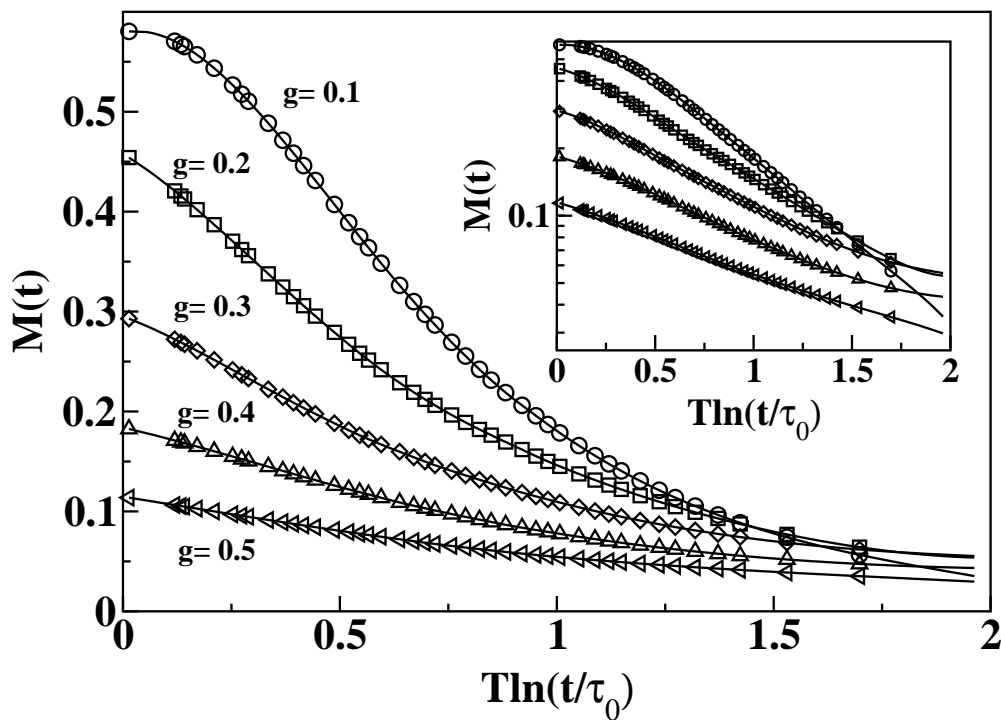


Figure 6.8: Master relaxation curves for different values of the dipolar interaction strength  $g$ . Inset: the same curves in log-log plot in order to make evident the power-law behaviour of the relaxation at high values of  $g$ .

The results of the master curves obtained from Fig. 6.6 by scaling the curves along the horizontal axis by multiplicative factors  $T$  are presented in Fig. 6.7 for a range of temperatures covering one order of magnitude. First, we observe that, in all the cases, there is a wide range of times for which overlapping is observed. Below the inflection point of the master curve, the overlap is better for the low  $T$  curves, whereas high  $T$  curves overlap only at long times above the inflection point, as it was also the case in the non-interacting case. Moreover, it seems that scaling is accomplished over a wider range of  $T$  the stronger

the interaction is, whereas in the weak interaction regime, scaling is fulfilled over a narrower range of times and  $T$ . As we will explain later, this fact is due to the different variation of the effective energy barriers contributing to the relaxation in the two regimes.

In order to see the influence of  $g$  on the relaxation laws, in Fig. 6.8, we have plotted together the master relaxation curves for different values of the interaction parameter  $g$  after a smoothing and filtering of the curves in Fig. 6.7. We can clearly see the qualitative change in the relaxation law with increasing  $g$ . In the weak interaction regime ( $g = 0.1, 0.2$ ), the magnetization decays slowly to the equilibrium with an inflection point around which the decay law is quasi-logarithmic. In the strong interaction regime, however, the relaxation curves have always downward curvature with no inflection point. When plotted in a  $\ln(M)$  vs.  $\ln(t/\tau_0)$  scale they are linear (see Inset of Fig. 6.8), indicating a power-law decay of the magnetization with time, since the energy scale can be converted to time through the  $T \ln(t/\tau_0)$  variable.

This power-law behaviour has also been found by Ribas et al. [34] in a 1D model of Ising spins and by Sampaio et al. [13, 35] in a Monte Carlo simulation of the time dependence of the magnetic relaxation of 2D array of Ising spins under a reversed magnetic field. It has also been observed experimentally in arrays of micromagnetic dots tracked by focused ion beam irradiation on Co layer with perpendicular anisotropy [12, 11].

## 6.6 Evolution of $f_{\text{eff}}(E_b)$ and of dipolar fields

In order to gain some insight on what are the microscopic mechanisms that rule the relaxation processes in the weak and strong interaction regimes, we will examine how the distribution of energy barriers and the dipolar fields change during the relaxation process. The initial distributions of energy barriers have already been shown in Fig. 6.5, but since the starting configurations are not uniform, it is not easy to infer its microscopic origin. Let us notice that the distribution of dipolar fields [Eq. (6.8)] does not depend on the anisotropy or easy-axis directions of the particles, so that it is only sensitive to the spin orientations and their positions in the lattice. For this purpose, it turns useful to perform histograms of the strength of the dipolar fields felt by all the spins at different values of  $g$ . We show the results in Fig. 6.9, where the dipolar fields having a component in the negative  $y$  direction have been given a negative sign. This means that the local field is pointing in the opposite direction with respect to the original spin orientation, which was along the positive  $y$  axis. Therefore, the existence of negative dipolar fields indicates a higher probability for the spin to jump towards the equilibrium state.

For weak interaction ( $g = 0.1$ ), the initial  $f(H_{\text{dip}})$  are strongly peaked at a value which is very close to the dipolar field for a FM configuration  $H_{\text{dip}}^{\text{FM}} = -2.0411381632g$ , and there are very few negative dipolar fields. This indicates that the equilibrated configuration is not far from the initial FM one. In this case, since the dipolar fields are weak, the spins will point near the anisotropy axis direction since the energy minima and the energy barriers between them do not depart very much from the non-interacting case. This is also corroborated by the shape of  $f(E_b)$ , which resembles that for  $g = 0$ .

However, in the strong interaction regime, the local fields start to destroy the energy barriers of the particles with lower  $K$ , and so negative dipolar fields are numerous because of the particles that have rotated into the field direction. There are still positive fields, but now the peak due to collinear spins blurs out with increasing  $g$  at the same time that a second peak, centered at higher field values, starts to appear and finally swallows the first (see the case  $g = 0.5$ ). This last peak tends to a value equal to  $H_{\text{dip}}^{\text{AF}} = \mp 4.808g$ , that would correspond to FM alignment along the chain.

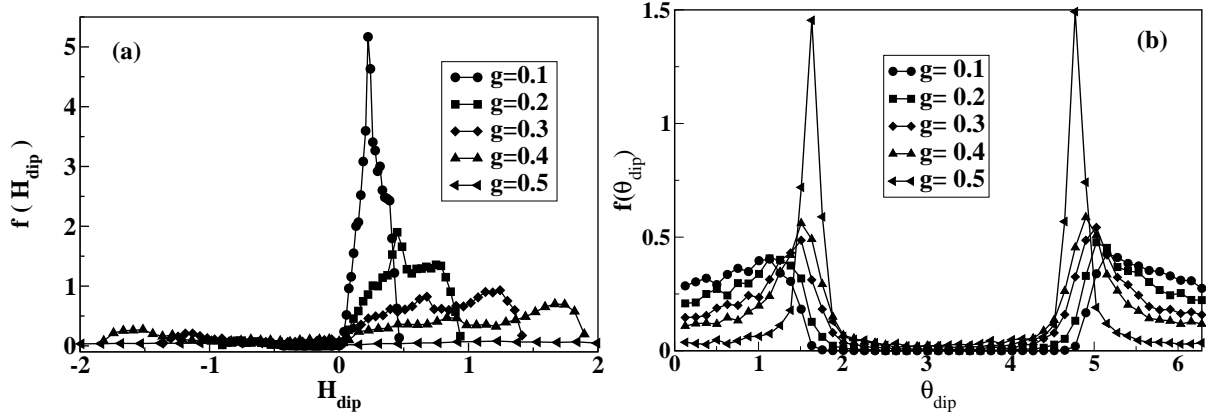


Figure 6.9: Left panel: Initial distribution of dipolar fields for a system of particles equilibrated at  $T = 0$  for different values of the interaction parameter  $g$ . All the magnetic moments are pointing along the local energy minima. Right panel: Initial distribution of dipolar field angles for the same system.

All these features are also supported by the distributions of dipolar field angles (right panel in Fig. 6.9). Now we can understand how the initial stages of the relaxation proceed. In order to gain a deeper insight into the microscopic evolution of the system during the relaxation, the histograms of energy barriers of intermediate configurations have been recorded at different MC steps. In Fig. 6.10, the time evolution of the energy barriers separating the occupied state of each spin from the other allowed state is shown for a relaxation at an intermediate temperature  $T = 0.1$ . In 6.10b, we have also kept track of the time dependence of the dipolar field histograms  $f(H_{\text{dip}})$ .

These evolutions are markedly different in the two interaction regimes. In the weak interaction regime, the relaxation is dominated by anisotropy barriers, so that the distributions are similar to the non-interacting case. As time elapses, particles with the lowest energy barriers relax towards a state with higher energy barriers. However, although during the relaxation process the energy barriers change locally, this change is compensated by the average over the anisotropy distribution and random orientations of the easy-axes. Thus, the global  $f(E_b)$  does not change significantly as the system relaxes, although the final configuration is much more disordered than the initial one. In spite of this, the distribution of dipolar fields, which is more sensitive to the local changes in spin configuration, presents evident changes with time. As relaxation proceeds, the high peak of positive  $H_{\text{dip}}$  progressively flattens, since it corresponds to particles whose magnetization is not pointing along the equilibrium direction. Particles that have already relaxed, create dipolar fields in the negative direction which are reflected in a subdistribution of negative  $H_{\text{dip}}$  of increasing importance as time evolves. Near the equilibrium state of zero magnetization, the relative contribution of positive and negative fields tend to be equal, since, in average, there are equal number of "up" and "down" pointing spins.

In the strong interaction regime, dipolar fields are stronger than anisotropy fields for the majority of the particles, even at the earlier stages of the relaxation process. As time elapses, the number of small energy barriers, corresponding to the particles with smaller anisotropies, continuously diminishes as they are overcome by thermal activation. When relaxing to their equilibrium state, now closer to the dipolar field direction, the particles with initially small  $E_b$  give rise to higher energy barriers and also higher dipolar fields on their neighbours. This is reflected in the increasingly higher peak in the  $f(E_b)$  that practically does not relax as time elapses, causing the final distribution to be completely different from the initial one. What is more, as more particles relax, more particles feel an  $H_{\text{dip}} > H_{\text{anis}}$  and, therefore, higher  $E_b$  for reversal

against the local field. This leads to faster changes in the dipolar field distribution and also is at the origin of the power-law character of the relaxations. Equilibrium is reached when  $f(H_{\text{dip}})$  presents equal sharp peaked contributions from negative and positive fields, since in this case there will be an equal number of particles with magnetizations with positive and negative components along the  $y$  axis.

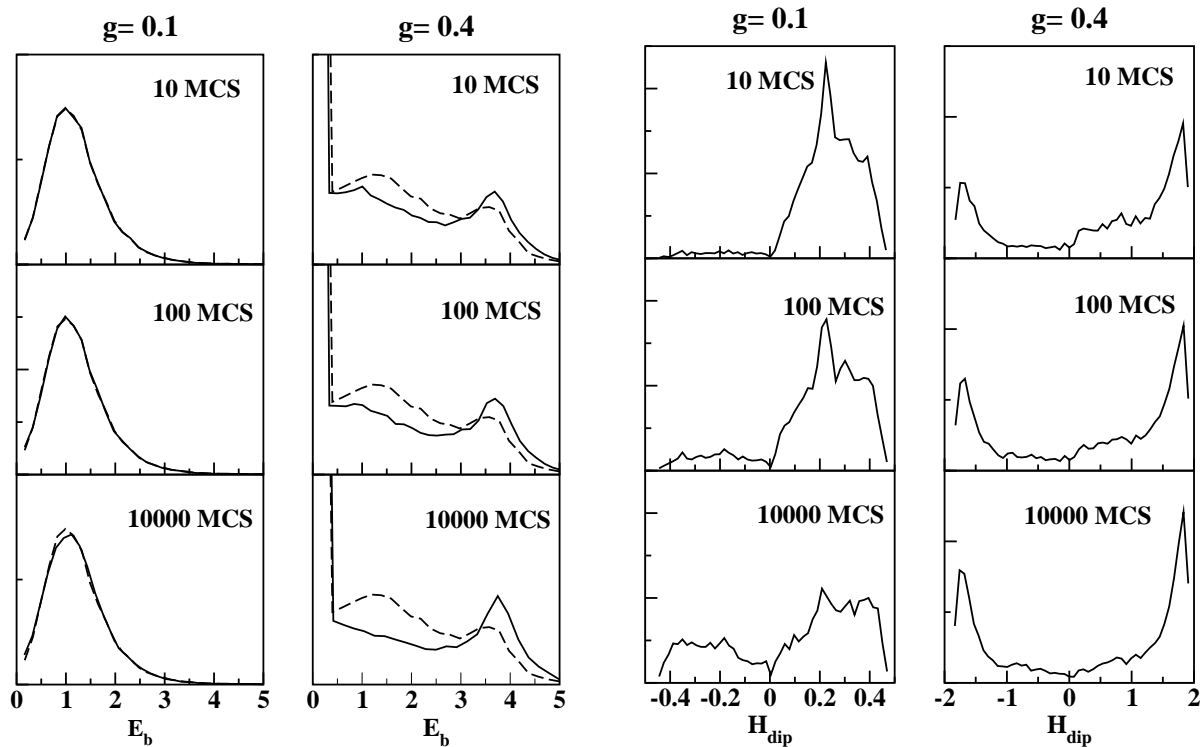


Figure 6.10: Left columns: Evolution with time of the energy barrier histograms during the relaxation process at  $T = 0.1$ . The initial distribution is shown in dashed lines. Right columns: Time dependence of the distribution of dipolar fields during the relaxation process.

## 6.7 Effective energy barrier distributions from $T \ln(t/\tau_0)$ scaling

In sections 4.5 and 5.16, we introduced a method to obtain an effective distribution of energy barriers from the master curves, showing that they can be obtained by performing the logarithmic time derivative of the master curves. The resulting effective energy barrier distributions obtained from the master curves in Fig. 6.8 are given in Fig. 6.11. It is worth remembering that these are not the real time evolving energy barrier distributions. Instead, they represent time independent distributions giving rise to the same relaxation curves obtained in the scaling regime. At difference with the non-interacting cases analyzed in previous chapters, these curves do not match the energy barrier distribution. The microscopic information given by them will be clarified in what follows.

For weak interaction ( $g = 0.1$ ), the effective distribution of energy barriers has essentially the same shape as for the non-interacting case. However, the distribution narrows as  $g$  increases up to a value where almost zero barriers start to appear, and the mean effective barrier is shifted towards lower values of the scaling variable. In some sense, this resembles the situation for the non-interacting system in an external

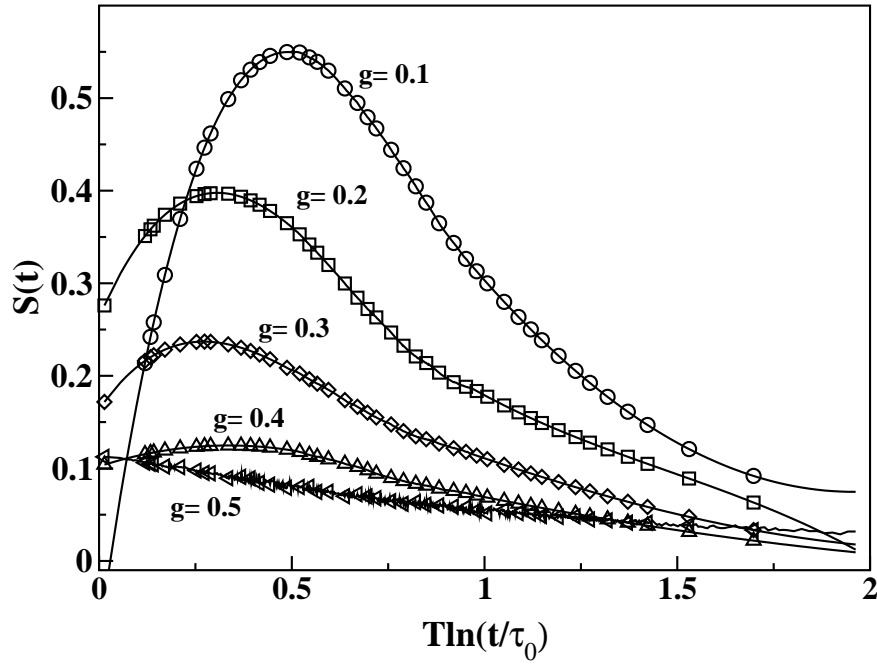


Figure 6.11: Derivatives of the master relaxation curves of Fig. 6.8 for different dipolar interaction strengths  $g$ .

magnetic field, in which this shift was associated to the decrease of the energy barriers for rotation towards the field direction.

When entering the strong interacting regime, an increasing number of low energy barriers appear that finally change the shape of the effective distribution into a quasi-exponential dependence. This change in the effective distribution is of course due to the power-law behaviour of the relaxation law in the strong  $g$  regime and, therefore, a genuine effect of the dipolar interaction. This striking behaviour has important consequences on the experimental interpretation of relaxation curves. As we already mentioned in Sections 4.1, 4.5 and 5.16, if magnetic relaxation is analyzed in terms of viscosity (*i.e.*, the slope of the logarithmic time dependence), it turns out that, since  $S \sim T f[T \ln(t/\tau_0)]$ , an energy distribution diverging as  $f(E) \sim 1/E$  would give a constant viscosity at low  $T$  that could be erroneously interpreted as an indication of quantum  $T$  independent relaxation phenomenon.

This change of behaviour in the effective energy barrier distributions and evidence of  $T \ln(t/\tau_0)$  scaling of the relaxation has been observed experimentally in ensembles of Ba ferrite fine particles [25]. The relevance of demagnetizing interactions in this sample was established by means of Henkel plots at different  $T$ . The relaxation curves of the thermoremanent magnetization for temperatures between 9 and 230 K can be scaled when plotted against the  $T \ln(t/\tau_0)$  variable with  $\tau_0 = 10^{-12}$  s (see Fig. 6.12, left panel). From the derivative of the master relaxation curve the distribution of effective energy barriers (see Fig. 6.12, right panel) was obtained and fitted a sum of two log-normal distributions as in Eq. 4.38. The addition low energy barrier contribution to the energy barrier distribution can be associated to the demagnetizing interactions, since the other contribution centered at higher energies can be ascribed to the volume and anisotropy distributions. Moreover, when cooling the sample in different external magnetic fields before the relaxation process was recorded (see Fig. 6.13), the authors found that, when increasing the cooling field, the effective distributions changed from a function with a maximum that extends to high energies to a narrower distribution with a peak at much lower energy scales for high cooling fields. The effective distribution at



high  $H_{FC}$ , which was there argued to be given by the intrinsic anisotropy barriers of the particles, appears shifted towards lower energy values with respect to the anisotropy distribution as derived from TEM due to the demagnetizing dipolar fields generated by the almost aligned spin configuration induced by the  $H_{FC}$ .

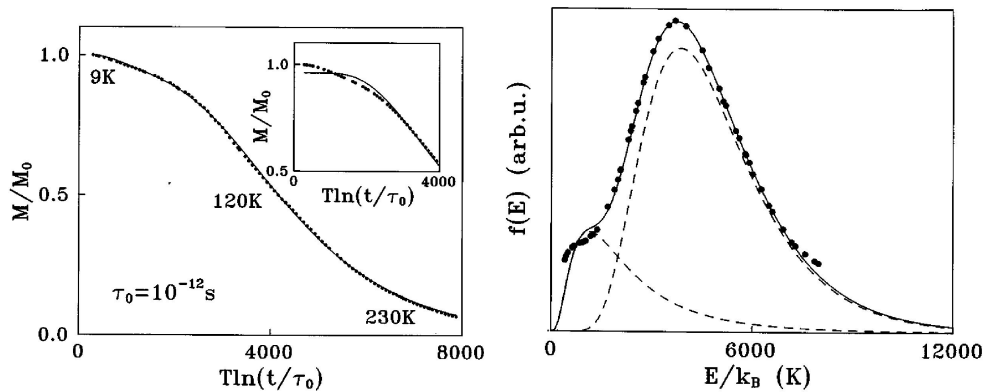


Figure 6.12: Left panel:  $M/M_0$  vs  $T \ln(t/\tau_0)$  scaling with  $\tau_0 = 10^{-12}$  s for 27 temperatures within 9 and 230 K. Solid line represents the best fit of data to Eq. (4.38) considering two log-normal distributions of energy barriers. Right panel: Energy barrier distributions obtained from the derivative of the experimental master curve with respect to the scaling variable (filled circles). The solid line indicates the fitted distribution, the dashed lines are the two log-normal subdistributions.

As we have established that the effective energy barrier distributions derived from the master relaxation curves do not coincide with the real energy barrier distributions, now we will try to further clarify the meaning of these distributions. To this end, we have computed the cumulative histograms of energy barriers that have been really jumped during the relaxation processes. The corresponding results are presented in Fig. 6.14 for systems in the weak and strong interaction regimes and  $T = 0.1, 0.2$ . As it is clear by comparison of the curves in this figure with those of Fig. 6.11, although one could think that the derivative of the master curves collects jumped energy barriers of the order of  $T \ln(t/\tau_0)$  as time elapses, the cumulative histograms overcount the number of small energy barriers at all the studied  $T$  and  $g$ . This small energy barriers that are not seen by the relaxation correspond to the those jumped by the superparamagnetic (SP) particles.

In fact, when the cumulative histograms are computed by counting only the  $E_b$  jumped by particles that have not jumped up to a given time  $t$ , the contribution of SP particles that have already relaxed to the equilibrium state is no longer taken into account. The histograms computed in this way are presented in Fig. 6.15. There, we see that when only the energy barriers jumped by the blocked particles are taken into account, the resulting histograms at advanced stages of the relaxation process tend to the effective energy barriers derived from the master relaxation curves (dashed lines in the figure). The difference between both quantities at high energy values is due to the existence of very high energy barriers, that can only be surmounted at temperatures higher than the one considered here.

## 6.8 Hysteresis Loops

Besides the time dependence of the magnetization, it is also interesting to study the effects of dipolar interactions on the hysteresis loops, since they give information about the reversal processes of the mag-

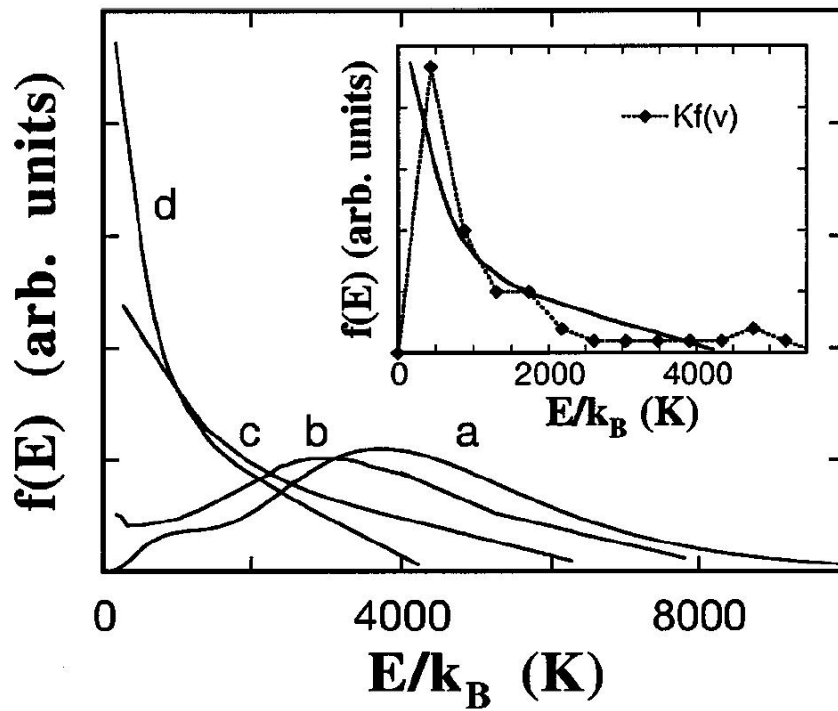


Figure 6.13: Effective energy barrier distributions obtained from relaxation measurements in a Ba ferrite fine particle system [26] after FC the sample at 200 Oe (a), 500 Oe (b), 10 kOe (c), and 50 kOe (d).  $M_0$  is an arbitrary normalization factor.

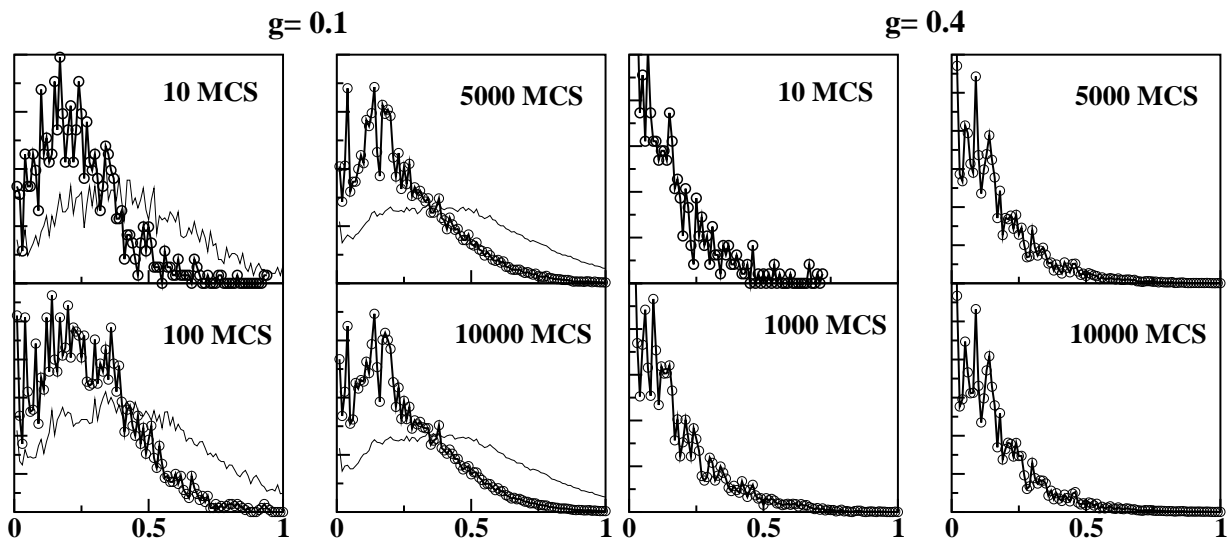


Figure 6.14: Cumulative histograms of the jumped energy barriers during the relaxation process. All the jumped energy barriers are taken into account. The temperature is  $T = 0.1$ . The value of the interaction parameter is  $g = 0.1$  on left panels and  $g = 0.4$  in right panels.

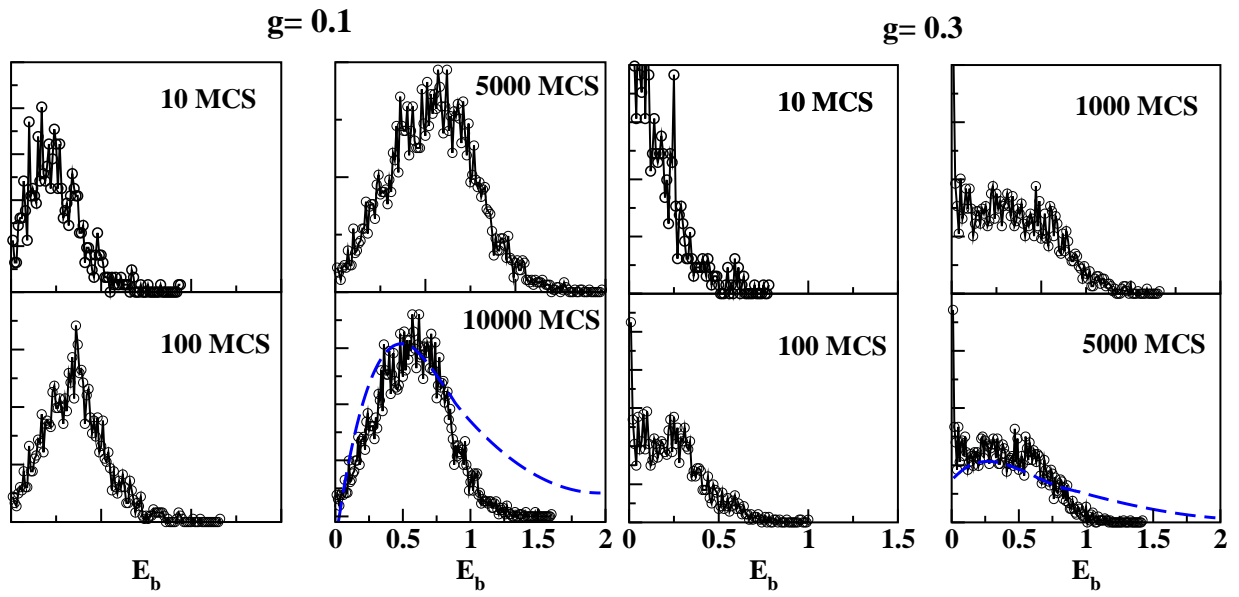


Figure 6.15: Cumulative histograms of the jumped energy barriers during the relaxation process. Only the  $E_b$  jumped by particles that have not jumped up to time  $t$  are taken into account. Symbols correspond to  $T = 0.1$ . The dashed lines stand for the derivatives of the master relaxation curves shown in Fig. 6.11. The value of the interaction parameter is  $g = 0.1$  on left panels and  $g = 0.3$  in right panels.

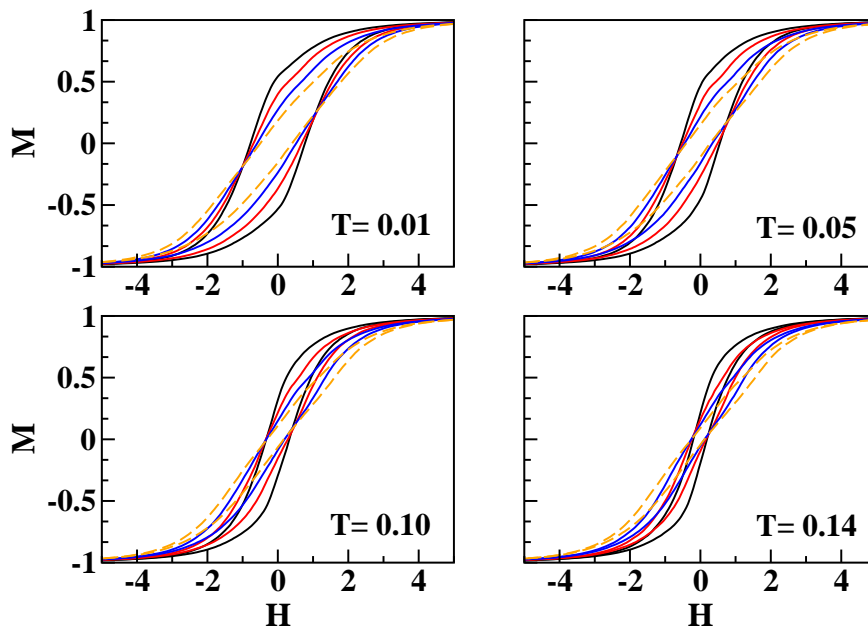


Figure 6.16: Hysteresis loops for different values of the dipolar coupling  $g = 0.1$  (black),  $g = 0.2$  (red),  $g = 0.3$  (blue),  $g = 0.4$  (orange, discontinuous line).

netization and are usual measurements in real samples. Since in this case we are not interested in how the system evolves with time but in finding the value of thermodynamic average of  $M$  at a given  $H$ , we will implement the MC dynamics by choosing the Model II previously introduced in Sec. 6.2. In this way, the phase space is sampled more efficiently, minimizing computational and improving the quality of thermal averages. The studied system consists again of an ensemble of 10000 randomly oriented particles with log-normal distribution of anisotropy constants with  $\sigma = 0.5$ . We start the loop at high enough fields with a FM configuration and subsequently decrease the field in constant steps  $\delta H = 0.05$ . At every field value, thermodynamic averages of the magnetization along the field direction are measured during a large but fixed number of MC steps.

In Fig. 6.16, we present the simulated hysteresis loops at different temperatures for values of  $g$  ranging from 0.1 to 0.4. As it is apparent from the figures, the area of the hysteresis loops decreases with increasing temperature as expected. The loops become more elongated with increasing interaction resembling the ones for a system with frustrated interactions. The closure fields becomes higher and the system becomes harder as the it is more difficult to reach saturation.

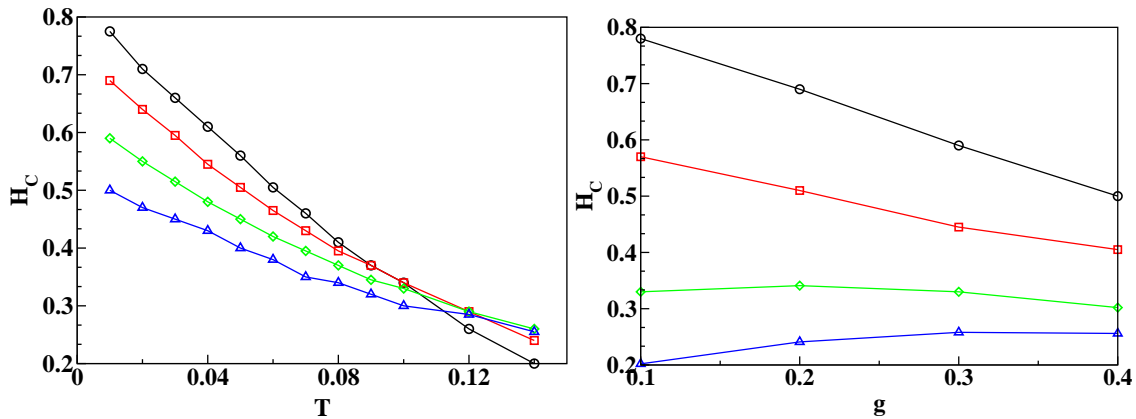


Figure 6.17: Left panel: Temperature dependence of the coercive field for  $g = 0.1, 0.2, 0.3, 0.4$  (from the uppermost curve). Right panel: Dependence of the coercive field on the interaction parameter  $g$  from temperatures  $T = 0.01, 0.05, 0.1, 0.14$  (starting from the uppermost curve).

The thermal dependence of the coercive field  $H_c$  shown in Fig. 6.17 for different values of the interaction parameter  $g$  shows that, at low  $T$ ,  $H_c$  decreases linearly with increasing  $T$  and also with increasing interactions. This observation is in agreement with experiments in interacting systems and simulations [36, 37]. However, at higher  $T$  (see the  $T = 0.1, 0.14$  curves in the right panel of Fig. 6.17),  $H_c(g)$  seems to have a maximum value at an intermediate  $g$  value before starting to decrease for higher values of  $g$ . Further evidence of the influence of the frustration induced by the dipolar interaction is given by the thermal dependence of the remanent magnetization  $M_R$ . As shown in Fig. 6.18, remanence values decrease with increasing interactions at all the considered  $T$ . Moreover, the thermal dependence of  $M_R$  displays an inflection point at intermediate  $T$  values, decaying smoothly towards zero for higher  $T$ , similarly to experimental results for the thermoremanent magnetization of FeN ferrofluids of different concentrations [38].

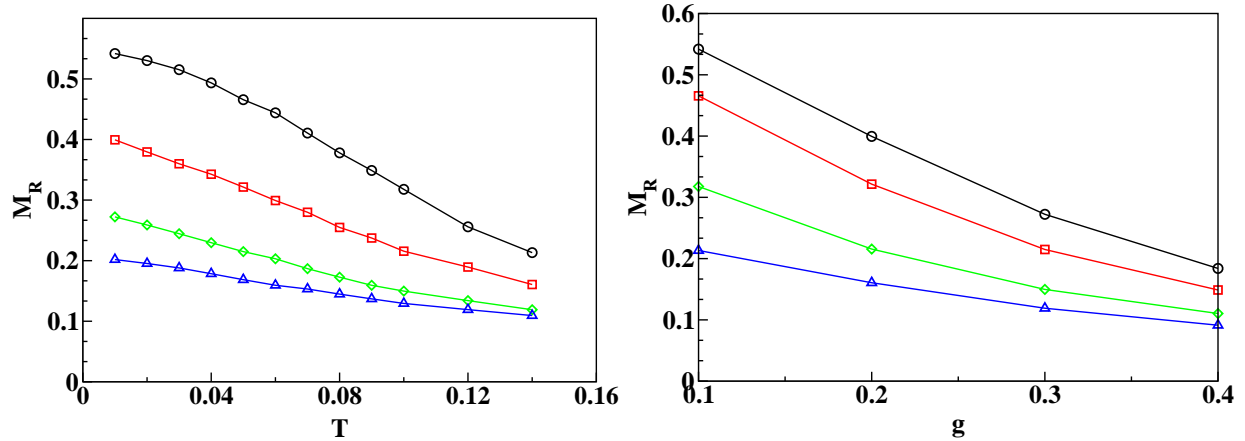


Figure 6.18: Left panel: Temperature dependence of the remanent magnetization for  $g = 0.1, 0.2, 0.3, 0.4$  (from the uppermost curve). Right panel: Dependence of the remanent magnetization on the interaction parameter  $g$  from temperatures  $T = 0.01, 0.05, 0.1, 0.14$  (starting from the uppermost curve).

## 6.9 Conclusions

We have shown that the dipolar interaction induces a faster relaxation of the magnetization, changing the time dependence of the magnetic relaxation from quasi-logarithmic to a power law as  $g$  increases, due to the intrinsic disorder of the system and the frustration induced by the dipolar interactions.  $T \ln(t/\tau_0)$  scaling of the relaxation curves at different  $T$  is accomplished even in the presence of interaction. From the obtained master curves, effective energy barrier distributions can be obtained, giving valuable information about the microscopic energy barriers and the change induced on them by the dipolar interaction which cannot be directly obtained experimentally. As the strength of the dipolar interaction  $g$  increases, the effective energy barrier distribution shifts towards lower  $E_b$  values and becomes wider, in qualitative agreement with experimental results. In spite of the dynamic change of the dipolar fields, the energy barrier distribution does not change appreciably during the relaxation due to the disorder induced by randomness of interaction. Moreover, the results of simulations of the hysteresis loops display a decrease of the coercive field and remanance with increasing interaction in agreement with most of the experimental findings. The hysteresis loops of this system resemble those of frustrated systems, with elongated shapes and high closure fields. A reduction in the coercive field and the remanent magnetization with increasing interaction is in agreement with experimental findings.

## Bibliography

- [1] C. L. Chien, in *Science and Technology of Nanostructured Magnetic Materials*, Vol. 259 of *NATO ASI Series E*, edited by G. C. Hadjipanajys and G. A. Prinz (Plenum, New York, 1991), p. 477.
- [2] J. L. Dormann, L. Bessais, and D. Fiorani, *J. Phys. C* **21**, 2015 (1988).
- [3] S. Gangopadhyay, G. C. Hadjipanajys, C. M. Sorensen, and K. J. Klabunde, *IEEE Trans. Magn.* **29**, 2619 (1993).
- [4] R. W. Chantrell, in *Magnetic Hysteresis in Novel Magnetic Materials Science and Technology of Nanostructured Magnetic Materials*, Vol. 338 of *NATO ASI Series E*, edited by G. C. Hadjipanajys (Kluwer Academic, Dordrecht, The Netherlands, 1997), p. 21.
- [5] R. W. Chantrell, M. El-Hilo, and K. O'Grady, *IEEE Trans. Magn.* **27**, 3570 (19).
- [6] M. El-Hilo, K. O'Grady, and R. W. Chantrell, *J. Magn. Magn. Mater.* **117**, 21 (1992).
- [7] K. O'Grady, M. El-Hilo, and R. W. Chantrell, *IEEE Trans. Magn.* **29**, 2608 (19).
- [8] W. Luo, S. R. Nagel, T. F. Rosenbaum, and R. E. Rosensweig, *Phys. Rev. Lett.* **67**, 2721 (1991).
- [9] S. Mørup and E. Tronc, *Phys. Rev. Lett.* **72**, 3278 (1994).
- [10] S. Mørup, F. Bødker, P. V. Hendriksen, and S. Linderorth, *Phys. Rev. B* **52**, 287 (1995).
- [11] T. Aign, P. M. S. Lemerle, J. Ferré, V. Mathet, J. Gierak, C. Vieu, F. Rousseaux, H. Launois, and H. Bernas, *Phys. Rev. Lett.* **81**, 5656 (1998).
- [12] R. Hyndman, A. Mougin, L. C. Sampaio, J. Ferré, J. P. Jamet, P. Meyer, V. Mathet, C. Chappert, D. Mailly, and J. Gierak, *J. Magn. Magn. Mater.* , To be published (2002).
- [13] L. C. Sampaio, R. Hyndman, F. S. de Menezes, J. P. Jamet, C. Meyer, J. Gierak, C. Chappert, V. Mathet, and J. Ferré, *Phys. Rev. B* **64**, 184440 (2001).
- [14] J. García-Otero, M. Porto, J. Rivas, and A. Bunde, *Phys. Rev. Lett.* **84**, 167 (2000).
- [15] J. L. Dormann, D. Fiorani, and E. Tronc, *Adv. Chem. Phys.* **98**, 283 (1997).
- [16] F. Luis, J. M. Torres, L. M. García, J. Bartolome, J. Stankiewicz, F. Petroff, F. Fettar, J. Maurice, and A. Vaurés, *Phys. Rev. B* **65**, 094409 (2002).
- [17] T. Jonsson, J. Mattson, C. Djurberg, P. Nordblad, and P. Svedlindh, *Phys. Rev. Lett.* **75**, 4138 (1995).
- [18] H. Mamiya, I. Nakatani, and T. Furubayashi, *Phys. Rev. Lett.* **80**, 177 (1998).

- 
- [19] T. Jonsson, P. Svedlindh, and M. F. Hansen, *Phys. Rev. Lett.* **81**, 3976 (1998).
- [20] C. Djurberg, P. Svedlindh, P. Nordblad, M. F. Hansen, F. S. Bødker, and S. Mörup, *Phys. Rev. Lett.* **79**, 5154 (1997).
- [21] W. Kleemann, O. Petravic, C. Binek, G. N. Kakazei, Y. G. Pogorelov, J. B. Sousa, S. Cardoso, and P. P. Freitas, *Phys. Rev. B* **63**, 134423 (2001).
- [22] P. Milténi, M. Gierlings, J. Keller, B. Beschoten, G. Guntherodt, U. Nowak, and K. D. Usadel, *Phys. Rev. Lett.* **84**, 4224 (2000).
- [23] U. Nowak, *Ann. Rev. of Comp. Phys.* **9**, 105 (2001).
- [24] M. Abramowitz and I. Stegun, *Handbook of Mathematical Functions* (Dover Publ., New York, 1972).
- [25] X. Batlle, M. García del Muro, and A. Labarta, *Phys. Rev. B* **55**, 6440 (1997).
- [26] M. García del Muro, X. Batlle, and A. Labarta, *Phys. Rev. B* **59**, 13584 (1999).
- [27] A. Lyberatos, *J. Phys. D: Appl. Phys.* **33**, R117 (2000).
- [28] D. K. Lottis, R. M. White, and E. D. Dahlberg, *Phys. Rev. Lett.* **67**, 362 (1991).
- [29] E. D. Dahlberg, D. K. Lottis, R. M. White, M. Matson, and E. Engle, *J. Appl. Phys.* **76**, 6396 (1994).
- [30] M. E. Matson, D. K. Lottis, and E. D. Dahlberg, *J. Appl. Phys.* **75**, 5475 (1994).
- [31] J. J. Préjean and J. Souletie, *J. Physique (France)* **41**, 1335 (1980).
- [32] R. Omari, J. J. Préjean, and J. Souletie, *J. Physique (France)* **45**, 11809 (1984).
- [33] B. Castaign and J. Souletie, *J. Phys. (France) I* **1**, 403 (1991).
- [34] R. Ribas and A. Labarta, *J. Appl. Phys.* **80**, 5192 (1996).
- [35] L. C. Sampaio, M. P. de Albuquerque, and F. S. de Menezes, *Phys. Rev. B* **54**, 6465 (1996).
- [36] D. Kechrakos and K. N. Trohidou, *J. Magn. Magn. Mater.* **177-181**, 943 (1998).
- [37] C. Xu, Z. Y. Li, and P. M. Hui, *J. Appl. Phys.* **89**, 3403 (2001).
- [38] H. Mamiya and I. Nakatani, *J. Appl. Phys.* **81**, 4733 (1997).

**Part II**

**THIN FILMS WITH PERPENDICULAR  
ANISOTROPY**





## CHAPTER 7

### 2D INTERACTING SYSTEMS

#### 7.1 Review of previous studies

The magnetic and transport properties of thin films and nanostructured materials have been the subject of intense research during at least the last two past decades because of their interest for magnetic recording and technological applications [1]. Among the interesting phenomena observed in this kind of materials there are the reorientation transitions of the magnetization with increasing temperature [2, 3, 4] or film thickness [2, 5, 6], the giant magnetoresistance effect [7, 8, 9], and the wide variety of magnetic patterns that can be stabilized depending on the interplay between the perpendicular induced surface anisotropy, the exchange interaction and the long-range dipolar forces between the microscopic entities.

The development of different microscopy techniques like MFM, AFM, LEM or SEMPA [10] have helped experimentalists to understand the interplay between the transport properties and the magnetic structure of the materials. Moreover, these techniques have shown that the magnetic structures formed in thin films are strongly influenced by the magnetic history of the sample. Thus, the observed patterns may display either out-of-plane ordering with labyrinthian striped domains [11, 12] or bubble-like patterns [6, 13] as well as in-plane vortex-like structures [14]. Most of the experimental samples being studied at present are epitaxial magnetic thin films of thickness ranging from 10 to 500 nm [6, 14, 15, 16, 17] or granular alloy films from 200 nm to 1  $\mu$ m thickness [18, 19]. Current experimental techniques allow to control the ferromagnetic content of granular alloys deposited on nonmagnetic metallic matrices [12] and, therefore, vary the range of dipolar and exchange interactions between the grains.

It seems clear that a realistic theoretical description of these experimental systems should be efficiently modeled by a two-dimensional lattice of spins. Spin coupling must include the exchange interaction, the on-site magnetocrystalline anisotropy, that provides the symmetry breaking required to establish long-range order in a quasi-2D system, and the dipolar interaction responsible for the long-range coupling between magnetic moments. The finite thickness of the samples can be taken into account by decreasing the value of the effective local anisotropy constant. The detailed nature of the magnetic anisotropy is determined by a subtle combination of the magnetocrystalline interactions, due to the structure of the crystal or presence of a surface, and the dipolar interaction, which is inherently anisotropic. The dipolar interaction, which is often ignored in theoretical studies of magnetic systems, plays an essential role in stabilizing long-range magnetic order in 2D systems, as well as in determining the nature and morphology of the ordered state. In addition to the inherent anisotropy of the dipolar interaction, its long-range character is also important in determining the magnetic properties of these materials. As discussed in the subsequent sections of this chapter, it is the interplay between the on-site, short-range, and long-range interactions that results in the rich variety of magnetic properties of these systems.

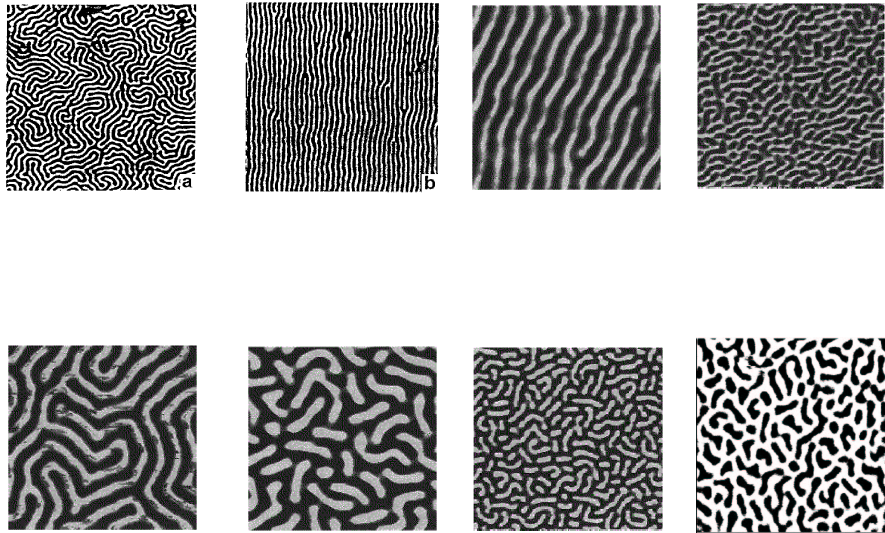


Figure 7.1: Several images of thin film configurations found experimentally.

The formation of ordered states, which are dependent on the long-range character of the dipolar interaction, including states with mesoscopic domain patterns, is a much wider phenomenon than the particular systems we have chosen to focus on this chapter. Indeed, this behavior is characteristic of a variety of quasi-twodimensional systems [20]. In this sense, the studies discussed in this chapter provide insight into a much wider class of physical systems than our particular examples.

The widespread appearance of macroscopic and mesoscopic equilibrium patterns displaying common structural features and exhibiting common modes of evolution suggests a possible universal mechanism to account for the formation of these textures. We can view them as a manifestation of modulated phases. Their periodic spatial organization is attributed to the presence of competing interactions favoring spatial inhomogeneities in an otherwise uniform ground state. In this picture, domains represent modulations in some order parameter [21], such as magnetization, as in epitaxial films of rare earth garnets, and polarization, as in ferroelectric films and Langmuir monolayers. The modulation period is set by the relative strengths of the competing interactions and can be tuned by varying parameters such as temperature and applied magnetic, electric, or other fields.

From the theoretical point of view, the current understanding of dipolar spin systems can be summarized as follows. It is well established that the ground state of a pure planar dipolar system (no anisotropy and no exchange interaction) is a continuously degenerate manifold of antiferromagnetic (AF) states [22, 23] (checkerboard phase). The introduction of exchange interactions ( $J > 0$ ) between the spins establishes a competition between the short-range ferromagnetic (FM) order and the long-range dipolar interaction that favours AF order [4, 24]. Contrary to what one would expect, increasing  $J$  does not serve to stabilize a FM ground state but instead results in the appearance of striped phases of increasing width that do not disappear at high  $J$ . A finite perpendicular anisotropy  $K$  favours the formation of out-of-plane configurations against the in-plane configurations induced by the dipolar interaction. Monte Carlo simulations [4, 25, 26, 27, 28, 29, 30] as well as theoretical analysis [23, 31, 32, 33, 34] have shown that there is a reorientation transition from out to in-plane order or from in to out-of-plane order depending on the ratio of  $K$  to  $J$  as the

temperature is increased [4, 25]. In the above mentioned works main attention was put on the determination of phase diagrams but apparently an accurate description of the detailed structure of the ground state has not been reported.

In this chapter we present the results of extensive Monte Carlo simulations of a model of a thin film with the aim to explain the variety of magnetic behaviours of the above mentioned experimental observations. We start by the description of the model Hamiltonian in Sec. 7.2. In Secs. 7.3, 7.4 and 7.5, some remarks on the dipolar interactions, the computational details and simulation procedure are given. In Sec. 7.6 the phase diagram and ground state configurations of the model are presented, demonstrating that it qualitatively reproduces the patterns observed in experiments. Finally, in Sec. 7.7, we present the results of two simulations that show the effect of two different magnetic histories on the magnetic order of the system.

## 7.2 Model Hamiltonian

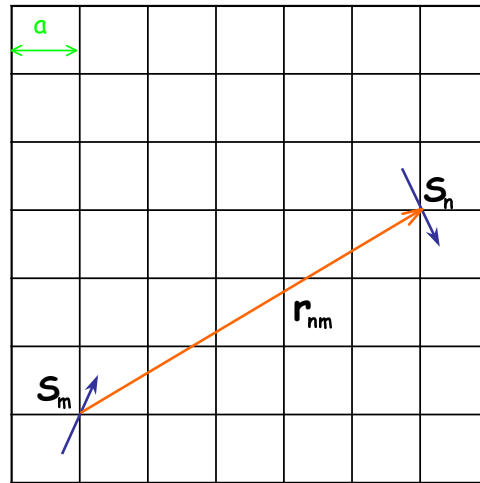


Figure 7.2: Diagram showing the lattice geometry and notations used in the definition of the Hamiltonian.

Our general model of a thin film consists of a two-dimensional square lattice (lattice spacing  $a$  and linear size  $N$ ) of continuous spins Heisenberg  $\mathbf{S}_i$  with magnetic moment  $\mu$  and uniaxial anisotropy  $K$  perpendicular to the lattice plane described by the Hamiltonian

$$\mathcal{H} = -\bar{J}\mathcal{H}_{exch} - \bar{K}\mathcal{H}_{anis} + \mathcal{H}_{dip} \quad (7.1)$$

where  $\bar{J}$ ,  $\bar{K}$ , and  $\mathcal{H}$  are given in units of

$$g \equiv \frac{\mu^2}{a^3} \quad (7.2)$$

with  $a$  the lattice spacing. The spins  $\mathbf{S}_i$  may represent either an atomic spin or the total spin of a grain.

The three terms in the Hamiltonian correspond to short-range nearest neighbour exchange interaction (direct between atomic spins or indirect through the matrix), uniaxial anisotropy energy perpendicular to the lattice plane, and long-range dipolar interaction

$$\mathcal{H}_{exch} = \sum_{n.n.} (\mathbf{S}_i \cdot \mathbf{S}_j) \quad (7.3)$$

$$\mathcal{H}_{anis} = \sum_{n=1}^{N^2} (S_n^z)^2 \quad (7.4)$$

$$\mathcal{H}_{dip} = \sum_{n \neq m}^{N^2} \left\{ \frac{\mathbf{S}_n \cdot \mathbf{S}_m}{r_{nm}^3} - \frac{(\mathbf{S}_n \cdot \mathbf{r}_{nm})(\mathbf{r}_{nm} \cdot \mathbf{S}_m)}{r_{nm}^5} \right\}. \quad (7.5)$$

In the last term  $\mathbf{r}_{nm}$  is a vector connecting spins at sites  $n$  and  $m$ . The first term favours antiferromagnetic long-range order while the second one introduces an effective easy-plane anisotropy.

Thus, the properties of the model depend only on two parameters.  $\bar{J}$ , which accounts for the competition between the ferromagnetic ( $J > 0$ ) interaction and the antiferromagnetic order induced by  $g$ , and  $\bar{K}$ , which accounts for the competition between the out-of-plane alignment favoured by  $K$  and the in-plane order induced by  $g$ .

We will present results for three kind of systems with different spin dimensionality:

- a. Ising spins pointing in the direction perpendicular to the film plane.
- b. Planar spins pointing in the direction of the film plane.
- c. Heisenberg spins free to point in any direction.

### 7.3 Dipolar interactions in spin systems

It is well known that long range order (LRO) is ruled out in a 2D spin model with continuous symmetry when the spin-spin interaction is short ranged [35, 36, 37]. On the other hand, long range interactions may or may not support LRO in the 2D planar model. For instance, spin-spin interactions decaying as  $1/r^3$ , where  $r$  is the spin-spin distance, are believed to support LRO when the interaction is ferromagnetic [38], whereas no LRO is expected when the interaction is antiferromagnetic on the basis of MC simulation [39].

Dipolar interactions in systems with reduced dimensionality have been widely studied in the literature. In the 40's, Luttinger and Tisza [40, 41] studied the magnetic order of 3D arrays of interacting dipoles in SC, FCC and BCC lattices without taking into account neither the exchange nor anisotropy energies, they were able to show that the type of ordering depends on the geometry of the lattice. They also applied their method to derive the ground state of AF in several lattices [42], a problem previously addressed by Anderson [43] in 1950. Their theory was latter generalized by Niemeijer and Blötte [44, 45] to include the exchange interaction and by Misra [46] to allow more than one spin per unit cell. More recently, Fernández and Alonso [47] extended the analysis to some tetragonal and triclinic lattices with pure dipolar interactions. Cohen and Keffer [48, 49] also made predictions similar to the classical theory based on a quantum spin-wave approximation technique.

Later on, Kittel [50] set up the context of the modern theory of ferromagnetic domains in magnetic materials. In terms of a micromagnetic model for continuous spins, he was able to deduce the structure of the striped domain configurations that appear in thin films with slab geometry as a function of the film thickness. In the micromagnetic approach, both short-range exchange interactions and anisotropy energies are considered and the dipolar interaction is usually taken into account through the demagnetizing energy.

Fortunately, in 2D, the equilibrium configurations of interacting dipoles can be more easily gazed due to the reduced dimensionality of the system. This situation has been addressed theoretically by Politi [51, 52], MacIsaac [22], Zimmerman et al. [53], and Prakash and Henley [23] by using spin-wave or mean-field methods to compute the free energy. These authors have shown that the ground state of dipolar 2D pure dipoles is highly degenerate. Prakash and Henley [23], and Romano [39] and Rastelli et al. [54, 55] later, showed that thermal fluctuations can remove the degeneracy by selecting certain configurations, in an example of what is called order by thermal disorder [56, 57].

However, the situation becomes more involved when short range interactions or anisotropy energies are taken into account. In this case, the existence of stripped phases complicates the calculations concerning the ground state of lattice models and, in order to obtain conclusive results, one is forced to treat the problem through computer simulations. In spite of that, theoretical models of thin films have faced the problem of reorientation transitions [51, 52, 58, 59] and domain structure [32, 60, 61] in the continuum approximation.

### 7.3.1 Dipolar interaction matrices

The expression for the dipolar energy is most conveniently treated in terms of a set of matrices  $W_{nm}^{\alpha\beta}$  ( $\alpha, \beta = x, y, z$ ) as

$$\mathcal{H}_{dip} = \sum_{n \neq m}^{N^2} \sum_{\alpha, \beta=1}^3 S_n^\alpha W_{nm}^{(\alpha\beta)} S_m^\beta. \quad (7.6)$$

Where the set of matrices  $W_{nm}^{\alpha\beta}$  representing the different components of the dipolar interaction between a pair of spins  $n, m$  has been defined as

$$W_{nm}^{\alpha\beta} = \frac{1}{r_{nm}^3} \left( \delta_{\alpha\beta} - \frac{3 \delta_{\alpha\gamma} \delta_{\beta\eta} r_{nm}^\gamma r_{nm}^\eta}{r_{nm}^2} \right) \quad (7.7)$$

$\alpha$  and  $\beta$  are indexes characterizing the kind of matrix while  $n, m$  characterize the different components. In two (three) dimensions, only 4 (6) matrices are necessary to compute the dipolar energy since they are symmetric with respect to  $\alpha$  and  $\beta$ . As an example, in Fig. 7.4, we show a representation of the matrix elements for  $N = 5$  in terms of a coloured pattern.

These matrices depend only on the lattice geometry and the boundary conditions and not on the particular spin configuration, so in order to save computer time they can be computed and stored at the beginning of the program before the Monte Carlo evolution starts. The inconvenience of this is that they have  $N^2 \times N^2$  components with double precision numbers and that for systems with a large number of spins the memory requirement are prohibitive. However, after inspection of their internal structure (see the patterns in Fig. 7.3), one realizes that they have some symmetry properties which reduce considerably the number of different independent components to be stored.

## 7.4 Computational details

The computer simulations have been performed using the Monte Carlo technique. In this section we will present some of the subtleties related to the application of this method that arise when long-range interactions such as the dipolar interactions are present.

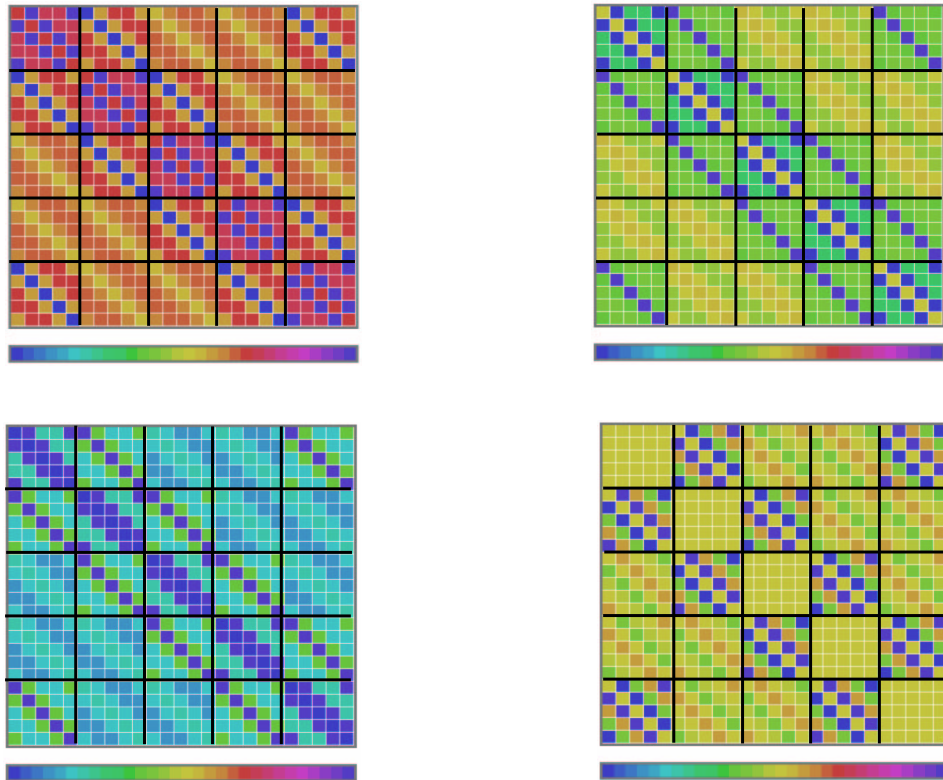


Figure 7.3: Dipolar interaction matrices for a system with  $N = 5$ :  $W^{xx}$ ,  $W^{yy}$ ,  $W^{xy}$ ,  $W^{zz}$  in clockwise sense. Each coloured square represents the matrix element  $W_{ij}^{\alpha\beta}$ . The matrix elements have been coloured according to the maps shown below each figure (with values increasing from negative to positive from left to right).

There are mainly two ways in which the dipolar interaction affects the Monte Carlo procedure.

- The most obvious complication arises as a consequence of the fact that the dipolar interaction is not a simple nearest-neighbour interaction. Indeed, flipping a spin affects every other spin in the system. This means that many of the procedures that have been developed to improve the efficiency of the algorithm used in the Monte Carlo simulation, that either implicitly or explicitly exploit the finite range of the interaction, either have to be modified or are no longer applicable. It also means that the time required to perform a Monte Carlo step for an  $N \times N$  site system increases as  $N^4$ , rather than  $N^2$  for a localized interaction. This makes the problem extremely computation intensive and limits the size of the system that can be investigated in practice.
- The other difficulty associated with including the dipolar interaction in a Monte Carlo simulation is how best to mitigate finite-size effects. Again, the long-range character of the dipolar interaction considerably complicates matters, as edge effects can give rise to an effective current loop around the boundary of the system if finite-size effects are not treated carefully.

We end these preliminary remarks by noting two points with regard to finite-size systems. The first point is that, while larger values of  $N$  generally lead to more reliable results, care has to be taken to ensure that the ground state is included in the subset of allowed spin configurations used in the analysis or, equivalently, that the ground state is commensurate with the imposed periodicity  $N$ . The second point is that the effective interaction can be used to calculate the dipolar energy of any spin configuration with a commensurate periodicity.

### 7.4.1 Boundary conditions

The long-range character of the dipolar interaction makes it difficult to treat the well-known problems associated with the finite-size effects by means of the standard finite-size analysis. The most effective way to circumvent this problem is by using a well-known method in the Molecular Dynamics and Monte Carlo simulations of liquids [62] and that was implemented to spin lattices by Kretschmer and Binder (KB) [63]. It consists on replacing the original finite spin lattice by an infinite set of copies (hereafter called "replicas") of the system surrounding the original lattice of spins. In this way the appearance of any artificial stray fields that would result from the cut-off of the long-range of the dipolar interaction by the finite extent of the  $N \times N$  spin lattice can be avoided by replacing periodic boundary conditions by interactions between the original spins and the corresponding partners on the infinite set of replicas.

Then the position of any spin (including those in the replicas) can be determined by the vector

$$\mathbf{R}_{mn} = \mathbf{r}_{mn} + \mathbf{G}, \quad (7.8)$$

where  $\mathbf{G} = N \times (i_g, j_g)$ , ( $i_g, j_g = 0, \pm 1, \pm 2, \dots$ ) are the vectors that join one spin of the original system with its equivalent partners on the corresponding replicas [64].

The technique restricts the sum over states to those which are periodic. In the case of a square lattice, the only spin configurations included in the summation are those that satisfy the requirement

$$S^\alpha(x, y) = S^\alpha(x + nN, y + nN) \quad (7.9)$$

where  $n$  and  $m$  are integers and where the  $x$  and  $y$  axes are within the square lattice and the  $z$  axis is perpendicular to it. Such configurations may be completely specified in terms of  $L^2$  spins in an  $L \times L$  unit



cell. Denoting by  $\vec{R}_n$  the  $L^2$  sites in the  $L \times L$  unit cell, and defining the lattice translation vector  $\vec{T}$  as

$$\vec{T} = L(n\hat{x} + m\hat{y}) \quad (7.10)$$

where  $n$  and  $m$  are integers, one may write the dipolar energy as

$$\mathcal{H}_{\text{dip}} = \sum_{n \neq m}^{N^2} S^\alpha(\vec{r}_n) W_{nm}^{(\alpha\beta)}(\vec{r}_{mn}) S^\beta(\vec{r}_m) = \quad (7.11)$$

$$\frac{N^2}{L^2} \sum_{n \neq m}^{L^2} S^\alpha(\vec{R}_n) \Gamma_{nm}^{(\alpha\beta)}(\vec{R}_{mn}) S^\beta(\vec{R}_m) + N^2 L^2 \sum_{\vec{T} \neq 0} \gamma_{nm}^{(\alpha\alpha)}(\vec{T}) \quad (7.12)$$

where we have defined  $\Gamma_{nm}^{(\alpha\beta)}(\vec{R}_{mn})$  as

$$\Gamma_{nm}^{(\alpha\beta)}(\vec{R}_{mn}) = \sum_{\vec{T}} \gamma_{nm}^{(\alpha\beta)}(\vec{R}_{mn} + \vec{T}). \quad (7.13)$$

Thus, the calculation of the dipolar energy can be written as a sum over the  $L^2$  spins that make up the  $L \times L$  unit cell, which interact through an effective interaction  $\Gamma^{(\alpha\beta)}(\vec{R}_{mn})$ .

Therefore, the interaction matrices  $W_{nm}^{(\alpha\beta)}$  have to be calculated as

$$W_{nm}^{(\alpha\beta)} = \sum_{\mathbf{G}} \left( \frac{\delta_{\alpha\beta}}{|\mathbf{r}_{nm} + \mathbf{G}|^3} - \frac{3\delta_{\alpha\gamma}\delta_{\beta\eta}(r_{nm} + G)^\gamma(r_{nm} + G)^\eta}{|\mathbf{r}_{nm} + \mathbf{G}|^5} \right). \quad (7.14)$$

In practice, the infinite sum over  $\mathbf{G}$  has to be cut-off to a finite number of replicas that, even if the Ewald sum technique [26] is used to improve convergence, has to be carefully considered because the sum converges very slowly. We have checked the numerical evaluation of the interaction matrices by reassuring that the dipolar energy in Eq. (7.3) gives the exact result when a configuration with perpendicular saturated spins is considered. In this case the dipolar sum becomes [65, 66]

$$E_{dip}^\perp = \sum_{ij} \frac{1}{(i^2 + j^2)^{3/2}} = \zeta(3/2, 0)[\zeta(3/2, 1/4) - \zeta(3/2, 3/4)] = 9.0336. \quad (7.15)$$

For simulation convenience these matrices can be calculated once before starting the simulation and stored in a look-up table to be used when necessary. It should be noted however that, although in the case of a 2D lattice only five of them [ $W_{nm}^{(xx)}$ ,  $W_{nm}^{(yy)}$ ,  $W_{nm}^{(xy)}$  and  $W_{nm}^{(zz)}$ ] are needed, the memory required to store them becomes prohibitive for large system sizes, they are  $N^2 \times N^2$  dimensional. However, a detailed study of their structure reveals that the translational symmetry of the replicas and the symmetries of the underlying squared lattice induce some symmetry properties in the  $W_{nm}^{(\alpha\beta)}$ 's.

#### 7.4.2 Symmetries of the dipolar matrices

The translational symmetry of the replicas with respect to the original system given by (7.8) can be exploited to reduce the number of independent components of  $W_{mn}^{\alpha,\beta}$  and thus to reduce considerably the computational time in the simulations. A detailed study of these  $N^2 \times N^2$  dimensional matrices shows that they can be reproduced with the help of only  $N$  submatrices  $w_{ij}[k]$  ( $i, j, k = 1, \dots, N$ ) of dimension  $N \times N$ . The box structure of the  $W$ 's and the internal structure of the  $w[k]$  submatrices is as follows:

1. The  $W$ 's are symmetric with respect to both diagonals.
2. The box structure of the  $W$ 's is also symmetric with respect to both diagonals as reproduced in the figure below and the boxes on the first row is formed by the  $N$  different submatrices  $w[k]$ .
3. Every submatrix  $w_{ij}[k]$  is also symmetric with respect to both diagonals, the  $N$  elements of the first row being different. Knowing them the rest of the submatrix can be reproduced.

$$\begin{pmatrix} W[1] & W[2] & \dots & W[N-1] & W[N] \\ W[2] & W[1] & W[1] & \dots & W[N-1] \\ W[3] & W[2] & W[1] & \dots & W[N-2] \\ & & & \ddots & \\ W[N] & W[N-1] & \dots & W[2] & W[1] \end{pmatrix}$$

Figure 7.4: Composition in boxes  $w[i]$  of the dipolar interaction matrices  $W_{nm}^{(\alpha\beta)}$ .

Consequently, knowing the first row of every one of the  $N$  submatrices  $w[k]$ , the whole interaction matrix  $W_{nm}^{(\alpha\beta)}$  can be reproduced. Thus, it is only necessary to compute  $N^2$  out of the  $N^4$  elements of every matrix  $W_{nm}^{(\alpha\beta)}$ .

## 7.5 Simulation procedure

In this section, we will specify the computational scheme and algorithmic details used in the MC simulations, focusing on the peculiarities associated with the use of continuous spins rather than Ising spins to represent the atomic magnetic moments of real samples.

### 7.5.1 Simulated annealing

Monte Carlo simulations of the ground state of the system were performed by the method of simulated thermal annealing [67, 68, 69, 70, 71, 72]. The system is initially prepared in a configuration of randomly oriented spins at high temperature. Then the spins are allowed to relax during a number of MCS necessary to achieve thermal equilibrium at the considered temperature (usually between 200 and 250 MCS per spin). The temperature is progressively lowered with a constant cooling rate  $\Delta T$  (we started with a temperature of 10 and we used a reduction factor of 0.9), and the relaxation process repeated until the ratio of proposed to accepted changes is lower than a given predetermined small value  $\varepsilon$ . The ground state of the system is

considered to be the configuration reached at the end of the lowest temperature relaxation. In this way, we have obtained the ground state energies and configurations of the system.

The dynamics used for the relaxation is based on the classical Metropolis algorithm but the choice of the method of proposal of spin flips at every MCS deserves some comments for Heisenberg spins. The details of the method are left to Appendix 10. Let us only mention here that, in this case, there is a continuum of possible states for the spin characterized by the spherical angles  $(\theta, \phi)$  and consequently many ways to attempt to change the state of a given spin. In order to ensure that the true ground state of the system is faithfully achieved by the considered simulated annealing procedure, we have found convenient to choose the proposed new state  $(\theta', \phi')$  for the change of a spin at every MCS randomly inside a cone of aperture  $\delta\theta$  with respect to the original orientation. This aperture of the cone is varied from the  $\delta\theta = \pi$  initial value (jumps to any direction) according to the following strategy. At every temperature  $\delta\theta$  is chosen in such a way that the acceptance rate of the proposed states is higher than a certain value. For this purpose, we use a small number of the first MCS at each temperature (10 in most cases) to sample the range of angles with higher acceptance probability.

This procedure results in a progressive reduction of  $\delta\theta$ , so that the closer is the system to the ground state, the smaller the deviation of the proposed jumps from the current configuration. In this way, we get rid of the inconvenience of trying non-effective jumps that would not allow the system to converge to the proper equilibrium configuration.

## 7.5.2 Calculation of dipolar fields

The most time consuming part of the program is of course the calculation of dipolar energy at each MCS, since it involves a double sum over all lattice spins. In order to minimize the CPU time needed for this computation, we have followed the following strategy:

1. At the beginning of the program the dipolar and exchange local fields on every spin  $n$ , defined as

$$\begin{aligned} (h_{dip})_n^\alpha &= \sum_{m \neq n} \sum_{\beta} W_{nm}^{\alpha\beta} S_m^\beta \\ (h_{exch})_n^\alpha &= \sum_{m=n.n} S_m^\alpha, \end{aligned} \quad (7.16)$$

are calculated and stored in an array.

2. In this way, the energy can be simply calculated as a product of the spin components by the local field acting on it as

$$\begin{aligned} (\mathcal{H}_{dip})_n &= \mathbf{S}_n \cdot \mathbf{h}_{dip} \\ (\mathcal{H}_{exch})_n &= \mathbf{S}_n \cdot \mathbf{h}_{exch}, \end{aligned} \quad (7.17)$$

with minimum time consumption.

3. Moreover, by updating the local dipolar field array only if the spin change is accepted, one can considerably save CPU time by a factor equal to the acceptance rate given by the Boltzmann distribution, which is particularly low at low temperatures.

## 7.6 Ground state properties

We start by studying the properties of the ground state of the model at zero temperature. For this purpose, we have followed the simulated thermal annealing method already described in previous sections. In this way, we have obtained the ground state energies and configurations of the system. In the phase diagrams, we have plotted separately the contributions of the different energy terms to the total energy. Moreover, the magnetizing and demagnetizing contributions (first and second contributions in  $\mathcal{H}_{dip}$  of Eq. 7.3 respectively) of the dipolar energy have been computed.

### 7.6.1 Phase diagram

#### Ising Model

Let us start by considering the case of Ising spins perpendicular to the thin-film plane, which corresponds to the case  $K = +\infty$ . Since now the spins are restricted to order either parallel or anti-parallel to the direction perpendicular to the plane, the ground state configuration is only dictated by the competition between the exchange interaction that tends to align neighbouring spins ferromagnetically and the dipolar interaction, which in this case has only the demagnetizing component and, therefore, favours AF alignment. As a result of this competition of short and long-range energies, striped phases will appear. The width of the stripes depends only on the value of the parameter  $\bar{J} = J/g$ . In Fig. 7.5, we show the energies of the ground states of the system as a function of  $\bar{J}$ , obtained by the simulated annealing method. The exchange and anisotropy contributions to the total energy are plotted separately. For the pure dipolar case ( $\bar{J} = 0$ ), the ground state corresponds to the checkerboarded configuration, with all spins having their nearest neighbours AF aligned. When increasing  $\bar{J}$ , the exchange energy progressively destroys the checkerboarded phase, and when a certain critical value  $J^*$  is attained, the exchange energy can be diminished by the formation of parallel stripes of AF ordered spins. As  $\bar{J}$  increases further it becomes energetically more favourable to form wider stripes in order to minimize the exchange energy even at the expenses of a gain in dipolar energy due to surface charges. As it has been shown elsewhere [24, 73], the increase of the stripe width with  $J$  follows approximately an exponential law of the type

$$h(\bar{J}) = h_0 e^{\bar{J}/4} \quad (7.18)$$

with  $h_0 = 0.871$ , valid in the limit  $h \rightarrow \infty$ . The authors also derive approximate expressions for the dipolar and exchange energies of striped phases in this limit

$$E_{exch} = -2J \left(1 - \frac{1}{h(\bar{J})}\right) \quad (7.19)$$

$$E_{dip} \simeq E_{FM} - \frac{1}{2h(\bar{J})} [A + B \ln h(\bar{J})] \quad (7.20)$$

where in the last formula  $A = 9.105$  and  $B = 8$ . The results of our simulations are in agreement with these predictions as can be seen in the dash-dotted lines of the right panel of Fig. 7.6, that approaches the simulation results for large  $\bar{J}$ .

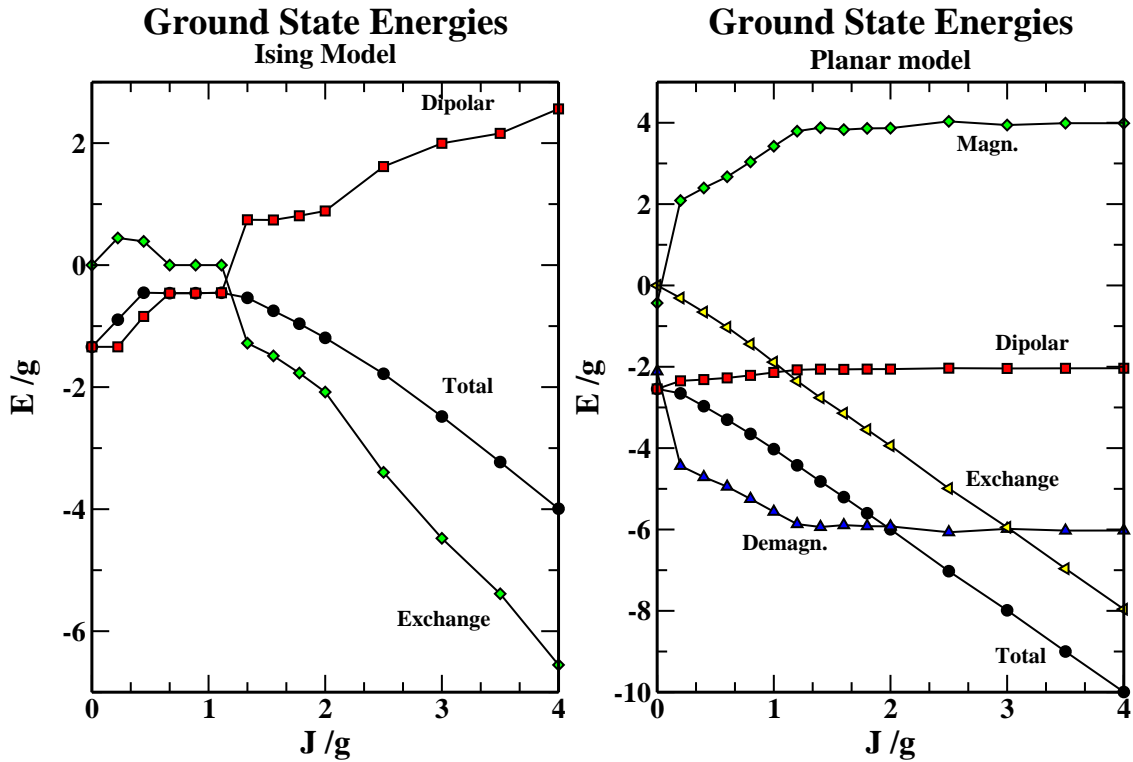


Figure 7.5: Energy contributions to ground state configurations of the Ising and XY Planar model.

### Planar Model

Let us see what happens in the opposite limit of spins confined to point into the direction of the thin-film plane ( $K = -\infty$ ). The spins considered are continuous and, in principle, can have both  $x$  and  $y$  components [ $\mathbf{S}_n = (S_n^x, S_n^y)$ ]. As already mentioned in Sec. 7.3, the ground state of pure dipolar planer lattices is AF [53, 54, 74, 75], that is to say, spins order ferromagnetically forming columns with adjacent columns Af aligned. However, this ground state is highly degenerate due to the symmetry  $\varphi \rightarrow \varphi \pm n\pi/2$  ( $\varphi$  measures the orientation of the spins inside the plane). When FM exchange interactions are included [22, 23], the situation is maintained, but now vortices can be formed due to the competition of the short and long-ranged interactions [30, 76, 29].

The energy of the ground state is shown in Fig. 7.5 (right panel) as a function of  $\bar{J}$ . Here, the magnetizing and demagnetizing parts (first and second terms in Eq. 7.3) of the dipolar energy have been distinguished. For small values of  $\bar{J}$ , the dipolar energy contribution is important enough to sustain a regular lattice of vortices of increasing diameter as  $\bar{J}$  increases. For  $\bar{J} > 2.0$  the dipolar energy contribution to the ground state equals the value corresponding to in-plane FM alignment (*i.e.*  $-2.0$ ) and the total energy becomes linear in  $\bar{J}$ . In this regime, the exchange interaction destabilizes the vortex lattice destroying the vortices and leading to a FM order of the spins into large sized domains with a small disalignment between them. This evolution is more clearly seen by looking at the variation of the vorticity order parameter (see Fig. 7.10) which is defined in Eq. (7.21) below.

### Finite $K$ Model

In this more general case, the spin direction is not restricted and Heisenberg spins with three components will be considered. Now, a richer variety of configurations arises due to the interplay of the perpendicular anisotropy with the exchange and dipolar interactions. In Fig. 7.6, we present the different contributions to the ground state energy for two values of  $K$ . For moderate anisotropy ( $\bar{K} = 5$ ), we observe a reorientation transition from out to in-plane magnetization with increasing  $\bar{J}$  signaled by the sudden decrease of the demagnetizing component of the dipolar energy together with the vanishing of the anisotropy energy. For strong anisotropy ( $\bar{K} = 10$ ), the film is perpendicularly magnetized for the range of  $\bar{J}$  values shown, and the variation of the energy with  $\bar{J}$  is similar to that of the Ising case.

In Fig. 7.7, we present the results of the simulations for the ground state energies of the finite  $K$  model as a function of the reduced exchange parameter  $\bar{J}$  and for different values of the anisotropy constant (open symbols). In filled circles the energy of the corresponding Ising model ( $K = +\infty$ ) is also given for comparison, the dashed lines correspond to the same curve with the corrections for the different finite anisotropy values added. The continuous line corresponds to the same calculation for the planar (XY) model.

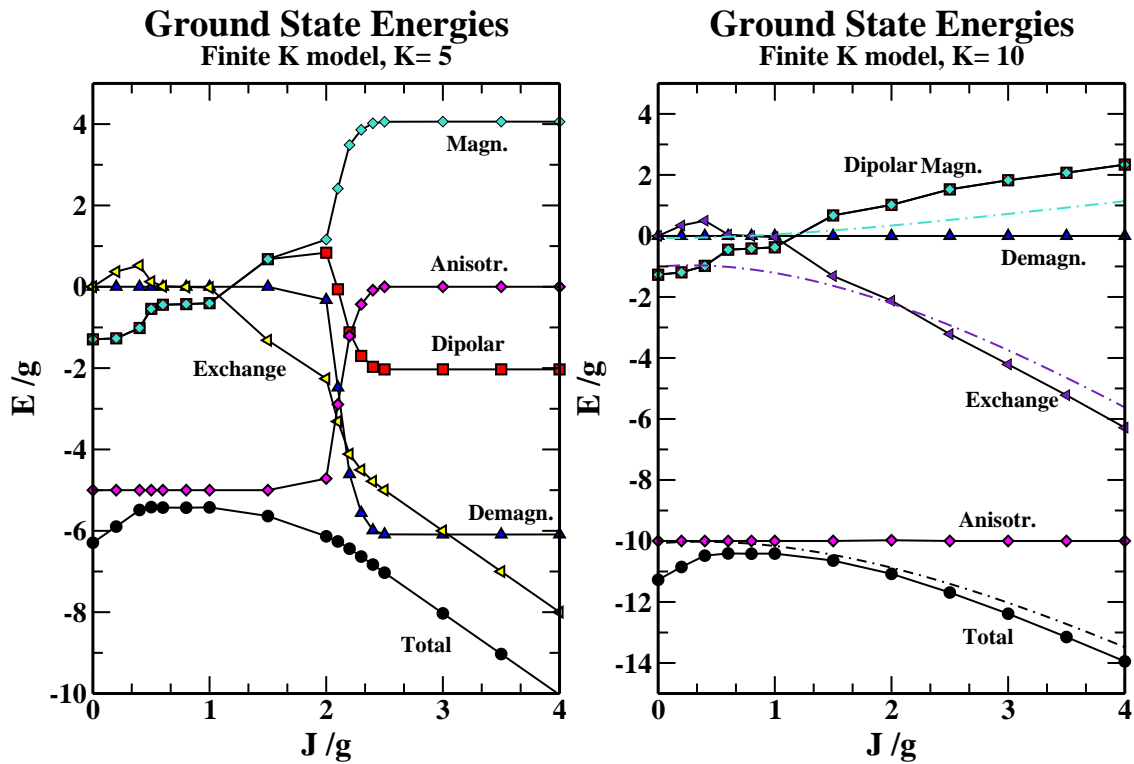


Figure 7.6: Energy contributions to ground state configurations of the finite  $K$  model.

A characteristic feature of the finite  $\bar{K}$  model is that it behaves in a bimodal way. For a given value  $\bar{K}$ , when  $\bar{J}$  is small ( $\bar{J} < \bar{J}^*$ ), it is completely equivalent to the corresponding Ising model, displaying out-of-plane order. However, for  $\bar{J} > \bar{J}^*$ , it behaves like the planar model and it orders in-plane. The value of  $\bar{J}^*$  at which the crossover occurs is simply the one for which the ground state energy of the planar model (thick solid line) equals the energy of the corresponding Ising model with the finite anisotropy correction corresponding to a given value of  $\bar{K}$  (dashed lines). Therefore, the phase diagram for the finite  $\bar{K}$  model

## Ground State Energies

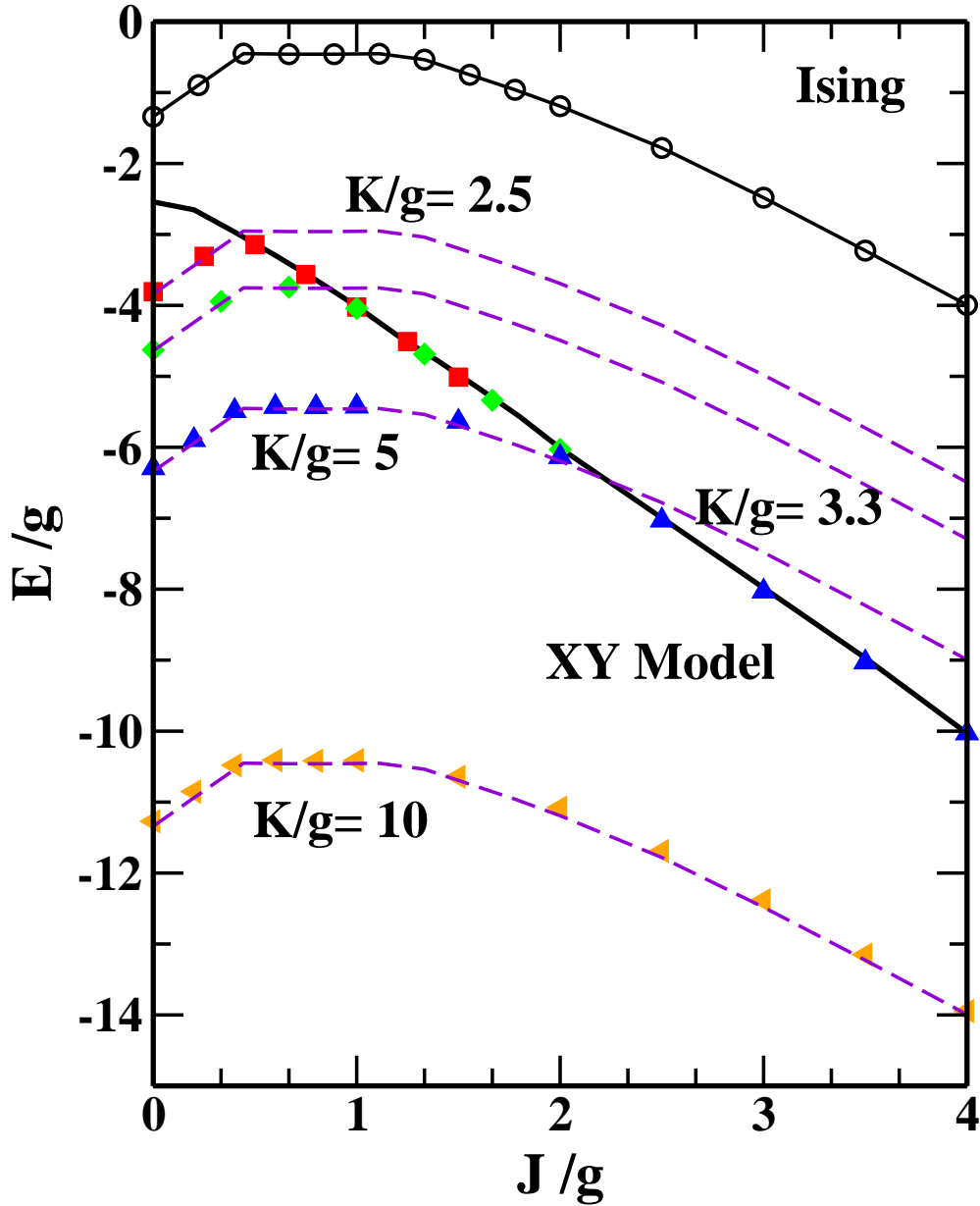


Figure 7.7: Ground state energy as a function of the reduced exchange constant  $\bar{J} = J/g$  for different values of the anisotropy constant  $\bar{K} = K/g$  as indicated in the figure. Filled symbols correspond to the general finite anisotropy case described by the Hamiltonian (7.1). Open circles correspond to the Ising model ( $K = +\infty$ ) and the continuous line to the planar (XY) model ( $K = -\infty$ ). The dashed lines show the ground state energy of the Ising model plus the anisotropy energy corresponding to the nearest finite  $\bar{K}$  curve.

can be directly obtained from the results for the planar model by shifting the energy of the Ising model with the corresponding value of  $\bar{K}$ . Consequently, the Heisenberg model for finite  $\bar{K}$  is the combination of the simpler Ising and planar models and its behaviour is dominated by the one having the lowest ground state energy.

The reorientation transitions from in-plane to out-of-plane order as the film thickness  $L$  is decreased observed in real samples can be easily understood by looking at the phase diagram. The decrease in  $L$  can be understood as an increase in the effective anisotropy of the film [2, 5, 60]. Therefore, the reorientation transition is signaled by the crossing of the finite  $\bar{K}$  curve with the curve of the planar model (continuous line in Fig. 7.7) at the corresponding value of  $\bar{J}$ .

The region of parameters of interest to us is precisely those values of  $\bar{J}$  around the crossover points  $\bar{J}^*$ , since in this region the out and in-plane configurations are quasi-degenerated in energy and the system displays metastability. That is to say, different kinds of ordering may be induced depending on how the system is driven to the quasi-equilibrium state, as we will show in the next sections.

### 7.6.2 Configurations

Before proceeding further, let us analyze the ground state configurations in more detail. On the one hand, for  $\bar{J} < \bar{J}^*$  (Ising regime) all the curves show three characteristic regions corresponding to different kinds of out-of-plane order. For small values of  $\bar{J}$ , the dipolar energy dominates over the exchange energy and the system orders antiferromagnetically (AF) in a checkerboarded phase of increasing energy as  $\bar{J}$  increases (two left columns in Fig. 7.8). At intermediate  $\bar{J}$  values, the system enters a constant energy region in which a phase of AF stripes of width  $h = 1$  is stabilized by the exchange interaction (third column from the left in Fig. 7.8). Out from this plateau, the FM ordering increases, resulting in a widening of the stripes and an almost linear decrease of the energy with  $\bar{J}$  (fourth and fifth columns for  $\bar{K} = 5.0, 10.0$  in the same figure). In the metastable region ( $\bar{J} \approx \bar{J}^*$ ), the system starts to turn to the planar regime, first displaying configurations with a regular array of vortices with remanent out of plane internal order. This fact can be observed for the case  $\bar{K} = 3.3$ ,  $\bar{J} = 1, 1.33$  in Figs. 7.6 and 7.9, where the in-plane projections of the spins are displayed with arrows. The diameter of the vortices progressively increases with increasing  $\bar{J}$  until the FM order induced by the exchange energy stabilizes the in-plane FM configuration.

Moreover, at small values of  $\bar{K}$ , the system can change to the planar phase without entering some or any of the above mentioned Ising regions. On the contrary, at high enough  $\bar{K}$ , the system never crosses to the planar phase, behaving as the Ising model for any value of  $\bar{J}$ .

Our results seem to confirm the predictions of a recent work on domain structures in thin films by P. Politi [51, 52] which has extended and refined similar previous calculations by Yafet and Gyorgy [32] and corrected some wrong conclusions made by Czech and Villain [77]. These works studied the classical ground state properties of the Heisenberg model defined by (7.1) in the continuum approximation. By taking into account the finite domain width of stripe configurations, the authors concluded that, for values of  $\bar{K} \approx 1$ ,  $K = g(1 - g/16J)$ , there is a narrow range of  $\bar{K}$  values for which the domain walls separating the stripes of the ground state configurations in the Ising regime acquire a finite width before turning into plane.

The vortex configurations observed in the simulations were also predicted by several theoretical studies. Among them, let us mention the work by Goueva et al. [78, 79], where they studied the classical 2D anisotropic model by means of analytic calculations based on a continuum description and also numerical



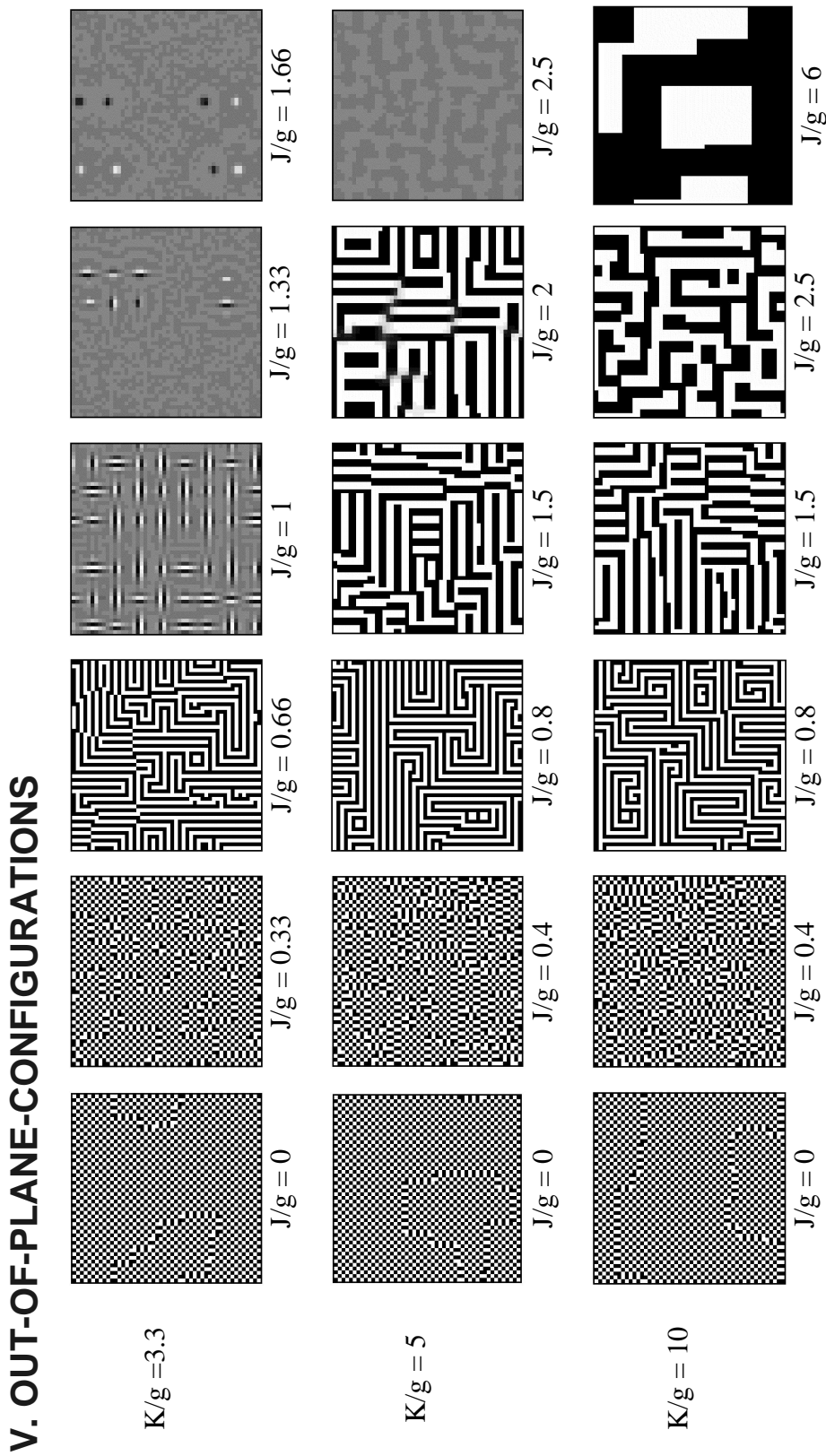
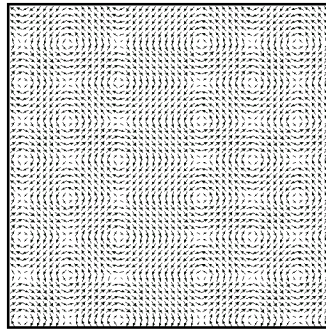


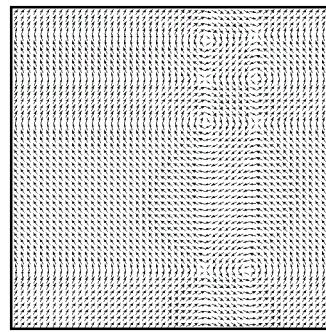
Figure 7.8: Ground state configurations obtained by the method of simulated annealing for the finite  $K$  model for a system of  $50 \times 50$  spins and some of the  $\bar{J}$  and  $\bar{K}$  values of the phase diagram of Fig. 7.7. Only the out-of-plane projections ( $S_z$ ) are shown in a grey scale ranging from white ( $S_z = +1$ ) to black ( $S_z = -1$ ).

## IN-PLANE-CONFIGURATIONS

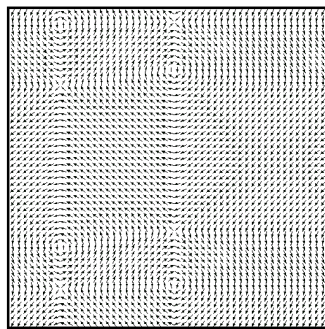
$K/g=3.3$



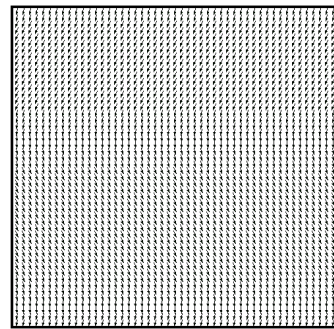
$J/g=1.0$



$J/g=1.33$

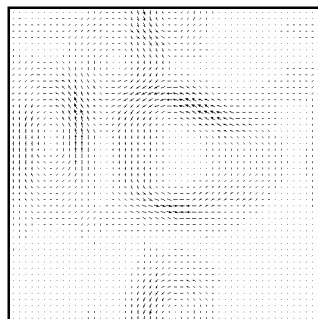


$J/g=1.66$

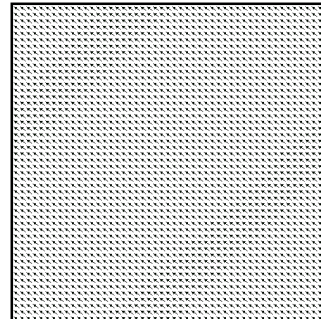


$J/g=2.0$

$K/g=5$



$J/g=2.0$



$J/g=2.5$

Figure 7.9: In-plane configurations of some of the cases shown in the previous figure 7.8. The arrows represent the projections of the spins into the plane of the film.

simulations for a discrete lattice. They identified two types of static vortices: below a critical anisotropy  $\delta_c$  in the perpendicular direction, planar vortex structures are stable with spins confined to the XY plane, while above  $\delta_c$  out-of-plane vortices are stabilized with a  $S^z$  component near the center. On the other hand, Nikiforov and Sonin [80] studied the isotropic Heisenberg model with local on-site anisotropy and obtained asymptotic equations for out-of-plane vortex solutions identical to the previous model with  $\delta = 1$  and now a vortex radius  $r_v = \sqrt{\frac{J}{2K}}$ .

### 7.6.3 Order parameters

The transitions among the different kinds of order found in the simulations can in fact be modelled by appropriate order parameters. In this section, we will introduce a set of order parameters that will allow us to characterize better the properties of the system. In particular, they must be able to signal the transitions from in to out-of-plane order, the formation of vortices and the appearance of striped phases.

1. *Vorticity*, which is the discretized version of the usual definition for a continuous field  $\rho_{vort} = \vec{\nabla} \times \vec{S}$ :

$$\rho_{vort} = \frac{1}{N^2} \sum_{i,j} \left\{ (S_{i+1,j}^y - S_{i,j}^y) - (S_{i,j+1}^x - S_{i,j}^x) \right\}. \quad (7.21)$$

This parameter ranges from 0 to 2 for vortices of radius 1.

2. *Out and in-plane n.n. correlation functions*

$$C_z = \frac{1}{4N^2} \sum_{n=1}^{N^2} S_n^z \left( \sum_{m=1}^{n.n} S_m^z \right), \quad (7.22)$$

$$C_{xy} = \frac{1}{4N^2} \sum_{n=1}^{N^2} \mathbf{S}_n^{\parallel} \cdot \left( \sum_{m=1}^{n.n} \mathbf{S}_m^{\parallel} \right), \quad (7.23)$$

where  $S_n^z$  and  $S_n^{\parallel}$  are the out-of-plane and in-plane projections of the spin vectors. Both  $C_z, C_{xy}$  range from -1 for AF order to +1 for FM order.

3. *Chain order parameter*

$$\rho_{chain} = \frac{1}{(N-1)N^2} \sum_{i,j=1}^N \frac{|N_{ij}^x - N_{ij}^y|}{\min\{N_{ij}^x, N_{ij}^y\}} \quad (7.24)$$

where

$$N_{ij}^{x/y} = 1 + \sum_{k|l \in E} S_{k,j/i,l}^z,$$

and  $E$  is the cluster of spins surrounding  $\mathbf{S}_{i,j}$  in the  $x/y$  directions having the same sign of  $S^z$  as  $S_{i,j}^z$ . This parameter is 1 for parallel stripes of width 1 along the  $x/y$  directions and decays to zero when no striped structures are formed.

The variation of the different order parameters with  $\bar{J}$  of the ground state configurations for some of the values of  $\bar{K}$  given in Fig. 7.7 is shown in Fig. 7.10.

First let us comment on the parameters signaling the transition from out to in-plane order, these are  $C_z$  and  $C_{xy}$ . In the case of moderate perpendicular anisotropy ( $\bar{K} = 3.3, 5$ ), the reorientation transition from out to in-plane order is signaled by the abrupt vanishing of  $C_z$  at a given value of the exchange coupling  $J^*$ . For lower values of  $\bar{J}$ , one enters the Ising-like regime where the dipolar coupling dominates over exchange interactions, favouring AF aligned structures as indicated by the negative value of  $C_z$ . This correlation function, which equals -1 in the checkerboard phase in the pure dipolar case ( $J = 0$ ), decreases progressively as the width of the stripes increases. In the same way,  $C_{xy}$  vanishes below  $\bar{J}^*$  and then progressively increases as the spins reorientate themselves into the plane. Its value tends to +1, as the increasing FM interaction progressively destroys the out-of-plane stripes and the in-plane vortices.

The vorticity and chain parameter help us to determine the range of  $\bar{J}$  for which coexistence of in and out-of-plane structures is observed (metastable region). In all the studied cases,  $\rho_{chain}$  remains below 1, the value for the ideal case of perfectly parallel stripes, because of the difficulty of achieving the exact ground state of the system in the simulation. Nevertheless, its non-zero value is clearly indicative of the formation of striped phases (independently of the width of the stripes) as soon as  $\bar{J}$  is high enough to break the AF ground state for the pure dipolar case. Note, however, that striped structures and vortices coexist in a region of  $\bar{J}$  parameter that becomes smaller the higher  $\bar{K}$  is. Finally, let also note that, for the range of parameters where vortex-like structures are observed, the vorticity parameter decreases with  $\bar{J}$ , indicating the progressive shrinking of the vortices radius by the exchange interaction.

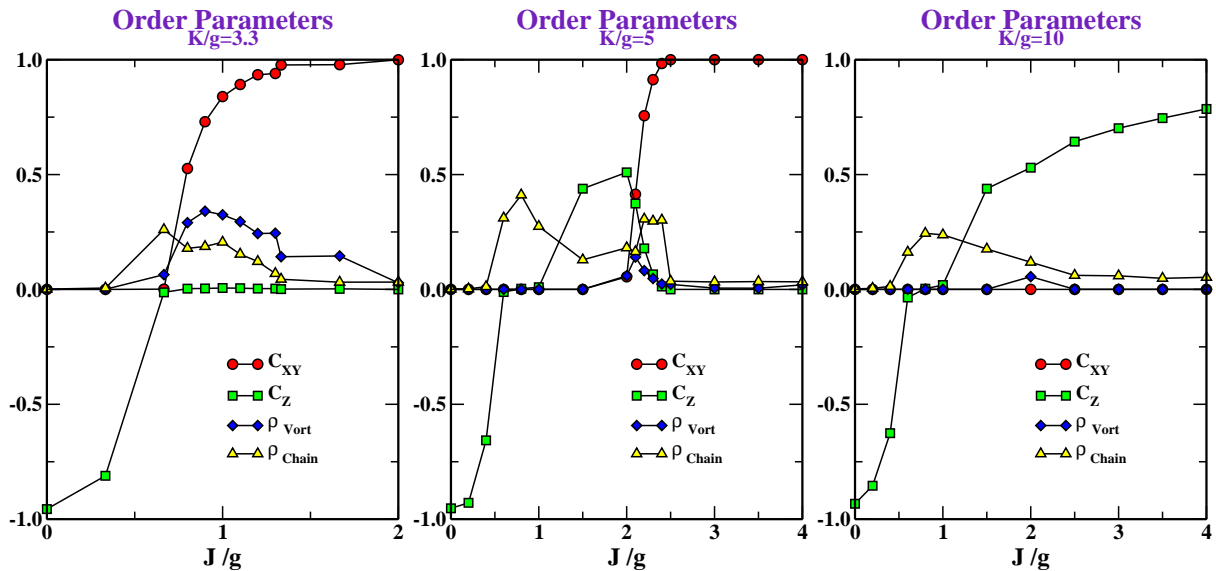


Figure 7.10: Order parameters defined in Eq. 7.21 through 7.24 of the ground state configurations of the finite  $K$  model.

## 7.7 Magnetic history dependence

In the previous section, we have verified the existence of a region of parameters  $\bar{J}$  and  $\bar{K}$  in which quasi-degenerate metastable states appear. Here we would like to study how thin films with parameters in this metastability region evolve in time when they are perturbed from their ground state configuration.

In particular, we will show simulations that mimic some of the experimental processes found in recent

experiments on thin films. In all of them the measuring protocol consists in taking the sample out of its equilibrium state by the application of an external perturbation that is subsequently removed. Usually this external perturbation is a magnetic field applied perpendicular to or in the thin film plane. The final state induced by this procedure may be very different from the initial one: magnetic domains may be erased or created depending on the magnetic history to which the sample has been submitted.

### 7.7.1 Relaxation after perpendicular saturation

In the first simulation experiment, we simulate the application of a saturating field perpendicular to the film plane by starting with a configuration with all the spins pointing along the positive easy-axis direction  $S_i^z = +1$  and we let the system relax to equilibrium in zero applied field during a long sequence of Monte Carlo steps during which we record the intermediate system configurations.

Before proceeding with the results of the simulation, let us make some previous remarks. If the system is prepared in a state saturated in the perpendicular direction to the film plane, its initial energy is

$$E_0^\perp = -K - H_{\text{loc}}, \quad (7.25)$$

where  $H_{\text{loc}} = 4J - gE_{\text{dip}}^\perp$  is the local field felt by the spin, being  $E_{\text{dip}}^\perp = 9.0336$  the dipolar contribution given by Eq. 7.15. When the MC simulation starts trying to flip a spin by an angle  $\theta$  with respect to the film plane, the energy of the new state becomes

$$E_f = -K \cos^2 \theta - H_{\text{loc}} \cos \theta, \quad (7.26)$$

so, the energy change in the Boltzmann factor is

$$\Delta E = K \sin^2 \theta - H_{\text{loc}}(1 - \cos \theta). \quad (7.27)$$

Therefore, the spins will not flip to the new orientation unless for some angle  $\theta$ , the energy difference  $\Delta E$  is negative. In other words, the initial dipolar field has to be stronger than the exchange field, so that the system can relax. It can be easily seen from the above expression that, for a given value of  $K$ , this requirement implies  $\bar{J} > E_{\text{dip}}^\perp/4 = 2.258$ . On the other hand, for a given value of  $\bar{K}$ , the spins will start to relax if initially the exchange interaction is less than a critical value  $\bar{J}_c = \bar{K}/2 - E_{\text{dip}}^\perp/4 = \bar{K}/2 - 2.2584$ . What we learn from this analysis is that, in order to make a computer relaxation experiment, the microscopic interaction parameters  $\bar{K}$  and  $\bar{J}$  have to be conveniently chosen according to these requirements.

As an example, we have considered a system with  $\bar{K} = 3.3$  and  $\bar{J} = 1.0$  which is just at the crossover between the Ising and planar regimes and has a ground state configuration with in-plane vortices. The temporal evolution is shown in Fig. 7.11 where we can see a sequence of snapshots of the system taken at different stages of the relaxation. In the first stages of the evolution, the system forms striped out-of-plane structures that evolve very slowly towards the equilibrium configuration of in-plane vortices. Similar results are obtained for other values of  $\bar{J}$  close to the intersection point of the Ising and planar regimes. For values of  $\bar{J}$  smaller than  $\bar{J}^*$  the system reaches the same state as after an annealing process.

Defects and imperfections in real thin films (commonly present in granular alloys) may act as pinning centers of these intermediate structures. This may be the explanation of the change observed in magnetic force microscopy (MFM) images of granular films with low concentration of the FM content [6, 12, 13, 17] that in the virgin state show no out-of-plane order but after the application of 10 kOe perpendicular to the film plane display striped and bubble-like domains similar to the ones obtained in the simulation.

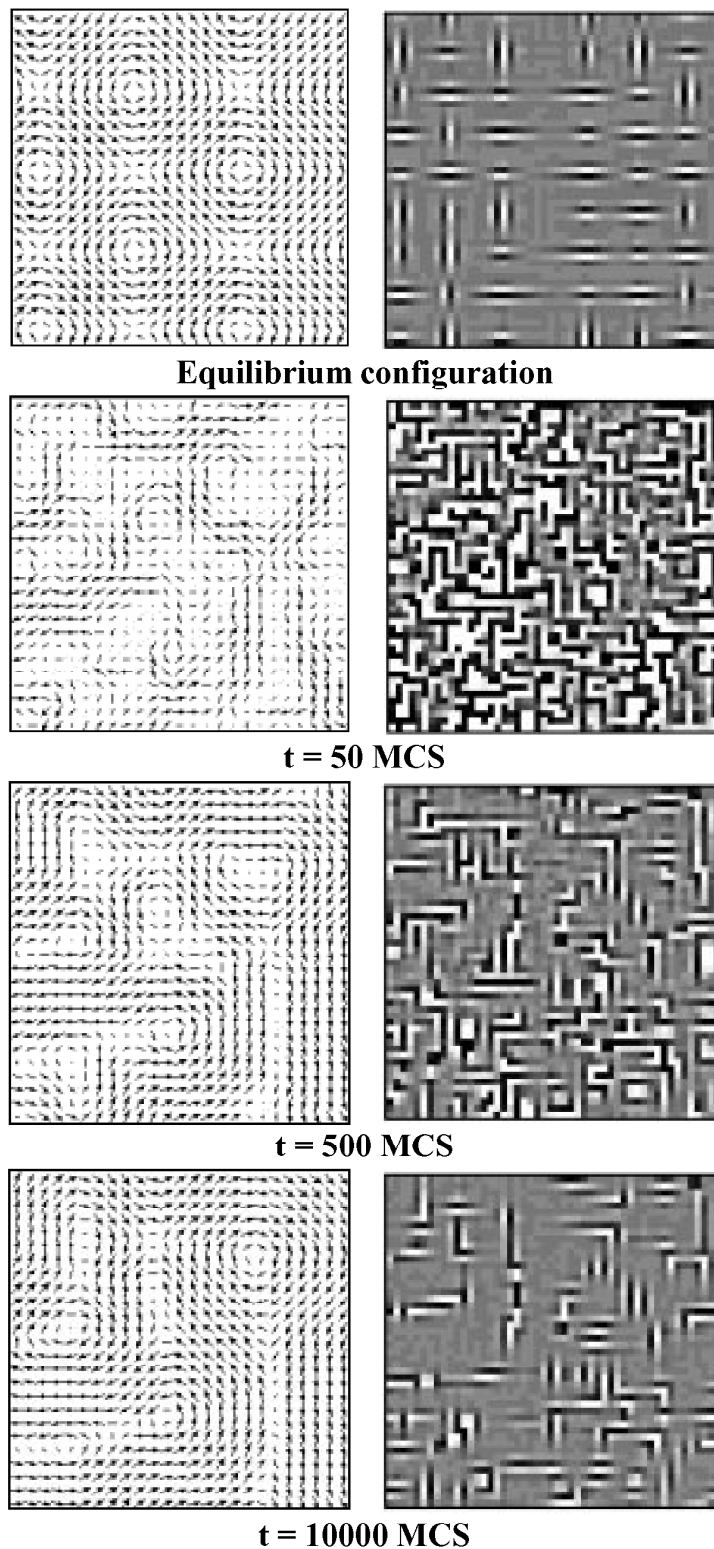


Figure 7.11: Snapshots of the configurations at different stages of the relaxation in zero field of an initially saturated sample with  $K/g = 3.3$ ,  $J/g = 1.0$  and spins pointing up along the anisotropy easy axis. Images in the right column indicate the out-of-plane component of the magnetization (ranging from white for up spins to black for down spins) while the left column corresponds to the in-plane projections of a detail of a  $25 \times 25$  region in the upper left corner of a  $50 \times 50$  system.

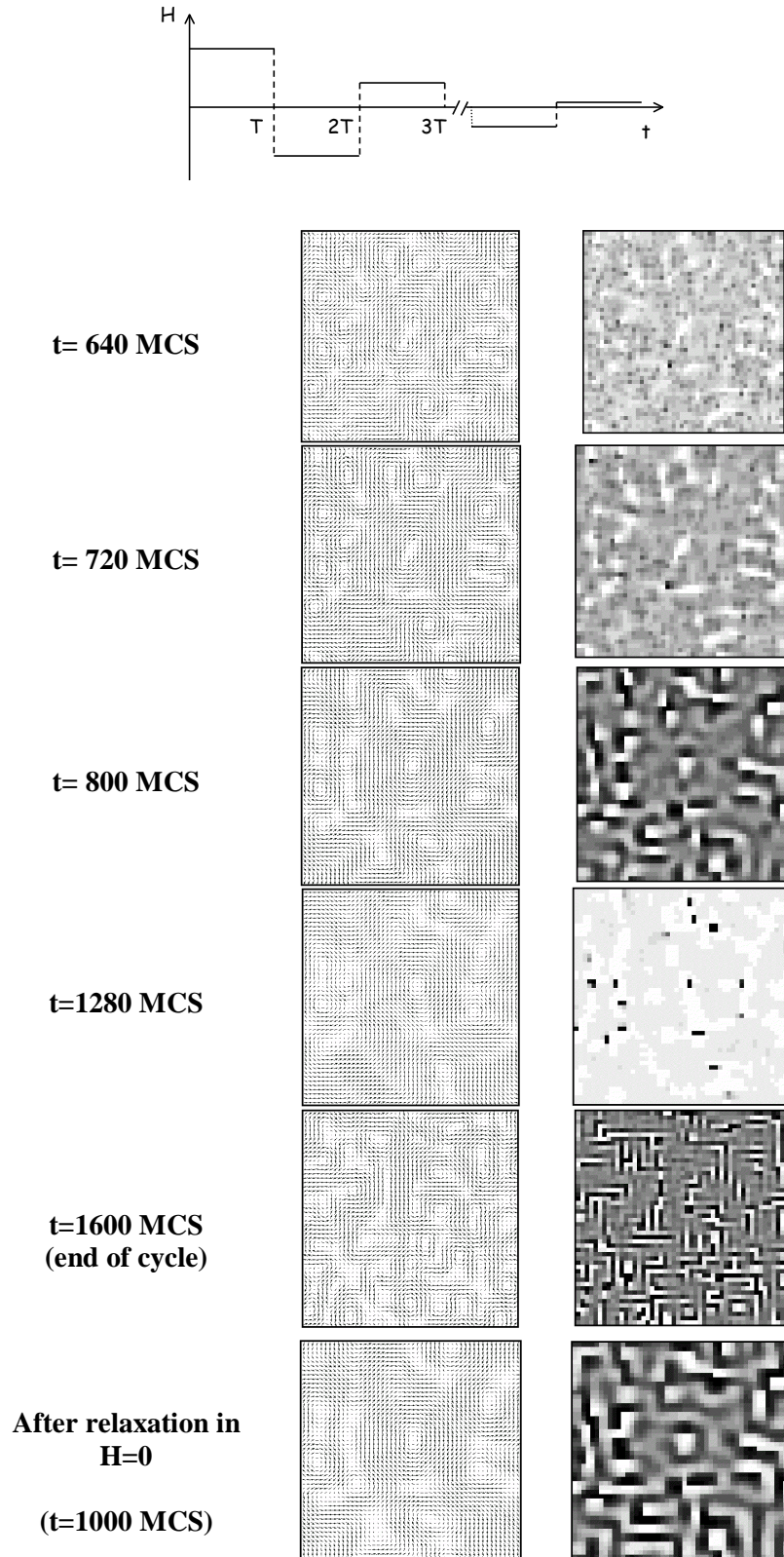


Figure 7.12: Snapshots of the configurations at different stages of a demagnetizing field cycling in the perpendicular direction applied to an initially saturated sample with  $K/g = 5.0$ ,  $J/g = 2.1$ . The drawing on the top shows the variation of the field with time, for this simulation the initial magnitude of the field is  $H_0 = 10.4$  and its period  $T = 40$  MCS. Left and right columns correspond to the in and out-of-plane projections of the spins in the same way that the preceding figure. The first five rows show snapshots during the field cycling. The configuration at the bottom is the one attained after relaxation in zero field.



### 7.7.2 Demagnetizing field cycling

The second kind of process consists in the application of a demagnetizing field cycling in the perpendicular direction [69, 70]. The aim now is to try to drive the system to a configuration different from the equilibrium configuration by perturbing the system with a time dependent external magnetic field, in such a way that it remains in this metastable state when the field is removed.

The parameters used for the simulation are in this case  $\bar{K} = 5.0$ ,  $\bar{J} = 2.1$ , also in the metastable region. As in the previous case, in the initial state the system is saturated in positive perpendicular direction with a field  $H_0$  but now the field is cycled from the positive to negative direction and progressively reduced in magnitude with a period  $T$  (see the drawing at the top of Fig. 7.12). In the simulation, the initial field has been chosen as the minimum value that allows the system to escape from the initial saturated state ( $H_0 = 10.4$ ) and the period ( $T = 40$  MC steps) is such that the system has time to reverse its magnetization during the reversal of the field.

The results are displayed in the sequence of snapshots of Fig. 7.12. At the first stages of the process (not shown in the figure) the spins reverse following at each reversal of the field. As the time elapses and the field decreases some reversed groups of spins start to nucleate (black spots in the two first rows). They continue to grow forming out-of-plane labyrinthian configurations separated by in-plane ordered zones (grey areas) arranged in vortices. As in the preceding experiment, we find that a system with an in-plane ordered ground state may be driven to a very different ordering state by the magnetic history. What is more remarkable in this case is that the state attained after the cycling process persists when the field is removed. Far from relaxing to the in-plane ordered ground state, when the system is allowed to relax in zero field, the incipient structure formed during the demagnetizing cycle is stabilized. The narrow adjacent stripes coalesce one with another to form wider stripes separated by narrower regions of in-plane spins.

These results reproduce some of the experimental results in real thin film systems when they are submitted to different magnetization processes. As an example, we show in Fig. 7.13. The top panel shows the image of the film in its virgin state, for which the MFM signal is relatively weak. When a magnetic field is applied perpendicular to the film plane, striped-like structures are clearly formed and a stronger contrast in the MFM signal is obtained, indicating a remanent state with perpendicular magnetization (right middle panel). This can also be reached by the application of a perpendicular field to a demagnetized sample. If a weak in-plane field is subsequently applied, a state with elongated stripes along the direction of the field is achieved, still presenting strong MFM contrast and showing out-of-plane order (right bottom panel). When an in-plane a.c. field is applied to this last state, the spins are combed into the field direction forming more parallel stripes with a weak out-of-plane magnetization component (left bottom panel). The application of an in-plane field either to this last state or to the virgin sample erases the magnetization patterns turning the magnetization into the sample plane (left middle panel).

## 7.8 Conclusions

We have shown that a model of 2D Heisenberg spins with anisotropy perpendicular to the plane and interacting via exchange and longrange dipolar forces is able to reproduce the different magnetic patterns observed in experiments, from perpendicular labyrinthian and striped domains to in-plane FM and vortex structures. The long-range character of the dipolar interaction plays an essential role to understand the ground state properties of this system, the results would have been very different if the dipolar field acting



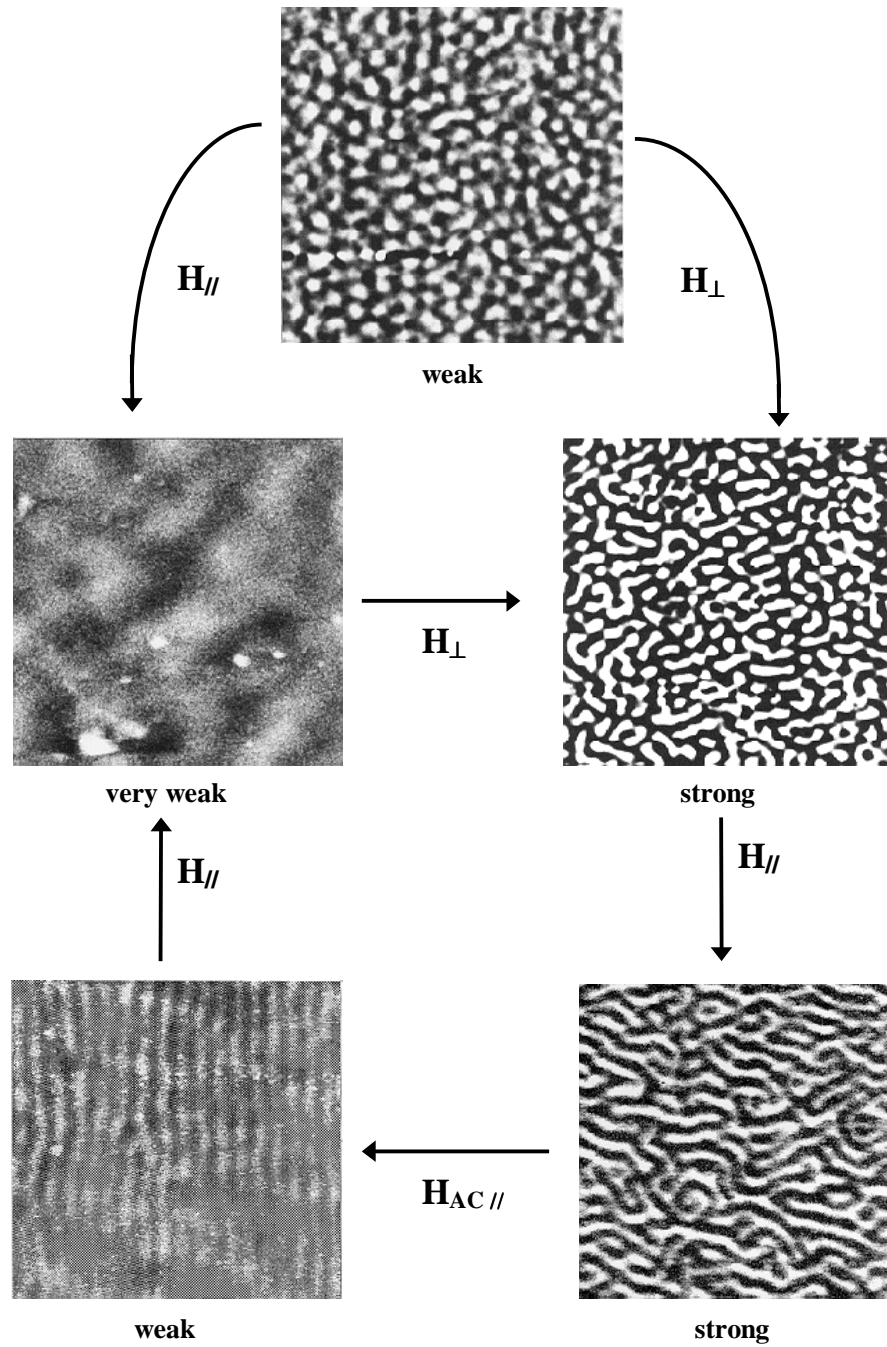


Figure 7.13: Experimental history dependence of the magnetization patterns of a CoFe-Ag thin film obtained by MFM microscopy.

---

on the spins had been replaced by a mean-field demagnetizing field as is usually done in some works. An interesting characteristic of the model is that it behaves as the limiting Ising of planar models depending on the values of  $\bar{J}$  for a given value of  $\bar{K}$ . However, for values of  $\bar{J}$  around the intersection between the Ising and the planar ground state lines, in-plane and out-of-plane configurations are quasidegenerated in energy and metastable. In this range of parameters our simulations are able to reproduce a surprising experimental observation ([6, 11, 12, 13, 17]): if a magnetic field perpendicular to the film plane is applied to a virgin sample with in-plane FM domains, the perpendicular component of the magnetization increases by a factor of 10 and the magnetic pattern displays well-contrasted domains. A similar situation happens after perpendicular demagnetizing cycles, now the domains elongate and become wider. The last case could be thought as a dynamic phase transition from in to out-of-plane order induced by a driving time-dependent magnetic field similar to that observed for Ising spins [81, 82]. Therefore, the application of an external perturbation that changes momentarily the energy landscape together with the existence of highly metastable states facilitates the driving of the system to a new stable configuration that nonetheless it is not the equilibrium one.



## Bibliography

- [1] G. Prinz and K. H. (eds.), *Physics Today* (AIP, New York, April 1995), pp. 24–63, special issue on the subject.
- [2] R. Allenspach and A. Bischof, *Phys. Rev. Lett.* **69**, 3385 (1992).
- [3] D. J. Webb and J. D. McKinley, *Phys. Rev. Lett.* **70**, 509 (1993).
- [4] A. B. MacIsaac, K. De’Bell, and J. P. Whitehead, *Phys. Rev. Lett.* **80**, 616 (1998).
- [5] R. Allenspach, M. Stampanoni, and A. Bischof, *Phys. Rev. Lett.* **65**, 3344 (1990).
- [6] M. Hehn, S. Padovani, K. Ounadjela, and J. P. Boucher, *Phys. Rev. B* **54**, 3428 (1996).
- [7] A. E. Berkowitz, J. R. Michell, M. J. Carey, A. P. Young, S. Zhang, F. E. Spada, F. T. Parker, H. Hutten, and G. Thomas, *Phys. Rev. Lett.* **68**, 3745 (1992).
- [8] J. Q. Xiao, J. S. Jiang, and C. Chien, *Phys. Rev. Lett.* **68**, 3749 (1992).
- [9] A. D. Kent, U. Rüdiger, J. Yu, L. Thomas, and S. S. P. Parkin, *J. Appl. Phys.* **85**, 5243 (1999).
- [10] E. D. Dahlberg and R. Proksch, *J. Magn. Magn. Mater.* **200**, 720 (1999).
- [11] V. Franco, X. Batlle, A. Valencia, A. Labarta, and K. O’Grady, *IEEE Trans. Magn.* **34**, 912 (1998).
- [12] V. Franco, X. Batlle, and A. Labarta, *Eur. Phys. J. B* **17**, 43 (2000).
- [13] J. F. Gregg, W. Allen, K. Ounadjela, M. Viret, M. Hehn, S. M. Thompson, and J. M. D. Coey, *Phys. Rev. Lett.* **77**, 1580 (1996).
- [14] D. M. Donnet, K. M. Krishnan, and Y. Yajima, *J. Phys. D* **28**, 1942 (1995).
- [15] R. L. Stamps, L. Louail, M. Gester, and K. Ounadjela, *J. Appl. Phys.* **81**, 4751 (1997).
- [16] G. Bochi, H. J. Hug, D. I. Paul, B. Stiefl, A. Moser, I. Parashikov, H.-J. Güntherodt, and R. C. O’Handley, *Phys. Rev. Lett.* **75**, 1839 (1995).
- [17] M. Hehn, K. Cherifi-Khodjaoui, K. Ounadjela, J. P. Boucher, and J. Arabski, *J. Magn. Magn. Mater.* **165**, 520 (1997).
- [18] A. Garvin, M. H. Kelley, J. Q. Xiao, and C. L. Chien, *Appl. Phys. Lett.* **66**, 1683 (1995).
- [19] A. Garvin, M. H. Kelley, J. Q. Xiao, and C. L. Chien, *J. Appl. Phys.* **79**, 5306 (1996).
- [20] M. Seul and D. Andelman, *Science* **267**, 476 (1995).

- 
- [21] L. D. Landau and E. M. Lifschitz, *Zh. Phys. Sowjet.* **8**, 153 (1935).
- [22] K. De'Bell, A. B. MacIsaac, I. N. Booth, and J. P. Whitehead, *Phys. Rev. B* **55**, 15108 (1997).
- [23] S. Prakash and C. L. Henley, *Phys. Rev. B* **42**, 6574 (1990).
- [24] A. B. MacIsaac, J. P. Whitehead, M. C. Robinson, and K. De'Bell, *Phys. Rev. B* **51**, 16033 (1995).
- [25] A. B. MacIsaac, J. P. Whitehead, K. De'Bell, and P. H. Poole, *Phys. Rev. Lett.* **77**, 739 (1996).
- [26] S. T. Chui, *Phys. Rev. B* **50**, 12559 (1994).
- [27] S. T. Chui, *Phys. Rev. B* **51**, 250 (1995).
- [28] S. T. Chui, *Phys. Rev. Lett.* **74**, 3896 (1995).
- [29] E. Y. Vedmedenko, H. P. Oepen, A. Gazali, J.-C. S. Lévy, and J. Kirschner, *Phys. Rev. Lett.* **84**, 5884 (2000).
- [30] E. Y. Vedmedenko, A. Gazali, and J.-C. S. Lévy, *Surf. Sci.* **402-404**, 391 (1998).
- [31] Y. Yafet, E. M. Gyorgy, and L. R. Walker, *J. Appl. Phys.* **60**, 4236 (1986).
- [32] Y. Yafet and E. M. Gyorgy, *Phys. Rev. B* **38**, 9145 (1988).
- [33] B. Kaplan and G. A. Gehring, *J. Magn. Magn. Mater.* **128**, 111 (1993).
- [34] M. B. Taylor and B. L. Gyorffy, *J. Phys.: Condens. Matter* **5**, 4527 (1993).
- [35] D. Mermin and Wagner, *Phys. Rev. Lett.* **17**, 1133 (1966).
- [36] D. Mermin and Wagner, *Phys. Rev. Lett.* **17**, 1307 (1966).
- [37] P. Bruno, *Phys. Rev. Lett.* **87**, 137203 (2001).
- [38] M. E. Fisher, S. Ma, , and B. G. Nickel, *Phys. Rev. Lett.* **29**, 917 (1972).
- [39] S. Romano, *Phys. Rev. B* **44**, 7066 (1991).
- [40] J. M. Luttinger and L. Tisza, *Phys. Rev.* **70**, 954 (1946).
- [41] J. M. Luttinger and L. Tisza, *Phys. Rev.* **72**, 257(E) (1947).
- [42] J. M. Luttinger, *Phys. Rev.* **81**, 1015 (1951).
- [43] P. W. Anderson, *Phys. Rev.* **79**, 705 (1950).
- [44] T. Niemeijer, *Physica* **57**, 281 (1972).
- [45] T. Niemeijer and H. W. J. Blöte, *Physica* **67**, 125 (1973).
- [46] S. K. Misra, *Phys. Rev. B* **6**, 2026 (1973).
- [47] J. Fernaández and J. J. Alonso, *Phys. Rev. Lett.* **63**, 53 (2000).
- [48] M. H. Cohen and F. Keffer, *Phys. Rev.* **99**, 1128 (1955).
- [49] M. H. Cohen and F. Keffer, *Phys. Rev.* **99**, 1135 (1955).

- [50] C. Kittel, *Rev. Mod. Phys.* **21**, 541 (1949).
- [51] P. Politi, *Comments Cond. Matt. Phys.* **18**, 191 (1998).
- [52] P. Politi and M. G. Pini, *Eur. Phys. J. B* **2**, 475 (1998).
- [53] G. O. Zimmerman, A. K. Ibrahim, and F. Y. Wu, *Phys. Rev. B* **37**, 2059 (1988).
- [54] E. Rastelli, A. Carbognani, S. Regina, and A. Tassi, *Eur. Phys. J. B* **9**, 641 (1999).
- [55] E. Rastelli and A. Tassi, *Eur. Phys. J. B* **4**, 285 (1998).
- [56] J. Villain, R. Bidaux, J. P. Carton, and R. Conte, *J. Phys. France* **41**, 1263 (1980).
- [57] C. L. Henley, *Phys. Rev. Lett.* **62**, 2056 (1989).
- [58] P. Politi, A. Rettori, M. G. Pini, and D. Pescia, *J. Magn. Magn. Mater.* **140-144**, 647 (1995).
- [59] D. Pescia and V. L. Pokrovsky, *Phys. Rev. Lett.* **65**, 2599 (1990).
- [60] A. B. Kashuba and V. L. Pokrovsky, *Phys. Rev. B* **48**, 10335 (1993).
- [61] G. A. Gehring and M. Keskin, *J. Phys.: Condens. matter* **5**, L581 (1993).
- [62] M. P. Allen and D. J. Tildesley, *Computer Simulation of Liquids* (Clarendon Press, Oxford, 1987).
- [63] R. Kretschmer and K. Binder, *Z. Phys. B* **34**, 375 (1979).
- [64] A. B. MacIsaac, J. P. Whitehead, K. De'Bell, and K. S. Narayanan, *Phys. Rev. B* **46**, 6387 (1992).
- [65] G. Hardy and E. Wright, *An Introduction to the theory of numbers* (Clarendon Press, Oxford, 1979).
- [66] A. Hucht, A. Moschel, and K. D. Usadel, *J. Magn. Magn. Mater.* **148**, 32 (1995).
- [67] S. Kirpatrick, D. C. Gellat, and M. P. Vecchi, *Science* **220**, 671 (1983).
- [68] G. S. Grest, C. M. Soukoulis, and K. Levin, *Phys. Rev. Lett.* **56**, 1148 (1986).
- [69] A. Lyberatos, E. P. Wohlfarth, and R. W. Chantrell, *IEEE Trans. Magn.* **21**, 174 (1985).
- [70] M. Fearon, R. W. Chantrell, A. Lyberatos, and E. P. Wohlfarth, *IEEE Trans. Magn.* **23**, 174 (1987).
- [71] C. Tsallis and D. A. Stariolo, in *Annual Review of Computational Physics II*, edited by D. Stauffer (World Scientific, Singapore, 1995), Chap. Optimization by simulated annealing: recent progress.
- [72] R. Salazar and R. Toral, *J. Stat. Phys.* **89**, 1047 (1997).
- [73] K. De'Bell, A. B. MacIsaac, and J. P. Whitehead, *Rev. Mod. Phys.* **72**, 225 (2001).
- [74] L. R. Corruccini and S. J. White, *Phys. Rev. B* **47**, 447 (1993).
- [75] A. Carbognani, E. Rastelli, S. Regina, and A. Tassi, *Phys. Rev. B* **62**, 1015 (2000).
- [76] E. Y. Vedmedenko, A. Gazali, and J.-C. S. Lévy, *Phys. Rev. B* **59**, 3329 (1999).
- [77] R. Czech and J. Villain, *J. Phys.: Condens. Matter* **1**, 619 (1989).
- [78] M. E. Gouvêa, G. M. Wysin, A. R. Bishop, and F. G. Mertens, *Phys. Rev. B* **39**, 11840 (1988).

- [79] M. E. Gouvêa, G. M. Wysin, and A. S. T. Pires, *Phys. Rev. B* **55**, 14144 (1997).
- [80] A. V. Nikiforov and E. B. Sonin, *Sov. Phys. JETP* **58**, 373 (1983).
- [81] S. W. Sides, P. A. Rivkold, and M. A. Novotny, *Phys. Rev. Lett.* **81**, 834 (1998).
- [82] A. Misra and B. K. Chakrabarti, *Phys. Rev. E* **58**, 4277 (1998).

## **Part III**

# **QUANTUM RELAXATION IN MAGNETIC SYSTEMS**





## CHAPTER 8

### QUANTUM RELAXATION EFFECTS

*en todo caso había un sólo túnel,  
oscuro y solitario: el mío*

ERNESTO SÁBATO  
*El Túnel*

One of the most striking manifestations of the quantum character of nature is the quantum tunneling (QT) effect and it is at the essence of most of the properties observed in physical systems ranging from the subatomic to the molecular level. In contrast to many other quantum properties, e.g. the ground state energy  $E_0$  of a quantum system, tunneling does not possess a classic analog.

In order to refresh basic concepts, let us start with an instructive an simple example that can be found in almost any introductory book of quantum mechanics [1, 2].

Let us consider a quantum system described by a coordinate  $x$  submitted to the action of a one-dimensional potential  $V(x)$  consisting of two infinite wells separated by a barrier of infinite height as the one in Fig. 8.1. The ground state wave functions of the system are doubly degenerated in energy

$$|L, R \rangle \equiv \psi_{1,2}(x) = \sqrt{\frac{2}{a}} \sin[k_0(a/2 + b \pm x)] \quad E_n = \frac{\hbar^2 k_n^2}{2m} \quad k_n = \frac{(n+1)\pi}{a}, \quad (8.1)$$

correspond to the particle being localized in the right or left well but do not have well-defined parity. Instead the linear combinations

$$\psi_{S,A}(x) = \frac{1}{\sqrt{2}} [\psi_1(x) \pm \psi_2(x)] \quad (8.2)$$

are also proper states of the system with the same energy but with defined parity.

As soon as the barrier separating the two wells becomes finite (see the right column in Fig. 8.1), the degeneracy of these two states is lifted because from Sturm theorem we know that the ground state has even parity. This opens a gap  $\Delta_0 = E_A - E_S$  between the energies of the lowest states that is the origin of the tunneling phenomenon. We know that because the Hamiltonian has even parity, its eigenstates have well-defined parity, which means that a particle initially localized in the right (left) well

$$|R \rangle = \frac{1}{\sqrt{2}} (|S \rangle + |A \rangle) \quad , \quad |L \rangle = \frac{1}{\sqrt{2}} (|S \rangle - |A \rangle) \quad , \quad (8.3)$$

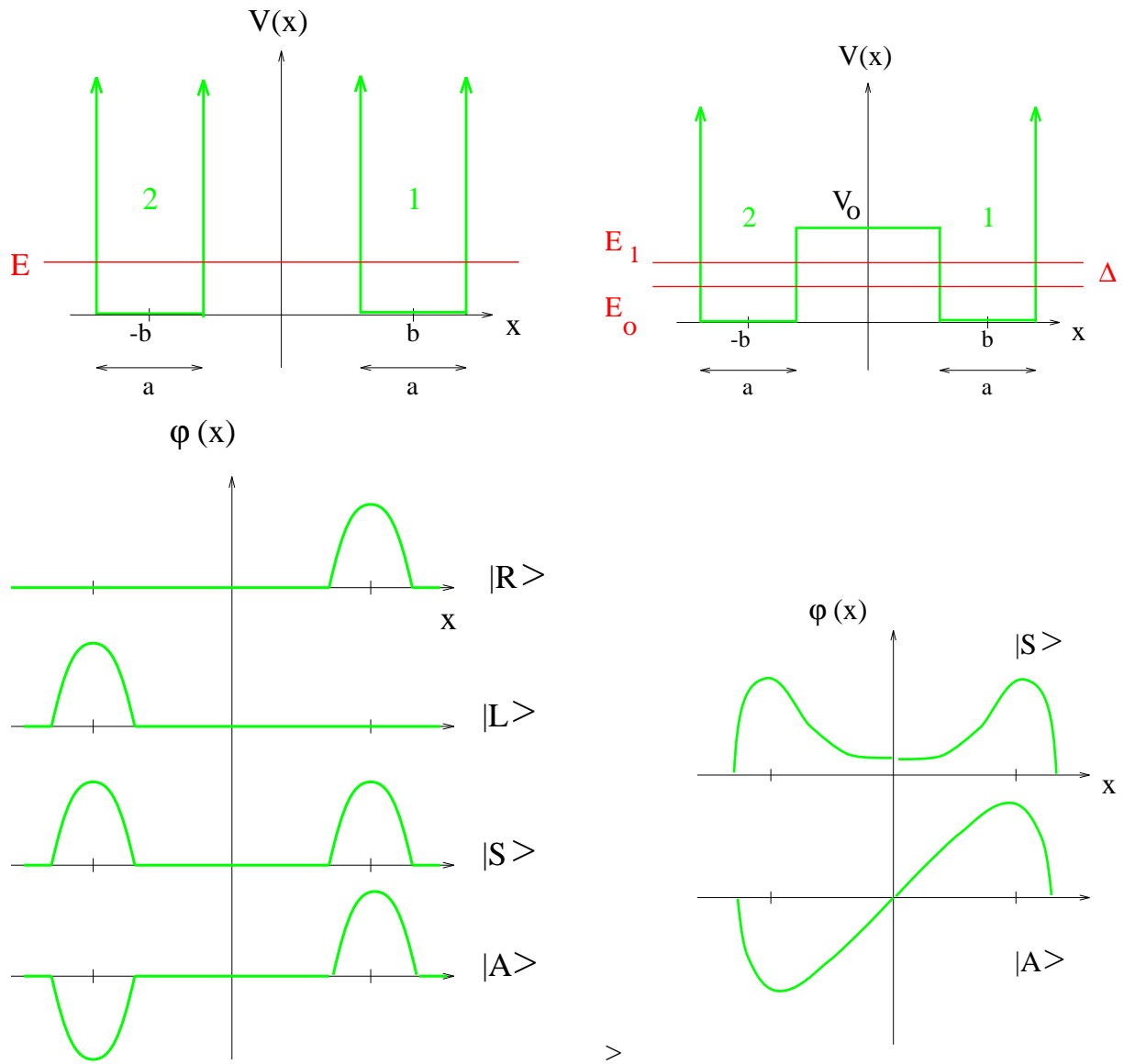


Figure 8.1: Left column: Double potential well with infinite barrier and the corresponding ground state eigenfunctions, all of them being degenerated. Right column: Double well with finite energy barrier  $V_0$  and the corresponding eigenfunctions.

has no defined parity, and therefore, it is not in a stationary state of the Hamiltonian. If the particle is initially prepared in  $|R\rangle$  state, after a time  $t$  it will be in a state

$$|R, t\rangle = \frac{1}{\sqrt{2}} e^{-iE_S t/\hbar} \left( |S\rangle + e^{-i(E_A - E_S)t/\hbar} |A\rangle \right), \quad (8.4)$$

with probability density

$$P(t) \sim \cos(\Delta_0 t/\hbar), \quad (8.5)$$

tunneling from the right to the left well in a coherent fashion with a characteristic frequency which is directly given by the ground state splitting

$$\nu_0 = \frac{\Delta_0}{\pi\hbar}. \quad (8.6)$$

## 8.1 Macroscopic Quantum Phenomena (MQP)

At the microscopic level one has no problem in admitting that a system with two or more available states can be represented as a linear superposition of these states. Think for example in an atom that, driven by an electromagnetic field, is in a linear combination of ground and excited states [3].

But, as first pointed out by Schrödinger [4] in his famous cat paradox, extrapolation of the formalism of quantum mechanics to the macroscopic world can lead to paradoxical consequences. It seems as though the predictions of quantum physics fail when applied to the macroscopic world. From Bohr's and Einstein's times to present days it is not clear how the transition from micro to macroscopic systems and the predictions of quantum mechanics to systems that are at the borderline between them have to be interpreted. During the last half of the twentieth century, the observation of quantum phenomena at the macroscopic level has been a continuous challenge to experimental physicists. We have now several clues to why quantum coherent states are so elusive to observation in usual experiments even at the microscopic scale. First, the difficulty to obtain low enough temperatures (in the range of the 0.1-1 mK) for the quantum superposition of states not to be completely blurred up or dominated by thermal fluctuations. Second, is the unavoidable coupling of the system under consideration to the environment surrounding it that acts as a measuring apparatus continuously monitoring the system and, therefore, destroys any trace of quantum coherence on it. This phenomenon has been termed decoherence. There has been a lot of progress in the understanding of this phenomenon, known usually as decoherence, attracting theoretical physicists from the different areas of both condensed matter and high energy physics. Up to now, we have gained some knowledge on the decoherent effect of a wide class of environments: oscillator baths [5], phonon [6, 7], magnon [8, 9, 7], or photon mediated dissipation, all of them studied within the scope of spin-boson Hamiltonian extensively studied by Leggett et al. in [10]; environments described by fermionic degrees of freedom; and most recently a whole class of spin bath environments explaining such important effects as the coupling to nuclear spins [11, 12, 13, 14, 15].

Therefore, one should be concerned about two questions for the observation of MQP:

1. First, the magnitude of the imaginary-time action associated with the quantum process; it should be small, say not to exceed  $30\hbar$ , otherwise quantum effects will be exponentially suppressed, as they are in the macroscopic world. For the tunneling of a macroscopic variable the value of the WKB exponent depends on the height  $U_0$  and the width  $d$  for the energy barrier, which should be therefore, made as small as possible, to observe the effect.

2. The second reason of concern comes from the coupling of the tunneling variable (say the magnetization vector  $\mathbf{M}(x, t)$ ) to other degrees of freedom as the already mentioned above. Since the limit of small barrier is of interest, it is not clear beforehand how weak the coupling should be, compared with other energies in the problem, in order not to undermine the tunneling. An answer to this question was given by Caldeira and Leggett [5]. They found that the most serious effects come from Ohmic couplings, for which the classical equation of motion of the tunneling macrovariable  $x$  has the form

$$\ddot{x} + \nu \dot{x} = -\frac{1}{m} \frac{\partial U}{\partial x}, \quad (8.7)$$

$\nu$  being the constant of Ohmic dissipation. The remarkable result for this case is that the effect of the environment on the WKB exponent,  $B$ , can be expressed in terms of  $\nu$  as

$$B \sim B_0 \left( 1 + \frac{\nu}{\omega_0} \right), \quad (8.8)$$

where  $B_0 \sim U_0/\hbar\omega_0 \gg 1$  is the WKB exponent in the absence of dissipation,  $U_0$  is the height of the barrier,  $\omega_0$  is a characteristic instanton frequency. Quantum mechanics gives  $\omega_0 \propto \sqrt{U_0/m}$ . Correspondingly, the effect of dissipation becomes significant in the limit of small  $U_0$ . The question of whether dissipation is important then becomes equivalent to the following two questions: (i) are there any processes yielding Ohmic dissipation and if so (ii) what is the dissipation coefficient  $\nu$ ?

The history of experimentally studied macroscopic quantum phenomena (MQP) goes back to the 1930's with the discovery of superfluids and superconductors, but it has not been until the recent advent of cryogenics at the millikelvin range and the emergency of nanotechnology that new experimental systems suiting the necessary conditions for the observation of MQP have come into play. Magnetic flux in SQUIDs, vortices in superfluids and superconductors, small magnetic particles or domain walls in nanowires and in thin films to cite only a few examples, have proved to be good candidates for the observation of MQP now that samples can be prepared with much more purity and control in the preparation techniques. After the first experimental studies on SQUIDs [16, 17, 18, 19, 20] supported the predictions by Caldeira and Leggett [5] for macroscopic flux tunneling, the experimental search for MQP has nowadays been focused on different kinds of magnetic systems.

Why are magnetic systems the preferred candidates for the observation of MQP?. Well, they fulfill some of the conditions required above:

- Due to the strong exchange interactions, the magnetic moments of atoms in ferromagnets act cooperatively as a single variable over length scales smaller than the single-domain particle limiting radius. This involves the cooperative dynamics of magnetic entities having a number of individual degrees of freedom ranging from  $10^3 - 10^4$  spins (small particles) to more than  $10^6$  spins (domain walls), rendering the effect clearly within the range of the meso(macro)scopic scales.
- Present preparation technology allows to obtain samples with high degree of purity and to design materials according to the hypothesis of the theoretical model to be tested [21].
- The measurement of magnetic properties can be done with fine experimental control of the external and microscopic parameters: field, temperature and so on.

## 8.2 Tunneling rates in the semiclassical approximation at $T=0$

Calculation of tunneling rates in the semiclassical approximation is most conveniently handled by path integral methods. Following this approach, the probability amplitude  $\mathcal{K}_{i,f}$  for the transition of a particle of mass  $m$  from a state  $|q_i\rangle$  at  $t = 0$  to another state  $|q_f\rangle$  at time  $t$  is given by the path integral [22] representation of the propagator

$$\mathcal{K}_{i,f}(t) = \langle q_f | e^{-iHt/\hbar} | q_i \rangle = \int_{q(x,0)=q_i}^{q(x,t)=q_f} \mathcal{D}q e^{iS[q]/\hbar} \quad (8.9)$$

where  $S[q]$  is the action functional

$$S[q] = \int_0^t dt L[q, \dot{q}] \quad (8.10)$$

and  $L$  is the Lagrangian of the particle. It is customary to perform Wick's rotation to imaginary time ( $t \rightarrow \tau = it$ )

$$\mathcal{K}_{i,f}(t) = \langle q_f | e^{-H\tau/\hbar} | q_i \rangle = \int \mathcal{D}q e^{-S_E[q]/\hbar} \quad (8.11)$$

and to work with the Euclidean action

$$S_E[q] = \int_0^\tau d\tau \left\{ \frac{m}{2} \left( \frac{dq}{d\tau} \right)^2 + U(x) \right\}, \quad (8.12)$$

so that motion in Euclidean time becomes equivalent to motion under an inverted potential  $-U(q)$ . Using the normalized eigenstates of the Hamiltonian  $H|\phi_n\rangle = E_n|\phi_n\rangle$  one may also write the propagator as [23]

$$\mathcal{K}_{i,f}(t) = \sum_n \phi_n^*(q_i) \phi_n(q_f) e^{-E_n\tau/\hbar}, \quad (8.13)$$

where  $E_n$  are the energy levels. An alternative form which will be useful when computing energy levels and ground state wave functions.

Now notice that due to the exponential dependence on  $S_E$  the main contribution to the path integral will come from trajectories for which the Euclidean action is stationary. These trajectories can be found by imposing the condition

$$\left. \frac{\delta S_E[q]}{\delta q} \right|_{q_{cl}} = 0, \quad (8.14)$$

which means that they are solutions of the classical equations of motion of the particle in an inverted potential  $-U(x)$ :

$$\frac{\delta S_E[q]}{\delta q} = 0 \Rightarrow m \frac{d^2 q_{cl}}{d\tau^2} - \frac{dU}{dq_{cl}} = 0 \quad (8.15)$$

with the boundary conditions  $q(0) = q_i, q(\tau) = q_f$ . They are usually called instantons because they are localized in time in the same way solitons are in space.

Moreover, if the zero of energies is chosen at the minimum of the potential then Eq. (8.15) can be integrated to give

$$m \left( \frac{dq_{cl}}{d\tau} \right)^2 - U(q_{cl}) = 0, \quad q_{cl}(\pm\infty) = 0, \quad (8.16)$$

which is nothing but energy conservation. With the help of this equation the contribution of the bounce trajectory to the classical action can be easily calculated without knowing explicitly  $q_{cl}$  as

$$S_{cl} = \int_0^{q_e} dq \sqrt{2mU(q)}. \quad (8.17)$$

Therefore, it is meaningful to calculate the path integral by expanding the action around its classical solutions  $q_{cl}(\tau)$ , so that, the gaussian approximation becomes a semiclassical expansion due to the presence of the small parameter  $\hbar$  in the exponential. By writing  $q(\tau) = q_{cl}(\tau) + \eta(\tau)$  with  $\eta \ll 1$  and after integrating by parts the second order term, the action becomes

$$S[q] = S_{cl} + \frac{1}{2} \int d\tau' \eta(\tau') \hat{K} \eta(\tau') + \dots, \quad (8.18)$$

where only quadratic terms in  $\eta$  have been retained. The operator

$$\hat{K} = -\frac{d^2}{d\tau^2} + U''(q_{cl})/m \quad (8.19)$$

arises from quantum fluctuations around the classical trajectory and is directly related to the curvature of the potential evaluated at the classical solutions.  $S_{cl} = S[q_{cl}]$  is the Euclidean action evaluated along the classical trajectory.

Finally, after substituting in Eq. (8.9), the following fundamental formula is obtained

$$\mathcal{K}_{if} = A e^{-S_{cl}/\hbar}. \quad (8.20)$$

Here the short-hand notation  $A$  has been employed for the preexponential factor which picks up the second order corrections to the transition amplitude due to fluctuations around the classical trajectories

$$A \simeq \int \mathcal{D}\eta e^{-\frac{1}{\hbar} \int d\tau' \eta(\tau') \hat{K} \eta(\tau')}. \quad (8.21)$$

This integral is gaussian and therefore can be easily performed in terms of the eigenvalues of the operator  $\hat{K}$  []. Then at first sight one is tempted to conclude that

$$A \sim (\det \hat{K})^{-1/2} \quad (8.22)$$

if  $\hat{K}$  has no zero or negative eigenvalue.

Result (8.20) is equivalent to the WKB approximation for potentials with an energy barrier  $U_b$  if the classical action is changed by the WKB exponent  $S_{WKB} = \sqrt{2mU_b}$  [1] and is the starting point for any calculation of quantum transition rates. We will now be more concrete and we will apply this result to specific potentials having one metastable minimum (MQT) or two classically degenerated minima (MQC).

### 8.2.1 Calculation of decay rates (MQT)

We will now focus on a potential with one minimum at  $q = 0$  and an exit point at  $q_e$  separated from the minimum by an energy maximum of height  $V_0$  (see Fig. (8.2a)). We will be interested in the decay rate of

the ground state at the  $q = 0$  minimum. Let be  $\psi(t)$  its wave function and  $E_0 = \epsilon + i\sigma$  its energy. Then its probability density decays with time as

$$|\psi(t)|^2 = e^{2\sigma t/\hbar} |\psi(0)|^2 \quad (8.23)$$

and therefore the decay rate is related to the imaginary part of the energy by

$$\Gamma = -\frac{2\text{Im}E_0}{\hbar}. \quad (8.24)$$

The ground state energy can be computed from the propagator with the help of the Feynman-Kac formula [2]

$$E_0 = -\hbar \lim_{\tau \rightarrow \infty} \frac{1}{\tau} \ln \mathcal{K}(q_0, -\tau/2 | q_0, \tau/2). \quad (8.25)$$

Therefore, in this case all what is needed is to find stationary trajectories of the action that give an imaginary contribution to  $E_0$ . What are the possible candidates?.

1. The trivial constant trajectory  $q_0 = 0$ ,  $U''(q_0) = \omega^2$  contributes with the well-known result for the harmonic oscillator,

$$\mathcal{K}_0 = \sqrt{\frac{\omega}{2\pi\hbar \sinh(\omega\tau)}} \rightarrow \sqrt{\frac{\omega}{\pi\hbar}} e^{-\omega\tau/2}, \quad (8.26)$$

and therefore gives no imaginary contribution to  $\mathcal{K}$ .

2. The instanton trajectory having the shape of a "bounce" that goes from the minimum  $q_0 = 0$  at time  $\tau = -\tau/2$  to the escape point  $q_e$  at time  $\tau = 0$  and then back to  $q = 0$  at  $\tau = +\tau/2$  as sketched in Fig. 8.2b. Its contribution is

$$\mathcal{K}_1 = A e^{-S_{cl}/\hbar}. \quad (8.27)$$

Now it is easy to see that due to the translational time invariance of the action, the operator  $\hat{K}$  has a zero-frequency mode  $y_0 \propto \dot{q}_{cl}$  that would give a disastrous infinite contribution to the prefactor  $A$ . Fortunately this problem can be healed by excluding the zero-mode in the path integral over fluctuations (8.21) and changing variables (this is the so-called shifting method employed in field theories for the calculation of determinants [] or method of collective variables in the condensed-matter literature []). It turns out that, in order to remove the infinite contribution, one has to replace  $\frac{1}{\sqrt{\lambda_0}} \rightarrow \sqrt{\frac{S_{cl}}{2\pi\hbar}} \tau$ . In this way, if the contribution of the trivial trajectory,  $\mathcal{K}_0$ , is factored out, the contribution of the bounce trajectory becomes

$$\tau \mathcal{K}'_1 = \tau \sqrt{\frac{S_{cl}}{2\pi\hbar}} \sqrt{\frac{\text{Det} \hat{K}_0}{\text{Det}' \hat{K}}} e^{-S_{cl}/\hbar} \quad (8.28)$$

From this expression we may now guess where the imaginary contribution may come. For this potential the zero-mode eigenfunction  $y_0(\tau)$  has a node and it is not the ground state wavefunction, so there must be a mode with a negative eigenvalue  $\lambda_{-1} < 0$  that will give the desired imaginary contribution to the ground state energy through its contribution to the product in the denominator of  $\mathcal{K}'_1$ .

3. Any trajectory consisting of a set of  $N$  well-separated bounces (as the one sketched in Fig. 8.2c) centered at different times  $\tau_i$  (dilute gas approximation) will also be a solution to the classical equations of motion with a contribution  $\mathcal{K}'_1^N$ .



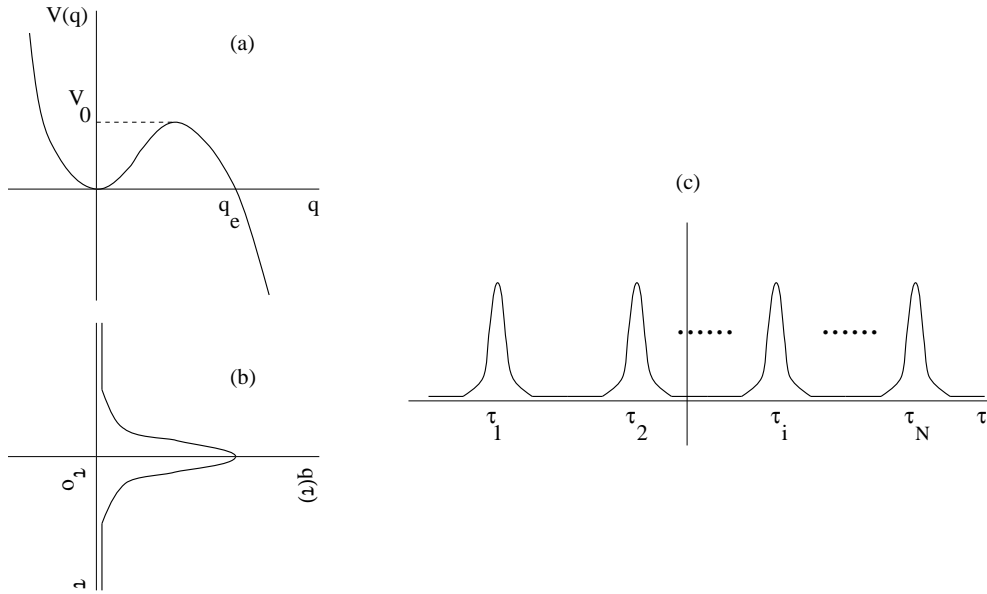


Figure 8.2: (a) Typical potential considered for the calculation of decay rates occurring in MQT phenomena. It has a minimum at  $q = 0$  and an escape point at  $q_e$  separated from the minimum by an energy barrier  $V_0 \gg q_e$ . (b) Bounce trajectory corresponding to the solution of the classical equation of motion for the above potential. (c) Multi-instanton trajectory make up of a set of  $N$  bounce solutions with widely separated centers  $\tau_i$ .

After these considerations, and taking into account all the possible  $n$ -bounce contributions, the propagator may be written as

$$\mathcal{K} = \mathcal{K}_0 \sum_n \frac{\tau^n}{n!} \mathcal{K}'_1{}^n = \mathcal{K}_0 e^{\tau \mathcal{K}'_1} \rightarrow \sqrt{\frac{\omega}{\pi \hbar}} e^{-\left(\frac{\omega}{2} - \mathcal{K}'_1\right) \tau}. \quad (8.29)$$

From Eq. (8.25) we obtain the ground state energy

$$E_0 = \frac{\hbar \omega}{2} - \hbar \mathcal{K}'_1{}^N, \quad (8.30)$$

and after substitution in Eq. (8.24) the decay rate <sup>1</sup>

$$\Gamma = \sqrt{\frac{S_{cl}}{2\pi \hbar}} \sqrt{\frac{Det \hat{K}_0}{Det' \hat{K}}} e^{-S_{cl}/\hbar}. \quad (8.31)$$

## 8.2.2 Calculation of ground state splitting (MQC)

For potentials with two minima at  $q_m = \pm a$  like the one sketched in Fig. 8.3a the quantity of interest is the ground state energy splitting or the frequency of quantum coherent oscillations between the two energy minima placed at  $q_0 = \pm a$ . If  $\psi_0(x), \psi_1(x)$  are the symmetric ground-state and first excited state

<sup>1</sup>The missing factor 2 is the result of proper calculation of the diverging contribution of the negative mode to  $A$  by analytical continuation of the integral (see [24, 25] for the details.)

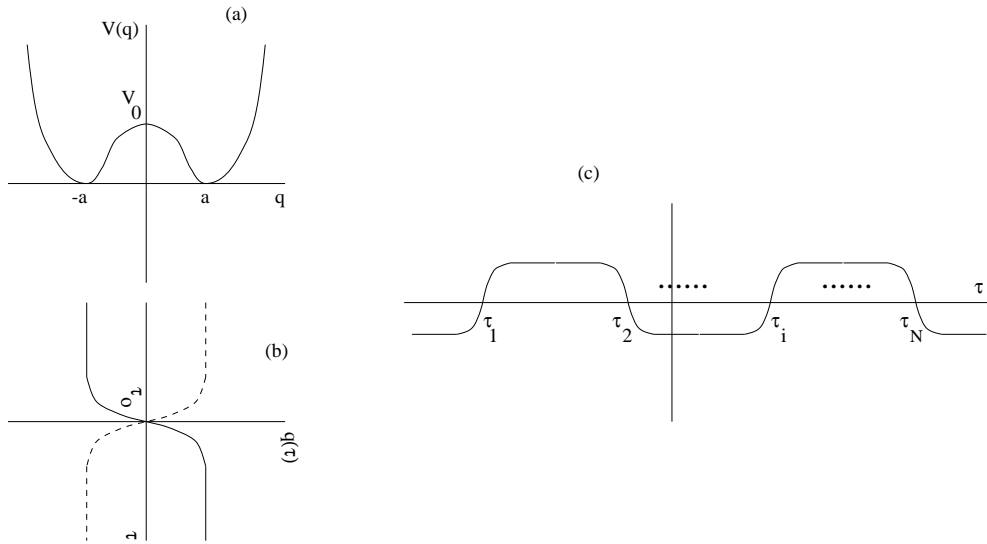


Figure 8.3: (a) Typical potential considered for the calculation of decay rates occurring in MQC phenomena. It has two degenerated minima at  $q = \pm a$  separated by an energy barrier  $V_0 \gg 2a$ . (b) Kink and anti-kink trajectories corresponding to the solution of the classical equation of motion for the above potential. (c) Multi-instanton trajectory make up of a set of  $N$  kink-anti-kink pairs with widely separated centers  $\tau_i$ .

antisymmetric wave functions respectively, then by Eq. (8.11) and with the help of the Feynman-Kac formula (8.25) we can obtain the ground state splitting from the long time behaviour of the propagators  $\mathcal{K}_{+-} \equiv \mathcal{K}(\pm a, -\tau/2 | \pm a, \tau/2)$ ,  $\mathcal{K}_{++} \equiv \mathcal{K}(\pm a, -\tau/2 | \mp a, \tau/2)$ .

The calculation of  $\mathcal{K}$  proceeds along the same lines as in the preceding case. First, the trajectories that make stationary the action are now:

1. There is a trivial constant solution to  $\mathcal{K}_{++}$  that corresponds to the particle sitting at  $q_0 = a$ , the top of the maximum of  $-U(q)$  with the same contribution  $\mathcal{K}_0$  as in the MQT case.
2. Instanton trajectories for the second propagator having the shape of a kink or antikink that start from one minimum  $q_m = \mp a$  at time  $\tau = -\tau/2$  and arrive at the other  $q_m = \mp a$  at time  $\tau = +\tau/2$ , crossing the energy barrier at an intermediate unspecified time  $\tau_0$  as sketched in Fig. 8.2b. Kink and anti-kink trajectories have the same contribution to the classical action. There is also a zero-frequency as before, but since now the potential is symmetric with respect to  $q$ , the zero-mode solution corresponds to the ground state of the operator  $\hat{K}$  governing fluctuations around the classical solution and therefore there is no negative eigenvalue.
3. Now for the multi-instanton solutions we have two possibilities: a) for the propagator  $\mathcal{K}_{+-}$ , a total odd number of kinks and anti-kinks with contribution  $2nS_{cl}$ ; b) for  $\mathcal{K}_{++}$ , a total even number of kinks and anti-kinks with contribution  $(2n + 1)S_{cl}$ .

This last point is the only difference with respect to the MQT. Now the sum in Eq. (8.29) case when summing up all the  $n$ -instanton contributions gives

$$\mathcal{K}_{++} = \mathcal{K}_0 \frac{\sinh(\tau \mathcal{K}'_1)}{\cosh(\tau \mathcal{K}'_1)}. \quad (8.32)$$

Taking the  $\tau \rightarrow \infty$  limit the ground-state energy splitting is readily obtained as

$$\Delta = E_1 - E_0 = 2\hbar \sqrt{\frac{S_{cl}}{2\pi\hbar}} \sqrt{\frac{\text{Det}\hat{K}_0}{\text{Det}'\hat{K}}} e^{-S_{cl}/\hbar}. \quad (8.33)$$

### 8.3 MQT of the Magnetization

One may feel uneasy about applying quantum mechanics to a classical variable such as the magnetization vector

$$\mathbf{M}(\mathbf{x}, t) = \left\langle 2\mu_B \sum_i \hat{s}_i \delta(\mathbf{x} - \mathbf{x}_i) \right\rangle. \quad (8.34)$$

Note in this connection that the problem is not essentially different from the  $\alpha$  decay of a nucleus. For the latter problem one ignores the fact that the  $\alpha$  particle is formed by four operators of nucleons (or 12 quark operators), which is justified by the strong coupling of nucleons inside the  $\alpha$ -particle. Similar to that problem, the strong exchange coupling of spins in a ferromagnet allows one to consider  $\mathbf{M}(\mathbf{x}, t)$ , not individual spins [26], as a tunneling variable. The Feynman approach to quantum field theory, Eq. (8.9), does not specify how fundamental the field should be. It allows one to develop quantum theory based upon a classical Lagrangian only.

How may one apply the techniques presented in Secs. 8.2.1 and 8.2.2 to the calculation of MQT and MQC rates to magnetic systems?. What are the variables that play the role of spacial and the canonically conjugated momentum?. Well, the starting point to answer these questions is to build a path integral for particles with spin. This has been well studied by Klauder [27] and other authors [28, 29, 30] and it turns out that using coherent-spin states the tunneling amplitudes can be written as

$$\mathcal{K}_{if} = \int \mathcal{D}\phi \mathcal{D}(\cos\theta) e^{-S_E/\hbar}. \quad (8.35)$$

Where the Lagrangian contained in the Euclidean action  $S_E = \int d\tau L_E$  is given by

$$L_E = i\hbar S \dot{\phi}(1 - \cos\theta) + E(\theta, \phi), \quad (8.36)$$

here the dot means derivative with respect to imaginary time,  $\dot{x} = \partial x / \partial \tau$ , and  $S$  is the spin of the particle, whose direction is characterized by the unit vector  $\mathbf{n}$  in terms of the spherical angles  $(\theta, \phi)$ , and  $E(\theta, \phi)$  is the "semi-classical" energy of the particle. Several comments are in order here:

- The kinetic energy is linear in time derivatives (not quadratic as usual). This is essentially due to the fact that in magnetic systems there exists a constraint on the magnetization, at low temperatures the length of the magnetization vector  $|\mathbf{M}|$  is constant.
- Apart from this, an additional total time derivative term arises naturally as a consequence of the topological properties of the spin variable. This is of the same form as the Wess-Zumino terms that appear in field theories and it is also related to the Kramers/Haldane phase which differs for integer and half-integer spins [31, 32]. Even though it has no influence on the classical equations of motion, it gives rise to topological oscillations or suppression of tunneling rates [33, 34, 35, 36, 37] when it is properly taken into account into instanton calculations. We will not treat this effects here, but let us only say that these effects are due to the different and eventually possible cancellation of the contributions of equivalent instanton paths to the tunneling amplitudes.

- The Lagrangian may be written in the canonical form  $L_E = p\dot{x} - E$  if we identify  $x \rightarrow \phi$  and the momentum with  $p \rightarrow S\hbar \cos \theta$ . This provides a mapping between the canonical formalism for point particles and particles with spin degrees of freedom. As we will see later, it is possible to further extend this mapping to spin systems with continuous degrees of freedom and to find effective actions of the form of that for a point particle with angle dependent "masses".
- Of course, the equations of motion derived from the action 8.36 coincide the imaginary time version of the LLG equations [38]

$$\dot{\theta} \sin \theta = \frac{\gamma}{M_0} \frac{\partial E(\theta, \phi)}{\partial \phi} \quad (8.37)$$

$$\dot{\phi} \sin \theta = -\frac{\gamma}{M_0} \frac{\partial E(\theta, \phi)}{\partial \theta}, \quad (8.38)$$

that were originally derived from phenomenological considerations. Note that these equations are highly non-linear and in general involve first and second order time derivatives. This fact complicates the solution but at the same time allows the existence of non-linear magnetic excitations like domain-walls, vortices and Bloch lines and points.

### 8.3.1 MQT in single domain particles

Calculation of tunneling rates in magnetic systems date back to 1986 from the semiclassical calculations in the works by van Hemmen and Sütto [39, 40] and Enz and Schilling [41, 42], although the first application of path integral techniques with predictions directly comparable with the experiments was done by Chudnovsky and Gunther in 1988 for the tunneling rates of the magnetization in single domain ferromagnetic particles [43]. In these systems the domain wall width is bigger than the characteristic system size because the ferromagnetic exchange coupling between the spins is much higher than typical anisotropy energies. Thus the particle is well described by its total magnetization vector, that rotates as a whole during tunneling or thermal processes (see Fig. 8.4). Such particles may have of the order of  $N = 10^4 - 10^6$  spins and may therefore be considered as "giant S" spins for which a semiclassical treatment neglecting the quantization of individual spin energy levels is more than justified. It turns out, however, that tunneling rates for this systems are rather small, pushing the crossover temperature to the milliKelvin region and difficulting the experimental tests. Moreover, in real small particle samples the particle sizes are not uniform and particles are not oriented in the same direction, which make more difficult a clear-cut interpretation of the experimental data. We will comment on this point in a subsequent section 8.7.

Later, these calculations were extended to the nucleation of non-uniform magnetization structures [44], domain walls [9] and antiferromagnetic particles [45]. Other authors have worked out the same MQT and MQC problems for different anisotropy symmetries [46, 47]. Here we will focus our attention in the tunneling of two kinds of magnetic solitons: domain-walls and non-uniform magnetization structures.

## 8.4 MQT of Domain Walls

### 8.4.1 The Model and the action

We will consider the domain wall as a surface (Fig. 8.5) of energy,  $\sigma_0$ , per unit area. In general the energy density  $\sigma(\mathbf{P}, \mathbf{R})$  is a functional of generalized coordinates  $\mathbf{R}(\xi)$  (the radius vector of the wall); here

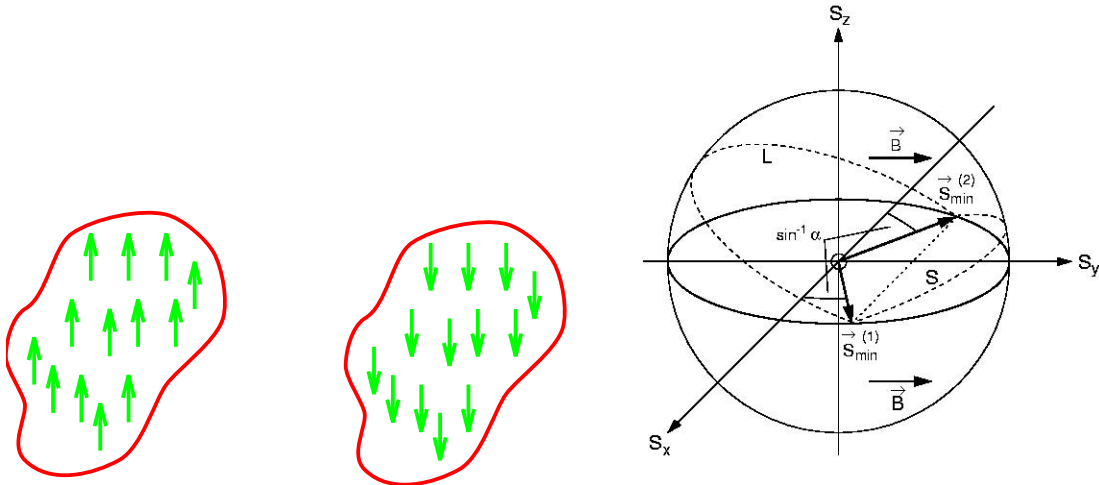


Figure 8.4: Left panel: Schematic drawing of the tunneling of the magnetic moments of a single domain particle. Right panel: Example of a tunneling trajectory in the spin space between two energy minima.

$\xi = (\xi_0, \xi_1, \xi_2)$  parameterizes the wall surface,  $\xi_0$  representing time, and  $(\xi_1, \xi_2)$ , the spatial coordinates on the wall. For a magnetic domain wall appropriate canonically conjugate variables may be defined by comparing the equations of motion for the magnetization vector (Landau-Lifschitz equations) to Hamilton's equations. In this way, if we identify the position variable with the wall displacement perpendicular to the wall surface, the associated "canonical momentum" is formally  $P = 2M\psi/\theta$  where  $\theta(x, y, t)$  is the angle that the vector normal to the surface makes with the  $Z$  axis.

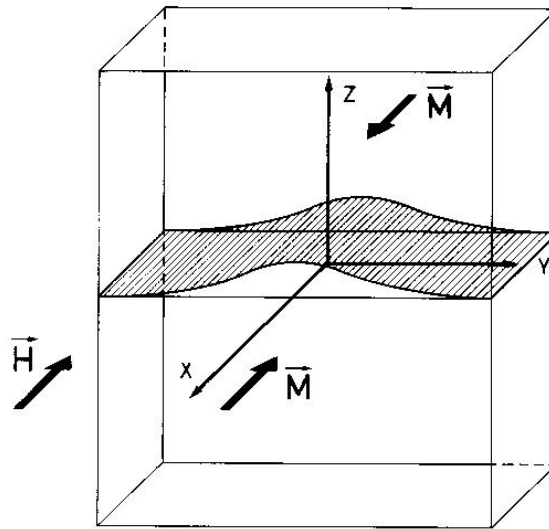


Figure 8.5: Decoupling of the domain wall from a planar defect located in the  $XY$  plane.

In general the dynamics of the wall is governed by the Slonczewski equations, [48] which take the form

$$\frac{\delta\sigma}{\delta\mathbf{R}(\xi)} = -\dot{\mathbf{P}}(\xi), \quad \frac{\delta\sigma}{\delta\mathbf{P}(\xi)} = \dot{\mathbf{R}}(\xi) \quad (8.39)$$

These equations can be obtained by direct integration of Landau-Lifschitz equations without dissipation over the wall thickness (see Chap. VI in [48]).

For an arbitrary wall, these equations can be very complicated, but for the gently curved wall of Fig. 8.5 we may take  $\mathbf{R}$  parallel to the  $z$  axis and interpret  $\sigma$  as the energy density projected on the  $xy$  plane. Then one has a wall energy density  $\sigma(\mathbf{P}, \mathbf{R})$  of the form

$$\sigma = \sigma_0 \left[ \left( 1 + \frac{\gamma^2 \delta^2}{4M_0^2} (\nabla P_\perp)^2 + \frac{\dot{Z}^2}{v_0^2 [1 + (\nabla Z)^2]} \right) [1 + (\nabla Z)^2] \right]^{1/2}, \quad (8.40)$$

where  $\mathbf{P}_\perp(x, y, t)$  is the component of wall momentum density perpendicular to the wall surface  $Z(x, y, t)$ ,  $\delta$  is the wall thickness,  $v_0$  is the limiting (Walker) velocity of the wall, and  $\sigma_0$  is the constant energy density of a planar stationary wall. Terms with  $\nabla Z$  represent the effect of increased wall surface due to curvature and would be absent in a 1D treatment of the wall.

The term proportional to  $(\nabla P_\perp)^2$  in Eq. (8.40) corresponds to a inhomogeneous exchange energy in the wall due to deviations of the the angle  $\psi$  from the normal direction to it. It has the order of  $\delta^2/R_0^2$  compared to the term  $\dot{Z}^2/v_0^2$ ;  $R_0$  being the curvature radius of the wall. The main approximation we shall make in our model is to assume weak curvature ( $R_0 \gg \delta$ ) and slow ( $|\dot{Z}| \ll v_0$ ) motion of the wall. We will see that these conditions are always satisfied for the tunneling problem in the limit of small barrier.

Under these approximations one can think of the domain wall as a membrane with some surface energy per unit area  $\sigma$  which permitted motions are in the perpendicular direction to the surface. We build the action upon the requirements usually imposed when constructing actions for point-particles or strings:

1. Invariance under global coordinate transformations.
2. Invariance with respect to reparameterizations.
3.  $S$  must have the form of an integral over the 3-dimensional world-sheet.

These requirements are fulfilled if  $S$  is proportional to the "volume" spanned by the surface when moving in space-time, the proportionality constant being the surface tension density  $\sigma(x, y)$ .

The equations of motion (8.39) then become equivalent to the covariant action,

$$S_0 = -\sigma \int d^3\xi \sqrt{g(\xi)}, \quad (8.41)$$

where  $g(\xi) = \det[g_{ij}(\xi)]$ ,  $g_{ij}$  is the metric tensor,

$$g_{ij} = \frac{\partial \mathbf{R}(\xi)}{\partial \xi_i} \cdot \frac{\partial \mathbf{R}(\xi)}{\partial \xi_j}. \quad (8.42)$$

This is the relativistic action for a surface which is actually used in field theories of extended objects [49] and it is derived in a purely geometrical way from invariance arguments. Topological invariant terms will be neglected because they do not contribute to the classical equations of motion.

To Eq. (8.41) we should also add the terms coming from a pinning potential  $U[\mathbf{R}(\xi)]$  and a volume magnetic energy coming from the magnetic field  $\mathbf{H}$  gives a further contribution  $S_p + S_m$  to the action,

where

$$S_p + S_m = - \int d^3\xi \sqrt{g(\xi)} U[\mathbf{R}(\xi)] - \int dt \int d^3R \mathbf{M}(\mathbf{R}) \cdot \mathbf{H}. \quad (8.43)$$

It is convenient now to convert to the parameterization  $\xi_0 = t$ ,  $\xi_1 = x$ ,  $\xi_2 = y$ , and describe the wall by the single-values function  $Z(x, y, t)$  [note that for cylindrical magnetic-bubble nucleation [44] this would not be convenient; a better choice would be  $Z = Z(\rho, \phi, t)$ , with  $z, \rho, \phi$  being cylindrical coordinates]. With the approximations described above we can then rewrite Eq. (8.41) as

$$S_0 = -\sigma_0 \int dt dx dy \left[ 1 + (\nabla Z)^2 - \frac{1}{v_0^2} \dot{Z}^2 \right]^{1/2}. \quad (8.44)$$

Having established the functional dependence of the action by purely geometrical arguments we will make contact with the description of the wall in terms of the different parameters in the micromagnetic energy. Within the above mentioned approximations of weak curvature and slow motion of the wall, we will see that one can think of the wall as a membrane with some surface energy per unit area  $\sigma$  which permitted motions are in the perpendicular direction to the surface. In this context the physical meaning of Eq. (8.44) becomes obvious in the limit of small velocity of the wall,  $|\dot{Z}| \ll v_0$ . Expanding the square root under the integral, one obtains

$$S_0 = -\sigma_0 \int dt dx dy \sqrt{1 + (\nabla Z)^2} \left[ 1 - \frac{1}{2v_0^2} \frac{\dot{Z}^2}{(1 + (\nabla Z)^2)} \right]. \quad (8.45)$$

Now notice that the  $\nabla$  in the denominator is by definition the tangent of the  $\theta$  angle ( $\nabla Z = \tan \theta$ ), so that we may write

$$\frac{1}{\cos^2 \theta} = 1 + (\nabla Z)^2 = [1 + (\partial_x z)^2 + (\partial_y z)^2]^{-1/2}. \quad (8.46)$$

Then the transverse component of the wall velocity is  $v_\perp = \dot{Z} \cos \theta$  and the Lagrangian corresponding to the action  $S_0$  can be seen as the sum of two terms  $S_0 = \int dt (T + V_{surf})$ :

1. The kinetic energy of the wall

$$T = \frac{m_0}{2} \int \frac{dx dy}{\cos \theta} v_\perp^2, \quad (8.47)$$

where  $m_0 = \frac{\sigma_0}{v_0^2}$  is the domain wall mass per unit area.

2. The surface energy

$$V_{surf} = \int \frac{dx dy}{\cos \theta} \sigma(x, y), \quad (8.48)$$

which is just the energy density integrated over the projection of the surface element into the perpendicular direction to the wall surface,  $dx dy / \cos \theta$ .

For uniaxial crystals, as we will show below,  $\sigma_0 = 4\sqrt{A_e K_\parallel}$  and  $m_0 = 2/\delta\gamma^2$ , so that domain wall velocity becomes  $v_0 = \sqrt{2A_e}\gamma$ . This is of the order of  $10^4$  (cm/s) for typical values of  $A_e \sim 10^{-6}$  (erg/cm<sup>3</sup>)

and  $\gamma \sim 10^7$  (1/Oe s). So that domain walls may be described in the low-velocity limit and the relativistic action reduces to

$$S_0 = \int dt \int \frac{dx dy}{\cos \theta} \frac{m_0 v_{\perp}^2}{2} - \int dt \int \frac{dx dy}{\cos \theta} \sigma_0. \quad (8.49)$$

Correspondingly, the two terms in Eq. (8.49) represent the kinetic and the surface energy contributions to the action of the wall.

It is convenient to consider the imaginary time  $\tau = it$  and to use dimensionless variables,

$$\begin{aligned} x_0 &= \omega \tau & x_1 &= x/\delta \\ x_2 &= y/\delta & \bar{z} &= z/\delta \\ u &= U(x, y, z)/\sigma_0 & h &= 2M_0 H \delta / \sigma_0, \end{aligned} \quad (8.50)$$

where  $\delta$  is the domain wall thickness. Then the total Euclidean action,  $S_E = iS$ , becomes

$$S_E = -\frac{\sigma \delta^2}{\omega} \int d^3 x \left\{ (1 + [\nabla \bar{z}(\mathbf{x})]^2)^{1/2} + u(x_1, x_2, \bar{z}) - h \bar{z}(\mathbf{x}) \right\}, \quad (8.51)$$

where  $\mathbf{x} = (x_0, x_1, x_2)$ ,  $\nabla = (\partial_0, \partial_1, \partial_2)$  and  $\omega = v_0/\delta$ .

### 8.4.2 Connection to micromagnetic theory

Up to now, no explicit connection between the geometrical description given above and the description of the wall in terms of the magnetization vector and the parameters of the micromagnetic theory describing the properties of ferromagnets. In this section we will illustrate by the example of a rhombic crystal the dependence of our parameters  $\sigma, \delta, \omega$  on the macroscopic parameters: exchange,  $A_e$  (erg/cm), and anisotropy,  $K$  (erg/cm<sup>3</sup>), constants.

The magnetic anisotropy energy of a rhombic crystal is characterized by two positive constants,  $K_{\parallel}$  and  $K_{\perp}$ :

$$E_a = -K_{\parallel} \frac{M_x^2}{M_0^2} + K_{\perp} \frac{M_z^2}{M_0^2}. \quad (8.52)$$

This describes a magnet having the  $X$  axis as the easy magnetization direction, and the  $XY$  plane as the easy plane (see Fig. 8.6). Consequently, the magnetization inside the domain wall rotates in the  $XY$  plane as can be seen in Fig. 8.5.

In the continuum approximation (valid whenever the domain wall thickness  $\delta$  is sufficiently larger than the lattice constant  $a$  between spins) we can consider the magnetization  $\mathbf{M}$  as a vector with constant magnitude  $M_0$  and variable direction  $\hat{m}$  across the domain wall. Introducing spherical coordinate angles  $\theta(\mathbf{r}, t)$  and  $\phi(\mathbf{r}, t)$ , the energy per unit area can be written as the sum of exchange and anisotropy energies as

$$E[\theta, \phi] = \int_{-\infty}^{+\infty} dx \frac{A_e}{2} [(\nabla \theta)^2 + (\nabla \phi)^2 \sin^2 \theta] + K_{\perp} \cos^2 \theta - K_{\parallel} \sin^2 \theta \cos^2 \phi. \quad (8.53)$$

The equations describing the magnetization configuration of the wall may be found with the help of the Landau-Lifshitz equations

$$\begin{aligned} \sin \theta \dot{\theta} &= -\frac{\gamma}{M_0} \frac{\delta E}{\delta \phi}, \\ \sin \theta \dot{\phi} &= \frac{\gamma}{M_0} \frac{\delta E}{\delta \theta}, \end{aligned} \quad (8.54)$$



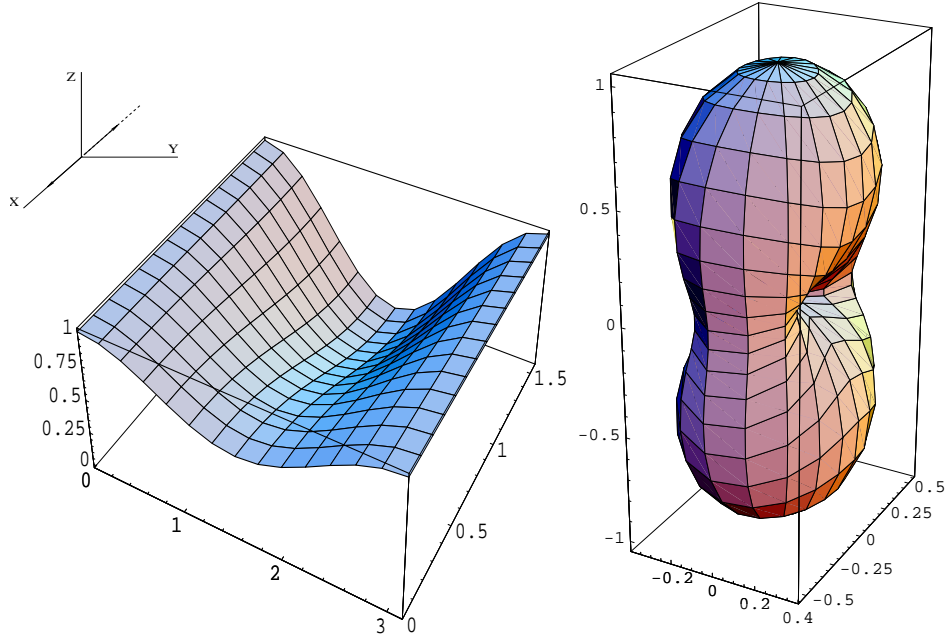


Figure 8.6: Left panel: Anisotropy energy for a rhombic crystal as a function of the spherical angles  $\theta$  and  $\phi$ , described by (8.52). Right panel: Energy surface in a parametric plot. The easy directions point along the X direction ( $\theta = \pi/2, \phi = 0, \pi$ ).

where  $\delta$  indicates a functional derivative. For the energy of Eq.(8.53) they read

$$\begin{aligned} \sin \theta \dot{\theta} - \frac{2A\gamma}{M_0} \frac{\partial}{\partial x} \left[ \sin^2 \theta \frac{\partial \phi}{\partial x} \right] &= -\frac{\gamma}{M_0} \frac{\partial E}{\partial \phi}, \\ \sin \theta \dot{\phi} + \frac{2A\gamma}{M_0} \frac{\partial^2 \theta}{\partial x^2} &= \frac{\gamma}{M_0} \frac{\partial E}{\partial \theta}. \end{aligned} \quad (8.55)$$

Soliton solutions to these equations exist with constant  $\phi = \phi_0$  and  $\theta(x, t) = \theta(x - vt)$  [50]. They describe Bloch walls traveling at constant velocity  $v$ . In order to find the explicit dependence on  $x$  and  $t$  let us make the following substitutions in (8.54)

$$\xi = x - vt, \quad \phi = \phi_0, \quad \frac{\partial}{\partial t} = -v \frac{\partial}{\partial \xi}.$$

With this, we arrive at the following pair of differential equations:

$$\begin{aligned} v \sin \theta \frac{\partial \theta}{\partial \xi} &= \frac{\gamma}{M_0} 2k_{\parallel} \sin^2 \theta \sin \phi_0 \cos \phi_0 \\ 0 &= -2A \frac{\partial^2 \theta}{\partial \xi^2} - 2k_{\perp} \sin \theta \cos \theta - 2k_{\parallel} \sin \theta \cos \theta \cos^2 \phi_0. \end{aligned} \quad (8.56)$$

The last identity gives the following differential equation for  $\theta$

$$\frac{\partial^2 \theta}{\partial \xi^2} = \frac{\bar{k}}{2A} \sin(2\theta). \quad (8.57)$$

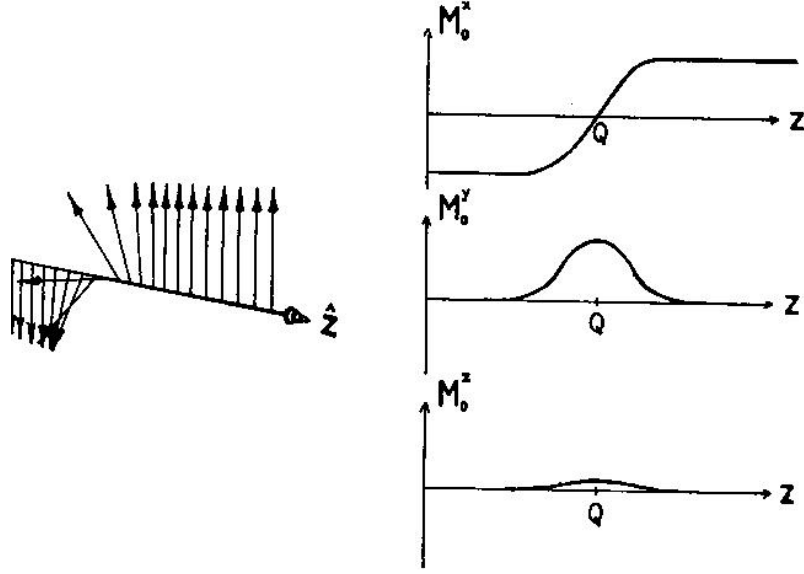


Figure 8.7: Domain wall profile for a rhombic crystal as given by (8.60).

Here, we have defined an effective anisotropy constant as  $\bar{k} = k_{\perp} - k_{\parallel} \cos^2 \phi_0$ .

This is nothing but the well-known Sine-Gordon equation [51, 52, 53, 54], the soliton solutions of which, satisfying the boundary conditions  $\theta(\sigma \rightarrow \pm\infty) = 0, \pi$ , are known to be

$$\tan\left(\frac{\theta}{2}\right) = e^{\pm(x-vt)/\delta}, \quad (8.58)$$

where

$$\delta = \delta_0 \left(1 + \frac{k_{\parallel}}{k_{\perp}} \cos^2 \phi_0\right)^{1/2} \quad (8.59)$$

is the width of the moving domain, contracted with respect to the width of a wall at rest  $\delta_0 = \sqrt{A/K_{\parallel}}$ .

With this, the profile of a static domain wall is given in terms of the magnetization vector components as (see Fig. 8.7)

$$\begin{aligned} m_x(\theta) &= \sin(\theta) \cos(\phi) \sim (1 - v^2/v_0^2) \text{sech}(\xi/\delta) \\ m_y(\theta) &= \sin(\theta) \sin(\phi) \sim v^2/v_0^2 \text{sech}(\xi/\delta) \\ m_z(\theta) &= \cos(\theta) = \tanh(\xi/\delta). \end{aligned} \quad (8.60)$$

Now, the velocity of a wall tilted an angle  $\phi = \phi_0$  from the x axis may be found by substituting

$$\frac{\partial \theta}{\partial \xi} = \sqrt{\frac{2}{\delta_0^2} (1 - \cos(2\theta))} = \frac{1}{\delta} \sin \theta \quad (8.61)$$

in the first of Eqs. (8.56) and solving for  $v$  with the result

$$v = \frac{\gamma k_{\parallel}}{M_0} \sqrt{\frac{A}{k_{\perp}}} \frac{\sin(2\phi_0)}{\sqrt{(1 - \kappa \cos^2 \phi_0)}} \quad (8.62)$$

where  $\kappa = k_{\parallel}/k_{\perp}$  is the ratio of anisotropy constants. The limiting (Walker) velocity is given by (see, e.g., Ref. [48])

$$v_0 = \frac{2\gamma}{M_0} (A_e K_{\parallel})^{1/2} \left[ \left( 1 + \frac{K_{\perp}}{K_{\parallel}} \right)^{1/2} - 1 \right]. \quad (8.63)$$

The energy of the wall can now be easily calculated by inserting (8.58) and (8.61) in (8.53) with the result

$$\sigma = \sigma_0 \sqrt{1 - \frac{K_{\perp}}{K_{\parallel} \cos^2 \phi_0}}. \quad (8.64)$$

For a static wall we have therefore the following energy density, mass and domain wall width

$$\sigma_0 = 4(A_e K_{\parallel})^{1/2}, \quad \delta_0 = (A_e/K_{\parallel})^{1/2}, \quad m_0 = \sigma_0/v_0^2. \quad (8.65)$$

Typical values of these parameters for usual ferromagnetic materials are given in Table 8.4.2.

Note, that in the limit of an uniaxial crystal,  $K_{\perp} = 0$ , the wall has an infinite mass,  $m_0 = \sigma/v_0^2$ , and, therefore, cannot move or tunnel. This is due to the fact that the Hamiltonian,  $-K_{\parallel} \hat{s}_x^2$ , produced in this limit by Eq.(8.52), commutes with the spin operator  $\hat{s}_x$ , so that  $s_x$  on each side of the wall becomes a conserved quantum number. In fact, however, the magnetic dipole interaction, which is not represented in Eq.(8.52), violates the commutation of the Hamiltonian with  $\hat{s}_x$  even for an uniaxial crystal, leading to the replacement of  $K_{\perp}$  by  $2\pi M_0^2$ . The frequency  $\omega$  depends on anisotropy constants, but not on the exchange,

$$\omega = \gamma H_a \left[ \left( 1 + \frac{K_{\perp}}{K_{\parallel}} \right)^{1/2} - 1 \right], \quad (8.66)$$

where we have introduced the anisotropy field  $H_a = 2K_{\parallel}/M_0$ . As we will see below,  $\hbar\omega/k_B$  determines the scale of the crossover temperature  $T_c$ .

Material	$M_0$ (G)	$K$ (J/m <sup>3</sup> )	$A_e$ (J/m)	$\delta_0$ (Å)	$m_0$ (Kg/m <sup>2</sup> )	$\sigma_0$ (J/m <sup>2</sup> )	$N$
SmCo <sub>5</sub>	800	$7.5 \times 10^6$	$1 \times 10^{-11}$	12	$1.7 \times 10^{-7}$	$3.5 \times 10^{-2}$	$10^4$
Co	1422	$4.12 \times 10^6$	$1.0 \times 10^{-11}$	50	$1.3 \times 10^{-10}$	$8.1 \times 10^{-3}$	$5 \times 10^4$
Fe	1707	$2.4 \times 10^4$	$1.2 \times 10^{-11}$	220	$2.3 \times 10^{-9}$	$2.1 \times 10^{-3}$	$4 \times 10^3$
Ni	508	$8 \times 10^4$	$1.0 \times 10^{-11}$	112	$4.6 \times 10^{-9}$	$3.6 \times 10^{-3}$	$2.4 \times 10^4$
YIG	1500	$2 \times 10^3$	$2 \times 10^{-11}$	1000	$2 \times 10^{-9}$	$8 \times 10^{-4}$	$3.4 \times 10^4$
SrRuO <sub>3</sub>	1590	$2 \times 10^3$	$2.3 \times 10^{-13}$	11	$4.8 \times 10^{-8}$	$6 \times 10^{-5}$	$3.4 \times 10^3$

Table 8.1: Domain wall characteristic parameters for usual ferromagnetic materials. Starting from the left: Saturation magnetization  $M_0$ , Anisotropy constant  $K$ , Exchange constant  $A$ , DW width  $\delta_0$ , DW mass per unit area  $m_0$ , Energy density  $\sigma_0$ , and number of spins  $N = 2\mathcal{A}\delta_0/a^3$  in a DW of dimensions  $\mathcal{A} = 50 \times 200$  Å<sup>2</sup>.

### 8.4.3 The Pinning Potential

Although we have not specified the pinning potential  $U$ , some important conclusion can be made on the magnitude of the reduced potential  $u = U/\sigma_0$  in Eq.(8.51). The surface energy of the wall depends on

the strength of the local exchange and anisotropy, Eq.(8.61). Fluctuations in  $A_e$  and  $K_{\parallel}$  due to defects, and resulting fluctuations in  $\sigma_0$ , are responsible for the pinning. The wall is attracted to regions where  $\sigma_0$  is less than it is in an ideal crystal. Correspondingly, the value of  $\sigma_0$  in an ideal crystal is the energy available for pinning. This suggests that the reduced pinning potential,  $u = U/\sigma_0$ , satisfies  $u < 1$ . A similar argument can be made about the reduced field  $h$ . From Eq.(8.61) we get  $h = H/H_a$ . Energy barriers in ferromagnets normally exist at  $H < H_c \leq H_a$ , which gives  $h \leq 1$ .

Equation (8.51) allows one to compute the WKB exponent for an arbitrary curvature of the wall and an arbitrary pinning potential. We will concentrate on the case of small curvature and "slow" instantons,  $(\nabla\bar{z})^2 \ll 1$ , whose significance will be explained below. To simplify the problem we will also study planar defects only, for which  $u = u(z)$ . The latter may be justified by the fact that, because of energy considerations walls tend to match with planar defects or with groups of defects concentrated in one plane. One can also imagine a specific experiment where the wall tunnels through a planar defect. In the limit of small space-time derivatives and  $u = u(z)$ ,  $S_E$  reduces to

$$S_E = -\frac{\sigma_0\delta^2}{\omega} \int d^3x \left\{ \frac{1}{2}(\nabla\bar{z})^2 + u(\bar{z}) - h\bar{z} \right\}. \quad (8.67)$$

#### 8.4.4 The WKB Exponent

##### Tunneling in 1+1 dimensions

Consider a flat domain wall of a small area  $A_w$ , tunneling through a planar defect of the same area. This may be treated as an approximation for the tunneling through a small defect, or may correspond to the situation when the wall is coupled to a planar defect within a very thin wire, with  $A_w$  being the cross-section of the wire. Then Eq.(20) becomes

$$S_E = -\frac{\sigma_0 A_w}{\omega} \int dx_0 \left[ \frac{1}{2} \left( \frac{d\bar{z}}{dx_0} \right)^2 + u(\bar{z}) - h\bar{z} \right]. \quad (8.68)$$

The extremal trajectory satisfies

$$\frac{d^2\bar{z}}{dx_0^2} = \frac{du}{d\bar{z}} - h. \quad (8.69)$$

The total potential,  $u(\bar{z}) - h\bar{z}$ , of the general form is shown in Fig. 8.8(a). The wall tunnels from  $\bar{z} = z_1$  to  $\bar{z} = z_2$ . As is shown in Fig.2b,  $z_1$  and  $z_0$  are solutions of  $du/d\bar{z} = h$ . At  $h = h_c$  the energy barrier disappears. This corresponds to  $z_2 \rightarrow z_0 \rightarrow z_1 \rightarrow 0$  at  $h \rightarrow h_c$ . In the case of a small barrier ( $h \rightarrow h_c$ ), the general form of  $du/d\bar{z}$  is [see Fig.8.8 (b)]

$$\frac{du}{d\bar{z}} = h_c - \frac{1}{2} \left( \frac{\bar{z} - r}{\bar{w}} \right)^2, \quad (8.70)$$

where  $\bar{w}$  is the parameter characterizing the shape of the potential,  $u(\bar{z})$ , produced by the defect. Equation 8.70 gives

$$z_1 = r - \bar{w}(2h_c\epsilon)^{1/2}, \quad z_0 = r + \bar{w}(2h_c\epsilon)^{1/2}, \quad (8.71)$$

where we have introduced a small parameter  $\epsilon = 1 - h/h_c$ . It is convenient to choose the  $Z$  axis such that  $z_1 = 0$ . Then  $r = \bar{w}(2h_c\epsilon)^{1/2}$ ,  $z_0 = 2\bar{w}(2h_c\epsilon)^{1/2}$ , and the total potential takes the form

$$u(\bar{z}) - h\bar{z} = \frac{1}{2\bar{w}}(2h_c\epsilon)^{1/2}\bar{z}^2 - \frac{1}{6\bar{w}^2}\bar{z}^3. \quad (8.72)$$

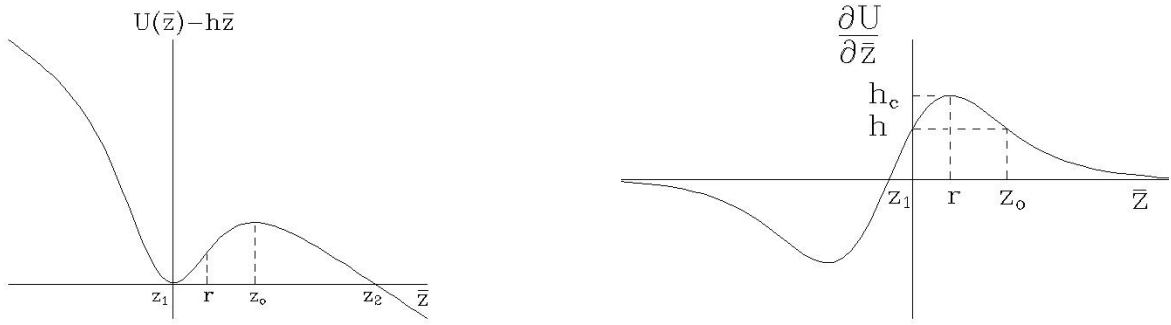


Figure 8.8: Left panel: The general shape of the potential,  $u(z) - hz$ . Right panel:  $\partial u(z)/\partial z$  vs  $z$ .

Consequently,  $z_2 = 3\bar{w}(2h_c\epsilon)^{1/2}$ .

With the help of Eq.(8.69) the extremal action can be presented as

$$S_E = -\frac{\sigma_0 A_w}{\omega} \int_{z_1}^{z_2} d\bar{z} \sqrt{2[u(\bar{z}) - h\bar{z}]} . \quad (8.73)$$

Substituting here the potential of Eq.(8.72) we obtain

$$S_E = -\frac{12}{5} \frac{\sigma_0 A_w}{\omega} \bar{w}^{3/2} (2h_c\epsilon)^{5/4} . \quad (8.74)$$

The tunneling rate can be presented as

$$P = A \exp(-B_0) , \quad (8.75)$$

where the WKB exponent is given by  $B_0 = -S_E/\hbar$ . In terms of the total number of tunneling spins,  $N = M_0 A_w \delta / \mu_B$ , with the help of Eqs.(8.50) and (8.74), we obtain

$$B_0 = \frac{48}{5} \frac{\gamma H_c}{\omega} (\bar{w})^{3/2} h_c^{1/4} 2\epsilon^{5/4} N . \quad (8.76)$$

Let us now verify the validity of our assumption that  $(d\bar{z}/dx_0)^2 \ll 1$ , under which Eq.(8.67) was obtained from Eq.(8.51). The first integral of Eq.(8.69) is

$$\frac{1}{2} \left( \frac{d\bar{z}}{dx_0} \right)^2 = u(\bar{z}) - h\bar{z} . \quad (8.77)$$

According to Fig.8.8(a) and Eq.(8.72) it has maximum at  $\bar{z} = z_0$ ,

$$\left( \frac{d\bar{z}}{dx_0} \right)_{max}^2 = \frac{8(h_c\epsilon)^{3/2}}{3\sqrt{2}\bar{w}} , \quad (8.78)$$

which is small in the limit of small  $\epsilon$  and  $h_c$ .

Another interesting observation is the universal form of the instanton in the limit of small barrier. Substituting Eq.(8.72) into Eq.(8.77) one obtains

$$\bar{z}(\tau) = z_2 / \cosh^2(\omega_0 \tau) , \quad (8.79)$$

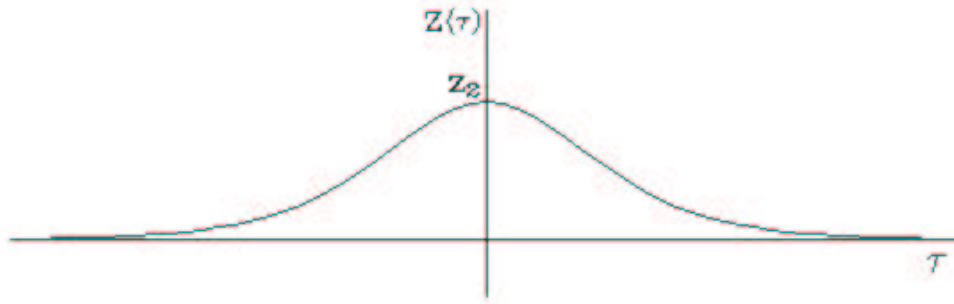


Figure 8.9: Instanton trajectory for the potential of Fig. 8.8

where

$$\omega_0 = \frac{2(2h_c\epsilon)^{1/4}}{\bar{w}^{1/2}} \omega. \quad (8.80)$$

Equation (8.80) describes the imaginary time motion from  $\bar{z} = 0$  at  $\tau = -\infty$  to  $\bar{z} = z_2$  at  $\tau = 0$ , and then back to  $\bar{z} = 0$  at  $\tau = +\infty$ . It corresponds to the classical motion in the inverted potential,  $h\bar{z} - u(\bar{z})$ .

### Tunneling in 2+1 dimensions

If the area of the domain wall coupled to a planar defect is large, the tunneling will occur via a nucleation process shown in Fig. 8.5. Once the critical portion of the wall is released due to tunneling, the nucleus will expand and eventually depin the entire wall. Let  $X$  be the direction of the anisotropy axis and  $l$  be the length of the defect in that direction. The Euclidean action for that problem is

$$S_E = -\frac{\sigma_0 l \delta}{\omega} \int d^2x \left\{ \frac{1}{2} (\nabla \bar{z})^2 + u(\bar{z}) - h\bar{z} \right\}, \quad (8.81)$$

where  $d^2x = dx_0 dx_2$ ,  $\bar{z} = \bar{z}(x_0, x_2)$ . In this case it is impossible to solve the problem analytically, even for a small barrier. Instead, one can perform a dimensional analysis of Eq.(8.81), in order to extract the dependence of the WKB exponent on the parameters of the ferromagnetic material. Consider

$$z' = \frac{\bar{z}}{r}, \quad x' = \frac{(2h_c\epsilon)^{1/4}}{\bar{w}^{1/2}} x. \quad (8.82)$$

Then, with the help of Eq.(8.72), at small barrier, we obtain

$$S_E = -\frac{\sigma_0 l \delta}{\omega} \bar{w}^2 h_c \epsilon \int d^2x' \left\{ \frac{1}{2} (\nabla' z')^2 + \frac{1}{2} z'^2 - \frac{1}{6} z'^3 \right\}. \quad (8.83)$$

The instanton satisfies

$$\nabla'^2 z' = z' - \frac{1}{2} z'^2. \quad (8.84)$$

According Eq.(8.82), the size of the nucleus is

$$Y_n \sim \frac{\bar{w}^{1/2}}{(2h_c\epsilon)^{1/4}} \delta. \quad (8.85)$$

Tunneling via the formation of the nucleus will occur if the size of the defect,  $d$ , in  $Y$  direction exceeds  $Y_n$ , that is, at

$$d/\delta > (\bar{w})^{1/2}/(2h_c\epsilon)^{1/4}. \quad (8.86)$$

After the nucleus is formed due to the tunneling, it expands in real time according the classical equation of motion, Eq. (8.38).

The integral in Eq. (8.83), evaluated along the instanton trajectory, is a number of the order of unity. Consequently, the factor before the integral gives the estimate of the extremal action. In terms of the number of tunneling spins,  $N = M_0 l Y_n \delta / \mu_B$ , we obtain

$$B_0 = 2^{1/4} k \frac{\gamma H_c}{\omega} \bar{w}^{3/2} h_c^{1/4} \epsilon^{5/4} N \quad (8.87)$$

where  $k \sim 1$  is the value of the integral. Comparison of Eq. (8.87) with Eq. (8.76) shows that in terms of  $N$  the geometry of the tunneling has little effect on the dependence of  $B$  on the parameters of the system. It appears to be quite universal in the limit of low barrier.

#### 8.4.5 The crossover temperature

In the absence of dissipation the temperature of the crossover from thermal to quantum regime is given by  $k_B T_c = U_0 / B_0$ . It requires, therefore, a calculation of the height of the energy barrier,  $U_0$ . As has been shown above, the limit of the small barrier automatically provides the condition of small derivatives,  $|\nabla z \ll 1|$ . In this limit the energy of the static configuration of the wall is given by the equation similar to Eq. (8.67),

$$E = \sigma_0 \delta^2 \int d^2 x \left[ \frac{1}{2} (\nabla \bar{z})^2 + u(\bar{z}) - h \bar{z} \right] \quad (8.88)$$

where  $d^2 x = dx_1 dx_2$ ,  $\nabla = (\partial_1, \partial_2)$ . For a flat wall studied in Sec. 8.4.4,  $\nabla \bar{z} = 0$  and the height of the barrier is

$$U_0 = \sigma_0 A_w u_0, \quad (8.89)$$

where  $u_0$  is given by Eq. (8.72) at  $\bar{z} = z_0$ ,  $u_0 = \left(\frac{2}{3}\right) \bar{w} (2h_c \epsilon)^{3/2}$ . In terms of the number of tunneling spins one obtains

$$U_0 = \frac{8\sqrt{2}}{3} \mu_B H_c \bar{w} h_c \epsilon^{3/2} N. \quad (8.90)$$

Together with Eq. (8.76) this gives

$$k_B T_c = \frac{5\sqrt{2}}{36} \hbar \omega (\bar{w})^{-1/2} h_c^{1/4} \epsilon^{1/4}. \quad (8.91)$$

Note, that  $k_B T_c \sim \hbar \omega_0$ , where  $\omega_0$  is the instanton frequency of Eq. (8.80).

Let us now turn to the 2+1 tunneling studied in Sec. (8.4.4) The energy of the nucleus is

$$E = \sigma_0 l \delta \int dx_2 \left[ \frac{1}{2} \left( \frac{d\bar{z}}{dx_2} \right)^2 + u(\bar{z}) - h \bar{z} \right]. \quad (8.92)$$

A dimensional analysis similar to that performed in Sec. 8.4.4 shows that for a small barrier Eq. (8.92) can be presented as

$$E = \sigma_0 l \delta \bar{w}^{3/2} (2h_c \epsilon)^{5/4} \int dy' \left[ \frac{1}{2} \left( \frac{dz'}{dy'} \right)^2 + \frac{1}{2} z'^2 - \frac{1}{6} z'^3 \right], \quad (8.93)$$

where the integral is of the order of unity is taken along the extremal trajectory. The latter satisfies

$$\frac{d^2 z'}{dy'^2} = z' - \frac{1}{2} z'^2. \quad (8.94)$$

the solution of this equation ,

$$\bar{z} = \frac{3\bar{w} (2h_c \epsilon)^{1/2}}{\cosh^2(2y/Y_n)}, \quad (8.95)$$

gives the shape of the critical nucleus shown in Fig. 8.92. Further integration in Eq. (8.93) gives

$$U_0 = \frac{6}{5} \sigma_0 l \delta \bar{w}^{3/2} (2h_c \epsilon)^{5/4} \quad (8.96)$$

or the equivalent expression

$$U_0 = \frac{24\sqrt{2}}{5} \mu_B H_c \bar{w} h_c^{1/2} \epsilon^{3/2} N, \quad (8.97)$$

where  $N = M_0 l Y_n \delta / \mu_B$  is the total number of spins inside the nucleus. Comparing Eq. (8.97) with Eq. (8.90) one finds that in terms of  $N$  the dependence of the barrier on the parameters is the same for different geometries of the tunneling.

Equations (8.87) and (8.97) allow one to obtain the crossover temperature for the nucleation process,

$$k_B T_c = \frac{12 \times 2^{1/4}}{5k} \hbar \omega \bar{w}^{-1/2} h_c^{1/4} \epsilon^{1/4}. \quad (8.98)$$

Comparison with Eq.(8.91) again demonstrates a universal dependence of  $T_c$  on the parameters. The only model-dependent parameter here is the width of the barrier, which one can associate with the size of the defect. Other parameters can be found from independent experiments.

### 8.4.6 The Pre-Exponential Factor

Let us now estimate the prefactor  $A$  in the expression for the tunneling rate,  $P = A \exp(-B_0)$ . It is determined by the contribution to the path integral of tunneling trajectories which are small perturbations of the instanton. The general expression for  $A$  in the case of the flat wall tunneling through a planar defect is given by Eq.(8.21) [24, 55, 56]

$$A = \left( \frac{B_0}{2\pi} \right)^{1/2} \left( \frac{\text{Det } \hat{K}_0}{\text{Det}' \hat{K}} \right)^{1/2}. \quad (8.99)$$

Here  $\text{det}'$  means exclusion of the zero mode corresponding to the translational time-invariance of the instanton. The operators  $\hat{K}_0$  and  $\hat{K}_1$  are fluctuation operators defined in Sec. 8.2.1

$$\hat{K}_0 = -\partial_\tau^2 + \omega_1^2, \quad \hat{K}_1 = -\partial_\tau^2 + \omega^2 u''(\bar{z}_i), \quad (8.100)$$

where  $\omega_1 = \omega_0/2$  is the frequency of small oscillations near the minimum of the potential at  $\bar{z} = z_1$  [Fig.8.8 (a)],  $\omega_0$  is the instanton frequency given by Eq.(8.80),  $\bar{z}_i = z_2 / \cosh^2(\omega_0 \tau)$  is the instanton trajectory, Eq.(8.79).

The computation of  $A$  is, in general, a difficult problem. It can be done rigorously, however, in the case of a small barrier, which is of primary interest here. With the help of Eqs.(8.72), (8.79) we obtain

$$u''(z_i) = \frac{1}{4} \left( 1 - \frac{3}{\cosh^2(\omega_0 \tau)} \right). \quad (8.101)$$



Each determinant in Eq.(8.99) is the product of eigenvalues of operators in Eq.(8.100). The problem, therefore, reduces, to the solution of

$$(-\partial_\tau^2 + \omega_1^2) \phi_n = \lambda_n \phi_n, \quad (8.102)$$

$$\left[ -\partial_\tau^2 + \omega_1^2 \left( 1 - \frac{3}{\cosh^2(\omega_0 \tau)} \right) \right] \psi_n = \mu_n \psi_n. \quad (8.103)$$

Exclusion of the zero mode,  $\mu_n = 0$ , leads to the proportionality of the ratio of determinants in Eq.(8.99) to  $\omega_0^2$ . So that up to a numerical factor  $C$  that depends on the ratio of the determinants we can write the prefactor as

$$A = C \omega_0 \sqrt{\frac{B}{2\pi\hbar}} \quad (8.104)$$

The evaluation of the constant  $C$  it is not an easy task and can be performed by two methods: one is the direct computation of the eigenvalues of  $\hat{K}$  that in our case can be done exactly, the other is a simpler way proposed by Coleman which only requires the knowledge of the asymptotic time behaviour of the zero mode eigenfunction [24, 25].

The eigenvalues of the first equation are those of the harmonic oscillator

$$\lambda_n = \left(n + \frac{1}{2}\right) \omega_1. \quad (8.105)$$

The second equation is equivalent to the Schrödinger equation for the potential  $1 - \frac{3}{\cosh^2(\omega_0 \tau)}$  and the problem reduces to find the spectrum of this potential. Fortunately this potential is of the form of the well-known Pöschl-Teller potential  $V(\tau) = \Omega^2 - \frac{V_0}{\cosh^2[m(\tau-\tau_0)]}$  which is solved in the textbooks (see p. 79 in [1] or p. 546 in [25]). There are  $n_{max}$  bound-state eigenvalues given by

$$\mu_n^2 = \Omega^2 - m^2(s-n)^2, \quad (n = 0, 1, 2, \dots, n_{max} < s) \quad (8.106)$$

where  $s$  is an integer defined by  $s = \frac{1}{2} \left[ -1 + \sqrt{a + \frac{4V_0}{m^2}} \right]$ . The continuum eigenvalues are

$$\mu_k = \Omega^2 + k^2. \quad (8.107)$$

In our case  $\Omega = \omega_1$ ,  $V_0 = 3\omega^2/2$ ,  $m = \omega/2$  so that  $s = 2$  and there are two bound states with eigenvalues

$$\mu_0 = 0, \quad \mu_1 = \frac{\sqrt{3}\omega}{2} \quad (8.108)$$

Evaluating this ratio by standard methods [8, 7] one obtains

$$\frac{\text{Det}(-\partial_\tau^2 + \omega_1^2)}{\text{Det}'[-\partial_\tau^2 + \omega_1^2(1 - 3/\cosh^2(\omega_0 \tau))]} = \frac{\prod_n \lambda_n}{\prod_n' \mu_n} = 15\omega_0^2. \quad (8.109)$$

This gives for the prefactor

$$A = \left(\frac{15}{2\pi}\right)^{1/2} B_0^{1/2} \omega_0, \quad (8.110)$$

where  $B_0$  and  $\omega_0$  are given by Eq. (8.76) and Eq. (8.80), respectively.

Observation of tunneling requires a not very large  $B$ . Consequently, the value of the prefactor  $A$  for any reasonable experiment will be somewhere between  $\omega_0$  and  $10\omega_0$ . Based upon dimensional arguments, one can see that this must be the case for any geometry of the tunneling, including the nucleation process studied above.

Case	$B$	$T_c$
FM particles	$\frac{8}{3} \frac{M_0 V}{\hbar \gamma} \left( \frac{k_{\parallel}}{k_{\perp}} \right)^{1/2} \epsilon^{3/2}$	$\frac{3\hbar \gamma \sqrt{k_{\parallel} k_{\perp}}}{8k_B M_0} \sqrt{\epsilon}$
AFM particles	$\frac{2\sqrt{\chi_{\perp} K}}{\hbar \gamma} V$	$\frac{\hbar \gamma}{2k_B} \sqrt{\frac{K}{\chi_{\perp}}}$
Nucleation	$37.8 \frac{M_0 \hbar \delta^2}{\hbar \gamma} \left( \frac{k_{\parallel}}{k_{\perp}} \right)^{1/2} \epsilon^{1/2}$	$0.62 \frac{\hbar \gamma \sqrt{k_{\parallel} k_{\perp}}}{k_B M_0} \sqrt{\epsilon}$
DW 1D	$\frac{48}{5} \frac{\gamma H_c}{\omega} (\bar{w})^{3/2} h_c^{1/4} 2\epsilon^{5/4} N$	$\frac{5\sqrt{2}}{36} \hbar \omega (\bar{w})^{-1/2} h_c^{1/4} \epsilon^{1/4}$
DW 2D	$2^{1/4} k \frac{\gamma H_c}{\omega} \bar{w}^{3/2} h_c^{1/4} \epsilon^{5/4} N$	$\frac{12 \times 2^{1/4}}{5k} \hbar \omega \bar{w}^{-1/2} h_c^{1/4} \epsilon^{1/4}$

Table 8.2: Tunneling exponents and crossover temperatures for different systems.

## 8.5 Quantum nucleation of nonuniform magnetic structures

In the previous section we analyzed in the detail MQT of a domain wall considering that it can be thought as a two dimensional surface and constructing an action in terms of purely geometrical considerations. The internal structure of the wall, that is to say the precise way the spins flip from up to down direction at both sides of the wall was not considered. In real materials non-uniform magnetic structures may be nucleated depending on the geometry of the sample and the type of anisotropy of the material that may not be simply considered as we did in the last section. Here we will present a general framework to calculate quantum transition rates for this kind of structures.

### 8.5.1 Effective action and Sine- Gordon models

Now, instead of using the domain wall displacement as a coordinate identifying the motion of the wall during the tunneling process, we start from the Gilbert's action 8.54 that gives the Landau-Lifschitz equations, in imaginary time it reads

$$S_E = \int d\tau \int d\mathbf{x} \left\{ \frac{\mathbf{M}_0}{\gamma} \dot{\phi} \cos \theta - \mathbf{E}(\theta, \phi) \right\}. \quad (8.111)$$

Therefore we are describing the non-uniform structure by the magnetization direction at every point in space using the spherical coordinate angles  $\theta(x, \tau)$ ,  $\phi(x, \tau)$ . Quantum tunneling rates involve the calculation of a path integral over coordinates  $\theta(x, \tau)$  and  $\phi(x, \tau)$

$$P_{QT} \sim \int \mathcal{D}\theta \int \mathcal{D}\phi e^{1/\hbar \int d\tau \int d\mathbf{x} L(\theta, \phi)} \quad (8.112)$$

in the semiclassical approximation by means of instanton methods, which can be done only if the anisotropy energy is specified. We will consider a quasi one-dimensional system with the geometry of a long slab, infinite along the x direction, xy easy-plane anisotropy with x the easy-axis and a magnetic field applied in the easy-plane at an angle  $\psi$  to the x direction. The energy per unit area considered will be

$$E = \int dx \left\{ J \left( \frac{d\mathbf{M}}{dx} \right)^2 + K_{\perp} M_z^2 - K_{\parallel} M_x^2 - \mathbf{M} \cdot \mathbf{H} \right\}, \quad (8.113)$$

where the first term is the exchange energy, the second and the third are a hard-axis and easy axis anisotropy terms respectively and  $K_{\parallel} \ll K_{\perp}$  will be assumed so that the magnetization direction will be mostly confined

to the  $xy$  plane  $\theta = \pi/2$ . In spherical coordinates this expression reads

$$E(\theta, \phi)/2K_{\parallel} = \int dx \left\{ \delta_0^2 (\theta'^2 + \sin^2 \theta \phi'^2) + \frac{\lambda}{2} \cos^2 \theta - \frac{1}{2} (\sin^2 \theta \cos^2 \phi - 1) - h(\sin \theta \cos \phi + 1) \right\}, \quad (8.114)$$

where the following definitions have been made

$$\lambda \equiv \frac{k_{\perp}}{K_{\parallel}}, \quad \delta_0^2 \equiv \frac{J}{2K_{\parallel}}, \quad \omega_0 \equiv \frac{M_0}{\gamma}. \quad (8.115)$$

To obtain an effective action the path integral over the  $\theta$  coordinate has to be performed and due to the non-linearity of the equations of motion this is only possible in the above mentioned limit  $\lambda \gg 1$  of strong in-plane anisotropy. In this case the dominant tunneling trajectories do not deviated too much from the easy-plane,  $\theta = \frac{\pi}{2} + \beta$  with  $\beta \ll 1$ ,  $\nabla\beta \ll 1$ , and the lagrangian may be expanded up to second order in  $\beta$  to end up with

$$\mathcal{L}/2K_{\parallel} \simeq -\frac{2M_0}{\gamma K_{\parallel}} \dot{\phi}\beta - \lambda\beta^2 - \delta_0^2 \phi'^2 - \frac{1}{2} \sin^2 \phi - h(1 + \cos \phi), \quad (8.116)$$

which is quadratic in  $\beta$  and involves a Gaussian path integral over  $\beta$  that can be easily computed. The resulting expression for the tunneling rate takes the form of a path integral for the relevant coordinate  $\phi$  only

$$P_{QT} = \int \mathcal{D}\phi e^{-S_{eff}^E}, \quad (8.117)$$

with an effective lagrangian density

$$\mathcal{L}_{eff} = \frac{M_0^2}{8\gamma^2 K_{\perp} K_{\parallel}} \dot{\phi}^2 + \frac{J}{2K_{\parallel}} \phi'^2 + \frac{1}{2} \sin^2 \phi + h(1 + \cos \phi), \quad (8.118)$$

and an effective action

$$S_{eff}^E = \frac{2K_{\parallel}\delta_0}{\omega_0} \int d\tau' \int x' \left\{ \frac{1}{2} \left( \frac{d\theta}{d\tau'} \right)^2 + \frac{1}{2} \sin^2 \theta \left( \frac{d\phi}{dx'} \right)^2 + \frac{1}{2} \sin^2 \phi + h(1 + \cos \phi) \right\}, \quad (8.119)$$

that now has been written using dimensionless variables

$$\tau' \equiv \omega_0 \tau, \quad x \equiv \frac{x}{\delta_0}. \quad (8.120)$$

The classical trajectories satisfy the equation

$$\frac{d^2 \phi}{d\tau'^2} + \frac{d^2 \phi}{dx'^2} = \sin \phi (\cos \phi - h) \quad (8.121)$$

that in the original coordinates looks like a double Sine-Gordon equation [57, 58, 59]

$$\frac{1}{\omega_0^2} \frac{d^2 \phi}{d\tau^2} + \delta_0^2 \frac{d^2 \phi}{dx^2} = \sin \phi (\cos \phi - h), \quad (8.122)$$

which have well-known solitonic solutions.

If all the terms that contribute to quadratic order in  $\beta$  are kept in the calculation we would have ended up with following effective lagrangian

$$\mathcal{L}_{eff} = \frac{M_0^2}{4\gamma^2 F(\phi)} \dot{\phi}^2 + J(\nabla\phi)^2 + K_{\parallel} \cos^2 \phi - \frac{M_0 H}{2} \cos \phi, \quad (8.123)$$

with  $F(\phi) \equiv K_{\perp} - J(\nabla\phi)^2 + K_{\parallel} \cos^2 \phi - \frac{M_0 H}{2} \cos \phi$ . Which corresponds to the lagrangian of a point particle with coordinate dependent mass  $M(\phi)$  moving in the potential  $V(\phi)$  given by the expressions

$$M(\phi) = \frac{M_0}{2\gamma F(\phi)}, \quad V(\phi) = K_{\parallel} \cos^2 \phi - \frac{M_0 H}{2} \cos \phi. \quad (8.124)$$

## 8.6 The role of dissipation

Up to this moment we completely neglected interaction of the domain wall with microscopic degrees of freedom like phonons, magnons, etc. The effect of these interactions on the tunneling rate must be computed along the lines of the approach developed by Caldeira and Leggett [5]. The idea is to write the action which includes all such interactions and then, integrating over microscopic variables, to obtain the effective action in terms of the macroscopic variable only. Contributions of various dissipation mechanisms are discussed below.

### 8.6.1 Conduction electrons

One may directly apply the results of Ref. [5, 60] to the Ohmic coupling of  $\mathbf{M}(\mathbf{x}, t)$  with conducting electrons, assuming  $\mathbf{M}(\mathbf{x}, t)$  couples linearly to the electronic coordinates. The heating rate in a ferromagnet is given by

$$\frac{dQ}{dt} = \frac{\eta}{2} \int d^3R \dot{\mathbf{M}}^2 \sim \frac{\eta M_0^2}{\delta} \int dx dy \dot{z}^2, \quad (8.125)$$

where  $z(x, y, t)$  describes propagation of the domain wall;  $\eta$  is a constant. The methods of Caldeira and Leggett [5] imply that this Ohmic dissipation adds a contribution

$$S_{dis} = -\frac{\eta \delta M_0^2}{4\pi} \int dx dy \int dx_0 \int dx'_0 \frac{(\bar{z}(x_0) - \bar{z}(x'_0))^2}{(x_0 - x'_0)^2} \quad (8.126)$$

to the tunneling action (8.68). Then the total Euclidean action becomes

$$S_{tot} = -\frac{\sigma_0}{\omega} \int dx dy \int dx_0 \left[ \frac{1}{2} \left[ \frac{d\bar{z}}{dx_0} \right]^2 + u(\bar{z}) - h\bar{z} + \beta \int dx'_0 \frac{(\bar{z}(x_0) - \bar{z}(x'_0))^2}{(x_0 - x'_0)^2} \right] \quad (8.127)$$

where

$$\beta = \frac{\eta M_0^2 v_0}{4\pi \sigma_0} \quad (8.128)$$

determines the relative contribution of this dissipation to the WKB exponent. In terms of the parameters, beta is of the order of the relative width of the ferromagnetic resonance. This suggests that materials with narrow FMR are better candidates for the observation of quantum tunneling of domain walls.

### 8.6.2 Magnons

Various branches of spin waves, including bulk magnons and magnons in the wall, may, in principle, contribute to the dissipation. The domain wall is a soliton of the nonlinear equation of motion for the magnetization, Eq. 8.38. As has been observed by Stamp [8], the problem of the macroscopic quantum tunneling

of solitons is essentially different from the problem studied by Caldeira and Leggett. Indeed, any soliton, being a solution of a nonlinear differential equation, does not have, by definition, a linear coupling with the excitations of the field describing the soliton. Consequently, the interaction of the domain wall with magnons starts with a term of the second order in magnon variables. Moreover, as shown in Ref. [8], for the case of planar walls, the important coupling between the wall and the magnons is not even the second order one, but the third order coupling. The detailed evaluation of the effects of the various magnon couplings, were treated in detail in Ref. [9], where the contribution of second and third-order processes to the friction coefficients were computed.

Now the problem is how to find the effects of this dissipation on tunneling. We cannot directly apply the Caldeira-Leggett scheme to our problem, because the crucial coupling is third order in the environmental variables; the Caldeira Leggett framework is based on a set of environmental couplings which are linear in the environmental coordinates. However, for Ohmic dissipation, it turns out we can circumvent this problem. We define a function

$$J_3(\omega, T; x, y) = \frac{2\pi}{\hbar} \sum_{k, k', q} |\mathcal{M}_{kk'q}^{(3)}|^2 F\{n_j\} \delta(\omega_k - \omega_{k'} - \epsilon_q - \omega), \quad (8.129)$$

and now observe that provided we may ignore back scattering processes in which magnons are reabsorbed by the wall, the equation of motion of the domain wall will be governed by the Slonczewski equations with an extra dissipative term acting on  $Z(\omega, x, y)$  of the form  $K_3(\omega, T; x, y)Z(x, y)$ , where

$$K_3(\omega, T; x, y) = \frac{2\omega^2}{\pi} \int_0^\infty d\epsilon g(\epsilon) \frac{J_3(\epsilon, T; x, y)}{\epsilon(\epsilon^2 - \omega^2)}, \quad (8.130)$$

where  $g(\epsilon)$  is a ‘‘cutoff’’ function, which smoothly cuts off the linear behavior of  $J_3(\omega)$  at large  $\omega$ ; the form of  $J_3(\omega, T; x, y)$  is just

$$J_3(\omega, T; x, y) = \frac{\omega}{16\pi^2\gamma^2\delta^3} \left( \frac{k_B T}{\Delta_0^2} \right) e^{-\Delta_0/k_B T} \equiv \omega\eta_3(x, y; T). \quad (8.131)$$

Thus, we have arrived at a dynamic equation for the wall, in which the Slonczewski equations have an Ohmic dissipation term added to them; for if we make a time Fourier transform of Eq. (8.131), it just gives a term  $\eta_3\dot{Z}(x, y; t)$  in the Slonczewski equations, with  $\eta_3$  coming from three magnon processes.

Now if  $|\dot{Z}(x, y)| \ll v_0$  and  $\omega \ll v_0/\delta$ , we may carry all of usual ideas of Leggett [61] over to our case, provided we now regard the bath as being a set of temperature dependent modes (each of which describes a triplet of magnons) which are coupled to the wall via a temperature dependent coupling function; all of this is encapsulated in Eq. (8.131). Furthermore, if we are interested in tunneling over a length scale  $\sim \epsilon^{1/2}\delta$  which is much less than the other length scales in the problem (as in the case here), this coupling can be treated as being linear in  $Z(x, y)$ . Then, quite remarkably, the entire effect of the wall magnon interactions can be absorbed into the nonlocal contribution to the imaginary time action of the form 8.127, with the following parameter  $\beta$ :

$$\beta = \frac{\hbar\omega k_B T}{4\pi\Delta_0^2} e^{-\Delta_0/k_B T}. \quad (8.132)$$

This contribution is of exactly the Caldeira Leggett form for Ohmic coupling; we notice that while it is nonlocal in imaginary time, it is local in the spatial coordinates of the wall. This latter result is only true for small wall curvature.

Now we see that for  $k_B T \ll \Delta_0$  we may always neglect dissipation from wall magnon coupling. However, at  $T \sim T_c$  this is not necessarily true. Generally,  $\hbar\omega$  and  $\Delta_0$  have the same order of magnitude [see Eqs.

(8.66)], unless very anisotropic crystals are considered. The crossover temperature (see Sec. 8.4.5) is  $(\sim h_c \epsilon)^{1/4} \hbar \omega$ . Consequently, at  $T \sim T_c$  the relative contribution of the magnon dissipation into the WKB exponent is  $(\sim h_c \epsilon)^{1/4} \exp[-1/(h_c \epsilon)^{1/4}]$ . Because of the conditions  $h_c \ll 1$ ,  $\epsilon \ll 1$ , this contribution cannot be large but may, in principle be of the order of one. It is small, however, in the case of a small barrier,  $h_c \epsilon \ll 1$ , provided that the most significant dissipation mechanism in insulators does not affect the possibility to observe quantum tunneling of domain walls.

### 8.6.3 Phonons

The problem of phonon dissipation turns out to be rather subtle. At first glance one might think that since the magnetoelastic coupling in most magnets is rather small, the effect of phonons should be rather negligible. This guess is certainly confirmed at the level of linear coupling between phonons and the domain wall, as it was for magnetic grain tunneling in Ref. [46, 6]. The argumentation is somewhat similar. In both, the coupling chosen is embodied in the action

$$S_{ph} = \int dt \int d^3x \left\{ \frac{1}{2} \rho \dot{\mathbf{u}}^2 - \frac{1}{2} \lambda_{iklm} u_{ij} u_{lm} - a_{iklm} u_{ij} M_l M_m \right\}, \quad (8.133)$$

where  $\mathbf{u}$  is the phonon displacement field,  $u_{ik} = \frac{1}{2}(\partial_i u_k + \text{partial}_k u_i)$  is the strain tensor,  $\hat{\lambda}$  and  $\hat{a}$  are the elastic and magnetoelastic tensors, respectively, and  $\rho$  is the mass density of the material. As Garg and Kim showed, for magnetic grains this leads to a Caldeira Leggett spectral function  $J(\omega) \sim \omega^3$ , which is infrared weak; moreover, it is small anyway, as one might expect from the fact that the adiabatic effects of this coupling are also weak. They lead to a relative change of the order of  $10^{-5}$  in the effective moment of inertia associated with the subbarrier rotation of  $\mathbf{M}$  and to the same change in the wall mass. Indeed, if the tunneling frequency  $\omega_0$  is small in comparison with  $s/\delta$ , where  $s$  is the speed of sound, then the elastic deformation of the solid due to magnetostriction simply follows the rotating magnetization as the wall moves in imaginary time. For  $\omega_0 \sim 10^{10} \text{ s}^{-1}$ ,  $s \sim 10^5 \text{ cm/s}$ , and  $\delta \sim 10^{-6} \text{ cm}$  it becomes a rather good approximation. The imaginary time dependence of the elastic deformation that adiabatically follows the motion of the wall is  $u(\tau) = u[Z - Z(\tau)]$ , where  $Z(\tau)$  is the instanton solution of Sec. 8.4.4. Substituting this into Eq. (8.133), we obtain that the magnetoelastic interaction contributes the term  $m' \sim \rho u_0^2 / \delta$  to the effective mass of the wall in Eq. (8.49). Here  $u_0$  is the deformation of the crystal, due to the magnetostriction, inside the wall. It can be estimated as  $u_0 \sim \Delta \delta$ , where  $\Delta \sim a M_0^2 / 2E$  is a small dimensionless constant,  $E$  being Young's modulus. Consequently, the relative increase in the wall mass due to the interaction with phonons is  $m'/m \sim \Delta^2 \rho v_0^2 \delta / \sigma_0$ . The constant  $\Delta$  is typically  $10^{-4}$ , which gives  $m'/m \sim 10^{-5}$ .

If one looks at the phonon effects on wall dissipation, the argument is similar, except that one now finds, in a similar way to the work of Wada and Schrieffer [62], that the main contribution to the dissipation is apparently from two phonon elastic processes. Again, the details of this process [8, 63] are not strongly affected by wall curvature, and the dissipative effects are very small ( $\sim T^3$ ). Nevertheless, we are not entirely sure that this is the end of the story. It has recently been shown [64] that in the grain tunneling problem, inelastic two phonon processes will dominate over the one phonon process considered by Garg and Kim, since they give an Ohmic dissipation [ $J(\omega) \sim \omega$ ]. Thus, the possibility of Ohmic dissipation arising from inelastic two phonon interactions with the domain wall remains to be considered.

### 8.6.4 Photons

To complete our picture we consider also the electromagnetic radiation produced by the domain wall tunneling in magnetic insulators. Since the tunneling is described quasiclassically, the analysis of the radiation problem can be also based upon a classical formula,

$$i = \frac{2}{3c^3} \ddot{\mathbf{M}}^2 \quad (8.134)$$

for the intensity of electromagnetic waves radiated by the rotating magnetic dipole  $\mathbf{M}$ . For the process of tunneling via nucleation studied in Sec. 8.4.4, the rotating magnetic moment is the moment of the nucleus. Substituting the corresponding instanton solution into Eq. (8.134) and integrating over the imaginary time from  $-\infty$  to  $+\infty$ , one obtains for the total radiated energy

$$e \sim \frac{M_0^2 V^2 \omega_0^3}{c^3} \quad (8.135)$$

where  $V$  is the volume of the nucleus. This energy is much less than  $\hbar\omega_0$  suggesting that the coupling to photons is irrelevant.

### 8.6.5 Dissipation in terms of mobility

The above considerations show that the most important dissipation effects (from conduction electrons in metals, and from magnons in insulators) are Ohmic. For that reason it is useful to express the relative contribution of the dissipation in terms of the mobility of the domain wall. The latter can be easily obtained from a macroscopic experiment.

The mobility of the domain wall with respect to the magnetic field,  $\mu_H$ , is defined as

$$v = \mu_H H. \quad (8.136)$$

One can connect it with a more conventional mobility,  $\mu_f$ , with respect to the force,  $F$ , on the unit area of the wall,  $v = \mu_f F$ . Since  $F = 2M_0H$  we get  $\mu_H = 2M_0\mu_f$ . According Eq. (8.7), the characteristic frequency associated with the dissipation is  $\nu = 1/\mu_f m_0$ , where  $m_0$  is the mass of the unit area of the wall,  $m_0 = \sigma/v_0^2$ . The Eq. (8.8) provides a rough estimate of the effect of dissipation on tunneling,

$$B = B_0 \left( 1 + \frac{M_0 v_0^2}{\mu_H \sigma \omega_0} \right). \quad (8.137)$$

The quantitative significance of dissipation is discussed in the next section.

## 8.7 Discussion and Experimental evidences of MQT and MQC of Domain Walls

An experiment that would study tunneling of a single-domain wall through a planar defect may be somewhat similar to experiments on tunneling of Josephson junctions. In the magnetic case, the junction can be made of a layer of the material which is different from the bulk. The material of the junction should be selected

such that it pins the wall. Modern evaporation techniques allow one to obtain thicknesses of the junction (defect) as small as one atomic monolayer. The critical field  $H_c$  will, in general, depend on the thickness  $w$  and the material of the junction. The width of the potential well, produced by the junction itself, can hardly be significantly less than the domain wall width. Correspondingly, one should expect that the parameter  $\bar{w}$  in our formulas is of the order of one for  $w < \delta$ , and is roughly given by  $w/\delta$  for  $w > \delta$ . For the narrow junction, from Eqs. 8.96 and 8.98, we have

$$k_B T_c \sim \hbar \omega (h_c \varepsilon)^{1/4} \quad (8.138)$$

for the crossover temperature, and

$$\begin{aligned} A &\sim B^{1/2} k_B T_c / \hbar \\ B &\sim \frac{\gamma H_a \omega^{5/4}}{h_c \varepsilon} N, \end{aligned} \quad (8.139)$$

respectively, for the prefactor and the WKB exponent of the tunneling rate,  $P = A \exp(-B)$ ;  $\omega = v_0/\delta$ ,  $h - c = H_c/H_a$ ,  $\varepsilon = 1 - H/H_c$ . These formulas allow one to estimate the effect based upon the data on the coercive field  $H_c$ , the anisotropy field  $H_a$ , and the parameters of the domain wall: the limiting velocity  $v_0$  and the thickness  $\delta$ .

Eq.(8.138) shows that the dependence of  $T_c$  on  $H_c$  and  $\varepsilon$  is rather weak, and  $T_c$  is mostly determined by the frequency  $\omega$ . In the limit of large transverse anisotropy  $K_\perp$ , Eq.(8.66) gives  $\hbar \omega \sim (4\mu_B/M_0)(K_\parallel K_\perp)^{1/2}$ . Up to a numerical factor, this coincides with the crossover temperature obtained by the exact solution of the equations of micromagnetic theory for tunneling of the magnetization in single-domain particles [43] and quantum nucleation of magnetic bubbles [44].

For a uniaxial ferromagnet,  $K_\perp$  in Eq.(8.66) must be replaced by the magnetic dipole energy  $2\pi M_0^2$ . In the limit of large uniaxial anisotropy,  $K_\parallel \gg 2\pi M_0^2$ , this gives  $\hbar \omega = 4\pi\mu_B M_0$ . This energy itself corresponds to the temperature 0.1 – 1 K for typical values of  $M_0$ ,  $M_0 \sim 10^2 - 10^3$  emu/cm<sup>3</sup>. Let us now estimate how many spins can participate in the tunneling process. For  $H_c \sim 10$  Oe and  $H_a \sim 10^5$  Oe, B of Eq. 8.139 is of the order of  $10^{-3} \varepsilon^{5/4} N$ . This suggests that even at  $\varepsilon \sim 0.1$ , that is without a very fine tuning of the magnetic field, as many as  $10^6$  spins can coherently tunnel through the energy barrier.

The relative contribution of the dissipation to the tunneling rate is of the order of

$$\beta_a \frac{\gamma \delta}{\mu_H} (h_c \varepsilon)^{1/4}, \quad (8.140)$$

where  $\beta_a$  is a factor determined by the structure of the magnetic anisotropy. (For a rhombic crystal  $\beta_a = [(1 + K_\perp/K_\parallel)^{1/2} - 1]$ ). For typical numbers,  $\beta_a \sim 10$ ,  $\delta \sim 10^{-6}$  cm,  $\mu_H \sim 10^2$  cm/s Oe,  $h_c \sim 10^{-4}$ ,  $\varepsilon \sim 0.1$ , this contribution is of the order of one. We may, therefore, conclude that, in materials with low mobility of domain walls, dissipation may significantly affect tunneling. In the case of high mobility, our formulas for undamped tunneling should provide a good estimate of the tunneling rate.

To date, a many of the experiments on the low temperature behaviour of domain walls have been performed in bulk samples. In this case the rate of quantum magnetic relaxation is determined by the statistical average over a large number of individual tunneling events for many domain walls. Although this problem is much more complicated than studied here, we believe that formulas (8.138), (8.139) provide a rough estimate of the effect. For a statistical distribution of barriers, one can hardly expect any smallness in Eqs.(8.138), (8.139) associated with the parameter  $\varepsilon$ . In materials with strong uniaxial anisotropy  $k_B T_c \sim 4\pi\mu_B M_0 (H_a/H_c)^{1/4}$  would be, therefore, a reasonable estimate of  $T_c$ .



A detailed comparison between the theory and experiment on quantum tunneling of magnetization remains a challenging task. In this connection the experiment with a single wall tunneling through a flat junction would be of great interest. One may also think about the possibility to test the effect of dissipation on tunneling in such an experiment. According to Eqs. 8.137, 8.140, it may become noticeable in materials with very low mobility of domain walls. Of course, the extraction of the contribution of the dissipation from experimental data would require the possibility to change the mobility (e.g., by changing the concentration of impurities) without a significant change in other parameters of the tunneling.

In the last years there have been a number of experiments which have given evidence of tunneling of domain walls in a variety of materials and systems specially designed for this purpose. In the following a brief account in historical order.

1. The first calculations on DW tunneling were done by Egami in a series of works published in Egami [65], [65], and [66]. In these articles, he made rough estimates of WKB exponent for DW tunneling and he analyzed his own experimental data as giving the first evidence of tunneling of DW. Bostanjoglo and Gemmund [67, 68] also studied tunneling in bulk disordered magnets. Baldwin et al. [69, 70, 71] first performed a series of experiments on DW mobility in grain-oriented NiFe alloys but failed to attribute unambiguously the results to DW tunneling. Later, Riehemann and Nembach [72, 73] studied the mobility of DW as a function of  $H$  and  $T$  in several Ni-based alloys, interpreting the results in the scope of a model that took into account both thermal activation and tunneling, and concluding that the DW motion was governed by tunneling below 2 K.
2. The group of Prof. Barbara and Uehara performed some of the first experiments to be interpreted as DW tunneling [74]. Previous studies of SmCoCu alloys already indicated [75, 76, 77] anomalies in the diffusion of DW below 50 K. These works were complemented later by a series of studies of the magnetization reversal of the same system in [78, 79, 80], where the authors extracted the field and temperature dependence of the relaxation time and assigned the observed transition from a thermally activated regime to a temperature independent regime below 10 K to tunneling of DW.
3. In the late 80's and at the beginning of the 90's some experiments [81, 82, 83] were performed to specifically address the question of a possible quantum diffusion of domain walls at low temperature. A temperature independent relaxation rate [79] has been observed in a single crystal of chemically disordered  $\text{SmCo}_{3.5}\text{Cu}_{1.5}$  ( $M_0 \sim 300$  e.m.u.,  $H_a \sim 1.2 \times 10^6$  Oe,  $H_c \sim 2 \times 10^4$  Oe). The same phenomenon has been observed by Paulsen et al. [81] in grains of  $\text{Tb}_{0.5}\text{Ce}_{0.5}\text{Fe}_2$  randomly embedded in a polymer matrix. ( $M_0 \sim 200$  e.m.u.,  $H_a \sim 5 \times 10^5$  Oe,  $H_c \sim 5 \times 10^3$  Oe) at  $T \sim 1$  K, in a qualitative agreement with our theoretical estimate. This gives strong confidence to the fact that quantum tunneling of domain walls has indeed been observed.
4. Another set of experiments has been performed by the group of Prof. Tejada and Arnaudus in several multilayered systems consisting of SmCo and FeTb [82],[83],[84],[85], [86]. They measured the time dependence of the thermoremanent magnetization at different  $T$ . From the slopes of the logarithmic part of the corresponding relaxation curves, they extracted the temperature dependence of the coefficient of magnetic viscosity (see Figs. 8.10 and 8.11), which becomes temperature independent below a temperature between 3-7 K depending on the system considered. This is in qualitative agreement with the crossover temperatures estimated from our formulas. Note, however, that some experiments may be also explained by quantum nucleation of magnetic bubbles [44] or by the uniform subbarrier rotation of the magnetization in small grains [43].
5. A more direct evidence of low  $T$  quantum relaxation phenomena of DW was given in a series of experiments by Prof. Giordano [87, 88, 89, 88, 90, 91] on thin Ni wires designed to observe the

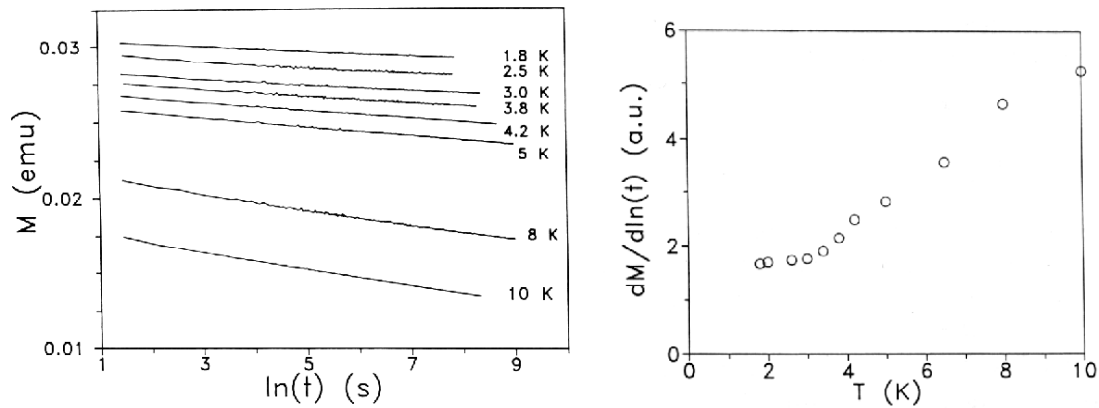


Figure 8.10: Two dimensional random magnet SmCo multilayer. (a) Time dependence of the thermoremanent magnetization at different  $T$  from 1.8 K to 10 K, after switching the magnetic field from 100 to  $-100$  Oe. (b) Temperature dependence of the magnetic viscosity extracted from the slopes of the relaxations curves.

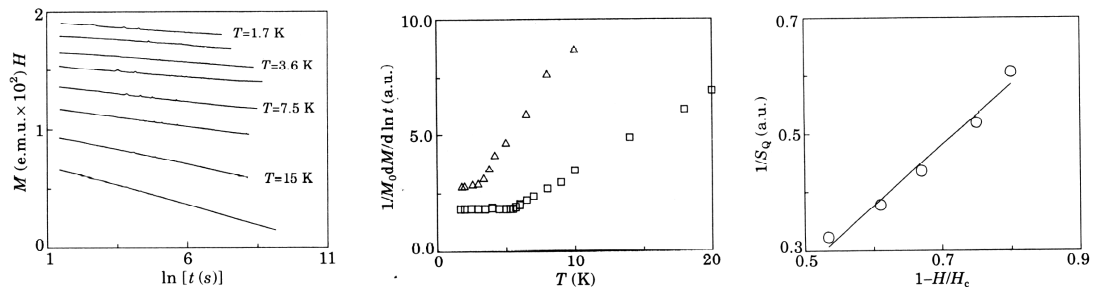


Figure 8.11: Two dimensional random magnet FeTb multilayer. (a) Time dependence of the thermoremanent magnetization at different  $T$  from 1.7 K to 20 K, after switching the magnetic field from 100 to  $-100$  Oe. (b) Temperature dependence of the magnetic viscosity extracted from the slopes of the relaxations curves. Squares: TbFe multilayer. Circles: SmCo multilayer. (c) Field dependence of the quantum viscosity coefficient  $S_Q$  of the FeTb sample on the applied field  $H$  during the relaxation experiments ( $H_c = 500$  Oe).

motion of individual DW along Ni wires. They performed magnetoresistance measurements in Ni wires with diameters in the range 320-600 Å as a function of magnetic field applied along the axis of the wire. The  $R(H)$  curves present dips that may be interpreted in terms of the motion of a domain wall past individual defects that pin the wall. The distribution of escape fields out from the pinning defects is presented in the left panel of Fig. 8.12, it becomes  $T$  independent below a certain temperature. When lowering  $T$  below the depinning field,  $H_c$  deviates from the linear increase expected if thermal activation was the responsible mechanism, and becomes constant below  $T \sim 2$  K, indicating that the depinning of the wall is due to MQT (see right panel of Fig. 8.12). In subsequent works, by irradiating the wires with microwaves, they were even able to induce depinning of the wall from the first excited state of the wall suggesting that the energy levels of the wall are quantized.

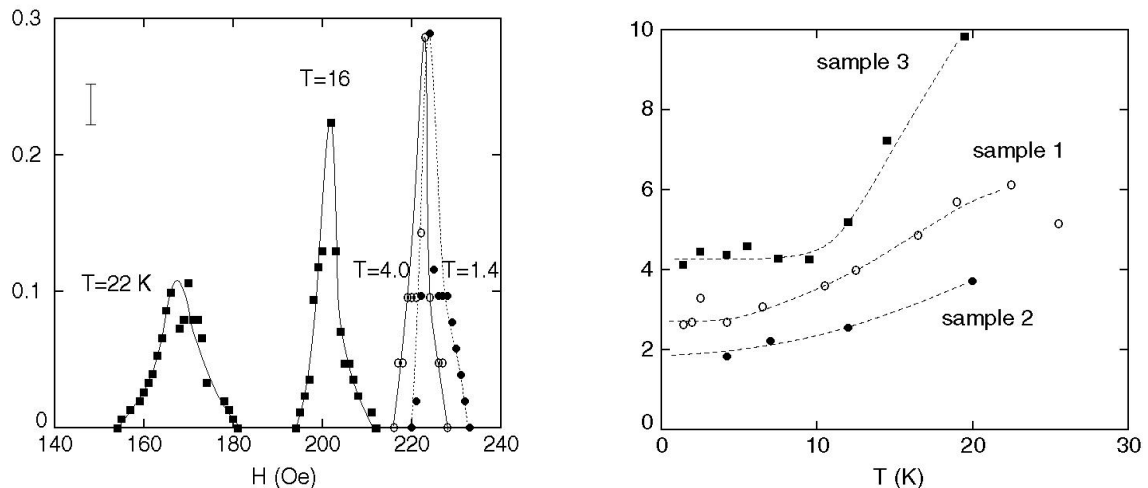


Figure 8.12: Experiments by Giordano et al. in Ni wires. (a) Distribution of escape fields for sample 1 at several temperatures. A typical uncertainty, due largely to the statistical errors, is shown by the bar. The smooth curves are guides to the eye. (b) Widths of the escape field distributions for three different samples. Samples 1, 2, and 3 had (average) diameters of 300, 420, and 350 Å, respectively. The dashed lines are guides to the eye.

6. The groups of Prof Barbara and Wernsdorfer [92], have also recently performed experiments studying the switching of the magnetization of single Ni wires with diameters 40-100 nm measured at temperatures between 0.13 and 6 K. Failing of  $T \ln(t/\tau_0)$  scaling for the waiting fields at low (less than 1 K) temperatures are indicative of quantum nucleation of magnetization reversal rather than motion of DW [93], although other interpretations are possible [94] (see Fig. 8.13). The same groups also performed an experiment [95] measuring the switching time and switching field of a single Co amorphous particle, showing agreement with thermally activated nucleation and annihilation of domain-walls.
7. Our idea of a magnetic domain wall junction proposed above has not been experimentally put into practice since the works by Barbara and Wernsdorfer [96, 97, 98, 99]. The idea of a domain wall junction was originally proposed by Barbara and Gunther [100] in search of a prototype analog of the superconducting Josephson junction in magnetism. It can be considered as a model system suitable for the study of the interaction between a 180 magnetic DW and a well-defined potential energy barrier. This device (see the drawing in Fig. 8.14) consists of a ferromagnetic or ferrimagnetic trilayer system, with an in-plane uniaxial anisotropy, in which a layer of hard magnetic material

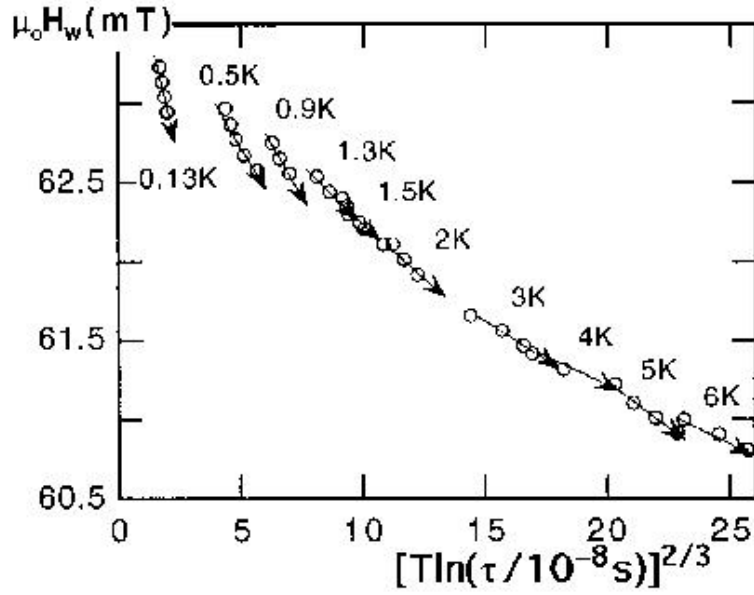


Figure 8.13: Experiments by Wernsdorfer et al. in Ni wires. Scaling plot of the mean switching time  $t(H_W, T)$  for several waiting fields  $H_W$  and temperatures  $[0.1 < t(H_W, T) < 60s]$ . Each arrow is a guide to the eye for data obtained at one temperature and several waiting fields. The field is applied at an angle of  $30^\circ$  with respect to the wire axes.

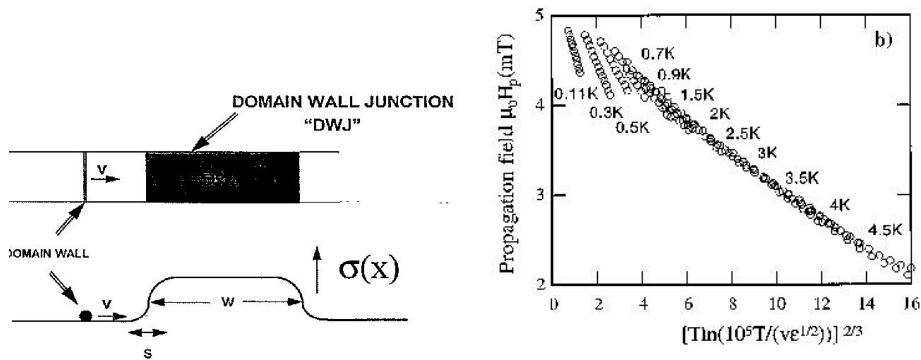


Figure 8.14: Experiments on DW junctions by the groups of Barbara and Wernsdorfer. (a) A depiction of a domain wall moving along a narrow channel of a sample of magnetic material encountering a domain wall junction. The potential energy in the absence of an applied field is depicted below. (b) Scaling plot of the mean propagation fields  $H_p(\alpha = 3/2)$  for field sweeping rates between 0.01 and 50 mT/s and for several temperatures.

separates two layers of soft magnetic material. The hard magnetic material, which presents the larger anisotropy constant, acts as a potential barrier field. Therefore, to move from one layer of soft magnetic material to the second one, the domain wall has to cross the hard magnetic material and the associated potential energy barrier. The junction studied in these works is a sandwich of three ferromagnetic films GdFe/TbFe/GdFe with in plane easy anisotropy. Evidence of MQT of a DW formed in the GdFe layer and depinning from the TbFe junction was achieved from experiments measuring the propagation field of the wall out of the junction at different temperatures. As in the experiments mentioned in the preceding paragraph, the failing of scaling of  $H_p$  with the variable  $T \ln(t/\tau_0)$  below 0.7 K [98] is indicative of quantum tunneling (see Fig. 8.14).

8. To finish, let us also mention the more recent work by Brooke et al. [101], which have performed an experiment on the disordered ferromagnet  $\text{LiHo}_{0.44}\text{Y}_{0.56}\text{F}_4$ , an experimental realization of the Ising FM in a transverse field. They extract the characteristic frequency for magnetic domain relaxation  $\nu_0$  from measurements of the real part of the a.c. susceptibility as a function of the frequency at different  $t$  and several values of the transverse external field  $\Gamma$ . At all the applied  $\Gamma$ ,  $\nu_0$  tends to a constant value (which increases with  $\Gamma$ ) below  $T \approx 0.1$  K, an unambiguous signature of a  $T$  independent tunneling regime, although in a somewhat different context than the one posed by our model.

## Bibliography

- [1] L. D. Landau and E. M. Lifschitz, *Quantum Mechanics* (Pergamon Press, London, 1965).
- [2] J. J. Sakurai, *Modern Quantum Mechanics* (Addison-Wesley, Reading, MA, 1994).
- [3] A. J. Leggett, in *Quantum Tunneling of the Magnetization-QTM'94*, Vol. 301 of *NATO ASI Series E*, edited by L. Gunther and B. Barbara (Kluwer Academic, Dordrecht, The Netherlands, 1995), pp. 1–18.
- [4] E. Schrödinger, *Die Naturwissenschaften* **23**, 844 (1935).
- [5] A. O. Caldeira and A. J. Leggett, *Ann. Phys. (N.Y.)* **149**, 374 (1983).
- [6] A. Garg and G. H. Kim, *Phys. Rev. B* **43**, 712 (1991).
- [7] M. Dubé and P. C. E. Stamp, *J. Low Temp. Phys.* **113**, 1079 (1997).
- [8] P. C. E. Stamp, *Phys. Rev. Lett.* **66**, 2802 (1991).
- [9] E. M. Chudnovsky, O. Iglesias, and P. C. E. Stamp, *Phys. Rev. B* **46**, 5392 (1992).
- [10] A. J. Leggett, S. Chakravarty, A. T. Dorsey, M. P. A. Fisher, A. Garg, and W. Zwerger, *Rev. Mod. Phys.* **59**, 1 (1987).
- [11] N. V. Prokof'ev and P. C. E. Stamp, *J. Phys.: Condens. Matter* **5**, L663 (1993).
- [12] N. V. Prokof'ev and P. C. E. Stamp, in *Quantum Tunneling of the Magnetization-QTM'94*, Vol. 301 of *NATO ASI Series E*, edited by L. Gunther and B. Barbara (Kluwer Academic, Dordrecht, The Netherlands, 1995), pp. 347–372.
- [13] P. C. E. Stamp, in *Quantum Tunneling of the Magnetization-QTM'94*, Vol. 301 of *NATO ASI Series E*, edited by L. Gunther and B. Barbara (Kluwer Academic, Dordrecht, The Netherlands, 1995), pp. 373–398.
- [14] N. V. Prokof'ev and P. C. E. Stamp, *J. Low Temp. Phys.* **104**, 142 (1996).
- [15] A. Garg, *Phys. Rev. Lett.* **74**, 11458 (1995).
- [16] R. F. Voss and R. A. Webb, *Phys. Rev. Lett.* **47**, 265 (1981).
- [17] S. Washburn, R. A. Webb, R. F. Voss, and S. M. Faris, *Phys. Rev. Lett.* **54**, 2712 (1985).
- [18] A. N. Cleland, M. H. Devoret, and J. Clarke, *Phys. Rev. B* **36**, 58 (1987).
- [19] D. B. Schwartz, B. Sen, C. N. Archie, and J. E. Lukens, *Phys. Rev. Lett.* **55**, 1547 (1985).

- 
- [20] J. Clarke, A. N. Cleland, M. H. Devoret, D. Esteve, and J. M. Martinis, *Science* **239**, 992 (1988).
- [21] G. Prinz and K. H. (eds.), *Physics Today* (AIP, New York, April 1995), pp. 24–63, special issue on the subject.
- [22] R. Feynman and A. R. Hibbs, *Quantum Mechanics and Path integrals* (McGraw-Hill, New York, 1965).
- [23] B. Hatfield, *Quantum Field Theory of point particles and strings, Frontiers in Physics, v. 75* (Addison-Wesley, Redwood City, CA, 1992).
- [24] S. Coleman, *The Whys of Subnuclear Physics* (Plenum, New York, 1979).
- [25] H. Kleinert, *Path integrals in quantum mechanics statistics and polymer physics* (World Scientific, Singapore, 1990).
- [26] E. M. Chudnovsky, *Sov. Phys. JETP* **50**, 1035 (1979).
- [27] J. Klauder, *Phys. Rev. D* **19**, 2349 (1979).
- [28] L. S. Schulman, *Techniques and Applications of Path Integration* (Wiley and Sons, New York, 1981).
- [29] E. Fradkin, *Field Theories of Condensed Matter Systems, Frontiers in Physics v. 82* (Addison Wesley, Redwood City, CA, 1991).
- [30] A. Garg and G. H. Kim, *Phys. Rev. B* **45**, 12921 (1992).
- [31] F. D. M. Haldane, *Phys. Rev. Lett.* **57**, 1488 (1986).
- [32] F. D. M. Haldane, *Phys. Rev. Lett.* **61**, 1029 (1988).
- [33] D. Loss, D. P. Di Vincenzo, and G. Grinstein, *Phys. Rev. Lett.* **69**, 3232 (1992).
- [34] J. von Delft and C. L. Henley, *Phys. Rev. Lett.* **69**, 3236 (1992).
- [35] J. von Delft and C. L. Henley, *Phys. Rev. B* **48**, 965 (1993).
- [36] E. C. M. Chudnovsky and D. P. Di Vincenzo, *Phys. Rev. B* **48**, 10548 (1993).
- [37] A. Garg, *Europh. Lett.* **22**, 205 (1993).
- [38] L. D. Landau and E. M. Lifschitz, *Zh. Phys. Sowjet.* **8**, 153 (1935).
- [39] J. L. Van Hemmen and S. Süttö, *Europhys. Lett.* **1**, 481 (1986).
- [40] J. L. Van Hemmen and S. Süttö, *Physica B* **141**, 37 (1986).
- [41] M. Enz and R. Schilling, *J. Phys. C* **19**, 1765 (1986).
- [42] M. Enz and R. Schilling, *J. Phys. C* **19**, L711 (1986).
- [43] E. M. Chudnovsky and L. Gunther, *Phys. Rev. Lett.* **60**, 661 (1988).
- [44] E. M. Chudnovsky and L. Gunther, *Phys. Rev. B* **37**, 9455 (1988).
- [45] B. Barbara and E. M. Chudnovsky, *Phys. Lett. A* **145**, 205 (1990).

- 
- [46] A. Garg and G. H. Kim, *Phys. Rev. Lett.* **63**, 2512 (1989).
- [47] A. Garg and G. H. Kim, *J. Appl. Phys.* **67**, 5669 (1990).
- [48] M. Malozemoff and J. C. Slonczewski, *Magnetic Domain Walls in Bubble Materials* (Academic Press, London, 1979).
- [49] A. Vilenkin, *Physics Reports* **121**, 263 (1985).
- [50] J. F. Dillon Jr., in *Magnetism*, edited by Rado and Suhl (Academic Press, London, 1956), Vol. III, pp. 415–464.
- [51] A. C. Scott, F. Y. F. Chu, and D. McLaughlin, *Proc. IEEE* **61**, 1443 (1973).
- [52] Y. S. Kivshar and B. A. Malomed, *Rev. Mod. Phys.* **61**, 765 (1989).
- [53] K. Hida and U. Eckern, *Phys. Rev. B* **30**, 4096 (1984).
- [54] A. C. Scott, *Am. J. Phys.* **37**, 52 (1969).
- [55] L. S. Langer, *Ann. Phys. (N.Y.)* **41**, 108 (1967).
- [56] L. S. Langer, *Ann. Phys. (N.Y.)* **54**, 258 (1969).
- [57] H. J. Mikeska and M. Steiner, *Adv. Phys.* **40**, 1991 (1991).
- [58] R. Rajaraman, *Solitons and Instantons* (North-Holland, Amsterdam, 1982).
- [59] U. Enz, *Helv. Phys. Acta* **37**, 245 (1964).
- [60] A. J. Leggett, *Phys. Rev. B* **30**, 1208 (1984).
- [61] A. J. Leggett and S. K. Yip, in *Helium Three*, edited by W. Halperin and L. P. Pitaevskii (Elsevier, New York, 1990), Chap. 8.
- [62] Y. Wada and J. R. Schrieffer, *Phys. Rev. B* **18**, 3897 (1978).
- [63] P. C. E. Stamp, E. M. Chudnovsky, and B. Barbara, *Int. J. Mod. Phys. B* **6**, 1355 (1992).
- [64] P. C. E. Stamp (unpublished).
- [65] T. Egami, *Phys. Status Solidi A* **19**, 747 (1973).
- [66] T. Egami, *Phys. Status Solidi B* **57**, 211 (1973).
- [67] O. Bostanjoglo and H. P. Gemmund, *Phys. Stat. Sol. A* **17**, 115 (1973).
- [68] O. Bostanjoglo and H. P. Gemmund, *Phys. Stat. Sol. A* **48**, 481 (1978).
- [69] J. A. Baldwin and F. Milstein, *J. Appl. Phys.* **45**, 4006 (1974).
- [70] J. A. Baldwin, F. Milstein, R. C. Wong, and J. L. West, *J. Appl. Phys.* **48**, 396 (1977).
- [71] J. A. Baldwin, F. Milstein, R. C. Wong, and J. L. West, *J. Appl. Phys.* **48**, 2612 (1977).
- [72] W. Riehemann and E. Nembach, *J. Appl. Phys.* **55**, 1081 (1984).



- [73] W. Riehemann and E. Nembach, *J. Appl. Phys.* **57**, 476 (1985).
- [74] B. Barbara, G. Fillion, D. Gignoux, and R. Lemaire, *Solid State Commun.* **10**, 1149 (1972).
- [75] B. Barbara, *J. Physique* **34**, 1039 (1973).
- [76] B. Barbara, J. Magnin, and H. Jouve, *Appl. Phys. Lett.* **31**, 133 (1977).
- [77] B. Barbara and M. Uehara, *Physica B* **86-88**, 1481 (1977).
- [78] M. Uehara and B. Barbara, *J. Phys. (Paris)* **47**, 235 (1986).
- [79] M. Uehara, B. Barbara, B. Dieny, and P. C. E. Stamp, *Phys. Lett. A* **114**, 23 (1986).
- [80] B. Barbara, P. C. E. Stamp, and M. Uehara, *J. Phys. (Paris)* **49**, C8 (1988).
- [81] C. Paulsen, L. C. Sampaio, B. Barbara, D. Fruchard, A. Marchand, J. L. Tholance, and M. Uehara, *Phys. Lett. A* **161**, 319 (1991).
- [82] X. X. Zhang, L. Balcells, J. M. Ruiz, O. Iglesias, J. Tejada, and B. Barbara, *Phys. Lett. A* **163**, 130 (1992).
- [83] X. X. Zhang *et al.*, *J. Phys. C* **4**, L163 (1992).
- [84] X. X. Zhang, J. Tejada, J. Roig, O. Nikolov, and E. Molins, *J. Magn. Magn. Mater.* **137**, L235 (1994).
- [85] J. Tejada, X. X. Zhang, L. Balcells, O. Iglesias, and B. Barbara, *Europh. Lett.* , 211 (1993).
- [86] J. I. Arnaudas, A. del Moral, C. de la Fuente, M. Ciria, and P. A. J. de Groot, *Phys. Rev. B* **50**, 547 (1994).
- [87] N. Giordano and J. D. Monnier, *Physica B* **194-196**, 1009 (1994).
- [88] K. Hong and N. Giordano, *J. Magn. Magn. Mater.* **151**, 396 (1995).
- [89] K. Hong and N. Giordano, in *Quantum Tunneling of Magnetisation-QTM'94*, edited by L. Gunther and B. Barbara (Kluwer Publishing, Dordrecht, The Netherlands, 1995), pp. 257–272.
- [90] K. Hong and N. Giordano, *J. Phys.: Condens. Matter* **8**, L301 (1996).
- [91] K. Hong and N. Giordano, *Europhys. Lett.* **36**, 147 (1996).
- [92] W. Wernsdorfer, Doudin, D. Mailly, K. Hasselbach, A. Benoit, J. Meier, J.-P. Ansermet, and B. Barbara, *Phys. Rev. Lett.* **77**, 1873 (1996).
- [93] W. Wernsdorfer, K. Hasselbach, A. Benoit, B. Doudin, J. Meier, J. P. Ansermet, and D. Mailly, *Phys. Rev. B* **55**, 11552 (1997).
- [94] J. E. Wegrove, J. Meier, B. Doudin, J. P. Ansermet, W. Wernsdorfer, B. Barbara, W. T. Coffey, Y. P. Kalmykov, and J. L. Dejardin, *Europh. Lett.* **38**, 329 (1997).
- [95] W. Wernsdorfer, K. Hasselbach, A. Sulpice, A. Benoit, J.-E. Wegrove, L. Thomas, B. Barbara, and D. Mailly, *Phys. Rev. B* **53**, 3341 (1996).

- 
- [96] B. Barbara, L. C. Sampaio, J. E. Wegrowe, B. A. Ratnam, A. Marchand, C. Paulsen, M. A. Novak, J. L. Tholence, M. Uehara, and D. Fruchart, *J. Appl. Phys.* **73**, 6703 (1993).
- [97] S. Mangin, G. Marchal, W. Wernsdorfer, A. Sulpice, D. Mailly, and B. Barbara, *J. Magn. Magn. Mater.* **165**, 13 (1997).
- [98] S. Mangin, G. Marchal, W. Wernsdorfer, A. Sulpice, K. Hasselbach, D. Mailly, and B. Barbara, *Europh. Lett.* **39**, 675 (1997).
- [99] S. Mangin, G. Marchal, C. Bellouard, W. Wernsdorfer, and B. Barbara, *Phys. Rev. B* **58**, 2748 (1997).
- [100] L. Gunther and B. Barbara, *Phys. Rev. B* **49**, 3926 (1994).
- [101] J. Brooke, T. F. Rosenbaum, and G. Aeppli, *Nature* **413**, 610 (2001).



## CHAPTER 9

### CONCLUSIONS

In this last chapter, we would like to summarize the most relevant results and conclusions presented in this work.

- We have studied the general equilibrium properties of single monodomain particles. Introducing the concept of effective distribution of energy barriers, we have shown how the magnetic field modifies the energy barriers of an ensemble of non-interacting particles. The inclusion of the finite anisotropy energy term, the distribution of anisotropy constants and random orientation of the particles on the calculation of the equilibrium magnetization curves, have evidenced clear deviations from the Langevin law when these features, that usually are non-negligible real samples, are taken into account.
- We have investigated finite-size and surface effects in fine particle systems by Monte Carlo simulations of a model of a maghemite single particle. Some outcomes of the model are in qualitative agreement with experimental findings such as the reduction of the magnetic ordering temperature, spontaneous magnetization, and coercive field as the particle size is reduced. However, in contradiction with the assumptions made by some authors, our model does not predict the freezing of the surface layer into a spin-glass-like state. The results indicate that magnetic disorder at the surface simply facilitates the thermal demagnetization of the particle at zero field, while the magnetization is increased at moderate fields, since surface disorder diminishes ferrimagnetic correlations within the particle. The change in shape of the hysteresis loops with the particle size demonstrates that the reversal mode is strongly influenced by the reduced atomic coordination and disorder at the surface.
- We have proposed a phenomenological approach to the study of the thermal relaxation processes in assemblies of noninteracting or weakly interacting magnetic entities. The method, based on a  $T \ln(t/\tau_0)$  scaling of the relaxation curves at different temperatures, allows one to extrapolate the relaxation behaviour at times which are experimentally completely unaccessible. From this scaling it is also possible to determine the attempt frequency  $1/\tau_0$ , as well as the width  $\sigma$  of the distribution of energy barriers contributing to the relaxation and the mean energy barrier. We have also critically discussed the validity of the logarithmic approximation proposing a phenomenological criterion to estimate the range in which it is accurate enough, and stressing the misinterpretations than can arise from an analysis only in terms of the so-called magnetic viscosity. Moreover, by the application of the proposed scheme to real experimental data, we have shown how the distribution of energy barriers of a magnetic system can be obtained from the logarithmic time derivative of the master relaxation curves.
- A model for the study of the time dependence of the magnetization in the presence of a magnetic

field, based in the a two state approximation valid at low temperatures, has been proposed. A numerical solution of the equations for  $m(t)$  has allowed us to extend the above mentioned  $T \ln(t/\tau_0)$  scaling method to cases in which the magnetic field drive the system to the equilibrium state. The importance of proper normalization whenever relaxation curves measured at different temperatures must be compared have been emphasized, since non-thermal contributions to the relaxation could be erroneously inferred. Moreover, through the analysis of the effective energy barrier distributions deduced form the master relaxation curves, we have shown that, in this case, it is possible to find a scaling variable for relaxation curves at different  $H$  and fixed  $T$ . This is a new kind of scaling analysis from which the field dependence of the energy barriers can be extracted from the relaxation experiments, an information that would be very difficult to obtain by other methods.

- The role of dipolar interactions on the time dependent processes has been studied by Monte Carlo simulations of 1D chain of interacting spins. We have concluded that the randomness of anisotropy easy-axis and the frustration induced by the dipolar interaction induce faster relaxation rates, changing the time dependence of the magnetic relaxation from quasi-logarithmic to a power-law as the interaction increases.  $T \ln(t/\tau_0)$  scaling of the relaxation curves has proved to be accomplished also for interacting systems, and has proved to be useful tool for the analysis of relaxation curves in this case. In particular, it has allowed us to extract the effective energy barriers contributing to the time dependence of  $m$  and to show that, as the interaction increases, they shift to lower values of the energy, in agreement with experimental results. The results of the simulation of hysteresis loops are in agreement with a reduction of the coercive field and the remanent magnetization with increasing interaction, and the shape of the loops resemble that of frustrated systems.
- From simulations of the ground state and magnetic relaxation of a model of a thin film consisting on a two-dimensional square lattice of Heisenberg spins with perpendicular anisotropy, exchange and long-range dipolar interactions, we have found that the model is able to reproduce the different magnetic configurations found in real samples for a wide range of the interaction parameters. There is a certain range of exchange and dipolar coupling values for which in-plane and out-of-plane configurations are quasi-degenerated in energy. We have show that when a system in this region of parameters is perturbed by an external force that is subsequently removed different kinds of ordering may be induced depending on the followed procedure. In particular, simulations of relaxations from saturation under an a.c. demagnetizing field or in zero field are in qualitative agreement with recent experiments on epitaxial and granular alloy thin films, which show a wide variety of magnetic patterns depending on their magnetic history.
- Finally, we have presented a theoretical study of the quantum relaxation processes in magnetic systems. In particular, we have addressed the calculation of the rate of quantum tunneling of a domain wall through the barrier formed by a planar defect, obtaining results for different depinning cases in terms of the macroscopic parameters of the ferromagnet and showing a universal behaviour of the WKB exponent in the limit of small barriers. The possible observation of these macroscopic quantum effects in ferromagnets has been discussed, concluding that the crossover temperatures from thermal to quantum dominated relaxation are attainable to experiments and that the effects of dissipation can be minimized by proper choice of the materials.

## **Part IV**

# **APPENDIX: MONTE CARLO METHOD**



## CHAPTER 10

### MONTE CARLO METHOD FOR CONTINUOUS SPIN SYSTEMS

In this appendix, we give an account of details concerning the Monte Carlo simulation algorithms used throughout this work, with specific reference to Chapters 6 and 7, where Heisenberg (continuous) spins were used. Moreover, we will present a brief study of the different possible choices for the simulation of the dynamics of continuous systems, exemplified with a simple 1D chain of spins with uniaxial anisotropy energy barriers. We will not give any detailed account of the Monte Carlo method, since, apart from the peculiarities mentioned in what follows, we have used standard implementations. As a reference, we have found useful the following books and reviews: [1, 2, 3, 4, 5, 6, 7, 8].

#### 10.1 Finding the ground states of a spin system: Simulated annealing

The problem of finding the ground state configuration of a system of interacting spins is a problem of finding the global minimum of the energy function in the multidimensional space of spin variables. The energy of the system may be viewed as a function of many continuous variables, the different spin components  $S_i$ , ( $i = 1, \dots, N$ ), that is to be minimized by the ground state configuration. Even for not too big system sizes, the direct search method becomes ineffective due to the large configuration space available, and even more for Heisenberg spins. Other methods as the downhill simplex or the gradient method [9] are likely to get stuck in one of the many local energy minima, not being able to reach the absolute minimum.

For this reason, the method employed to find the ground state is the so called Simulated Annealing. In its simplest version, first introduced by Kirkpatrick et al. [10], the method mimics the well known fact that physical systems settle down themselves in the ground state after being slowly cooled down to zero temperature from a very high temperature. Since the probability of being in a state with energy  $E$  is given by the Boltzmann factor

$$P \sim e^{-E/T}, \quad (10.1)$$

high energy states can only appear with an appreciable probability during the annealing process at high  $T$ . As  $T$  is lowered, these high energy states become less probable and, when approaching  $T = 0$ , only the states near the minimum of the energy function are likely to be reached, provided that the cooling process has been slow enough so as to allow the system to equilibrate at every intermediate temperature.

The implementation for spin systems is as follows. The system is initially prepared in a disordered configuration with the spins randomly oriented at a high enough temperature. This initial temperature  $T_0$  is chosen so that the acceptance rate is practically 100%, that is to say,  $T_0$  must be higher than the highest energy barrier of the system, in our case we choose  $T_0 = 10 - 20$  in reduced units. During every step  $k$  the system is kept at fixed well defined temperature  $T(k)$  and it is allowed to evolve during a number  $t$  of



MC steps long enough (usually between 200 and 250 MCS per spin in our systems) so as to reach thermal equilibrium at the given temperature. At every subsequent step, the temperature is reduced according to a certain cooling protocol  $T(k)$ , which depends on the implementation of the annealing method, until the temperature reaches  $T = 0$ .

The different annealing schemes differ in the way the trial configurations are chosen at every MCS, in the election of the acceptance probability and in the cooling protocol. Of course, the freedom in choosing the protocol is limited by the detailed balance condition, that guarantees that the Boltzmann distribution is properly sampled. Moreover, the cooling protocol must be chosen consistently with the proposal probability so that the configuration space is efficiently sampled. The interest is in maximizing the cooling rate by choosing an adequate proposal probability.

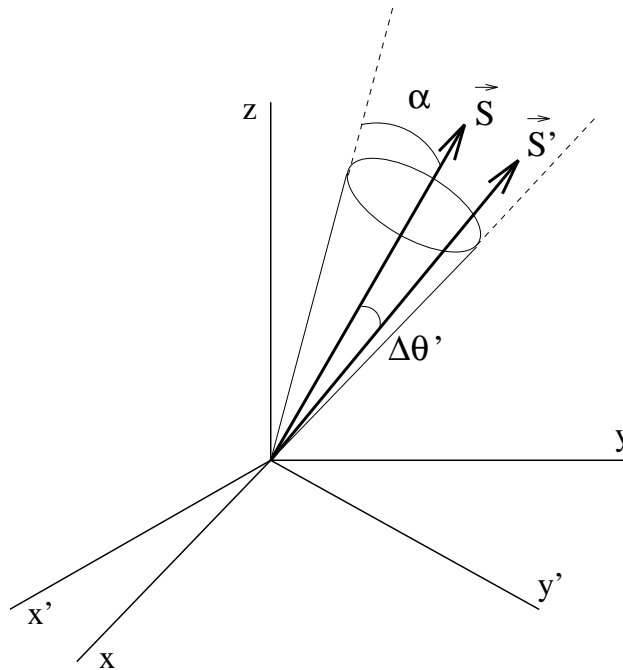


Figure 10.1: Schematic representation of the election of the new spin direction for the trial jump in a Monte Carlo step.  $\vec{S}$  and  $\vec{S}'$  are the directions of the current and the trial direction for the spin. The spin is attempted to be moved in a direction inside of a cone of aperture  $\alpha$  around the current direction of the spin.

### 10.1.1 Adaptive method for the cone of trial angles

The dynamics used for the relaxation is based on the classical Metropolis [11] algorithm, but the choice of the method of proposal of spin flips at every MCS deserves some comments for Heisenberg spins, as they have been used in the simulations of Chapters 6 and 7. In this case, there is a continuum of possible states for the spin characterized by the spherical angles  $(\theta, \phi)$  and consequently many ways to attempt to change the state of a given spin. In order to ensure that the true ground state of the system is faithfully achieved by the considered simulated annealing procedure, we have found convenient to choose the proposed new state  $(\theta', \phi')$  for the change of a spin at every MCS randomly inside a cone of aperture  $\delta\theta$  with respect to the original orientation. This aperture of the cone is varied from the  $\Delta\theta = \pi$  initial value (jumps to any direction) according to the following strategy. At every temperature  $\Delta\theta$  is chosen in such a way that

the acceptance rate of the proposed states is higher than a certain value. For this purpose, we use a small number of the first MCS at each temperature (10 in most cases) to sample the range of angles with higher acceptance rate. For this, we divide the cone in a constant number of intervals and at the end of the first 10 MCS we compute the acceptance rate of trials inside every interval. If some interval corresponding to the higher angles has an acceptance rate smaller than 0.001, we reduce the aperture of the cone of trial angles to the angle corresponding to the maximum of this interval.

This procedure results in a progressive reduction of  $\delta\theta$ , so that the closer is the system to the ground state, the smaller the deviation of the proposed jumps from the current configuration. In this way, we get rid of the inconvenience of trying non-effective jumps that would not allow the system to converge to any equilibrium configuration.

## 10.2 Simulation of dynamics: relaxation

### 10.2.1 Election of trial jumps

The selection of the new trial direction when one spin is attempted to flip in one Monte Carlo step is a delicate point when dealing with Heisenberg spins because of the continuum of accessible states, this is at difference with the case of Ising spins where only up and down states are allowed. When one is interested only on the equilibrium thermodynamic properties of spin systems with interaction the election is guided by computing time economy in finding the equilibrium state of the system, but when one is concerned about time dependent phenomena it is not always obvious what this election must be, changing the trial angle criteria can completely change the dynamic response of the system.

In order to check what is the influence of trial jump in the relaxation of the magnetization of the system, the new orientation  $\vec{S}'(\theta', \phi')$  of the spin is randomly chosen inside a cone of aperture  $\alpha$  around the direction of magnetization of the spin in such a way that, independently of the actual orientation of the spin, the new orientations are uniformly distributed inside the cone:

$$\begin{aligned}\theta' &= \cos^{-1}(1 - (1 - \cos \alpha)\xi_1) \\ \phi' &= 2\pi\xi_2\end{aligned}\tag{10.2}$$

where  $\xi_1, \xi_2$  are two random variables uniformly distributed in the interval  $[0, 1]$ . The case  $\alpha = \pi$  corresponds to random selection of the new orientation, a choice that is commonly taken in the literature.

Some authors make other choices for the trial jump. Many times the new spin orientation is taken as  $\theta' = \theta + \Delta\theta$ ,  $\phi' = \phi + \Delta\phi$  where  $\Delta\theta, \Delta\phi$  are random variables chosen uniformly inside the interval  $[-\alpha, \alpha]$  with  $\alpha$  the maximum permitted angle. The resultant distribution of trial angles is clearly not uniformly distributed over the surface of sphere of radius  $S$ . It is  $\cos \theta$ , and not  $\theta$  itself, the variable that uniformly distributed. If the sampling is not performed in this way, the orientations closer to the original orientation of the spin are favoured, producing slower relaxation rates.

### 10.2.2 Variation of the relaxation rates with $\alpha$ and $T$

The influence of the aperture of the cone of trial angles  $\alpha$  on the relaxation curves has been tested in a simulation of a very simple model consisting on a collection of  $N$  identical non-interacting Heisenberg

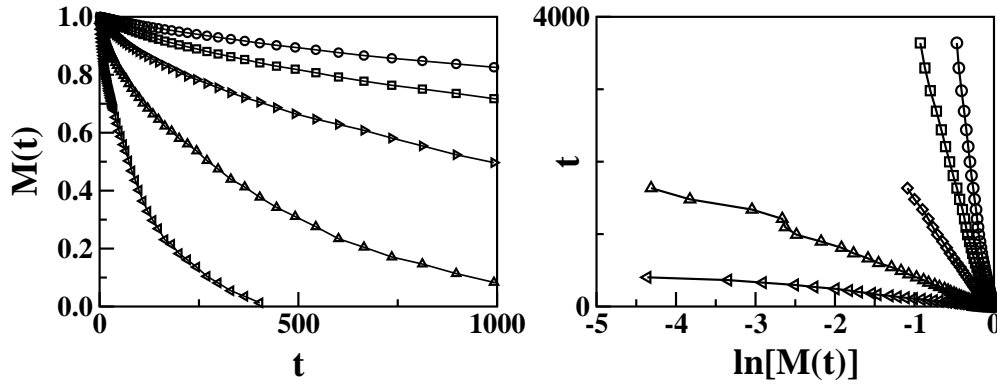


Figure 10.2: (a) Relaxation curves  $M(t)$  at  $T = 0.2$  for different apertures of the cone of trial angles  $\alpha = 2^\circ, 3^\circ, 5^\circ, 10^\circ, 20^\circ$  (from upper to lowermost curve). (b) The same curves as in panel (a) have been plotted in semi-logarithmic scale to emphasize the exponential behaviour  $\ln M(t) \sim C - t/\tau$ . The slopes of these curves are the inverse of the relaxation times  $\tau$ .

spins with energy barriers given by uniaxial anisotropy. The anisotropy energy of the system is then given by

$$H_{anis} = -K \sum_{i=1}^N \sin^2 \theta_i \quad (10.3)$$

where  $\theta$  is the angle between the spin and the easy-axis direction, the same for all the spins. The anisotropy constant will be taken as  $K = 1$ . Therefore, the spins have two local energy minima at  $\theta_i = 0, \pi$  separated by an energy barrier  $E_b = K$ . We will consider that initially the spins are pointing along the positive easy-axis direction  $M(0) = 1$  and that they towards the equilibrium state of zero magnetization under zero magnetic field.

In Fig. 10.2, we present the results of relaxation curves for a fixed temperature  $T = 0.5$  and different apertures of the cone of trial angles  $\alpha$  for a system of  $N = 5000$  spins. The relaxations follow exponential decay as expected for a single energy barrier

$$M(t) = M_0 e^{-t/\tau} \quad (10.4)$$

with  $\tau$  the relaxation time given in principle by the Arrhenius law

$$\tau = \tau_0 e^{E_b/T}, \quad (10.5)$$

$E_b$  being the energy barrier in units of  $k_B$ .

First of all, we observe that, in all the cases, our method for the election of the trial angles produces faster relaxation rates than the method of random trials, being the fluctuations smaller in our case. This indicates that our choice of dynamics is more efficient in sampling the local energy landscape of the spins. But more important is the fact that, for a given temperature, the curves for different  $\alpha$  can be superimposed by appropriate shifts in the time coordinate as demonstrated in Fig. 10.3. By fitting the curves to Eq. 10.4 (see Fig. 10.3b) we have extracted the dependence of  $\tau$  on  $\alpha$  for different temperatures as shown in Fig. 10.3. From these plots, we have been able to deduce the following scaling law for the relaxation times

$$\tau = \frac{F(T)}{\alpha^A}, \quad (10.6)$$

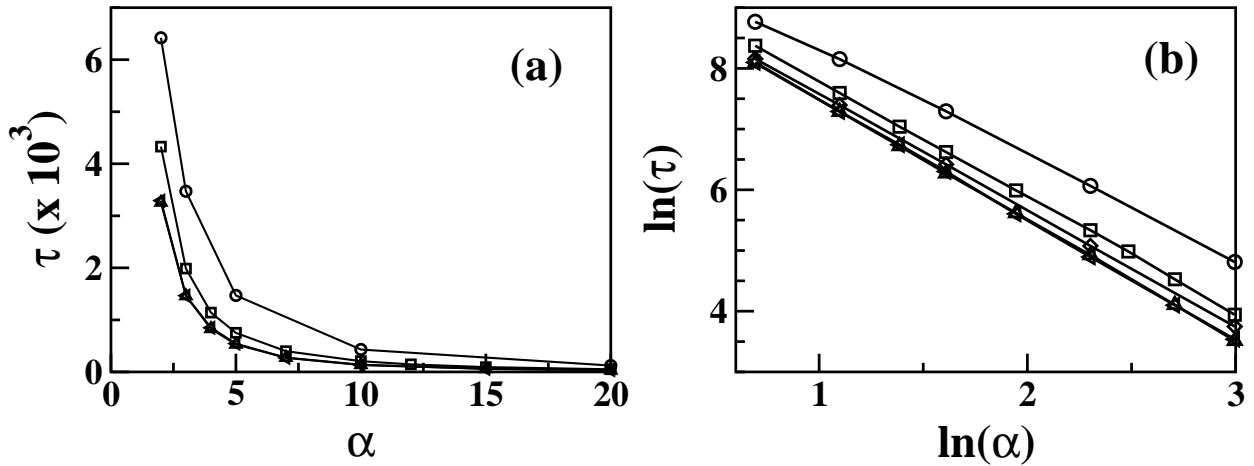


Figure 10.3: (a) Dependence of the relaxation rate  $\tau$  on the aperture of the cone of trial angles  $\alpha$  for  $T = 0.2, 0.5, 1, 5, 10$  starting from the uppermost curve. The values of  $\tau$  have been deduced from the slopes of the straight lines in Fig. 10.2b. (b) Same as panel (a) in a log-log scale. From a linear fit to a law of the type  $\ln(\tau) = \ln(F(T)) - A \ln(\alpha)$  the constant  $A$  and the temperature dependent prefactor  $F(T)$  can be deduced.

where  $F(T)$  is a temperature dependent function and  $A$  an almost temperature independent constant that has been evaluated by fitting  $\ln \tau$  vs.  $\ln \alpha$  to a linear law, with the result  $A = 1.855$  (see Fig. 10.4). The result seems to contradict the *a priori* expected value  $A = 1$  which would indicate a linear dependence. This result clearly indicates that  $\alpha$  only modifies the attempt time  $\tau_0$  in the Arrhenius law (10.5), it only changes the unit of time of the experiment and it is not equivalent to an effective temperature or energy, which would be catastrophic for the Monte Carlo dynamics.

The numerical value obtained for the exponent  $A$  can also be interpreted by the following argument: if spins were Ising spins, their orientation would change always by  $180^\circ$  in a typical time of the order of  $\tau_0$  when the jump attempt is accepted, but if we limit the maximum attempt angle to  $\alpha$ , the number of attempts that produce the reversal of the spin is  $180^\circ/\alpha$  if the accepted changes are in the forward direction but  $(180^\circ/\alpha)^2$  if they are given forward or backward in a random way, thus resulting in the typical relaxation time by a factor  $\alpha^2$ . In our case the attempts are not completely random and that is why the  $A$  exponent is not exactly 2. We have also studied the rate of acceptance of trial jumps, confirming that it decreases when

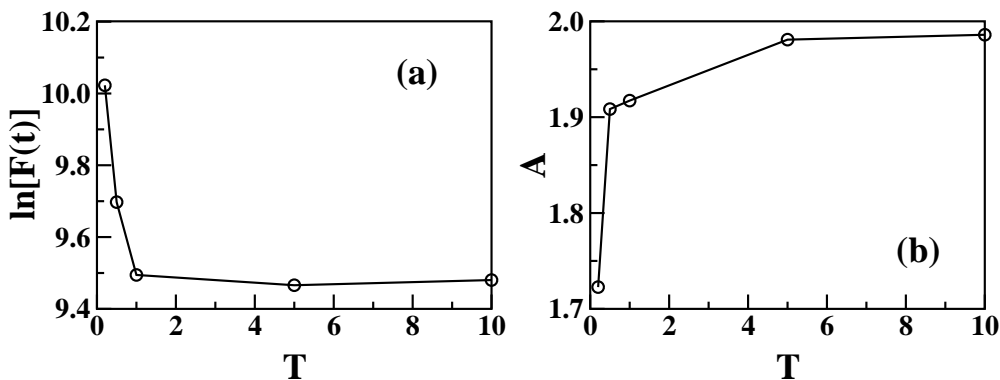


Figure 10.4: Temperature dependence of the parameters  $F(T)$  and  $A$  in (10.6).

$\alpha$	T= 0.01	T= 0.1	T= 0.5
2°	58.34	59.34	59.86
5°	41.84	57.3	59.24
10°	30.28	51.48	58.04
20°	15.56	40.82	54.18

Table 10.1: Acceptance rates (in %) for different apertures of the cone of trial angles ( $\alpha$ ) and temperatures  $T$ .

$\alpha$  is decreased as expected. For a given  $T$ , there is no value of  $\alpha$  that optimizes the acceptance rate. On the other hand, an increase in the temperature always increases the acceptance rate for all  $\alpha$ 's, although this increase is more pronounced for higher  $\alpha$  values (see Table 10.2.2).

### 10.2.3 Low temperature dynamics: Non-Arrhenius behaviour

When studying the low temperature relaxation curves in order to obtain the relaxation time  $\tau$ , we have realized that the relaxation law becomes non-exponential, independently on the method chosen for the trial jumps (see Fig. 10.5, where the relaxation curves for several temperatures and  $\alpha = 20^\circ$  are shown using a logarithmic time scale). This surprising fact, may be better appreciated in the right panel of the same figure, where the curves have been displaced so they coincide with a perfect exponential (curve in open symbols), the lower temperature curve displays a clear deviation from an exponential.

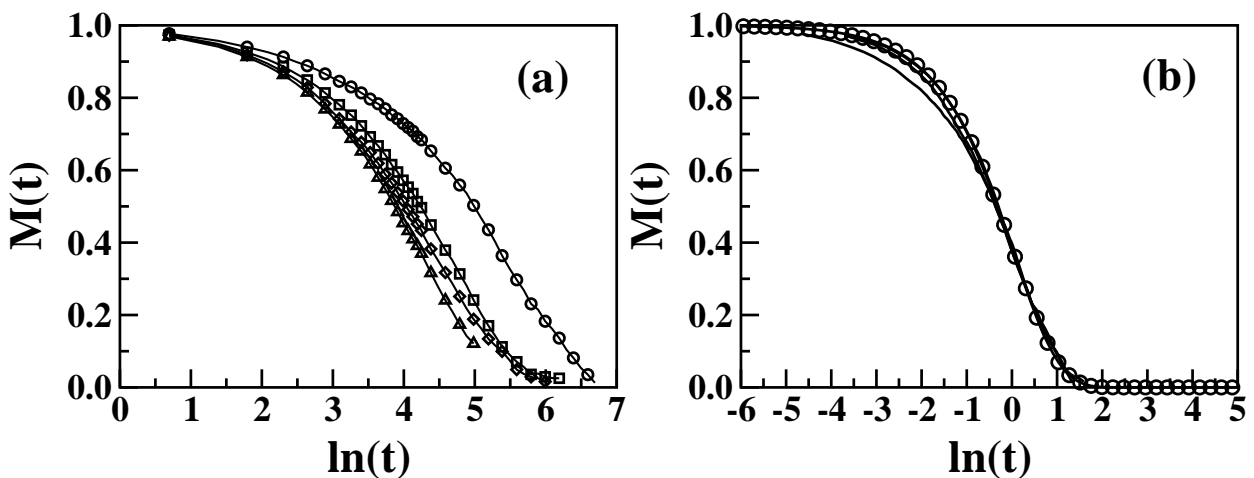


Figure 10.5: Relaxation curves for a trial angle cone of aperture  $\alpha = 20^\circ$  and  $T = 0.2, 0.5, 1, 10$  (from the uppermost curve). At low  $T$ , the relaxation law becomes non-exponential. Right panel: The same set of relaxation curves has been displaced along the horizontal axis to superimpose them to an exponential function (open symbols), the lowermost continuous line corresponds to  $T = 0.2$ .

Analyzing in detail the relaxation curves in a lower temperature range, we see in fact that the relaxation law strongly deviates from the Arrhenius law at short times. In Fig. 10.6, we see that the general behaviour of the relaxations is an initial transient decay, faster for the highest  $\alpha$ , followed by a plateau in which the system spends some time before continuing to relax in a pseudo-exponential decay towards the final equilibrium state. The magnetization value at the region of the plateau is independent on the aperture  $\alpha$ ,

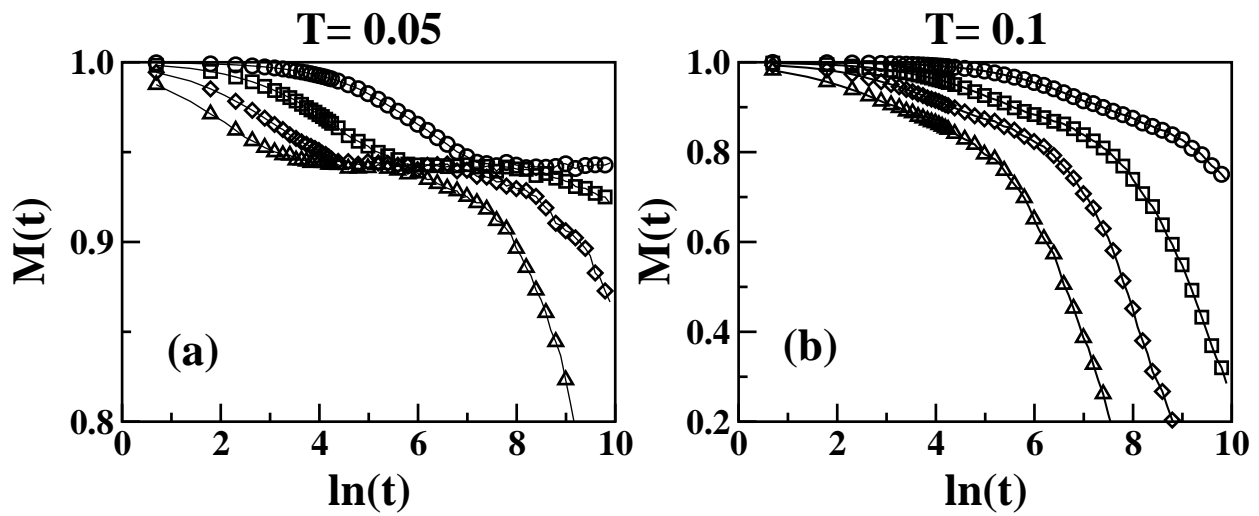


Figure 10.6: Low temperature relaxation curves for different apertures of the cone of trial angles  $\alpha = 2^\circ, 5^\circ, 10^\circ, 20^\circ$  (Starting from the uppermost curve) and temperatures (a)  $T = 0.05$ , and (b)  $T = 0.1$ .

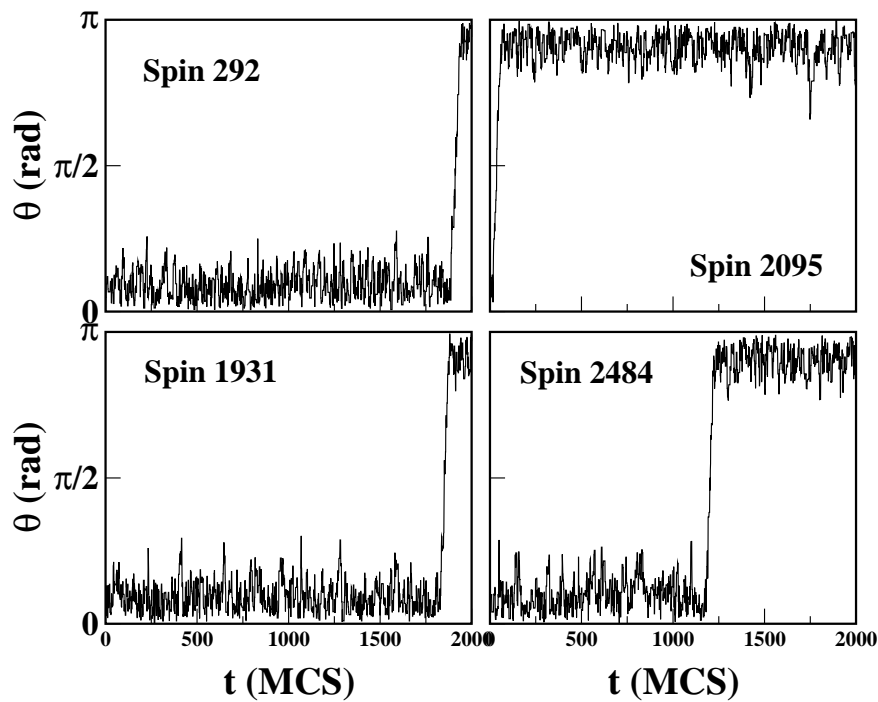


Figure 10.7: Time dependence of the orientation  $\theta$  of four selected spins of the system for the case  $\alpha = 20^\circ$  and  $T = 0.05$ .

and it progressively disappears when increasing the temperature. We have checked that the value of the magnetization at the plateau corresponds in fact to the equilibrium magnetization at the given temperature. The initial decay corresponds to the equilibration of the spins around the local energy minima. At higher temperatures, the equilibration time is so small that this state is attained in very few MC steps and it cannot be observed. This interpretation is supported by the curves in Fig. 10.7, that show the temporal evolution

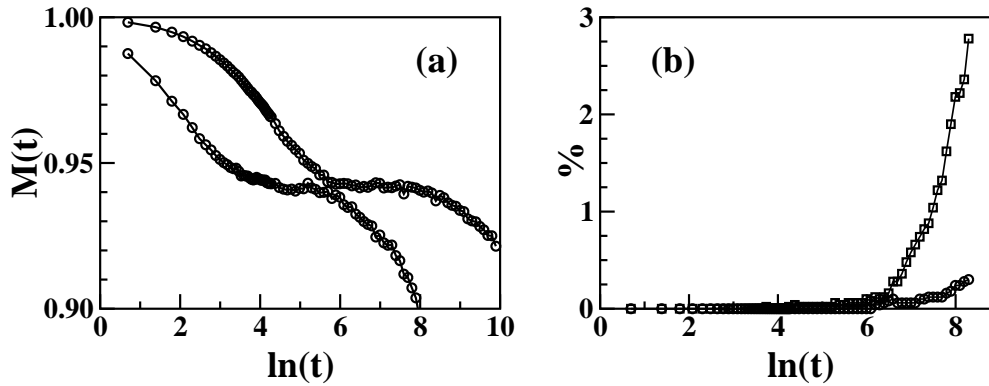


Figure 10.8: Time dependence of the ratio of spins with orientations  $\theta > 90^\circ$  that have crossed the anisotropy energy barrier. The evolution corresponds to the same case as in Fig. 10.6:  $T = 0.05$  and  $\alpha = 5^\circ, 20^\circ$ .

of the orientation of four spins that relax at different times. Spins 292 and 1931 reverse in the exponential decay region after the plateau while spins 2095 and 2484 are amongst the few that relax at times in the plateau region. In all the cases, we observe that the spins spend most of the time fluctuating around the  $\theta = 0, \pi$  minima because most of the trial jumps are ineffective to reverse their magnetization. The reversal takes place when a consecutive sequence of successful trial jumps allows the spin to climb the energy barrier. Further support to this interpretation is given in Fig. 10.8 where we have followed the temporal evolution of the number of reversed spins, that is to say spins with orientations  $\theta > 90^\circ$ . In this figure, we see that before the plateau region the most of the spins remain with orientations fluctuating around the  $\theta = 0$  minimum and only after the plateau the spins start to jump over the energy barrier with fast exponential relaxation.

## Bibliography

- [1] K. Binder, *Monte Carlo methods in Statistical Physics*, Vol. 7 of *Topics in Current Physics* (Springer-Verlag, Berlin, 1979).
- [2] K. Binder, *Applications of the Monte Carlo methods in Statistical Physics*, Vol. 36 of *Topics in Current Physics* (Springer-Verlag, Berlin, 1987).
- [3] K. Binder and D. W. Heermann, *Monte Carlo Simulation in Statistical Physics*, Vol. 80 of *Springer Series in Solid-State Sciences* (Springer-Verlag, Berlin, 1988).
- [4] K. Binder, *Rep. Prog. Phys.* **60**, 487 (1997).
- [5] O. G. Mouritsen, *Computer Studies of Phase Transitions and Critical Phenomena*, Vol. 36 of *Springer series in computational physics* (Springer-Verlag, Berlin, 1984).
- [6] A. D. Sokal, *Monte Carlo Methods in Statistical Mechanics: Foundations and New Algorithms*, 1996, lectures at the Cargèse Summer School.
- [7] F. James, *Rep. Prog. Phys.* **43**, 73 (1980).
- [8] M. P. Allen and D. J. Tildesley, *Computer Simulation of Liquids* (Clarendon Press, Oxford, 1987).
- [9] W. H. Press, S. A. Teukolsky, W. T. Vetterling, and B. P. Flannery, *Numerical Recipes: The Art of Scientific Computing*, 2nd ed. (Cambridge University Press, Cambridge, England, 1992).
- [10] S. Kirkpatrick, D. C. Gellat, and M. P. Vecchi, *Science* **220**, 671 (1983).
- [11] N. Metropolis, A. W. Rosenbluth, M. N. Rosenbluth, A. H. Teller, and E. Teller, *J. Chem. Phys.* **21**, 1087 (1953).





## CHAPTER 11

### LIST OF PUBLICATIONS

*El autor tiene que callar la boca cuando su obra abre la suya.*

FRIEDRICH NIETZSCHE

*El Nacimiento de la Tragedia*

1. E. M. Chudnovsky, O. Iglesias, and P. C. E. Stamp.  
Quantum tunneling of domain walls in ferromagnets.  
Phys. Rev. B , **46**, 5392, 1992.
2. J. Tejada, X. X. Zhang, Ll. Balcells nad C. Ferraté, J. M. ruiz, F. Badia, O. Iglesias, and B. Barbara.  
Observation of quantum tunneling of the magnetization vector in small particles with and without domain walls. Part I.  
In J. L. Dormann and D. Fiorani, editors, *Studies of Magnetic Properties of Fine Particles and their Relevance to Materials Science.*, pages 225–233, The Netherlands, 1992. Elsevier Science Publishers.
3. X. X. Zhang, Ll. Balcells, J. M. Ruiz, O. Iglesias, J. Tejada, and B. Barbara.  
Time dependent phenomena at low temperatures in SmCo multilayers: quantum nucleation phenomena.  
Phys. Lett. A, **163**: 130–134, 1992.
4. J. M. Ruiz, X. X. Zhang, O. Iglesias, A. García, and J. Tejada.  
Structural disorder in two-dimensional random magnets: Very thin films of rare earths and transition metals.  
Phys. Rev. B , **47**: 11848–11851, 1993.
5. J. Tejada, X. X. Zhang, Ll. Balcells, O. Iglesias, and B. Barbara.  
Non-thermal viscosity in the magnetic relaxation of 2d random magnets.  
Europhys. Lett., **22**: 211–216, 1993.
6. A. Labarta, O. Iglesias, Ll. Balcells, and F. Badia.  
Magnetic relaxation in small particle systems:  $T \ln(t/\tau_0)$  scaling.  
Phys. Rev. B , **48**: 10240–10246, 1993.
7. O. Iglesias, F. Badia, A. Labarta, and Ll. Balcells.  
 $T \ln(t/\tau_0)$  scaling in small-particle systems: low temperature behaviour.  
J. Magn. Magn. Mater. , **140-144**: 399–400, 1995.

8. O. Iglesias, F. Badia, A. Labarta, and Ll. Balcells.  
Energy barrier distributions in magnetic systems from the  $T \ln(t/\tau_0)$  scaling.  
*Z. Phys. B*, **100**: 173–178, 1996.
9. Ll. Balcells, O. Iglesias, and A. Labarta.  
Normalization factors for magnetic relaxation of small particle systems in non-zero magnetic field.  
*Phys. Rev. B*, **55**: 8940–8944, 1997.
10. O. Iglesias, A. Valencia, and A. Labarta.  
Monte carlo simulation of the magnetic ordering in thin films with perpendicular anisotropy.  
*J. Magn. Magn. Mater.*, **196-197**: 819–820, 1999.
11. O. Iglesias and A. Labarta.  
Magnetic history dependence of metastable states in thin films with dipolar interactions.  
*J. Magn. Magn. Mater.*, **221**: 149–157, 2000.
12. O. Iglesias, F. Ritort, and A. Labarta.  
Finite size effects in small particle systems.  
In George. C. Hadjipanajyis, editor, *Magnetic Storage Systems Beyond 2000*, volume 41 of *NATO ASI Series II*, pages 363–367, Dordrecht, The Netherlands, 2001. Kluwer Academic Press.
13. O. Iglesias, A. Labarta, and F. Ritort.  
Monte carlo study of the finite-size effects on the magnetization of maghemite small particles.  
*J. Appl. Phys.*, **89**: 7597–7599, 2001.
14. O. Iglesias and A. Labarta.  
Finite-size and surface effects in maghemite nanoparticles: Monte carlo simulations.  
*Phys. Rev. B*, **63**: 184416–184427, 2001.
15. O. Iglesias and A. Labarta.  
Magnetic field scaling of relaxation curves in small particle systems.  
*J. Appl. Phys.*, **91**: 4409–4419, 2002.
16. O. Iglesias and A. Labarta.  
Effects of the magnetic field on the relaxation of small particle systems.  
*Journal of Computational Material Science*, : 1–16, 2002.  
(To be published).
17. C. de Graaf, I. de P. R. Moreira, F. Illas, O. Iglesias, and A. Labarta.  
The magnetic structure of  $\text{Li}_2\text{CuO}_2$ : from ab initio calculations to macroscopic simulations.  
Submitted to *Phys. Rev. B*, 2002.

## **CAPÍTOL 12**

### **RESUM EN CATALÀ**

# **Processos de dependència amb el temps en sistemes magnètics**

## 12.1 Presentació

El camp dels materials magnètics és un dels camps amb major auge en les últimes dècades per la seva rellevància en aplicacions tecnològiques i en el camp de l'enregistrament magnètic. La necessitat d'enginyar materials per augmentar la densitat d'emmagatzematge digital ha fet créixer l'interès en la física dels sistemes de partícules magnètiques petites en les últimes dècades. En els últims anys, hi ha hagut un interès creixent en la física dels sistemes de partícules magnètiques petites, a causa de la necessitat d'enginyar materials per augmentar la densitat d'emmagatzematge digital. Actualment, la mida típica es troba en l'escala del nanòmetre i estem fregant els límits físics per la mínima unitat de gravació. Aquesta progressiva miniaturització s'ha de dur a terme intentant evitar la desmagnetització induïda per efectes tèrmics, efectes de superfície i per la interacció entre partícules, temàtiques en les quals s'han centrat gran part dels estudis actuals.

Les propietats magnètiques dels materials tenen el seu origen en els efectes quàntics a escala atòmica. No obstant, l'objectiu d'aquest treball no és un tractament basat en la física atòmica si no una descripció del processos de magnetització a escala macroscòpica. Així doncs, els sistemes magnètics d'interès al nostre estudi seran considerats com a medis continus amb propietats que varien també de manera continua en l'espai i en el temps, l'estàtica i la dinàmica dels quals seran descrits per les equacions diferencials que els descriuen. Aquesta aproximació és l'essència de la branca del magnetisme que es coneix amb el nom de Micromagnetisme, un apropament que adoptarem per descriure sistemes en els quals les interaccions entre els spins són menyspreables. En aquest cas, podem trobar solucions numèriques, fins i tot analítiques quan sigui possible, de les equacions fonamentals micromagnètiques. En presència d'interaccions, qualsevol intent de trobar solucions analítiques o numèriques per un sistema de mida macroscòpica s'ha d'abordar des de l'aproximació dels medis continus i s'han d'emprar simulacions per ordinador per tractar problemes plantejats, en principi, en base a una descripció a nivell macroscòpic. Per aquest motiu, els mètodes utilitzats en aquest treball abarquen des de models teòrics i solucions numèriques, a models fenomenològics i simulacions per ordinador, amb l'inclusió esporàdica de resultats experimentals.

Des d'un punt de vista microscòpic, la histèresi i les propietats que depenen del temps estan relacionades amb les propietats de l'energia lliure del sistema. A causa de la complexitat de les interaccions entre els constituents que contribueixen a l'energia i la presència de desordre estructural i propietats distribuïdes, l'energia lliure dels sistemes magnètics presenta una complicada estructura en forma d'un paisatge amb múltiples valls i barreres d'energia, amb molts mínims locals en els quals el sistema pot quedar atrapat. Aquesta metastabilitat microscòpica, junt amb les fluctuacions tèrmiques, és l'origen de la dependència amb el temps de les propietats magnètiques macroscòpiques. La manera per la qual un sistema arriba al seu veritable estat d'equilibri, depèn, en general, de l'estat inicial en el qual s'ha preparat i en la història magnètica a la qual s'ha vist sotmès. Aquestes són les condicions que determinaran el camí que el sistema seguirà a través del complex paisatge energètic per arribar a l'estat final d'equilibri. Així doncs, aquest estudi tractarà fenòmens de la termodinàmica del no-equilibri i se centrarà principalment en la descripció de les lleis per les quals els sistemes magnètics s'apropen als estats d'equilibri.

## 12.2 Models d'una única partícula

En aquesta part del treball ens hem concentrat en l'estudi de les propietats magnètiques d'una única partícula ferromagnètica, és a dir, estudiarem una partícula nanomètrica sense tenir en compte la seva interacció amb la resta de partícules. Hem proposat dos nivells de descripció: a) En una primera aproximació, tractem

la partícula com un macrospin, sense considerar la distribució interna de la seva magnetització. Aquest nivell de descripció en ha permès entendre les propietats d'equilibri de conjunts de partícules monodomini sense interacció. b) Un segon pas ha consistit en la consideració de l'estructura interna de la partícula, tenint en compte la seva estructura cristal·logràfica i les interaccions entre els spins.

### 12.2.1 Propietats d'equilibri

Respecte a l'estudi de les propietats d'equilibri, hem presentat un model general per la descripció d'una partícula monodomini, tenint en compte les diferents contribucions a la seva energia magnètica a través de l'expressió

$$\bar{E}(\theta, \psi) = E/KV = -\cos^2\theta - 2h\cos(\theta - \psi), \quad (12.1)$$

on el primer terme prové de l'anisotropia magnetocristalina  $K$  i el segon de la interacció amb un camp magnètic extern. Una anàlisi matemàtica d'aquesta expressió permet calcular les barreres energètiques que separen les direccions d'equilibri estables per la magnetització en funció del camp magnètic extern  $h$  i de la orientació de la partícula  $\psi$ . El càlcul d'aquestes barreres i la seva variació amb  $h$  i  $\psi$  són fonamentals per l'estudi de les propietats d'equilibri i de dependència temporal, donat que són l'ingredient bàsic pel càlcul de les probabilitats de transició.

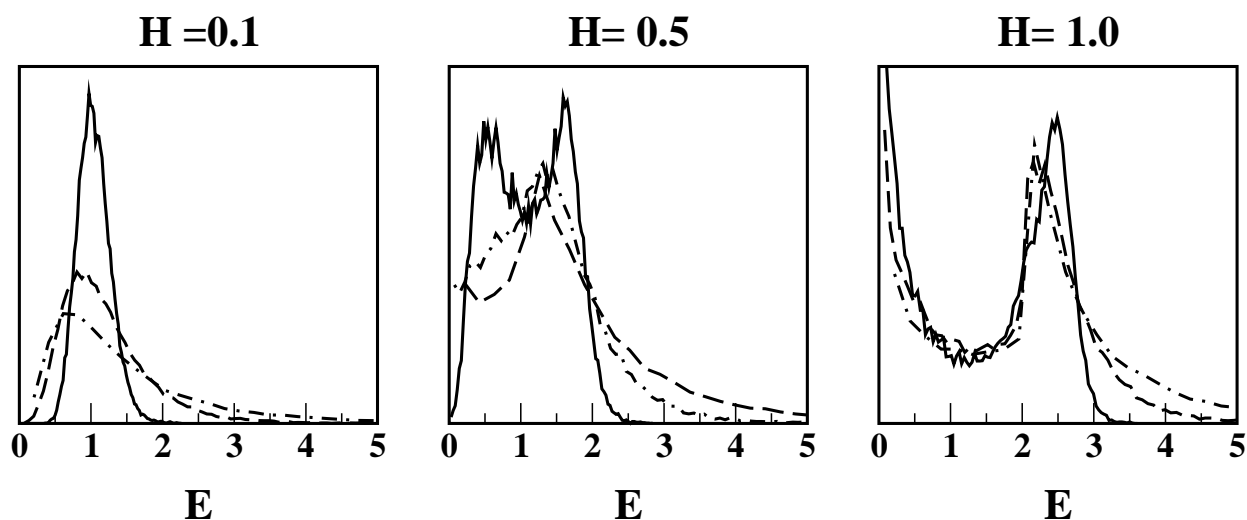


Figura 12.1: Distribucions efectives de barreres d'energia per partícules amb orientacions d'eixos d'anisotropia a l'atzar i distribució lognormal de constants d'anisotropia centrades a  $K_0 = 1$  i d'amplades  $\sigma = 0.2$  (línies contínues), 0.5 (línies discontinúes), 0.8 (línies discontinúes i a punts), per diferents valors de  $h$ .

En els sistemes de partícules estudiats experimentalment, les propietats intrínseques com el volum, les constants i els eixos d'anisotropia es troben distribuïdes, donant lloc a una distribució de barreres d'energia  $f(E_b^0)$ . Paràmetres externs, com el camp magnètic, modifiquen aquestes distribucions transformant-les en distribucions efectives  $f_{\text{eff}}(E_b)$ . Un càlcul numèric de les mateixes (Fig. 12.1) ens fa veure que el camp magnètic estreta les distribucions i les desplaça cap a valors menors de l'energia.

Aquesta anàlisi general ha estat utilitzada posteriorment per calcular les corbes de magnetització, en les quals, normalment, no es té en compte l'anisotropia magnètica. El càlcul es basa en la següent expressió

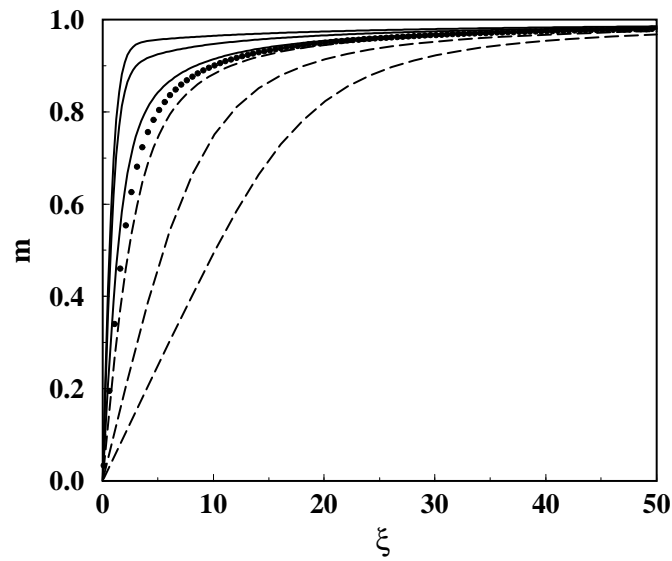


Figura 12.2: Corbes de magnetització per una sistema de partícules en 3D en funció de l'energia Zeeman  $\xi = \mu HV/k_B T$ . Les línies contínues són per partícules alineades en la direcció del camp  $\mathbf{h}$  ( $\psi = 0$ ) i energies d'anisotropia  $\alpha = 1, 5, 10$  (des de la corba superior). Han estat evaluades a partir de l'expressió exacta Eq. (12.2) per partícules orientades ( $\psi = 0$ ). Les línies discontinúes són el resultat de l'evaluació numèrica de la mateixa expressió per partícules orientades a l'atzar. Per comparació es mostra també la llei de Langevin corresponent ( $\alpha = 0$ ) en símbols.

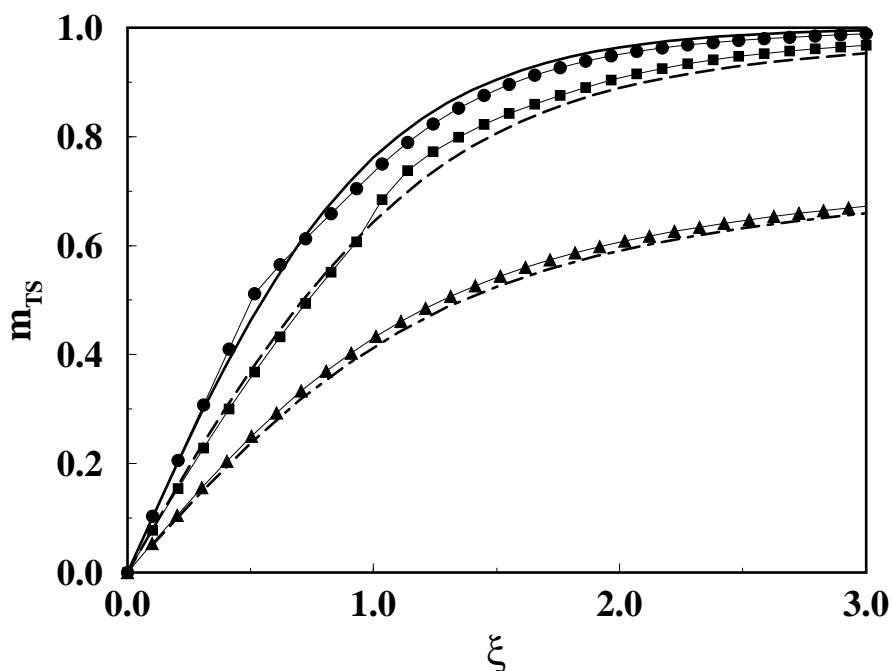


Figura 12.3: Corbes de magnetització en funció de l'energia Zeeman adimensional  $\xi = \mu HV/k_B T$  en la TSA. Els símbols representen els resultats per a partícules orientades a l'atzar amb  $K_0 = 0.5, 1.0, 10.0$  (des de la corba superior). El cas  $K_0 = 10$  es compara amb el resultat exacte donat per l'Eq. (12.2) en 2D (línia discontinua i a punts). El cas  $K_0 = 1$  es compara amb un de partícules amb  $f(K)$ ,  $K_0 = 1$  i  $\sigma = 0.5$  (línia discontinua). El resultat per partícules alineades,  $m_{TS} = \tanh(\xi)$ , es mostra amb una línia contínua ( $m_{TS}$  és independent de  $\sigma$  en aquest cas).

pel promig termodinàmic de la magnetització d'una partícula orientada en la direcció  $\psi$

$$m(\alpha, \xi, \psi) = \frac{1}{Z} \int_{\Omega} d\Omega \cos \theta e^{-U(\theta, \varphi, \psi)}, \quad (12.2)$$

on  $\Omega$  és l'angle solid i  $Z$  la funció de partició. Aquí l'energia  $U(\theta, \psi)$  que apareix a la probabilitat Boltzmann, ha estat reescrita en la forma

$$U(\theta, \varphi, \psi) = -\alpha \sin^2 \theta + \xi (\cos \theta \cos \psi + \sin \theta \sin \psi \cos \varphi), \quad (12.3)$$

on s'han introduït els dos paràmetres adimensionals

$$\alpha \equiv \frac{\mu KV}{k_B T} \quad \xi \equiv \frac{\mu HV}{k_B T}. \quad (12.4)$$

Nosaltres hem extès el càlcul tenint en compte el terme d'energia d'anisotropia, l'orientació a l'atzar dels eixos s'anisotropia i la distribució de valors de  $K$ ,  $f(K)$ . Els resultats es mostren a la Fig. 12.2. Com es pot observar, els càlculs demostren que, quan es té en compte l'anisotropia, s'observen clares desviacions de la llei de Langevin. Per una banda, per partícules alineades amb el camp, la magnetització augmenta per tots els valors del camp. Per l'altra, quan els eixos de fàcil imantació estan distribuïts a l'atzar, l'efecte és el contrari.



Finalment, hem introduït l'anomenada aproximació de dos estats (TSA) pel càlcul de les propietats d'equilibri, ja que ens serà d'utilitat en l'estudi de la relaxació magnètica que presentarem en la següent secció. Aquesta aproximació considera el límit de baixes temperatures, tals que l'energia tèrmica  $K_B T$  és petita en comparació amb les barreres d'energia rellevants, típicament de l'ordre de l'energia d'anisotropia  $KV$  ( $\alpha = KV/k_B T \gg 1$ ). En aquest cas, la principal contribució a les mitjanes termodinàmiques prové dels estats propers als mínims d'energia. Per tant, hom pot truncar el continu d'estats possibles per l'orientació de la magnetització  $\theta$  als dos estats donats per les direccions d'equilibri estable per  $m$ . D'aquesta manera, el càlcul de la magnetització d'equilibri [Eq. (12.2)], per una partícula amb  $\varphi = 0$  (2D model) orientada en la direcció de  $\psi = 0$ , esdevé

$$\bar{m}_{TS}(K, \psi) = \frac{1}{Z} \sum_{i=1,2} \cos[\theta_{\min}^i(\psi)] e^{-E_{\min}^i(K, \psi)\beta}, \quad (12.5)$$

on  $\beta = 1/k_B T$ . Per un sistema de partícules orientades a l'atzar, i distribució d'anisotropies  $f(K)$ , l'Eq. 12.5 s'ha d'integrar sobre les orientacions, un cop pesada amb  $f(K)$ . Aleshores, l'aproximació a l'Eq. (12.2) en la TSA és

$$m_{TS}(H, T) = \int_0^\infty dK \int_0^\pi d\psi f(K) \bar{m}_{TS}(K, \psi). \quad (12.6)$$

Els resultats del càlcul numèric d'aquesta expressió es mostren a la Fig. 12.3. Com veiem, les corbes per la TSA coincideixen amb les corresponents a l'expressió exacta per valors de  $K_0$  prou alts (compareu el cas  $K_0 = 10$  amb la línia discontinua a punts de la Fig. 12.3). A més a més, per valors suficientment petits de  $K_0$ , la TSA reproduïx el resultat exacte per partícules alineades (compareu la línia contínua amb el cas  $K_0 = 0.5$ ).

### 12.2.2 Model d'una partícula

Les propietats magnètiques de les partícules nanomètriques estan fortament influenciades per efectes de mida finita i de superfície, que esdevenen més importants quan la mida de les partícules es redueix. El efectes de mida finita són a causa de la mida nanomètrica de les partícules, mentres que els efectes de superfície estan relacionats amb el trencament de la simetria translacional de l'estructura cristal·lina a la frontera que limita cada partícula. Aquests efectes es manifesten en una àmplia varietat de propietats magnètiques anòmales respecte a les de materials massius. La caracterització d'aquests sistemes ha posat de manifest la controvertida qüestió de distingir quines contribucions a les propietats magnètiques peculiars provenen d'efectes de mida finita i quines són degudes a efectes de superfície.

Gran part dels estudis recents se centren en partícules d'òxids ferrimagnètics, que presenten una singular fenomenologia a baixes temperatures. Entre les propietats estàtiques, els experiments han mostrat que els cicles d'histeresi presenten alts camps de tancament i que no se saturen [1, 2, 3], fins i tot a camps de l'ordre de 50 T, la qual cosa indica que el camp d'anisotropia no pot ser l'únic mecanisme responsable per inversió de la magnetització. També s'observen baixes magnetitzacions respecte als materials massius, cicles desplaçats després d'un refredament amb camp i irreversibilitats entre els processos de refredat amb i sense camp, fins i tot a camp alts [4, 2, 3]. Si aquest fenomen es poden atribuir a propietats intrínseques de la partícula (vidre d'spin a la superfície que crea un camp d'intercanvi en el seu interior) [1, 3]), o són causats per un comportament col·lectiu induït per les interaccions entre partícules [5, 6, 7], és encara una qüestió que espera resposta [8].

El nostre treball pretén aclarir aquests punts foscos des del punt de vista experimental i anar un pas més enllà en les simulacions numèriques ja publicades. Així doncs, presentem resultats de simulacions Monte

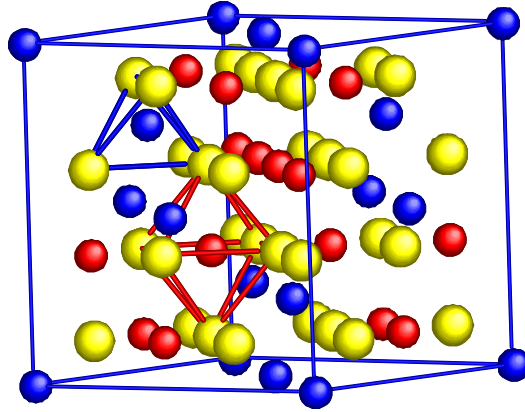


Figura 12.4: Cella unità de la maghemita. Els ions magnètics  $\text{Fe}^{3+}$ , que ocupen les dues subxarxes, amb diferent coordinació amb els ions  $\text{O}^{2-}$  (en blanc), s'han acolorit en negre (subxarxa T, coordinació tetraèdrica) i en gris (subxarxa O, coordinació octaèdrica).

Carlo (MC) amb la intenció d'esbrinar el rol específic de la mida finita i de la superfície en les propietats magnètiques de la partícula, sense tenir en compte els efectes de la interacció entre partícules.

La maghemita,  $\gamma\text{-Fe}_2\text{O}_3$ , és un dels sistemes de nanopartícules més estudiats [9] que presenta la fenomenologia esmentada. La seva estructura d'espínella, (veure Fig. 12.4) pot ser representada pel següent Hamiltonià atòmic

$$\mathcal{H}/k_B = - \sum_{\alpha,\beta=T,O} \sum_{i=1}^{N_\alpha} \sum_{n=1}^{N_{\alpha\beta}} J_{\alpha\beta} S_i^\alpha S_{i+n}^\beta - h \sum_{\alpha=T,O} \sum_{i=1}^{N_\alpha} S_i^\alpha, \quad (12.7)$$

on  $h = \frac{\mu H}{k_B}$ , essent  $S$  i  $\mu$  els valors de l'spin i del moment magnètic respectivament. Hem representat els moments atòmics per spins tipus Ising  $S_i = \pm 1$ . Els valors de les constants d'intercanvi a primers veïns són [9, 10]:  $J_{TT} = -21$  K,  $J_{OO} = -8.6$  K,  $J_{TO} = -28.1$  K, i són antiferromagnètiques. Els subíndexs  $T$  i  $O$  fan referència a les dues subxarxes ocupades pels ions magnètics  $\text{Fe}^{3+}$  (veure Fig. 12.4). A baixes temperatures, aquest compost s'ordena ferrimagnèticament, amb els spins de cada subxarxa ordenats ferromagnèticament i les subxarxes ordenades antiparal·lelament entre elles.

Hem utilitzat condicions periòdiques (PB) de contorn per simular el comportament massiu del material amb dimensions lineals del sistema  $N > 8$  cel·les unità per minimitzar els efectes de mida finita. Per estudiar els efectes de mida finita, hem considerat partícules esfèriques amb  $D$  cel·les unità de diàmetre amb  $3 \leq D \leq 10$  i condicions de frontera lliures. Hem distingit dues zones en la partícula: l'interior i la superfície, formada per la cel·la unità més externa. També hem tingut en compte l'existència de vacants en la subxarxa  $O$  en la maghemita. El codi del program ens permet de variar la concentració d'aquestes vacants, bé a tota la partícula o només a la seva superfície. A cada pas MC hem fet mesures de l'energia, la calor específica, la susceptibilitat i diferents magnetitzacions: les de les subxarxes ( $M_O, M_T$ ), la de la superfície i l'interior ( $M_{Surf}, M_{Core}$ ), i la total ( $M_{Total}$ ). Cadascuna ha estat normalitzada al respectiu nombre d'spins, de manera que varï de 1 a  $-1$ .

Els resultats obtinguts reproduïeixen satisfactòriament propietats característiques dels sistemes de na-

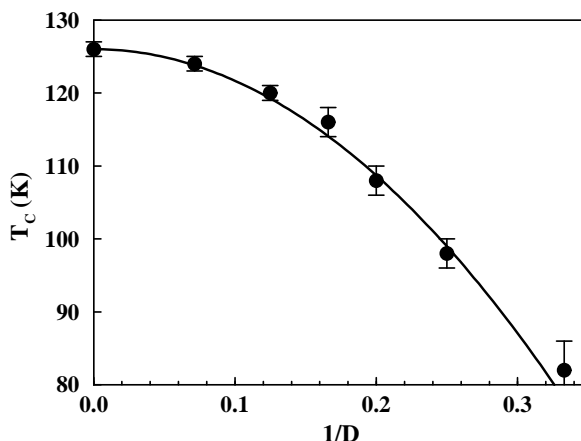


Figura 12.5: Dependència de la temperatura de transició  $T_c$  entre les fases paramagnètica i ferrimagnètica en la mida de partícules esfèriques amb FB. Els valors que es mostren han estat obtinguts del màxim de la calor específica. La línia contínua és un ajust a la llei d'escala  $\frac{T_c(\infty)-T_c(D)}{T_c(\infty)} = \left(\frac{D}{D_0}\right)^{-1/\nu}$ .

no partícules ferrimagnètiques que a continuació detallam:

1. La reducció de la temperatura crítica  $T_c$ , la magnetització espontània  $M_{Total}$  i el camp coercitiu  $H_c$ , per grandàries petites, a mesura que  $D$  decreix. Hem trobat que  $T_c(D)$  segueix les lleis d'escalat de mida finita convencionals, descartant cap efecte de superfície important en aquesta quantitat. Efectes similars s'han trobat en partícules de  $MnFe_2O_4$  [11], però amb un sorprenent increment de  $T_c(D)$  en disminuir  $D$ . En canvi, la magnetització espontània  $M_{Total}$  segueix, a totes les temperatures, un comportament quasi-lineal amb  $1/D$ , vegeu la Fig. 12.6, indicant que la reducció de  $M_{Total}$  és simplement proporcional a la ràtio d'espins superficials respecte els interiors a la partícula, indicant que és principalment un efecte de superfície. S'ha trobat un comportament semblant en experiments amb  $\gamma\text{-Fe}_2\text{O}_3$  [12] i el sistema anteriorment citat [11].
2. L'increment, amb la reducció de la mida de la partícula i amb l'increment del desordre a la seva superfície, de la susceptibilitat diferencial i l'elongació dels cicles d'histeresi de manera semblant a com passa per sistemes frustrats. La reducció per efectes tèrmics de  $h_c(T)$  per partícules esfèriques (veure Fig. 12.9) es troba en acord qualitatiu amb els resultats experimentals per partícules de magnetita de mides compreses entre 9-10 nm que es mostren a la Fig. 4 de la Ref. [3], tenint en compte que a les mostres reals hi ha contribucions addicionals que provenen del procés de bloqueig associat a la distribució de grandàries de les partícules ( $h_c$  cau a zero per sobre de la temperatura de bloqueig). En ambdós casos, la curvatura de la corba  $h_c(T)$  és similar, suggerint una progressiva inversió de la magnetització, fet que confirma la forma dels cicles d'histeresi al voltant de  $h_c$ . No obstant això, el nostre model per partícules esfèriques dóna coercitivitats reduïdes respecte el material massiu (representat pel cas PB). Aquest fet contrasta amb l'increment trobat experimentalment [1, 3, 5], i indica que no pot ser causat per l'efecte de mida finita. L'increment de l'anisotropia a la superfície en pot ser la causa. En qualsevol cas, el model reproduïx qualitativament la reducció en  $h_c$  amb  $D$  [vegeu la Fig. 1 de la Ref. [1]], que pot molt bé ser un efecte de mida finita.
3. L'existència d'una capa superficial amb més desordre magnètic que a l'interior. Les dependències de  $M(T)$  and  $M(h)$  obtingudes en les nostres simulacions ens porten a concloure que, en partícules esfèriques, hi ha una capa superficial amb un grau de desordre magnètic superior que a l'interior.

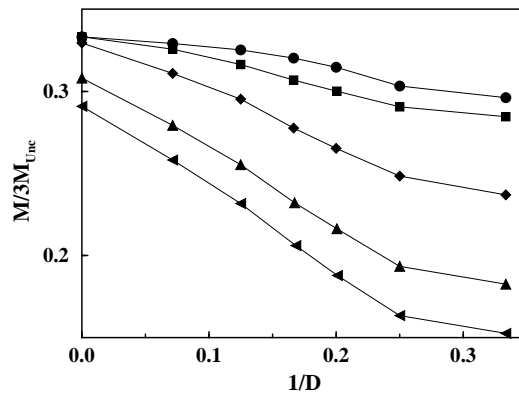


Figura 12.6: Dependència de la magnetització d'una partícula esfèrica en el diàmetre  $D$  a diferents temperatures  $T = 0, 20, 40, 60, 70$  K (de dalt a baix).

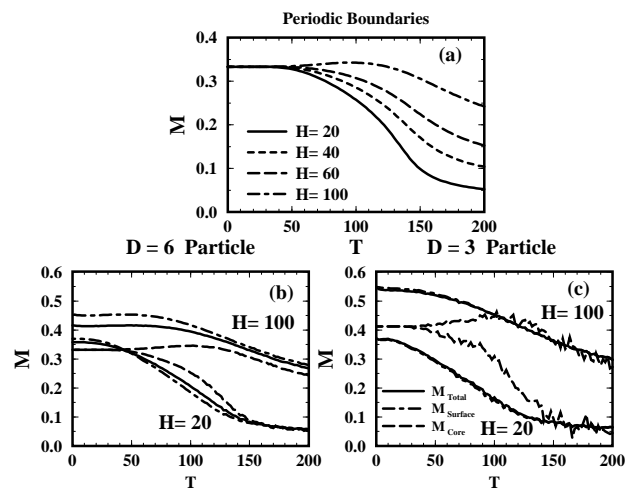


Figura 12.7: Dependència tèrmica de la magnetització després d'un procés de refredament als camps que mostren les llegendes. (a) Mostra els resultats pel material massiu obtinguts per un sistema de mida lineal  $D = 8$  i condicions periòdiques de contorn. Els panells (b) i (c) corresponen un procés de FC a camp baix  $H = 20$  i alt  $H = 100$  per partícules esfèriques de diàmetres  $D = 3, 6$  respectivament. Hem distingit les contribucions de la superfície i l'interior de la partícula tal com es mostra a la llegenda.

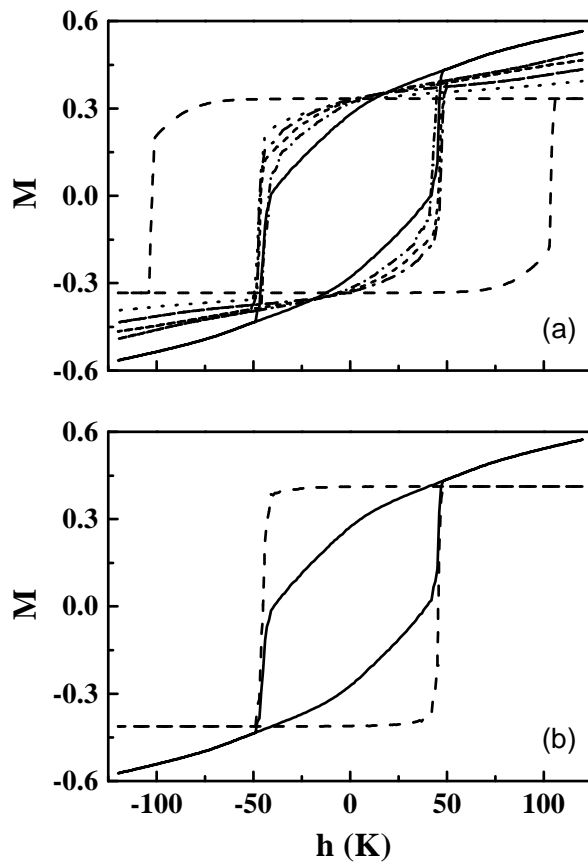


Figura 12.8: (a) Cicles d'histèresi per partícules de diàmetres  $D = 3, 4, 6, 8, 10$  (des de la corba interior a l'exterior) i condicions periòdiques (línies discontinúes) a  $T = 20$  K. (b) Contribucions de la superfície (línia contínua) i de l'interior (línia discontinúes) per una partícula de diàmetre  $D = 3$  a  $T = 20$  K.

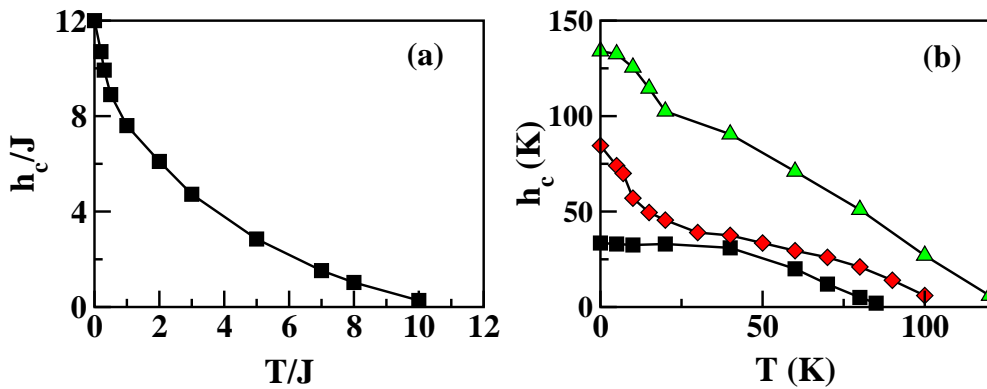


Figura 12.9: (a) Dependència tèrmica del camp coercitiu  $h_c$  per un sistema amb la mateixa estructura que la maghemita per interaccions ferromagnètiques ( $J_{\alpha\beta} = J$ ) i condicions periòdiques de contron amb  $N = 8$ ; (b) Dependència tèrmica del camp coercitiu pels valors AF reals de les constants d'intercanxi per la maghemita pel cas de partícules esfèriques de diàmetres  $D = 3$  (cercles),  $D = 6$  (quadrats), i per un sistema de mida lineal  $N = 8$  amb condicions periòdiques (diamants).

### 12.3 Efectes col·lectius

En aquesta part, hem centrat el treball en l'estudi de la dependència en el temps de les propietats magnètiques de conjunts de partícules petites. En una primera fase, no tindrem en compte encara les interaccions entre partícules. Les úniques propietats col·lectives considerades seran la distribució dels paràmetres físics que tenen a veure amb les propietats magnètiques del sistema. Entre elles, les més importants són la distribució de volums, de constants d'anisotropia i d'eixos de fàcil magnetització. Així doncs, hem establert primer un model fenomenològic de relaxació per sistemes de partícules no interactuants quan no s'aplica camp magnètic extern. En una extensió del mateix, passarem a descriure els efectes del camp magnètic sobre la relaxació magnètica.

Posteriorment, tindrem en compte les interaccions dipolars de llarg abast entre les partícules, a més de les propietats ja mencionades. D'aquesta manera, estudiarem l'influència de les interaccions dipolars en les propietats magnètiques, aprofitant el concepte de distribucions de barreres efectives anteriorment introduït. Finalment, presentarem resultats de simulacions Monte Carlo de la relaxació en presència d'interacció.

#### 12.3.1 Processos de relaxació en absència de camp magnètic

Com ja hem mencionat a la introducció, la pèrdua de magnetització dels materials en passar el temps, és un fenomen ben conegut de rellevància tecnològica donada la progressiva reducció de les dimensions dels constituents dels materials que s'empren en aplicacions tecnològiques durant la segona meitat del segle passat.

En disminuir la mida de les partícules, hom s'apropa al límit superparamagnètic i, per tant, la barrera energètica que separa les dues orientacions de la magnetització degenerades en energia esdevé prou petita com per què pugui ser superada mitjançant les fluctuacions tèrmiques, comportant el canvi espontani de la magnetització. Aquest fenomen provoca una degradació de la informació enregistrada i per això el repte per l'enginyeria de l'enregistrament magnètic ha estat intentar mantenir l'altura de les barreres d'energia de les partícules individuals, sense que els materials deixin de ser prou tous per poder-hi fer gravació. Així doncs,

per millorar la qualitat dels materials emprats en la gravació d'alta densitat, és essencial entendre la física dels conjunts de partícules nanomètriques a prop del límit superparamagnètic. Per què la magnetització d'un material canvia amb el temps i com es pot modelitzar aquest fenomen, són les qüestions a les quals hem intentat donar resposta en el nostre estudi.

Els experiments de relaxació magnètica es limiten a un rang de temps no superior a quatre dècades, però durant aquest interval de temps la magnetització varia normalment en un petit percentatge del seu valor inicial, de manera que el rang de barreres d'energia que s'exploren durant l'experiment es veu limitat a una petita fracció de la distribució real  $f(E)$ . Això és així per la dispersió en les propietats físiques dels sistemes i per la variació exponencial dels temps de relaxació. Així doncs, seria interessant trobar un mètode que permetés estendre les corbes de relaxació experimentals a escales de temps més llargues, sense haver de realitzar mesures de durada inabastable. Aquest és el propòsit del mètode fonomenològic de l'escalat  $T \ln(t/\tau_0)$  que presentem.

La base del mètode descansa en el fet que, sota certes condicions, hi ha una variable d'escala natural en la llei de relaxació que relaciona escales de temps i de temperatura, possibilitant d'aquesta manera deduir corbes de relaxació per temps llargs, i per una temperatura donada, del coneixement de les relaxacions a temps curts i a diferents temperatures. La idea té semblança amb allò proposat en treballs previs de Préjean et al. en el context de la relaxació de vidres d'spin a principis dels anys 80 [17].

Si no hi ha cap perturbació externa (camps magnètics) i tenint en compte que només les fluctuacions tèrmiques porten el sistema cap l'equilibri tèrmic, la llei de relaxació ve donada per

$$m(t) = \int_0^{\infty} dE f(E) e^{-t/\tau(E)}. \quad (12.8)$$

El factor exponencial és la probabilitat clàssica Boltzmann que una partícula canviï la seva magnetització i  $\tau(E)$  és el temps de relaxació introduït a la teoria de Néel [18], donat per

$$\tau(E) = \tau_0 e^{E/k_B T}, \quad (12.9)$$

on  $1/\tau_0$  és una freqüència d'intent de l'ordre de  $10^8 - 10^{12} \text{ s}^{-1}$ ,  $k_B$  la constant de Boltzmann i  $T$  la temperatura.

El límit inferior de la integral en aquesta expressió es pot tallar a  $E_c(t) = k_B T \ln(t/\tau_0)$  en el límit de baixes temperatures ( $k_B T$  menors que l'amplada de la distribució d'energies  $f(E)$ ) i per tant podem expressar l'última equació com

$$m(t) \simeq \int_{E_c(t)}^{\infty} dE f(E). \quad (12.10)$$

De l'Eq. (12.10) concluïm que la magnetització romanent  $M(t)$  és funció només del paràmetre  $E_c(t)$ . L'existència d'aquesta variable d'escala implica que mesurar la magnetització en funció de la temperatura a un temps determinat és equivalent a mesurar-la en funció de  $\ln(t)$  a una temperatura fixa.

Per verificar aquestes hipòtesis, hem calculat les relaxacions de la magnetització d'un sistema de partícules amb distribució log-normal de barreres d'energia integrant numèricament l'expressió (12.8). Els resultats d'aquests càlculs es mostren a la Fig. 12.10 per a tres valors de  $\sigma$  i temperatures reduïdes que van des de 0.001 a 0.5. Com es pot veure, el rang de validesa de la llei d'escala s'incrementa en augmentar l'amplada de la distribució. A més, l'escalat s'acompleix en gairebé tot el rang de la variable d'escala  $T/T_0 \ln(t/\tau_0)$  per temperatures per sota o al voltant de la temperatura mitjana de bloqueig, que en unitats reduïdes és 0.04.

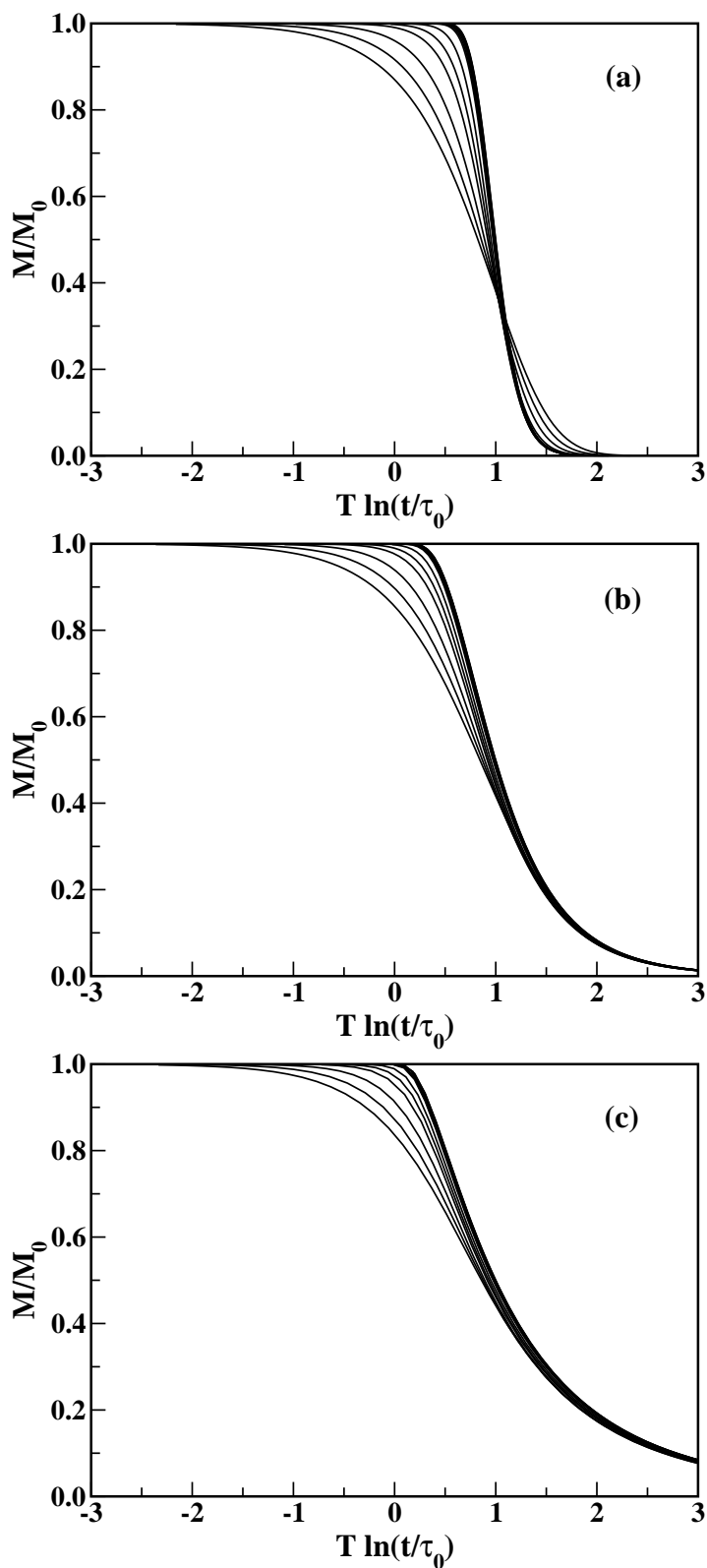


Figura 12.10: (a) Gràfics de l'escalat de les corbes calculades per integració numèrica de l'Eq. (12.8) per una distribució log-normal de barreres d'energia d'amplada adimensional,  $\sigma=0.2$ . Les temperatures,  $T/T_0$  (amb  $T_0 = E_0/k_B$  i  $E_0$  l'energia corresponent al pic de la distribució) corresponents a cada corba són: 0.001, 0.005, 0.01, 0.02, 0.04, 0.1, 0.2, 0.3, 0.4 and 0.5. La temperatura més baixa correspon a la corba superior. (b) El mateix que a) per  $\sigma=0.5$ . (c) El mateix que a) per  $\sigma=0.8$ .



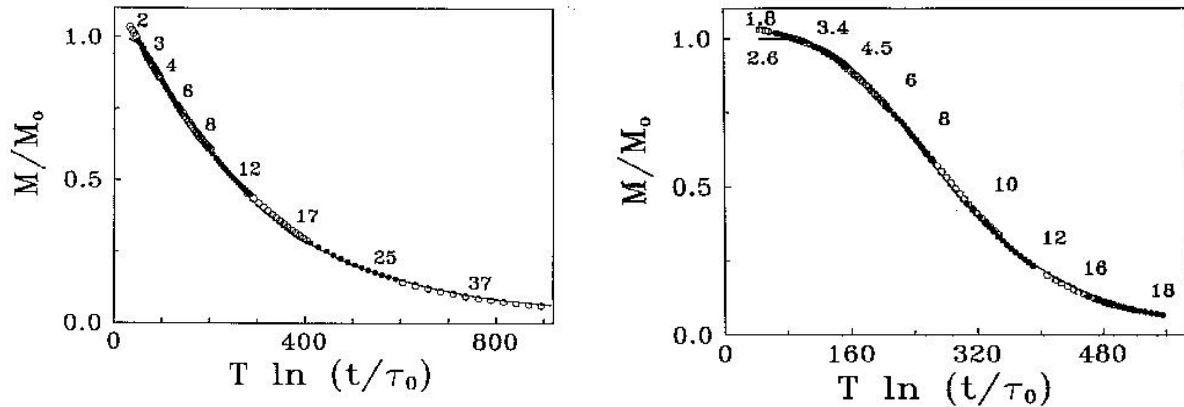


Figura 12.11: Corbes mestres obtingudes amb un escalat  $T \ln(t/\tau_0)$  de les corbes de relaxació per una mostra de ferrofluid de partícules petites de  $\text{Fe}_3\text{O}_4$ . La figura mostra la magnetització reduïda en funció de la variable d'escala. Els cercles oberts i plens corresponen, alternativament, a temperatures contigües, indicades, en els corresponents intervals. La línia contínua correspon a la corba teòrica calculada mitjançant l'Eq. (12.8) i els següents valors dels paràmetres ajustats. Mostra 1:  $\tau_0 = (4.7 \pm 5) \times 10^{-7}$  s,  $\sigma = 0.85 \pm 0.05$ ,  $T_0 = 245 \pm 50$  K. Mostra 2:  $\tau_0 = (3.5 \pm 5) \times 10^{-11}$  s,  $\sigma = 0.44 \pm 0.05$ ,  $T_0 = 287 \pm 50$  K.

Per verificar la validesa de la llei d'escalat  $T \ln(t/\tau_0)$  en sistemes reals, hem analitzat la relaxació magnètica de dos sistemes diferents: un ferrofluid de partícules de  $\text{Fe}_3\text{O}_4$  [19] amb diàmetres mitjans de 50 a 60 Å, i partícules de FeC amb diàmetre mitjà de 36 Å Linderothjm93. En ambdós sistemes les partícules es troben disperses en un oli hidrocarbonat i la interacció entre elles és molt petita. Com es mostra a la Fig. 12.11, desplaçant les corbes de relaxació en l'eix  $T \ln(t)$  en una quantitat igual a  $T \ln(\tau_0)$  (on  $\tau_0$  és un temps característic que governa el procés de relaxació a escala atòmica que s'escull igual per totes les  $T$  i és el que fa que les diferents corbes col·lapsin en una d'única), s'aconsegueix obtenir una única corba mestra corresponent a la relaxació a temps llargs de la corba de  $T$  més baixa.

Aquesta descripció fenomenològica de la relaxació permet també obtenir informació sobre les distribucions de barreres d'energia. L'Eq. 12.10 ens permet deduir una expressió per l'anomenada viscositat magnètica, definida com la derivada logarítmica respecte el temps de la llei de relaxació

$$S(t) = \frac{\partial M(t)}{\partial(\ln t)} \simeq k_B T f(\bar{E}), \quad (12.11)$$

expressió que té el mateix rang de validesa que la llei d'escala  $T \ln(t/\tau_0)$  i on  $\bar{E} = T \ln(t/\tau_0)$ , és a dir, val a baixes  $T$  i per distribucions amples. D'aquesta manera, veiem que, si grafiquem  $S/T$  enfront de la variable d'escala  $T \ln(t/\tau_0)$  a  $T$  prou baixes, la corba resultant en donarà la distribució de barreres d'energia de la mostra. Efectivament, quan hom obté  $S$  fent la derivada numèrica de les corbes mestres (Fig. 12.11) de les dues mostres considerades, el resultat obtingut (vegeu la Fig. 12.12) coincideix amb la derivada de la termoromanència respecte  $T$  [20] que és proporcional a la distribució de temperatures de bloqueig [21] i, per tant, a la distribució de barreres d'energia. L'autoconsistència del mètode queda garantida pel bon acord obtingut en comparar la  $f(E)$  obtinguda de la viscositat amb l'obtinguda per un ajust de la corba master a l'Eq. 12.8 assumint una disteibució log-normal (línia contínua a la Fig. 12.11). Només s'observen discrepàncies per valors petits de l'energia, que es poden associar a la presència d'una subdistribució de barreres de molt baixa energia deguda a efectes de superfície o de la interacció entre partícules.

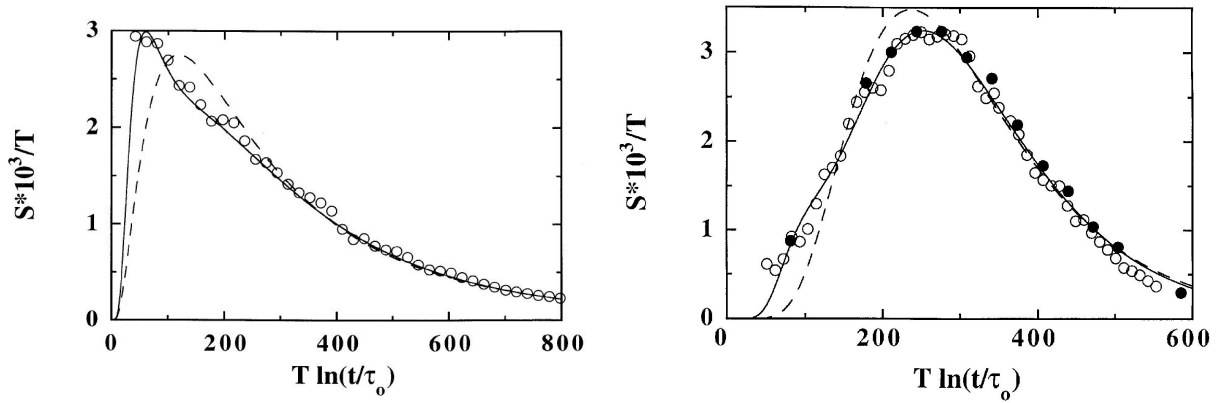


Figura 12.12: Panell esquerre: derivada numèrica de la corba mestra respecte la variable d'escala per la mostra 1 (cercles oberts) i distribucions de barreres obtingudes d'un ajust de la corba mestra de relaxació a l'expressió (12.8) assumint una única distribució log-normal (corba discontinua) i la suma de dues distribucions log-normal (corba contínua). Panell dret: el mateix que al panell esquerre per la mostra 2. En aquest cas, la derivada de la termoromanència respecte  $T$  es representa enfront  $T \ln(t/\tau_0)$  en cercles plens per comparació.

### 12.3.2 Processos de relaxació en presència de camp

L'aplicació d'un camp magnètic defineix una direcció preferencial per la magnetització i trenca la degeneració en energia entre els estats d'equilibri equivalents induïts per l'anisotropia. En aquest cas, els ritmes de relaxació passen a dependre del camp magnètic aplicat i el càlcul de les corbes de relaxació no es pot presentar segons el marc simplificat introduït a l'apartat anterior. Ara, una equació equivalent a l'Eq. (12.8) s'ha de tornar a derivar partint de principis més bàsics, ja que el ritme de relaxació  $\tau$  que entra en l'ementada llei depèn ara de l'orientació de la partícula i del valor del camp magnètic. En aquesta secció, estendrem l'aproximació fenomenològica de l'anterior secció a la relaxació en presència de camp, mostrant com es pot dur a terme un escalat  $T \ln(t/\tau_0)$  de les corbes de relaxació i trobant una variable d'escala per corbes mesurades a una  $T$  donada i diferents camps.

El propòsit és donar compte dels estudis experimentals de la relaxació en partícules petites que mesuren essencialment l'adquisició de magnetització d'una mostra, inicialment desmagnetitzada, sota l'aplicació d'un camp magnètic [22, 23, 24, 25, 26]. En aquest tipus d'experiments, el camp modifica les barreres d'energia del sistema que són responsables de la variació de la magnetització amb el temps, i també l'estat final d'equilibri cap al qual el sistema es relaxa. el fet que, normalment, les propietats magnètiques de les partícules en mostres reals no siguin uniformes, afegeix algunes dificultats a l'anàlisi per què, com ja hem presentat a la Sec. 12.2.1, l'efecte del camp magnètic depèn d'ells d'una forma complicada.

El model proposat parteix d'una equació mestra per  $P_i$ , la probabilitat de trobar la magnetització en el mínim  $i$ , que, en l'aproximació de dos estats (TSA) presentada en la Sec. 12.2.1, es pot escriure

$$\frac{dP_i}{dt} = \sum_{k=1,2} \sum_{j \neq i} \{w_{ji}^{(k)} P_j - w_{ij}^{(k)} P_i\}, \quad (12.12)$$

on  $w_{ij}^{(k)}$  designa el ritme de transició per un salt de l'estat  $i$  a l'estat  $j$  separats pel màxim  $k$ , que hem escollit

com

$$w_{ij}^{(k)} = \frac{1}{\tau_{ij}^{(k)}} = \frac{1}{\tau_0} e^{-E_b^{ki}\beta}. \quad (12.13)$$

La solució d'aquestes equacions dóna finalment les equacions per la dependència temporal de la magnetització en les quals hem basat els nostres càlculs:

$$\begin{aligned} m(t; K, \psi) &= \bar{m}_{TS}(K, \psi) + [m_0 - \bar{m}_{TS}(K, \psi)]e^{-t/\tau(K, \psi)} \\ m(t) &= \int_0^\infty dK f(K) \int_0^\pi d\psi m(t; K, \psi), \end{aligned} \quad (12.14)$$

on la primera expressió és per una partícula orientada en l'angle  $\psi$  respecte la direcció del camp i  $\bar{m}_{TS}(K, \psi)$  és la magnetització d'equilibri en la TSA.

L'evaluació numèrica d'aquesta expressió per un sistema inicialment desmagnetitzat ( $m_0 = 0$ ) a diferents temperatures i camps magnètics ens ha permès concloure els següents resultats:

1. Les corbes a diferents  $T$  i un camp donat, es poden escalar utilitzant la variable d'escala  $T \ln(t/\tau_0)$ , de manera semblant al cas de la relaxació en camp nul, com es mostra a la Fig. 12.13. Ara però s'ha de tenir en compte que, per poder comparar relaxacions a diferents temperatures, aquestes s'han de normalitzar al valor de la magnetització d'equilibri, que ara depèn de  $T$  tal i com es mostra a la Fig. 12.3. L'escalat és vàlid fins a  $T$  tant més altes com més gran és el camp aplicat, un efecte que s'explica per l'eixamplament i desplaçament de les distribucions efectives de barreres que aquest provoca.
2. Aquest model fenomenològic ha estat probat experimentalment en una mostra consistent en un ferrofluid de partícules petites de  $\text{Fe}_3\text{O}_4$  disperses en un oli hidrocarbonat, amb distribució log-normal de volums de diàmetre mitjà 4 nm i  $\sigma = 0.24$ . Les relaxacions mesurades en presència d'un camp de 10 Oe, després d'un refredament sense camp fins la temperatura de mesura, poden ser escalades en funció de la variable  $T \ln(t/\tau_0)$ , un cop normalitzades a la magnetització d'equilibri (vegeu la Fig. 12.14).
3. Les corbes de viscositat, deduïdes a partir de les relaxacions a diferents camps, presenten un màxim característic a un valor de la variable d'escala  $E_{\max}$ , la dependència del qual amb  $h$  es representa a la Fig. 12.15. En el cas d'un sistema amb distribució d'anisotropies i eixos a l'atzar, la posició dels màxims es desplaça cap a valors menors d'energia seguint la variació de les barreres més baixes de les partícules orientades a  $\psi = \pi/4$ . A la vegada, el màxim ritme de relaxació  $S_{\max}$  es fa constant per sota d'un cert valor del camp  $h_0$  i  $T$  prou baixes.
4. Aquestes darreres observacions fan possible que corbes de relaxació, a diferents camps i una  $T$  fixada, es puguin unir mitjançant desplaçaments al llarg de l'eix  $T \ln(t/\tau_0)$  d'acord amb la variació d' $E_{\max}(h)$ . Les corbes resultants es mostren a la Fig. 12.15 per  $\sigma = 0.2, 0.5$ . Aquestes corbes són les equivalents a les corbes mestres per  $h$  fixat i diferents  $T$ . Ara, la variable d'escala apropiada és

$$E_{\text{sca}} = T \ln[t/t_{\max}(h)], \quad (12.15)$$

que generalitza l'escalat a  $T$  fixada. Aquest nou escalat val per camps menors que  $h_0$ , el camp al qual les barreres més petites comencen a desaparèixer i per sobre del qual la relaxació es veu dominada per barreres energètiques gairebé nulles. Mentre que l'escalat  $T \ln(t/\tau_0)$  a camp fix permet extreure la distribució de barreres per diferenciació de la corba mestra [27], els desplaçaments en l'eix  $T \ln(t/\tau_0)$  necessaris per produir l'escalat en presència de camp magnètic donen la dependència de les barreres mitjanes que contribueixen a la relaxació, una informació microscòpica que no es pot inferir fàcilment per altres mètodes [28].

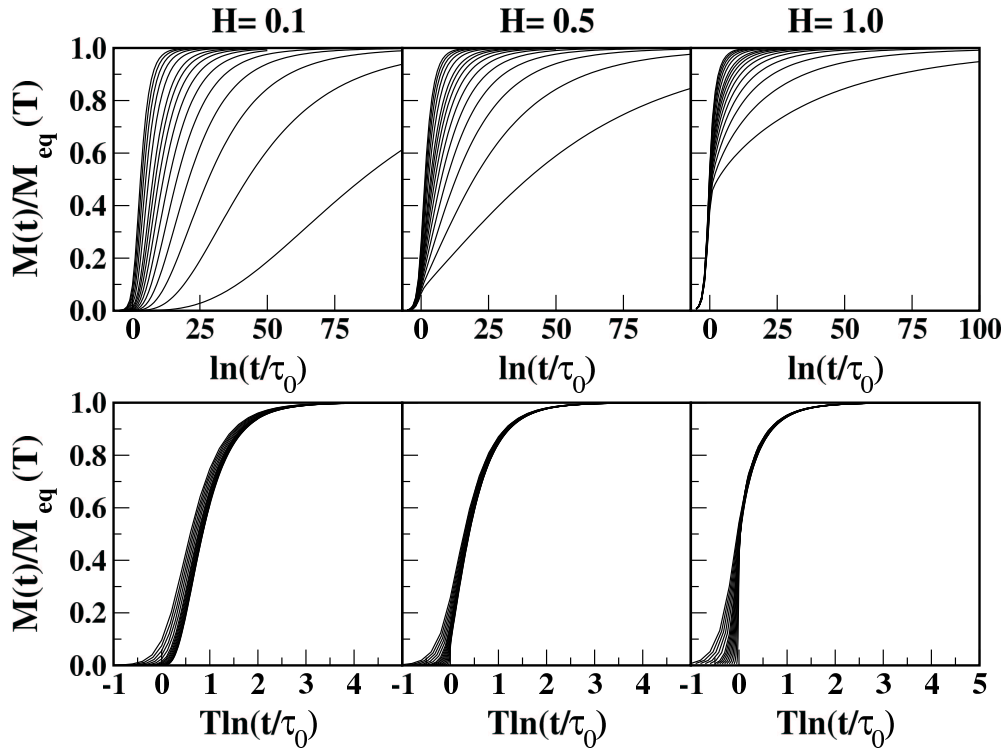


Figura 12.13: Corbes de relaxació per un conjunt de partícules amb eixos d'anisotropia orientats a l'atzar i distribució log-normal d'anisotropies  $f(K)$ , d'amplada  $\sigma = 0.5$  i  $K_0 = 1$ , calculades per integració numèrica de l'Eq.(12.14). Les magnetitzacions inicials s'han pres com  $m_0 = 0$ . Les temperatures reduïdes  $T/T_0$ , començant pre la corba inferior, van des de 0.01 a 0.1 amb increments de 0.01, i des de 0.1 a 0.2 amb increments de 0.02. Els camps aplicats són  $H = 0.1, 0.5, 1.0$  com s'indica. Els panells superiors mostren les corbes originals normalitzades a la magnetització d'equilibri  $m_{TS}(T)$  donada per l'Eq.(12.5). Als panells inferiors, hem representat les mateixes corbes en funció de la variables d'escala  $T \ln(t/\tau_0)$ .

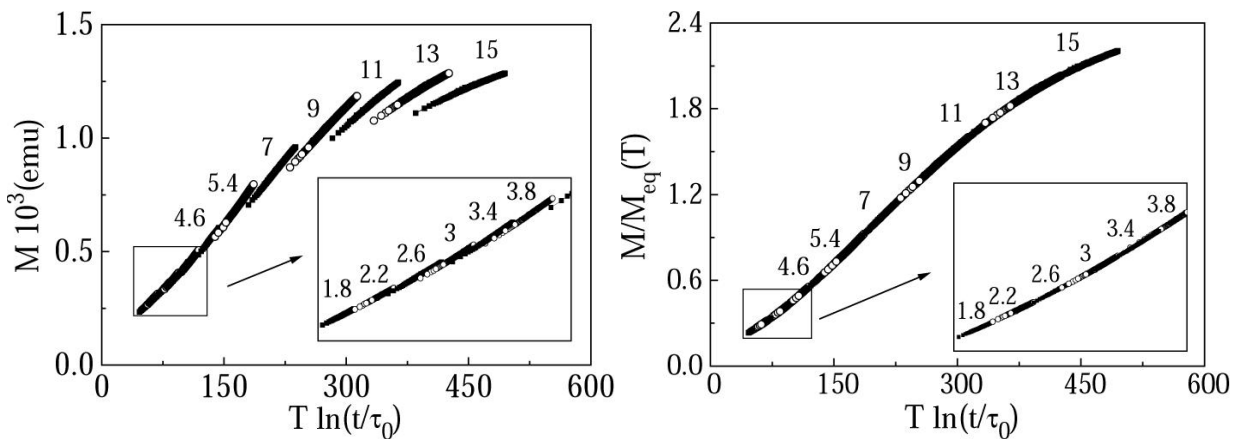


Figura 12.14: Panell esquerre: Mesures de relaxació enregistrades per temperatures entre 1.8 i 15 K sota l'aplicació d'un camp magnètic de 10 Oe, després d'un refredament de la mostra a camp nul, en funció de la variable d'escala  $T \ln(t/\tau_0)$ . Els símbols oberts i tancats corresponen alternativament a les temperatures indicades. Figures insertes: detall de la regió de baixes temperatures. Panell dret: gràfica d'escala per les mesures de relaxació mostrades en el panell esquerre.

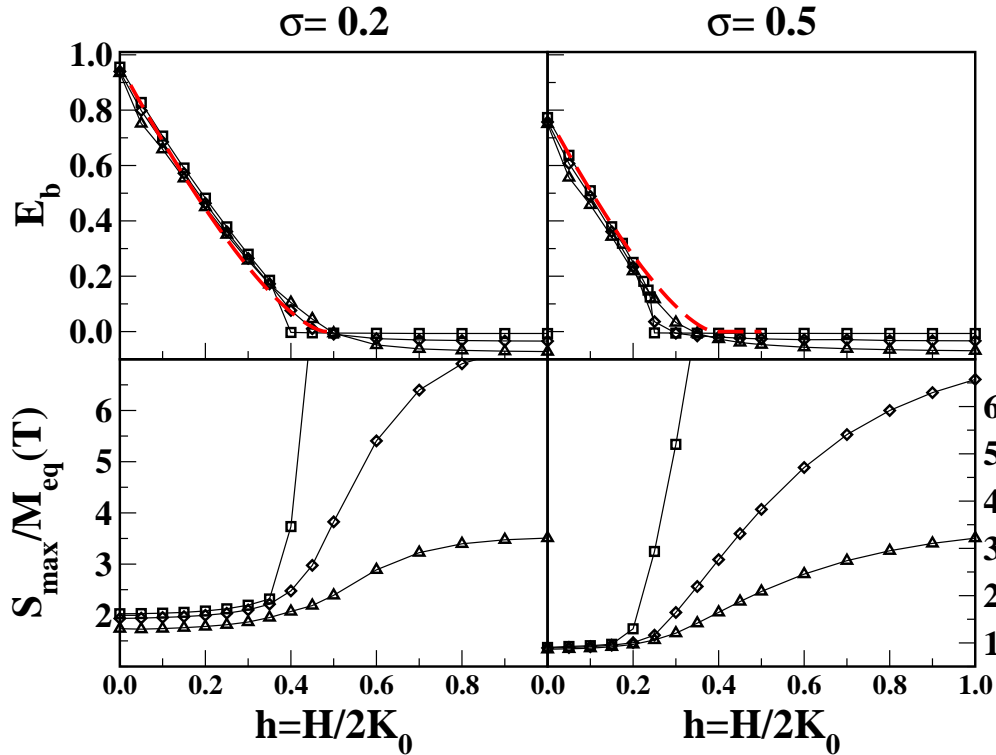


Figura 12.15: Panells superiors: dependència en el camp de l'energia corresponent al ritme màxim de relaxació  $T \ln(t_{max}/\tau_0)$ , extret de les corbes de viscositat per temperatures  $T = 0.01$  (cercles),  $0.05$  (quadrats),  $0.1$  (diamants). Les línies discontinúes indiquen la variació amb el camp de les barreres d'energia més baixes per partícules orientades a  $\psi = \pi/4$  i amb  $K = K_{max}$ . Panells inferiors: dependència en el camp del màxim ritme de relaxació  $S_{max}$  per les mateixes corbes i temperatures. La columna esquerra és per  $\sigma = 0.2$  i la de la dreta per  $\sigma = 0.5$ .

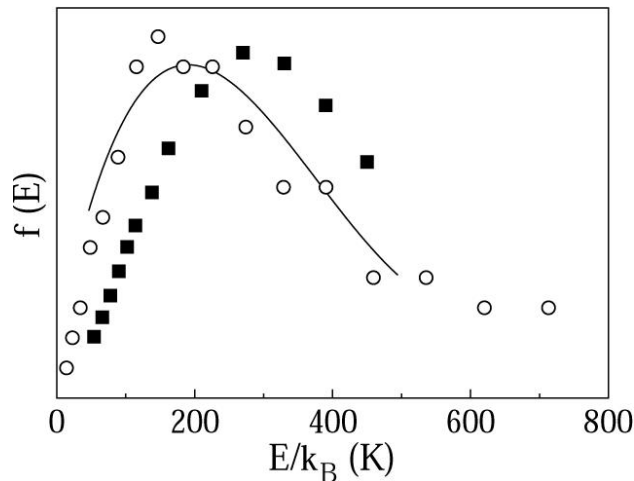


Figura 12.16: Distribució efectiva de barreres d'energia obtinguda de la derivada numèrica de la corba mestra de relaxació (línia contínua). Viscositat magnètica  $S(T)$  obtinguda de la derivada logarítmica respecte el temps de les mesures de relaxació a les temperatures indicades a la Fig. 12.14 (quadrats sòlids). La distribució d'energies  $f(E)$  obtinguda de  $f(V)$  (distribució de volums) es mostra en cercles buits per comparació.

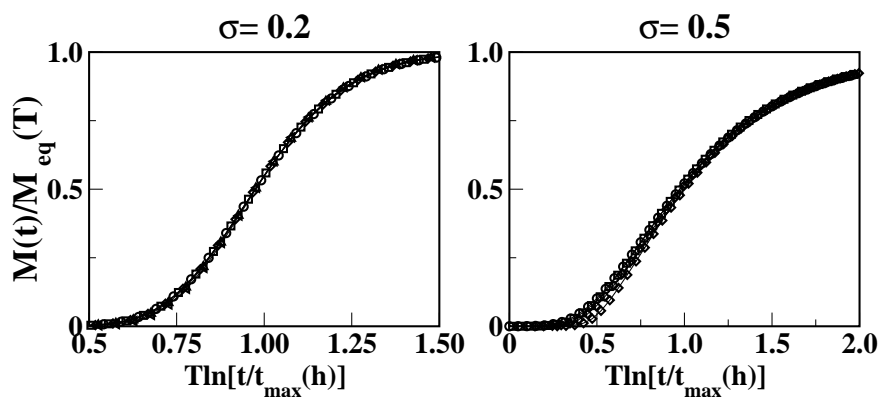


Figura 12.17: Corbes de relaxació normalitzades en funció de la variable d'escala  $T \ln[(t/t_{max}(h))]$  per  $T = 0.05$ ) obtingudes de la Fig. 12.13 by shifting the curves in the horizontal axis with the position of the maximum relaxation rate (upper panels in Fig. 12.15). (a)  $\sigma = 0.2$  and  $H = 0.1, 0.2, 0.3, 0.4, 0.5$ ; (b)  $\sigma = 0.5$  and  $H = 0.1, 0.2, 0.3, 0.4$  (starting from the uppermost curve)

### 12.3.3 Sistemes interactuants en 1D

Fins ara, els sistemes considerats consistien bé en partícules individuals amb spins que interactuaven només a través de forces de curt abast o bé en conjunts de partícules no interactuants. No obstant això, en sistemes de partícules petites reals, les forces de llarg abast d'origen dipolar juguen un paper que en molts casos no es pot menyspreuar. Als superparamagnets (sòlids de mida nanomètrica o agregats), les interacció d'intercanvi o altres interaccions competents, normalment, es poden descartar enfront de les interaccions entre partícules, de manera que, en principi són candidats apropiats per l'estudi de les interaccions dipolars pures.

Mentre que s'ha arribat a una comprensió força bona dels sistemes diluïts, els resultats experimentals per sistemes densos són encara objecte de controvèrsia. Algunes de les seves propietats magnètiques peculiars han estat atribuïdes a les interaccions dipolars, encara que molts dels resultats són encara polèmics. Mesures experimentals diferents de les mateixes de les mateixes quantitats físiques arriben a resultats contradictoris i les interpretacions teòriques moltes vegades són inconcloents o poc clares.

Sembla clar que, per aclarir la interpretació d'aquests fenòmens, els mètodes numèrics, tals com la simulació Monte Carlo, constitueixen la única manera d'incorporar tots els ingredients involucrats en aquest problema. En aquest treball, nosaltres ens hem centrat en l'estudi de les propietats depenents del temps basant-nos en un model simple que permeti extreure la màxim quantitat de conclusions fefaents. Per estudiar l'efecte de les interaccions de llarg abast, començarem amb el model més simple que pugui capturar la física essencial del problema. Hem considerat una cadena lineal de  $N$  spins Heisenberg  $\mathbf{S}_i$   $i = 1, \dots, N$ , on cadascun representarà una partícula monodomini de moment magnètic  $\mu_i = \mu \mathbf{S}_i$ . Cada spin té una anisotropia uniaxial que apunta en la direcció  $\hat{\mathbf{n}}_i$ , orientada a l'atzar i constant d'anisotropia  $K_i$ , distribuïda s'acord amb una funció de distribució  $f(K)$ . Un camp magnètic extern  $\mathbf{H}$  pot actuar sobre tots els spins amb el mateix valor i apuntant en la direcció de perpendicular a la cadena.

Per simplicitat, hem considerat partícules sense estructura interna, de manera que la única interacció

considerada ha estat la dipolar. L'Hamiltoniana que descriu el sistema es pot expressar doncs com:

$$\mathcal{H} = - \sum_{i=1}^N \{K_i(\mathbf{S}_i \cdot \hat{\mathbf{n}}_i)^2 + \mathbf{S}_i \cdot \mathbf{H}\} + g \sum_{i=1}^N \sum_{j \neq i}^N \left\{ \frac{\mathbf{S}_i \cdot \mathbf{S}_j}{r_{ij}^3} - 3 \frac{(\mathbf{S}_i \cdot \mathbf{r}_{ij})(\mathbf{S}_j \cdot \mathbf{r}_{ij})}{r_{ij}^5} \right\}, \quad (12.16)$$

on  $g = \mu^2/a^3$  caracteritza la magnitud de l'energia dipolar i  $r_{ij}$  é la distància que separa els spins  $i$  i  $j$ ,  $a$  és la separació entre spins veïns a la xarxa, que s'ha pres com 1.

Com a estudi previ a la relaxació, hem analitzat la influència de la interacció dipolar en la funció d'energia magnètica de les partícules, de manera semblant a com hem fet pel cas sense interacció amb l'aplicació d'un camp magnètic. Per a això, hem calculat numèricament els histogrames de barreres per 40000 partícules. Per partícules en configuració ferromagnètica al llarg de l'eix  $y$  (vegeu Fig. 12.18, esquerra), hem vist que la introducció d'interacció desplaça el pic de la distribució original cap a valor menors de l'energia i, per  $g$  prou grans, a mesura que el pic original desapareix, fa aparèixer un pic de barreres d'energia quasi nul·la causa de la disminució de l'alçada de les barreres amb la interacció. Com que en aquesta configuració el sistema és àltament metastable, amb la orientació dels spins lluny dels mínims d'energia, abans d'iniciar les relaxacions hem sotmès al sistema a un procés d'equilibrat previ a  $T = 0$ . Després d'aquest procés, aconseguim que els spins apuntin en la direcció del mínim d'energia més proper, tal com demostra la desaparició del pic a altes energies en les distribucions efectives (vegeu Fig. 12.18, dreta).

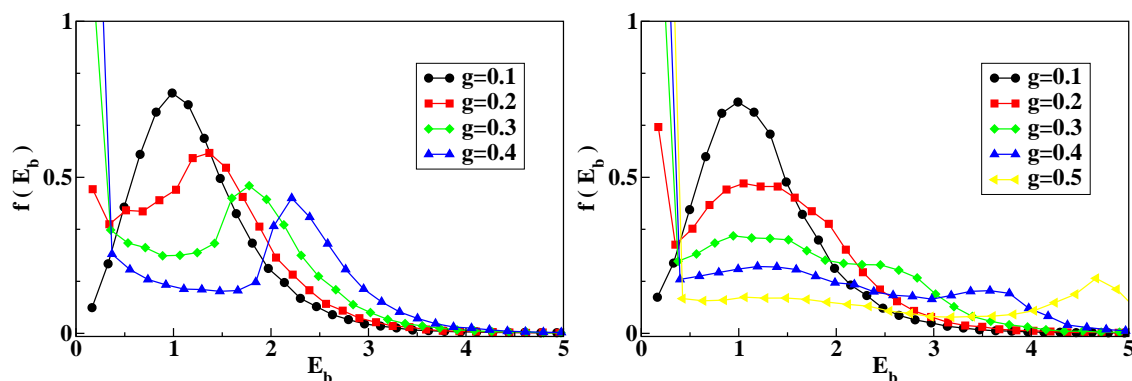


Figura 12.18: Distribucions efectives de barreres d'energia  $f(E_b)$  per un sistema amb distribució log-normal de constants d'anisotropia ( $\sigma = 0.5$ ) i eixos d'anisotropia a l'atzar. Panell dret: spins apuntant en la direcció positiva de les  $y$ . Panell esquerre: configuració d'spins assolida després d'un equilibrat a  $T = 0$ , durant el qual els spins han estat reorientats de forma iterativa en la direcció del mínim de l'energia més proper, havent partit d'una configuració FM inicial.

El càlcul de les corbes de relaxació de la magnetització en el cas amb interacció no es pot basar ara en cap model analític a causa del llarg abast de la interacció. Per això hem emprat el mètode de simulació de Monte Carlo per obtenir les relaxacions. Els valors del paràmetre d'interacció considerats van del règim d'interacció feble ( $g = 0.1$ ) a forta ( $g = 0.5$ ). L'algorisme Monte Carlo considera intents de canvi de la direcció dels spins només entre els mínims de l'energia, que en el model proposat poden ser calculats exactament utilitzant una expressió anàloga a l'Eq. 12.1 tenint en compte que al camp magnètic aplicat s'ha d'afegir el camp dipolar general per la resta de partícules. Això permet que, en el càlcul de les probabilitats de transició (factor Boltzmann), el canvi d'energia a considerar correspongui sempre a una de les barreres energètiques presents al sistema i per tant que, si bé l'escala de temps MC no té connexió directa amb el

temps real, la dinàmica sigui més realista. Els resultats de les simulacions es resumeixen a les Fig. 12.19 i Fig. 12.20, l'anàlisi de les quals porta a les següents conclusions:

1. El ritme de les relaxacions s'accelera en augmentar la interacció, però amb una dependència amb el temps que no és logarítmica més que per una petita finestra que varia amb la  $T$ .
2. Encara que hom podria pensar que les hipòtesis que sustentaven l'escalat  $T \ln(t/\tau_0)$  presentat per sistemes sense interacció deixen de ser vàlides en introduir la interacció, hem observat que les corbes de relaxació a diferents  $T$  poden ser escalades seguint el procediment anteriorment comentat. De fet, a través d'un recompte mitjançant histogrames de les barreres d'energies presents a diferents estadis del procés de relaxació, hem vist que les distribucions efectives de barreres d'energia no canvien substancialment.
3. Les distribucions efectives de barreres deduïdes a partir de les corbes metres de relaxació (vegeu la Fig. 12.20), no corresponen en aquest cas a les distribucions de barreres obtingudes per càlcul directe a diferència del que passava en els casos sense interacció. Ara representen les distribucions independents del temps que donarien lloc a les mateixes corbes de relaxació en el règim on l'escalat és vàlid. Per  $g$  petites (interacció feble), aquestes distribucions mantenen essencialment la forma que tenien en el cas sense interacció. S'observa un estretament de les distribucions i un desplaçament del pic cap a baixes energies en augmentar  $g$ , de manera semblant al que s'observava per l'efecte d'un camp magnètic en un sistema sense interacció. En el règim d'interacció forta, a mesura que els camps dipolars que noten les partícules comencen a destruir barreres, s'observa un progressiu augment del nombre de barreres de baixa energia que acaba fent desaparèixer el màxim i convertint les distribucions efectives en quasi exponencials.
4. Per aclarir el significat físic de les distribucions deduïdes a partir de l'escalat  $T \ln(t/\tau_0)$ , hem calculat els histogrames acumulatius de les barreres que se salten durant la relaxació, comparant-los amb els corresponents a les barreres reals presents en el sistema, obtinguts a partir de les configuracions d'espins durant la relaxació. Hem vist que, quan en els histogrames acumulats es tenen en compte només les barreres saltades per partícules que fins el temps  $t$  no havien saltat, aquests tendeixen cap a les distribucions efectives obtingudes de l'escalat. D'aquesta manera, hem vist que aquesta aproximació fenomenològica a la relaxació, en termes de barreres efectives, permet extreure informació sobre les barreres microscòpiques responsables de la pèrdua de magnetització i estudiar els efectes que la interacció entre partícules té sobre aquest fenomen.

## 12.4 Capes primes amb anisotropia perpendicular

Les propietats magnètiques i de transport de les capes primes i materials nanoestructurats han estat objecte d'una intensa recerca almenys en les dues dècades passades a causa del seu interès per les aplicacions tecnològiques i en la gravació magnètica [29]. Entre els fenòmens d'interès observats en aquests materials, trobem les transicions de reorientació de la magnetització en augmentar la temperatura [30, 31, 32] or o el gruix de les capes [30, 33, 34], l'efecte de magnetoresistència gegant [35, 36, 37], i la gran varietat d'estructures magnètiques que es poden establir depenent de la interrelació entre l'anisotropia perpendicular induïda a la superfície, la interacció d'intercanvi i les forces dipolars de llarg abast entre les entitats microscòpiques que constitueixen la capa.



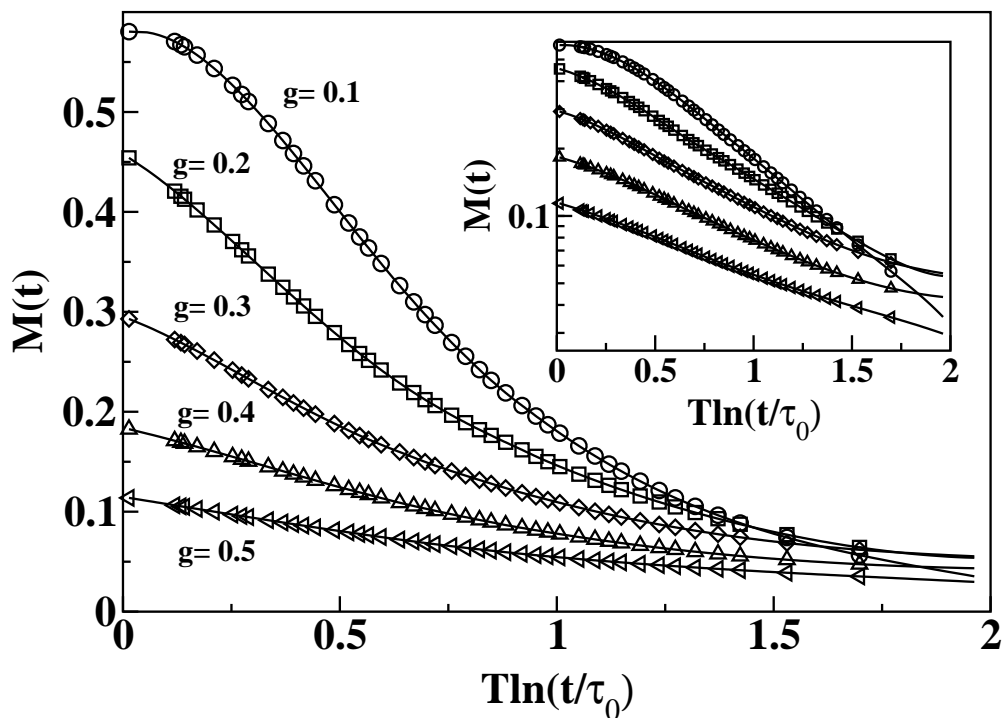


Figura 12.19: Corbes mestres de relaxació per diferents valors de la intensitat de la interacció dipolar  $g$ . Figura inserta: les mateixes corbes en una gràfica log-log per evidenciar el comportament potencial de la llei de relaxació a valors grans de  $g$ .

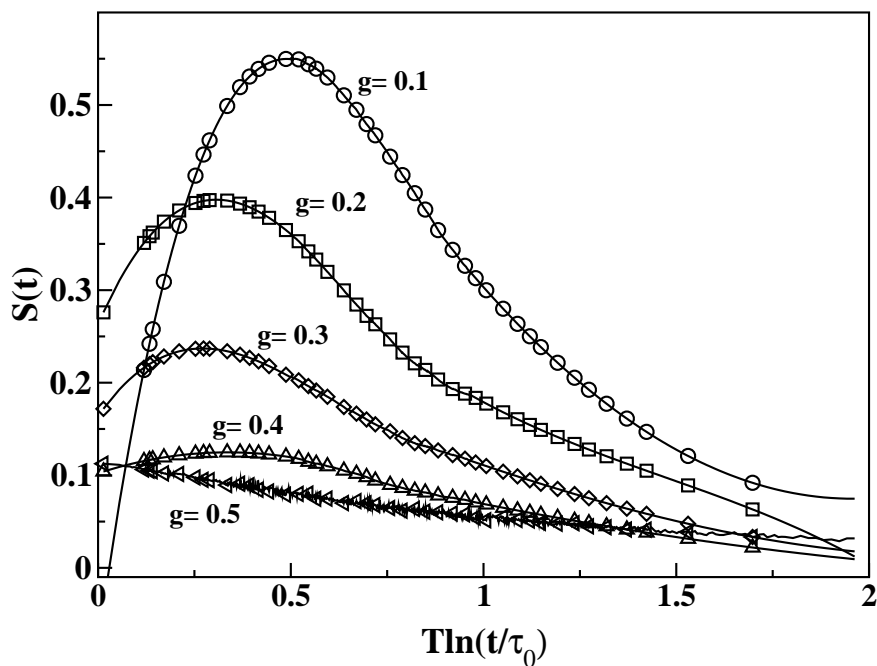


Figura 12.20: Derivades de les corbes mestres de relaxació de la Fig. 12.19 per diferents valors de la intensitat de la interacció dipolar.

El desenvolupament de diferents tècniques de microscòpia com la MFM, AFM, LEM o SEMPA [38] ha ajudat els experimentals a entendre la interrelació entre les propietats de transport i l'estructura magnètica d'aquests materials. A més, aquestes tècniques ens han mostrat que les estructures magnètiques que es formen en les capes primes estan fortament influenciades per la història magnètica de la mostra. D'aquesta manera, els patrons observats en les capes primes poden mostrar tant ordre fora del pla amb dominis en forma de franjes laberíntiques [39, 40] o patrons en forma de bombolla [34, 41], com estructures de vòrtexs dins del pla de la capa [42]. Les tècniques experimentals actuals permeten a més controlar el contingut ferromagnètic dels aliatges que es depositen sobre matrius metàl·liques no magnètiques [40] i, per tant, variar el rang de les interaccions dipolars i d'intercanvi entre els grans.

Sembla clar doncs, que una descripció teòrica realista d'aquests sistemes pot ser modelitzada convenientment per una xarxa bidimensional d'espins. L'acoblament entre espins ha d'incloure la interacció d'intercanvi, l'anisotropia magnetocristal·lina local, que proveeix el trencament de simetria necessari per establir ordre de llarg abast en un sistema quasi 2D, i la interacció dipolar responsable de l'acoblament de llarg abast entre moments magnètics. El gruix finit de les mostres es pot tenir en compte controlant el valor de la constant d'anisotropia efectiva local. Com veurem, l'influència recíproca entre les interaccions locals, de curt abast i de llarg abast és la responsable de la gran varietat de propietats magnètiques d'aquets sistemes. En aquesta secció, presentarem els resultats de simulacions Monte Carlo extensives per un model de capa prima amb la intenció d'explicar la fenomenologia experimental esmentada.

El model general de capa prima consisteix en una xarxa quadrada 2D d'espins continus tipus Heisenberg  $\mathbf{S}_i$  (amb espaiat de xarxa  $a$  i mida lineal  $N$ ), que poden representar tant espins atòmics com el spin total dels grans. El Hamiltonià considerat ha estat

$$\mathcal{H} = -\bar{J}\mathcal{H}_{exch} - \bar{K}\mathcal{H}_{anis} + \mathcal{H}_{dip} \quad (12.17)$$

on  $\bar{J}$ ,  $\bar{K}$ , i  $\mathcal{H}$  es donen en unitats de la constant

$$g \equiv \frac{\mu^2}{a^3}, \quad (12.18)$$

on  $\mu$  és el moment magnètic de l'spin i  $K$  la constant d'anisotropia uniaxial perpendicular al pla de la capa. Els tres termes en aquesta expressió corresponen la interacció d'intercanvi a primers veïns (directa entre espins atòmics o indirecta a través de la matriu), l'anisotropia uniaxial, i la interacció dipolar de llarg abast:

$$\mathcal{H}_{exch} = \sum_{n.n.} (\mathbf{S}_i \cdot \mathbf{S}_j) \quad (12.19)$$

$$\mathcal{H}_{anis} = \sum_{n=1}^{N^2} (S_n^z)^2 \quad (12.20)$$

$$\mathcal{H}_{dip} = \sum_{n \neq m}^{N^2} \left\{ \frac{\mathbf{S}_m \cdot \mathbf{S}_m}{r_{nm}^3} - \frac{(\mathbf{S}_n \cdot \mathbf{r}_{nm})(\mathbf{r}_{nm} \cdot \mathbf{S}_m)}{r_{nm}^5} \right\}. \quad (12.21)$$

A l'últim terme,  $\mathbf{r}_{nm}$  és el vector que connecta els espins  $n$  i  $m$ . El primer terme afavoreix l'ordre antiferromagnètic de llarg abast mentre que el segon introdueix una anisotropia efectiva dins del pla de la capa. Considerarem tres tipus de sistemes atenent a la dimensionalitat dels espins: 1) Espins Ising apuntant en la direcció perpendicular al pla, 2) Espins planars (XY) amb components en el pla, 3) Espins Heisenberg amb tres components i projections tant dins com fora del pla.

Les propietats del model depenen doncs de dos paràmetres.  $\bar{J}$ , que té en compte la competència entre la interacció FM ( $J > 0$ ) i l'ordre AF induït per  $g$ , i  $\bar{K}$ , que mesura la competència entre l'alineament fora

## Ground State Energies

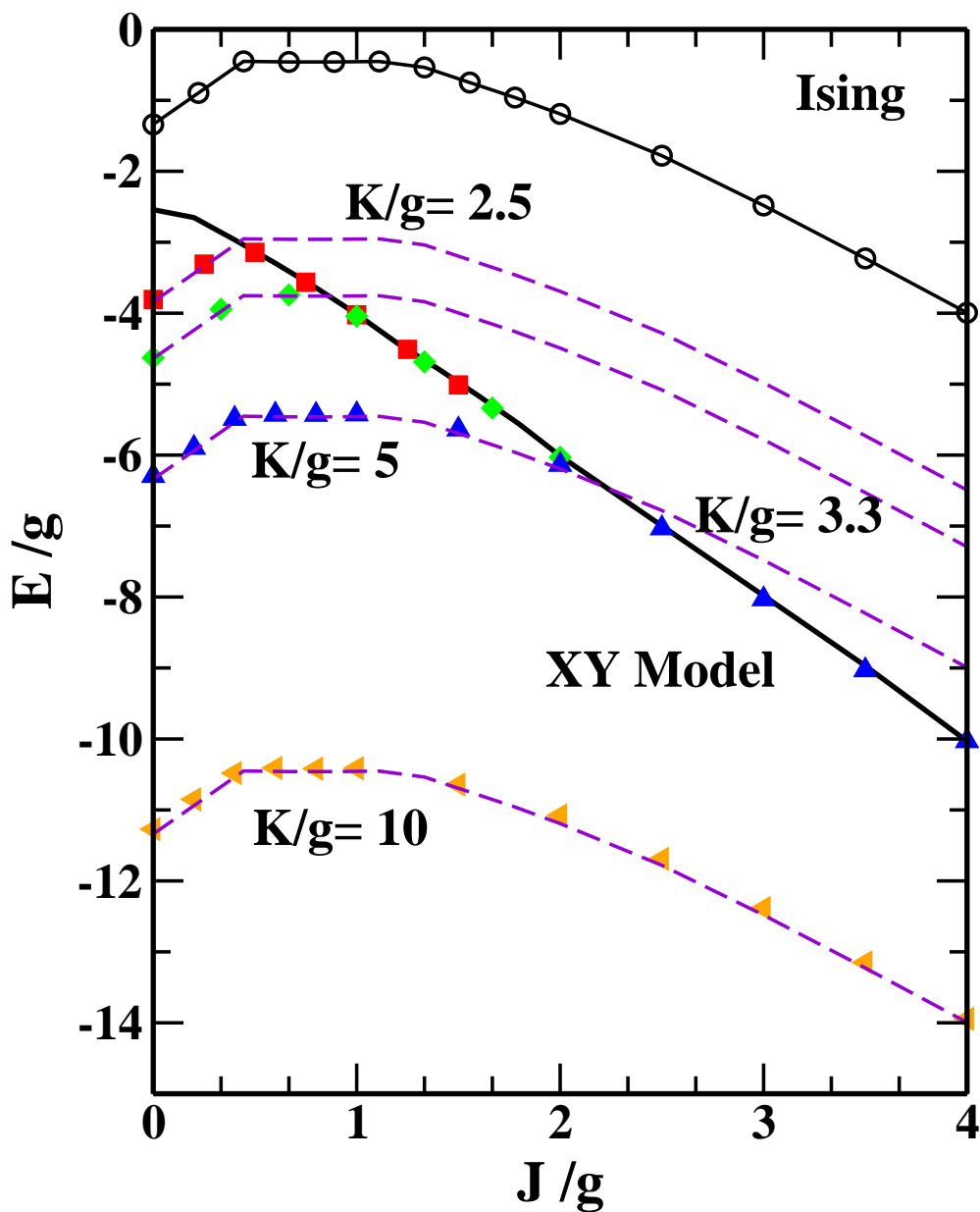


Figura 12.21: Energies dels estats fonamentals en funció de la constant d'intercanvi reduïda  $\bar{J} = J/g$  per diferents valors de la constant d'anisotropia  $\bar{K} = K/g$  indicats a la figura. els símbols plens corresponen al cas general amb anisotropia finita descrit pel Hamiltonià (12.17). Els cercles oberts corresponen al model d'Ising del mateix Hamiltonià ( $K = +\infty$ ) i la línia contínua al model planar (XY) ( $K = -\infty$ ). Les línies discontinües mostren l'energia de l'estat fonamental del model d'Ising més l'energia d'anisotropia corresponent a la corba amb  $\bar{K}$  finita més propera.

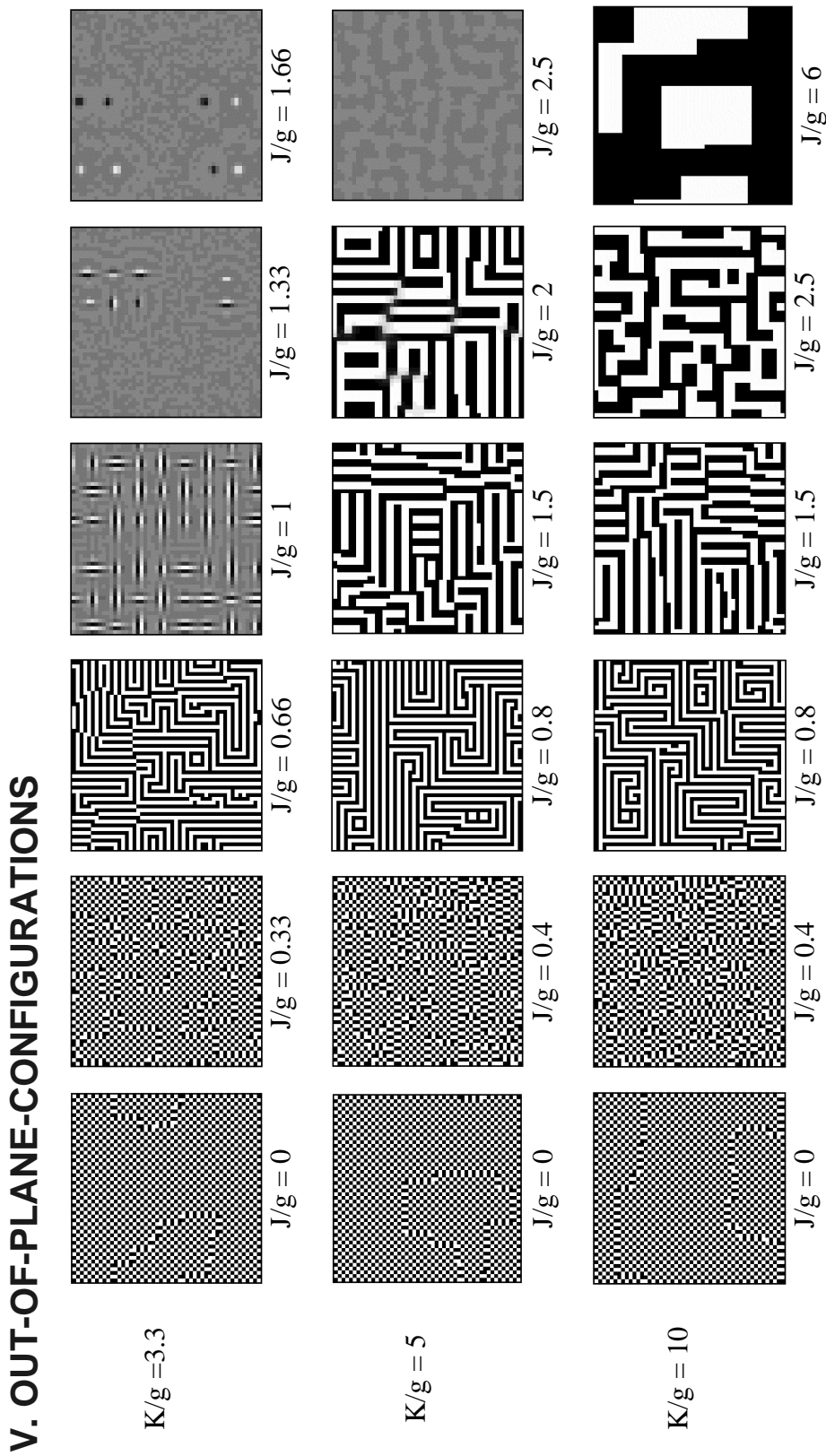


Figura 12.22: Configuracions dels estats fonamentals obtingudes pel mètode de annealing simulat per model amb  $K$  finita per un sistema de  $50 \times 50$  spins i alguns valors dels valors de  $\bar{J}$  and  $\bar{K}$  del diagrama de fases de la Fig. 12.21. Només es mostren les projeccions fora del pla ( $S_z$ ) en una escala de grisos que va del blanc ( $S_z = +1$ ) al negre ( $S_z = -1$ ).

del pla afavorit per  $K$  i l'ordre en el pla induït per  $g$ . Hem començat per l'estudi de les propietats de l'estat fonamental del model a temperatura zero. Per això, hem aplicat el mètode de temperat tèrmic simulat ('simulated thermal annealing') [43], consistent bàsicament en refredat a ritme constant des d'una fase desordenada a alta temperatura fins la temperatura d'interès. D'aquesta manera hem obtingut les energies i configuracions dels estats fonamentals. Les conclusions principals es poden resumir en els següents punts:

1. El tret característic del model amb  $\bar{K}$  finita és que es comporta de manera bimodal. És a dir, per un valor donat de  $\bar{K}$ , quan  $\bar{J}$  és petita ( $\bar{J} < \bar{J}^*$ ), és completament equivalent al corresponent model d'Ising, presentant ordenament fora del pla. En canvi, per a  $\bar{J} > \bar{J}^*$ , es comporta com el model planar equivalent i s'ordena dins el pla. El valor de  $\bar{J}^*$  al qual s'observa aquest canvi de comportament, és senzillament aquell pel qual l'energia de l'estat fonamental del model planar (línia sòlida gruixuda) iguala la del model d'Ising corresponent amb la correcció d'anisotropia finita corresponent a un valor donat de  $\bar{K}$  (línies discontinües). D'aquesta manera, el diagrama de fases per  $\bar{K}$  finita es pot obtenir directament dels resultats pel model planar desplaçant l'energia del model d'Ising amb el corresponent valor de  $\bar{K}$ . Conseqüentment, el model de Heisenberg per  $\bar{K}$  finita és la combinació dels models més simples d'Ising i planar. El seu comportament està dominat pel model l'estat fonamental del qual té menor energia.
2. Les transicions de reorientació des del pla cap enfora del pla a mesura que el gruix de la capa  $L$  disminueix poden entendre's fàcilment mirant el diagrama de fase. Una disminució de  $L$  pot entendre com un increment de l'anisotropia efectiva de la capa [30, 33, 44]. Així doncs, la transició de reorientació ve marcada pel creuament de la corba de  $\bar{K}$  finita amb la corba del model planar (línia contínua a la Fig. 12.21) en el corresponent valor de  $\bar{J}$ .
3. La regió de paràmetres d'interès pel nostre estudi és precisament la de valors de  $\bar{J}$  al voltant dels punts de canvi de comportament  $\bar{J}^*$ , doncs és en aquesta regió on les configuracions amb ordre planar i fora del pla són quasi-degenerades en energia i en les quals el sistema mostra metastabilitat. És a dir, s'hi poden induir diferents tipus d'ordenament depenent de com el sistema s'hagi portat a l'estat de quasi equilibri.
4. Per demostrar aquesta darrera possibilitat, hem realitzat dos tipus d'experiments numèrics que emulen els reals. El primer consisteix en una relaxació després d'haver saturat la capa en la direcció perpendicular. Els paràmetres considerats han estat  $\bar{K} = 3.3$ ,  $\bar{J} = 1.0$ , que corresponen a la regió de trànsit entre els règims d'Ising i Planar i pels quals la configuració de l'estat fonamental consta de vòrtexs en el pla de la capa. En el seu camí cap la configuració d'equilibri, el sistema passa per configuracions intermitjes en les quals es formen franjes amb spins orientats fora del pla, de manera semblant al que s'obté en els experiments [34, 40, 41, 45]. En un segon tipus d'experiment numèric, hem sotmès el sistema a un ciclat de camps desmagnetitzants. La idea en aquest cas ha estat intentar portar al sistema a una configuració diferent de la d'equilibri mitjançant una pertorbació externa consistent en un camp magnètic oscil·lant de magnitud decreixent aplicat en la direcció perpendicular al pla a la capa. En aquest cas, als primers estadis de la relaxació, els spins s'inverteixen seguint el camp, però, a mesura que el camp decreix, comencen a nuclear-se grups d'espins invertits que creixen per finalment formar configuracions laberíntiques fora del pla separades per zones amb ordre en el pla en forma de vòrtexs. El fet més remarcable ara és que, l'estat atès al final del ciclat persisteix quan deixem d'aplicar camp i, lluny de tendir a l'estat fonamental dins del pla, l'estructura incipient s'estabilitza en retirar el camp i deixar passar el temps.

## 12.5 Relaxació quàntica

En aquesta última secció hem adreçat la influència dels efectes quàntics, a temperatura zero, en la dinàmica de la magnetització. Més concretament, ens hem interessat en el problema del desancoratge (depinning) de parets de domini ferromagnètiques a causa de l'efecte túnel macroscòpic de la magnetització. Així doncs, hem calculat el ritme de transició túnel d'una paret de domini a través d'una barrera en forma d'un defecte planar que l'ancora.

Hom pot sentir certa incomoditat en intentar aplicar la mecànica quàntica a una variable clàssica tal com el vector de magnetització

$$\mathbf{M}(\mathbf{x}, t) = \left\langle 2\mu_B \sum_i \hat{s}_i \delta(\mathbf{x} - \mathbf{x}_i) \right\rangle. \quad (12.22)$$

Tot i així, aquest problema no és massa diferent a la desintegració  $\alpha$  d'un nucli. En aquest cas, hom no té massa problemes en ignorar que la partícula  $\alpha$  està formada per nucleons o quarks i justifica aquesta aproximació pel fort acoblament entre els nucleons a l'interior de la partícula  $\alpha$ . De manera semblant, el fort acoblament d'intercanvi en un ferromagnet ens permet considerar  $\mathbf{M}(\mathbf{x}, t)$ , i no els spins individuals [46], com una variable túnel. Noteu que l'aproximació de Feynman a la teoria quàntica de camps, en la qual es basa el càlcul quàntic d'amplituds de transició, no especifica com de fonamental ha de ser el camp considerat. Només requereix disposar d'una Lagrangiana clàssica que descriu el sistema en qüestió. Aquesta funció Lagrangiana, en el cas de la magnetització, es pot construir pel mateix procediment que s'obté la integral de camí per partícules amb spin [47, 48, 49, 50], arribant-se a la següent expressió per l'amplitud túnel

$$\mathcal{K}_{if} = \int \mathcal{D}\phi \mathcal{D}(\cos \theta) e^{-S_E/\hbar}. \quad (12.23)$$

On la Lagrangiana que apareix a l'acció Euclídea  $S_E = \int d\tau L_E$  ve donada per

$$L_E = i\hbar S \dot{\phi} (1 - \cos \theta) + E(\theta, \phi), \quad (12.24)$$

on  $S$  és l'spin de la partícula, la direcció del qual ve caracteritzada pel vector unitari  $\mathbf{n}$  en termes dels angles esfèrics  $(\theta, \phi)$ , i  $E(\theta, \phi)$  és l'energia "semi-clàssica" de la partícula. Les equacions del moviment que es deriven d'aquesta acció coincideixen amb la versió en temps imaginari de les equacions de Landau-Lifschitz [51].

En el model per la paret de domini hem considerat aquesta com una superfície d'energia  $\sigma_0$ , per unitat d'àrea. Sota la hipòtesi de curvatura feble i moviment lent de la paret, vàlides pel problema de tunelatge quàntic en el límit de barreres d'energia petites, estarem interessats a descriure només moviments de la paret en la direcció transversal al seu pla. Parametritzant la paret amb la coordenada  $Z(x, y, t)$ , podem finalment escriure l'acció Euclídea,  $S_E = iS$ , en la forma

$$S_E = -\frac{\sigma\delta^2}{\omega} \int d^3x \left\{ (1 + [\nabla\bar{z}(\mathbf{x})]^2)^{1/2} + u(x_1, x_2, \bar{z}) - h\bar{z}(\mathbf{x}) \right\}, \quad (12.25)$$

on  $\mathbf{x} = (x_0, x_1, x_2)$ ,  $\nabla = (\partial_0, \partial_1, \partial_2)$  i  $\omega = v_0/\delta$ . En aquesta expressió s'han emprat les variables adimensionals

$$\begin{aligned} x_0 &= \omega\tau & x_1 &= x/\delta \\ x_2 &= y/\delta & \bar{z} &= z/\delta \\ u &= U(x, y, z)/\sigma_0 & h &= 2M_0H\delta/\sigma_0, \end{aligned} \quad (12.26)$$

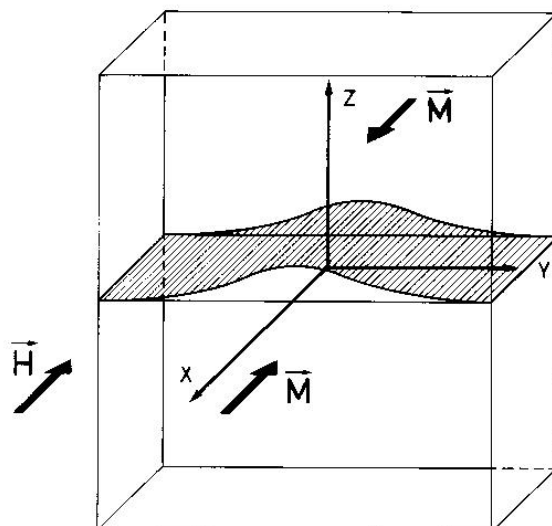


Figura 12.23: Desacoblament d'una paret de domini d'un defecte planar localitzat al pla XY.

on  $\delta$  és l'amplada de la paret de domini,  $U(x, y, z)$  és el potencial d'ancoratge i  $H$  el camp magnètic aplicat. Si considerem centres d'ancoratge en forma de defectes plans, i en el límit de curvatura petita de la paret ( $(\nabla\bar{z})^2 \ll 1$ ),  $S_E$  es redueix a

$$S_E = -\frac{\sigma_0 \delta^2}{\omega} \int d^3x \left\{ \frac{1}{2} (\nabla\bar{z})^2 + u(\bar{z}) - h\bar{z} \right\}. \quad (12.27)$$

Partint d'aquesta expressió, hem evaluat els exponents túnel WKB i els ritmes de tunelatge a través del potencial d'ancoratge en els casos particulars d'una paret d'àrea  $A_w$  petita (1+1 dimensions) i àrea gran en comparació a la del defecte planar (2+1 dimensions). El potencial d'ancoratge considerat és de la forma més general possible, amb un mínim a  $\bar{z} = \bar{z}_1$  i un punt d'escapament a  $\bar{z} = \bar{z}_2$ , tal i com es mostra a la Fig. 12.24, entre els quals la paret de domini tuneleja. El mètode de càlcul de la probabilitat túnel es basa en el càlcul d'instantons, segons el qual aquesta quantitat es pot escriure com

$$P = A \exp(-B_0), \quad (12.28)$$

on l'exponent WKB ve donat per  $B_0 = -S_E/\hbar$ . L'acció Euclídea  $S_E$  resulta de substituir la trajectòria clàssica en temps imaginari (instantó) en l'acció de l'Eq. 12.27. El prefactor  $A$  recull la contribució a l'acció de trajectòries que són petites pertorbacions al voltant de la trajectòria clàssica i, per tant, d'ordre superior.

En (1 + 1) D, aquesta trajectòria es pot trobar exactament, amb el resultat

$$\bar{z}(\tau) = z_2 / \cosh^2(\omega_0 \tau), \quad (12.29)$$

on

$$\omega_0 = \frac{2(2h_c \epsilon)^{1/4}}{\bar{w}^{1/2}} \omega. \quad (12.30)$$

El càlcul demostra doncs un fet interessant: en el límit de barrera petita, la forma de l'instantó és universal i no depèn dels detalls del potencial d'ancoratge considerat. Substituint a l'acció, s'obté finalment

$$B_0^{(1+1)} = \frac{48}{5} \frac{\gamma H_c}{\omega} (\bar{w})^{3/2} h_c^{1/4} 2\epsilon^{5/4} N. \quad (12.31)$$

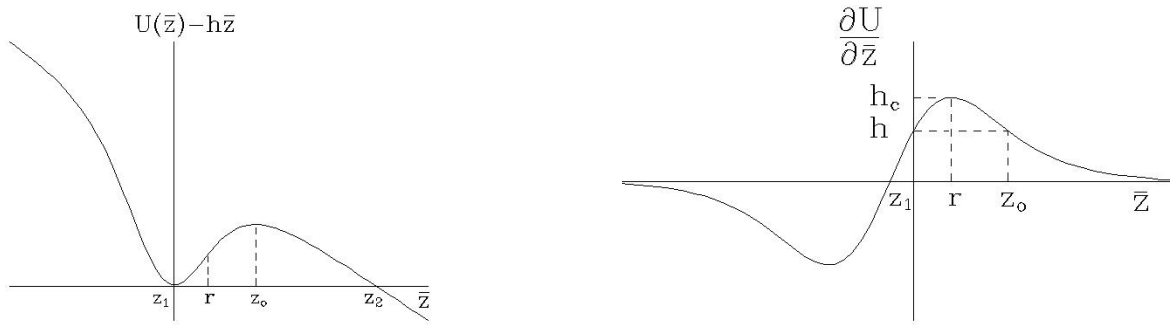


Figura 12.24: Esquerra: Forma general del potencial d'ancoratge,  $u(z) - hz$ . Dreta:  $\partial u(z)/\partial z$  vs  $z$ .

El càlcul del factor preexponencial només es pot dur a terme de forma analítica en el cas (1 + 1)D i requereix l'avaluació dels determinants dels operadors associats a les equacions del moviment donades per l'acció Euclídea, amb i sense el potencial d'ancoratge. Expressions que venen donades en termes del nombre d'espins que tunelejen,  $N = M_0 A_w \delta / \mu_B$ , del camp crític per la desaparició de la barrera  $h_c$  ( $\epsilon = 1 - h/h_c$ ) i on  $\bar{W}$  és un paràmetre que caracteritza la forma del potencial.

En 2 + 1 dimensions, en càlcul procedeix de manera semblant, encara que en aquest cas l'instàntó no es pot calcular de manera exacta. Ara, l'exponent WKB ve donat per

$$B_0^{(2+1)} = 2^{1/4} k \frac{\gamma H_c}{\omega} \bar{w}^{3/2} h_c^{1/4} \epsilon^{5/4} N, \quad (12.32)$$

on  $k \sim 1$ . Comparant aquesta expressió amb l'obtinguda en 1 + 1 dimensions (Eq. 12.31), veiem que la dependència en els paràmetres que controlen la forma del potencial i el camp magnètic és la mateixa i per tant veiem un cop més que el càlcul sembla ser força universal.

Per poder evaluar a partir de quina temperatura els efectes quàntics considerats fins ara predominaran sobre els processos de relaxació tèrmica clàssics, hem definit la temperatura de canvi de règim  $T_c$  com aquella per la qual els ritmes de transició tèrmic i quàntic són del mateix ordre, és a dir  $k_B T_c = U_0/B_0$ , on  $U_0$  és l'altura de la barrera energètica que separa el mínim i el punt d'escapament del potencial. Aquesta quantitat es pot calcular fàcilment en ambdós casos com

$$U_0^{1+1} = \frac{8\sqrt{2}}{3} \mu_B H_c \bar{w} h_c \epsilon^{3/2} N \quad (12.33)$$

$$U_0^{2+1} = \frac{24\sqrt{2}}{5} \mu_B H_c \bar{w} h_c^{1/2} \epsilon^{3/2} N. \quad (12.34)$$

D'aquesta manera les temperatures de transició esdevenen

$$k_B T_c^{1+1} = \frac{5\sqrt{2}}{36} \hbar \omega (\bar{w})^{-1/2} h_c^{1/4} \epsilon^{1/4} \quad (12.35)$$

$$k_B T_c^{2+1} = \frac{12 \times 2^{1/4}}{5k} \hbar \omega \bar{w}^{-1/2} h_c^{1/4} \epsilon^{1/4}. \quad (12.36)$$

Comparant ambdues expressions veiem altre cop la dependència universal en els paràmetres.



Finalment, hem estudiat els efectes dissipatius en el ritme de tunelatge quàntic. Aquests efectes recullen la interacció de la paret de domini amb graus de llibertat microscòpics de l'entorn, com poden ser electrons de conducció, magnons, fonons i fotons. En general, les contribucions dels diferents mecanismes de dissipació a l'exponent WKB es poden recollir sota la forma

$$B \sim B_0 \left(1 + \frac{\nu}{\omega_0}\right), \quad (12.37)$$

on  $B_0$  és l'exponent WKB en absència de dissipació,  $\omega_0$  la freqüència característica de l'instatò i  $\nu$  la constant de dissipació Ohmica, l'expressió de la qual depèn del mecanisme dissipatiu considerat.

De les expressions deduïdes veiem que, per tal que la temperatura de transició  $T_c$  al règim quàntic sigui assolible al laboratori, la possibilitat d'observació d'efecte túnel de parets de domini es veu afavorida en materials amb alta anisotropia uniaxial i amb alta mobilitat de les parets per disminuir els efectes dissipatius. Tanmateix, l'ajust del camp magnètic a valors propers al del camp crític  $H_c$  (disminuint així  $\varepsilon$ ) disminueix la barrera d'energia, incrementant la probabilitat de túnel quàntic, però amb l'inconvenient de disminuir  $T_c$ .

## 12.6 Conclusions

- Hem estudiat les propietats d'equilibri de partícules monodomini. Mitjançant la introducció del concepte de distribució efectiva de barreres d'energia, hem mostrat com el camp magnètic modifica les barreres d'energia d'un conjunt de partícules sense interacció. La inclusió en el càlcul de les corbes de magnetització d'equilibri d'un terme d'energia d'anisotropia finita, de la distribució de valors de les constants d'anisotropia i de l'orientació aleatòria de les partícules, posa de manifest les desviacions de la dependència  $m(h)$  respecte la llei de Langevin quan aquests, trets característics de les mostres reals, es tenen en compte.
- Hem investigat els efectes de mida finita i de superfície en sistemes de partícules petites mitjançant simulacions Monte Carlo d'un model d'una partícula de maghemita. Alguns dels resultats de l'aplicació del model estan qualitativament d'acord amb resultats experimentals tals com la reducció de la temperatura d'ordenament magnètic, la magnetització espontània i el camp coercitiu amb la reducció de la mida de les partícules. No obstant això, en contradicció de les hipòtesis fetes per alguns autors, el nostre model no prediu cap transició de la capa superficial cap a un estat de tipus vidre d'spin. El resultat indiquen que el desordre magnètic a la superfície facilita simplement la desmagnetització tèrmica de la partícula a camp nul, mentre que la magnetització es veu incrementada a camp moderats, ja que el desordre superficial disminueix les correlacions ferrimagnètiques a l'interior de la partícula. El canvi en la forma dels cicles d'histeresi amb la mida de la partícula demostra que el mode d'inversió està fortament influenciat per la reducció de la coordinació atòmica i el desordre a la superfície.
- Hem proposat un model fenomenològic a l'estudi dels processos de relaxació tèrmica en conjunts d'entitats magnètiques no interactuants o amb interaccions febles. El mètode, basta en l'escalat  $T \ln(t/\tau_0)$  de les corbes de relaxació a temperatures diferents, permet extrapolar el comportament de la llei de relaxació a temps que són completament inaccessibles experimentalment. A partir d'aquest escalat, es pot determinar també la freqüència d'intent  $1/\tau_0$ , així com l'amplada  $\sigma$  de la distribució de barreres d'energia que contribueixen a la relaxació i la barrera mitjana. També hem discutit críticament la validesa de l'aproximació logarítmica proposant un criteri per estimar el seu rang de validesa i remarcant els malentesos que poden sorgir d'una anàlisi només en termes de l'anomenada

viscositat magnètica. A més, mitjançant l'aplicació de l'esquema proposat a dades experimentals, he mostrat com es pot obtenir la distribució de barreres d'energia d'un sistema magnètic a partir de la derivada logarítmica de les corbes mestres de relaxació.

- Hem proposat un model per l'estudi de la dependència de la magnetització en el temps en presència d'un camp magnètic, basat en una aproximació de dos estats vàlida a baixa temperatura. La solució numèrica de les equacions per  $m(t)$  ens ha permès estendre el mètode de l'escalat  $T \ln(t/\tau_0)$  a casos en els quals el camp magnètic porta el sistema cap l'estat d'equilibri. Hem remarcat la importància que té una normalització adequada quan s'han de comparar corbes de relaxació mesurades a temperatures diferents, destacant que se'n podrien derivar contribucions d'origen no tèrmic a la relaxació erròniament. A més, a través de l'anàlisi de les distribucions efectives de barreres d'energia deduides de les corbes de relaxació mesures, hem mostrat com, en aquest cas, és possible trobar una variable d'escala per les corbes de relaxació a diferents camps i una temperatura fixada. Aquest és un nou tipus d'anàlisi d'escalat del qual es pot extreure la dependència de les barreres d'energia amb el camp a partir d'experiments de relaxació, una informació que seria molt difícil d'obtenir per altres mètodes.
- El paper de les interaccions dipolars en els processos de dependència temporal s'ha estudiat amb simulacions Monte Carlo d'una cadena 1D d'espins interactuants. Hem conclòs que l'aleatorietat dels eixos d'anisotropia i la frustració induïda per les interaccions dipolars donen lloc a ritmes de relaxació més ràpids, canviant la dependència en el temps de quasi logarítmica a llei potencial en augmentar la interacció. Hem demostrat que l'escalat  $T \ln(t/\tau_0)$  de les corbes de relaxació s'acompleix també per sistemes interactuants i hem provat que és una eina útil per l'anàlisi de les corbes de relaxació, també en aquest cas. En particular, el mètode ens ha permès d'extreure les barreres efectives d'energia que contribueixen a la dependència en el temps de  $m$  i mostrar que, a mesura que la interacció augmenta, es mouen cap a valors menors de l'energia, d'acord amb els resultats experimentals. Els resultats de la simulació dels cicles d'histeresi estan d'acord amb una reducció del camp coercitiu i de la romanència en augmentar la interacció, i la forma dels cicles s'assembla a la dels cicles de sistemes amb frustració magnètica.
- De les simulacions de l'estat fonamental i la relaxació magnètica d'un model de capa prima consistent en una xarxa bidimensional quadrada de spins Heisenberg amb anisotropia perpendicular, interaccions d'intercanvi i dipolars de llarg abast, hem trobat que el model es capaç de reproduir les diferents configuracions magnètiques que es troben en mostres reals per un ampli rang de valors dels paràmetres d'interacció. Hi ha un cert rang de valors dels acoblaments d'intercanvi i dipolars pels quals configuracions amb ordre fore i dintre del pla de la capa presenten degeneració en energia. Hem mostrat que quan un sistema en aquesta regió de paràmetres és pertorbat per una força externa que posteriorment es retira, es poden induir diferents tipus d'ordre depenent del procedimnet seguit. Concretament, les simulacions de les relaxacions des de l'estat de saturació sota un camp desmagnetitzant a.c. o sota camp nul reproduïxen qualitativament amb resultats experimentals recents en capes primes epitaxials i i d'aliatges granulars, que mostren una àmplia varietat de configuracions magnètiques depenent de la història magnètica a la qual han estat sotmeses.
- Finalment, hem presentat un estudi teòric dels processos quàntics de relaxació en sistemes magnètics. Hem abordat el càlcul del ritme de tunelatge quàntic d'una paret de domini a través de la barrera formada per un defecte planar, obtenint resultats per diferents casos d'ancoratge en termes dels paràmetres macroscòpics dels ferromagnets i mostrant el comportament universal de l'exponent WKB en el límit de barreres petites. Hem discutit la possible observació d'aquests efectes quàntics macroscòpics en ferromagnets, concloent que les temperatures de canvi de règim de relaxació dominada per efectes tèrmics a quàntics són a l'abast dels experiments i que els efectes de la dissipació es poden minimitzar amb l'elecció adequada dels materials.



## Bibliografia

- [1] R. H. Kodama, S. A. Makhlof, and A. E. Berkowitz, *Phys. Rev. Lett.* **79**, 1393 (1997).
- [2] M. García del Muro, X. Batlle, and A. Labarta, *Phys. Rev. B* **59**, 13584 (1999).
- [3] B. Martínez, X. Obradors, L. Balcells, A. Rouanet, and C. Monty, *Phys. Rev. Lett.* **80**, 181 (1998).
- [4] J. Z. Jiang, G. F. Goya, and H. R. Rechenberg, *J. Phys.: Condens. Matter* **11**, 4063 (1999).
- [5] X. Batlle, M. García del Muro, and A. Labarta, *Phys. Rev. B* **55**, 6440 (1997).
- [6] J. Dormann, R. Cherkaoui, L. Spinu, M. Nogués, F. Lucari, F. D’Orazio, D. Fiorani, A. García, E. Tronc, and J. Jolivet, *J. Magn. Magn. Mater.* **187**, L139 (1998).
- [7] S. Mørup and E. Tronc, *Phys. Rev. Lett.* **72**, 3278 (1994).
- [8] P. Jonsson and P. Nordblad, *Phys. Rev. B* **62**, 1466 (2000).
- [9] R. H. Kodama and A. E. Berkowitz, *Phys. Rev. B* **59**, 6321 (1999).
- [10] H. Kachkachi, A. Ezzir, M. Nogués, and E. Tronc, *Eur. Phys. J. B* **14**, 681 (2000).
- [11] Z. X. Tang, C. M. Sorensen, K. J. Klabunde, and G. C. Hadjipanayis, *Phys. Rev. Lett.* **67**, 3602 (1991).
- [12] D. H. Han, J. P. Wang, and H. L. Luo, *J. Magn. Magn. Mater.* **136**, 176 (1994).
- [13] J. M. D. Coey, *Phys. Rev. Lett.* **27**, 1140 (1971).
- [14] A. H. Morrish and K. Haneda, *J. Appl. Phys.* **52**, 2496 (1981).
- [15] R. H. Kodama, A. E. Berkowitz, E. J. McNiff, and S. Foner, *Phys. Rev. Lett.* **77**, 394 (1996).
- [16] D. Lin, A. C. Nunes, C. F. Majkrzak, and A. E. Berkowitz, *J. Magn. Magn. Mater.* **145**, 343 (1995).
- [17] J. J. Préjean and J. Souletie, *J. Physique (France)* **41**, 1335 (1980).
- [18] L. Néel, *C. R. Acad. Sci. Paris* **228**, 664 (1949).
- [19] S. W. Charles and R. E. Rosensweig, *J. Magn. Magn. Mater.* **39**, 190 (1983).
- [20] S. Linderöth, L. Balcells, A. Labarta, J. Tejada, P. V. Hendriksen, and S. A. Sethi, *J. Magn. Magn. Mater.* **124**, 269 (1993).
- [21] R. W. Chantrell, M. El-Hilo, and K. O’Grady, *IEEE Trans. Magn.* **27**, 3570 (1991).
- [22] E. Vincent, J. Hammann, P. Prené, and E. Tronc, *J. Phys. I France* **4**, 273 (1994).

- [23] P. L. Kim, C. Lodder, and T. Popma, *J. Magn. Magn. Mater.* **193**, 249 (1999).
- [24] A. Lisfi, J. C. Lodder, P. de Haan, T. Bolhuis, and F. J. G. Roesthuis, *J. Magn. Magn. Mater.* **193**, 258 (1999).
- [25] I. D. Mayergoyz, A. Adly, C. Korman, M. Huang, and C. Krafft, *J. Appl. Phys.* **85**, 4358 (1999).
- [26] M. García del Muro, X. Batlle, and A. Labarta, *Phys. Rev. B* **59**, 13584 (1999).
- [27] L. Balcells, O. Iglesias, and A. Labarta, *Phys. Rev. B* **55**, 8940 (1997).
- [28] R. Sappey, E. Vincent, N. Hadacek, F. Chaput, J. P. Boilot, and D. Zins, *Phys. Rev. B* **56**, 14551 (1997).
- [29] G. Prinz and K. H. (eds.), *Physics Today* (AIP, New York, April 1995), pp. 24–63, special issue on the subject.
- [30] R. Allenspach and A. Bischof, *Phys. Rev. Lett.* **69**, 3385 (1992).
- [31] D. J. Webb and J. D. McKinley, *Phys. Rev. Lett.* **70**, 509 (1993).
- [32] A. B. MacIsaac, K. De’Bell, and J. P. Whitehead, *Phys. Rev. Lett.* **80**, 616 (1998).
- [33] R. Allenspach, M. Stampanoni, and A. Bischof, *Phys. Rev. Lett.* **65**, 3344 (1990).
- [34] M. Hehn, S. Padovani, K. Ounadjela, and J. P. Boucher, *Phys. Rev. B* **54**, 3428 (1996).
- [35] A. E. Berkowitz, J. R. Michell, M. J. Carey, A. P. Young, S. Zhang, F. E. Spada, F. T. Parker, H. Hutten, and G. Thomas, *Phys. Rev. Lett.* **68**, 3745 (1992).
- [36] J. Q. Xiao, J. S. Jiang, and C. Chien, *Phys. Rev. Lett.* **68**, 3749 (1992).
- [37] A. D. Kent, U. Rüdiger, J. Yu, L. Thomas, and S. S. P. Parkin, *J. Appl. Phys.* **85**, 5243 (1999).
- [38] E. D. Dahlberg and R. Proksch, *J. Magn. Magn. Mater.* **200**, 720 (1999).
- [39] V. Franco, X. Batlle, A. Valencia, A. Labarta, and K. O’Grady, *IEEE Trans. Magn.* **34**, 912 (1998).
- [40] V. Franco, X. Batlle, and A. Labarta, *Eur. Phys. J. B* **17**, 43 (2000).
- [41] J. F. Gregg, W. Allen, K. Ounadjela, M. Viret, M. Hehn, S. M. Thompson, and J. M. D. Coey, *Phys. Rev. Lett.* **77**, 1580 (1996).
- [42] D. M. Donnet, K. M. Krishnan, and Y. Yajima, *J. Phys. D* **28**, 1942 (1995).
- [43] S. Kirpatrick, D. C. Gellat, and M. P. Vecchi, *Science* **220**, 671 (1983).
- [44] A. B. Kashuba and V. L. Pokrovsky, *Phys. Rev. B* **48**, 10335 (1993).
- [45] M. Hehn, K. Cherifi-Khodjaoui, K. Ounadjela, J. P. Boucher, and J. Arabski, *J. Magn. Magn. Mater.* **165**, 520 (1997).
- [46] E. M. Chudnovsky, *Sov. Phys. JETP* **50**, 1035 (1979).
- [47] J. Klauder, *Phys. Rev. D* **19**, 2349 (1979).
- [48] L. S. Schulman, *Techniques and Applications of Path Integration* (Wiley and Sons, New York, 1981).

- 
- [49] E. Fradkin, *Field Theories of Condensed Matter Systems*, *Frontiers in Physics* v. 82 (Addison Wesley, Redwood City, CA, 1991).
- [50] A. Garg and G. H. Kim, *Phys. Rev. B* **45**, 12921 (1992).
- [51] L. D. Landau and E. M. Lifschitz, *Zh. Phys. Sowjet.* **8**, 153 (1935).



## Agraïments

*Nadie emprende  
este camino salvo  
el crepúsculo de otoño*  
BASHO

No voldria acabar aquest treball sense agrair i recordar a tots aquells que l'han acompanyat durant aquest llarg camí. En primer lloc vull donar les gràcies al director d'aquesta tesi, el Dr. Amílcar Labarta per la confiança que ha dipositat en mi des que vàrem començar aquest treball i l'atenció incondicional que m'ha dedicat. Al seu costat he intentat treballar amb el rigor i l'exigència que sempre m'ha demostrat tenir. Amb ell he tingut el plaer de viure la ciència i compartir música, lectures i quelcom més que treball. També a la resta de membres del grup de magnetisme i propietats de transport en el qual he realitzat la meua recerca, i en especial al Dr. Xavier Batlle pel seu ajut i amistat. Sense el suport i dedicació de tots ells, no hauria mai arribat a posar fi a aquest treball que més d'un cop he vist com a inacabable.

Voldria agrair al Dr. Javier Tejada l'oportunitat que va donar-me en entrar a treballar al seu grup durant els primers estadis del meu treball com a científic. Així mateix, la meua recerca no hauria estat la mateixa sense el suport dels professors Eugene Chudnovsky i Philip Stamp, que em van brindar l'oportunitat d'aprendre al seu costat en les estades a New York i Vancouver, d'ells em queda més que un bon record.

Vull també agrair als membres del tribunal per acceptar formar part del mateix: Dr. José Rivas (Univ. Santiago Compostela), Dr. Xavier Batlle (UB), Dr. Antoni Planas (UB), Dr. Fèlix Ritort (UB) i Dr. Jesús González (ICMM-CSIC).

No m'agradaria oblidar als molts amics que, a fora i dins del treball m'han acompanyat durant aquest temps. De ben segur ningú m'ha hagut d'aguantar tant de temps com la Montse, com ella diria, la meua altra mitat de lo meu despatx. Companya d'ocupació d'aquestes quatre parets cada cops menys blanques des que en Llorenç Vallès va marxar, gràcies a ell em guanyo les garrofes. Recordant els meus principis, he d'agrair a *mon petit frère* i amic Lluís per haver-me fet baixar dels núvols de la Física Teòrica i fer-me adonar que també es pot fer ciència tocant de peus a terra. Gràcies a ell vaig començar a treballar en el món del magnetisme i aquí continuo, després d'un munt d'estones agradables junts. Els innombrables col·legues de planta 3 i del Departament de Física Fonamental, Les Frères Fonamentaux i el Gduppo de Mannetimmo. En Víctor per la seva imaginació més que científica i en Bart pel seu ajut i recolzament, pels molts tallats i estones que em passat junts. També, per què no, els cents d'alumnes que m'han hagut de suportar a les classes, d'ells he après moltes coses. A la Victòria per haver fet part d'aquest viatge amb mi i haver suportat els ninotets ballarucs que ara dancen en aquestes pàgines. Als logians i les lògies dels dijous, que m'han estalviat moltes hores de psicoanalista. Em sap greu no escriure els noms de tots els amics que han estat i



estan al meu costat, ells saben que estan sempre presents, estic segur que es sabran reconèixer.

Com haureu vist, la meva apacible vida de teòric que es remou les neurones davant d'un paperot amb un llapis a la ma, va acabar el dia que la teoria va passar a ser fenomenologia i més tard computologia. Des d'aleshores, i gràcies a l'herència que em va llegar en Roberto, vaig reconvertir els spins en bits, i el paper en un ordinador que anat canviant al llarg del temps. Un record cibernètic per: Littlefly, Hermes, Macbeth, Cronopio, Mbote i al CESCO pel suport en el temps de càlcul i el maquinari que he utilitzat per realitzar les simulacions d'aquest treball. Des d'aquells dies, la meva esquena ja no ha estat el que va ser. Encara que no et vegi, gràcies per aguantar el cos que porta el meu nom. Aquest ha estat un llarg viatge, no només a través del món del magnetisme, he recorregut quilòmetres d'estanteries de biblioteca, navegat per milers de pàgines web, i he llegit centenars d'articles. Però també la pols del camí i les llargues esperes africanes en companyia del meu amic Miquel han estat responsables de la meva tardança.

Un petó ben gros a la família, per estar incondicionalment al meu costat, sense que els hagi pogut explicar que caram volen dir tots aquests símbols i equacions que he anat deixant pel camí.

Finalment, agraeixo de manera especial l'Anna, la meva estimada companya, que ha compartit la seva vida amb mi i el físic que porto dintre, per tot el suport i afecte que m'ha sabut donar. Ella ha estat el meu impuls constant i m'ha donat la força per acabar aquest treball.

*Then take me disappearin' through the smoke rings of my mind,  
Down the foggy ruins of time, far past the frozen leaves,  
The haunted, frightened trees, out of the windy beach,  
Far from the twisted reach of crazy sorrow.  
Yes, to dance beneath the diamond sky with one hand waving free,  
Silhouetted by the sea, circled by the circus sands,  
With all memory and fate driven deep beneath the waves,  
Let me forget about today until tomorrow.*

BOB DYLAN  
*Mr. Tambourine man (Bring it all back home)*